INFORMATION TO USERS

This manuscript has been reproduced from the microfilm master. UMI films the text directly from the original or copy submitted. Thus, some thesis and dissertation copies are in typewriter face, while others may be from any type of computer printer.

The quality of this reproduction is dependent upon the quality of the copy submitted. Broken or indistinct print, colored or poor quality illustrations and photographs, print bleedthrough, substandard margins, and improper alignment can adversely affect reproduction.

In the unlikely event that the author did not send UMI a complete manuscript and there are missing pages, these will be noted. Also, if unauthorized copyright material had to be removed, a note will indicate the deletion.

Oversize materials (e.g., maps, drawings, charts) are reproduced by sectioning the original, beginning at the upper left-hand corner and continuing from left to right in equal sections with small overlaps.

Photographs included in the original manuscript have been reproduced xerographically in this copy. Higher quality 6" x 9" black and white photographic prints are available for any photographs or illustrations appearing in this copy for an additional charge. Contact UMI directly to order.

Simulation of Fluctuating Wind Pressures on Low Building Roofs

Kumaresannair Suresh Kumar

A Thesis

in

The School for Building

Presented in Partial Fulfilment of the Requirements
for the Degree of Doctor of Philosophy at
Concordia University
Montreal, Quebec, Canada

August 1997

The author has granted a non-exclusive licence allowing the National Library of Canada to reproduce, loan, distribute or sell copies of this thesis in microform, paper or electronic formats.

The author retains ownership of the copyright in this thesis. Neither the thesis nor substantial extracts from it may be printed or otherwise reproduced without the author's permission.

L'auteur a accordé une licence non exclusive permettant à la Bibliothèque nationale du Canada de reproduire, prêter, distribuer ou vendre des copies de cette thèse sous la forme de microfiche/film, de reproduction sur papier ou sur format électronique.

L'auteur conserve la propriété du droit d'auteur qui protège cette thèse. Ni la thèse ni des extraits substantiels de celle-ci ne doivent être imprimés ou autrement reproduits sans son autorisation.

0-612-39782-3

Canada

ABSTRACT

Simulation of Fluctuating Wind Pressures
on Low Building Roofs

Kumaresannair Suresh Kumar, Ph.D
Concordia University, 1997

Wind pressure fluctuations acting on low building roofs are important for the prediction of peak pressure values and for fatigue design purposes. Collection of several time histories of pressure fluctuations, using traditional wind tunnel measurements is time consuming and expensive. Within this context, a systematic study on the development of an efficient and practical method of digitally simulating realizations of local wind pressure time series has been carried out.

The stochastic characteristics of wind pressure fluctuations acting on various low building roofs have been investigated by using systematic wind tunnel measurements. Thereafter, based on the Fourier representation of time series, a new time series generation technique capable of simulating Gaussian as well as non-Gaussian wind pressure fluctuations is developed. Both Fourier amplitude and phase, which are required for the simulations, are modelled individually. The Fourier amplitude part is constructed either from sample time history or from sample spectra, while a simple stochastic model is proposed for the generation of Fourier phase of non-Gaussian time series. In the present study, the criterion for successful modelling is set to preserve the first four moments (mean, variance, skewness and kurtosis) and spectra of the corresponding pressure fluctuations.

The efficiency of this novel methodology is illustrated with several examples.

Several measured wind pressure spectra have been investigated to determine characteristic spectral shapes and derive a suitable mathematical representation. Based on the similarities among normalized spectra, an empirical model has been suggested for the synthetic generation of normalized spectra. Such artificially produced pressure spectra have been utilized for the generation of Fourier amplitude part in subsequent simulations. Thereafter, for easy generation of pressure time histories on roofs, normalized spectra are categorized for each roof and the standard spectral shapes associated with various zones of each roof and their parameters are established.

Further, potential applications of the proposed simulation methodology in extreme value as well as fatigue analysis are presented. In particular, the fatigue analysis of roof cladding using simulated pressure fluctuations has been described in detail.

"....*The oldest voice in the world is the wind. When it murmurs in summer's leaves, it seems an idle trifler. When in the night it goes wandering by, setting the old house faintly to groaning, it sounds like a pilgrim that has lost the road. When you see it fitfully turning the blades of a mill lazily to draw water, you think of it as an unreliable servant of man. But in truth it is one of our masters, obedient only to the lord sun and the whirling of the great globe itself....*"

Donald Culross Peattie,
A Cup of Sky

ACKNOWLEDGEMENTS

TABLE OF CONTENTS

CHAPTER 7
SPECTRA OF WIND PRESSURES ON LOW BUILDING ROOFS 135

CHAPTER 8
SIMULATION OF PRESSURE TIME SERIES
ON LOW BUILDING ROOFS 163

LIST OF FIGURES

LIST OF TABLES

NOMENCLATURE

a	autoregressive parameter
A	projected area of the object facing wind
$A(\omega_k)$	Fourier coefficient
a_1, a_2, a_3	position constants
A_k	Fourier coefficient
b	probability parameter
b	width of building
c, c_j	Weibull constant
c_1, c_2, c_3	shape constants
Cp, Cp	pressure coefficient
Cp_{mean}	mean pressure coefficient
Cp_{peak}	peak pressure coefficient
Cp_{rmax}	maximum pressure cycle range
Cp_{rms}	root-mean-square pressure coefficient
d	phase shift parameter
D	damage index
D_g	damage due to Gaussian time series
D_{ng}	damage due to non-Gaussian time series
E	mathematical expectation operator
E_t	exponential random variables
F	reduced frequency

$F(t)$	force experienced by the object due to wind
$f(\omega)$	continuous spectral density of $\{X_t\}$
f, f_k	frequency
f_s	sampling frequency
g	dimensionless peak factor
h	mean roof height of the building
h_l	lower eave height
$[H]$	cycle histogram
$I(\omega_k)$	periodogram
I_t	random variables having the discrete PDF Eq. (B.2)
$\sqrt{I_k}$	Fourier amplitude
k	total number of blocks, Weibull constant
K	intercept of the S-N curve plotted on a log-log graph
k_j	Weibull constant
Ku	kurtosis
l	length of building
L	geometric length
m	mean of the time history
m_1	slope of the S-N curve plotted on a log-log graph
m_i	spectral moments
n	time series length
N	number of cycles
N_0	zero up-crossing or down-crossing rate
$N_0 T$	number of zero up-crossing or down-crossing in time T

n_i	total number of cycles in the ith block of constant pressure range, S_{ri}
N_i	number of cycles to failure under S_{ri}
N_m	number of pressure cycles in model scale
N_p	number of pressure cycles in full-scale
N_p	positive or negative peak rate
$N_p(x)$	rate of maxima occurring in the interval $(x, x+dx)$
N_pT	number of positive or negative peaks in time T
N_x	mean x-upcrossing rate
$\bar{n}$	number of cycles per hour per one m/s of mean hourly wind velocity at building height
$[N_T]$	total load cycle distribution
P	probability of X_m less than a particular value
p_j	probability of wind coming from a particular direction
Q	number of observed extreme values
r	rank assigned to an extreme value
$R(\tau)$	autocorrelation function
s	dispersion of extreme values
$S(f)$	spectral density function
$S(\omega_k)$	spectral density of $\{X_t\}$
Sk	skewness
$S_m(f_k)$	mathematical spectrum
S_{mi}	mean pressure
$S_p(f_k)$	physical spectrum
S_{ri}	pressure range associated with S_{mi}
S_{th}	threshold pressure

S_u	ultimate pressure of roofing component
t	time (data points)
T	time
T	time, design life
$\overline{T}$	fatigue mean life time
u	mode of extreme values
$U(t)$	wind velocity
U, $U1$, $U2$	uniform random numbers
V	mean velocity at height Z, mean hourly wind velocity at building height
V	mean velocity at mean roof height
Vg	mean velocity at gradient height Zg
V_i	mean hourly wind velocity at building height
Vrms	root-mean-square velocity
$\overline{V}$	design mean hourly wind velocity at building height corresponding to a specific return period
X_m	random variable associated with extreme values
X_t	target time series, time series
$\overline{X}$	mean of $\{X_t\}$
y	reduced y-variate
Y_t	preliminary signal, skeleton signal, test signal
Z	height
Zg	gradient height
Z_t	simulated time series
$2\pi/n$	fundamental Fourier frequency

Greek symbols

α	roof angle
α_k, β_k	*i.i.d* Gaussian random variables
β	bandwidth parameter
$\gamma(\tau)$	auto-covariance function
Δf	frequency resolution
ΔT	time step
ΔV	small interval of velocity
ε	irregularity factor
ε_t	intermittent exponential random numbers
λ	exponential parameter
μ	shape factor
μ_1	mean of extreme values
ρ	density of air
σ	standard deviation
σ_1	standard deviation of extreme values
σ^2	variance
σ_k^2	variance associated with each frequency ω_k
τ	time shift
$\phi_k , \phi(\omega_k)$	Fourier phase
ω_k	Fourier frequencies

Subscripts

G	Gaussian

m	model scale
NG	non-Gaussian
p	full-scale

Abbreviations

ACF	Auto-Correlation Function
AR	Auto-Regressive
ARIMA	Auto-Regressive Integrated Moving Average
ARMA	Auto-Regressive Moving Average
CDF	Cumulative Distribution Function
DFT	Discrete Fourier Transform
EAR	Exponential Auto-Regressive
EARPG	Exponential Auto-Regressive Peak Generation
EPG	Exponential Peak Generation
FFT	Fast Fourier Transform
GAR	Gamma Auto-Regressive
i.i.d	independent identically distributed
PDF	Probability Density Function
QS	Quasi-Steady
rms	root-mean-square
SDF	Spectral Density Function
SSE	Sum of the Squared Errors
UPS	Uniform Phase Shift

CHAPTER 1
INTRODUCTION

"....we rely on hazard. There is no existence, even for the less imaginative beings, that does not leave room for it in its most obscure forecasts. To count only on hazard is foolish; counting without hazard is even more foolish...."

Remy de Gourmont
Epilogues. Reflexions sur la vie, 1906.

1.1 OVERVIEW

The necessity of providing allowance for expected wind loading in the design of almost all structures is now recognized. Nevertheless, wind hazards are rather common, as clearly shown in Fig. 1.1 indicating that 88% of the total insured property loss from U.S catastrophes during the period of January 1986 to October 1992 resulted from wind storms. In order to accomplish wind hazard reduction, it is necessary to focus on various areas of wind engineering which are presented in Jones et al. (1995).

Wind induces unsteady (fluctuating) loads on earth bound structures along with steady (mean) loads. Extreme localized loads over the surface of a structure are the result of wind-induced pressure fluctuations. The design of cladding and fasteners is based on local pressures, whereas the structural response/structural design is dependent on the integrated effect of pressures over the surface. The characteristics of wind pressure fluctuations depend on numerous features such as mean wind speed and direction, terrain conditions, surroundings, structural geometry, surface texture etc. In general, the pressure fluctuations on the surface of a structure are a result of the turbulence inherent in (1) approach flow, (2)

1
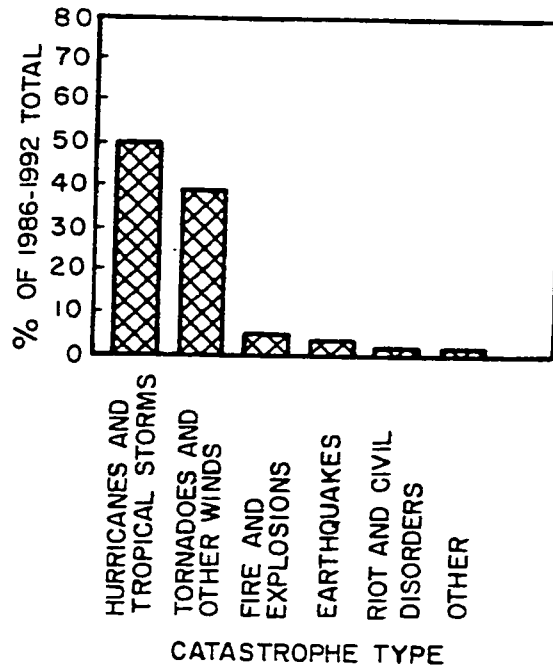
Fig. 1.1 Total insured property loss from U.S. catastrophes, after Jones et al. (1995).

flow separation and potential reattachment, (3) induced motion in case of wind sensitive structures, and (4) vortices shed by upstream structures. It is often assumed that such pressure fluctuations on a building are directly related to oncoming atmospheric turbulence and therefore can be predicted by Quasi-Steady (QS) theory (Cook 1985). QS approach attributes all fluctuations in pressure to fluctuations in wind velocity and its direction. However, QS theory fails to predict unsteadiness in pressure caused by building generated turbulence on roof corners and other flow separation zones on the building envelope with very few notable exceptions (Stathopoulos 1983; Tieleman and Hajj 1995). It has been noted that the frequency content of the pressure at the separated flow faces is quite different from that of the approach velocity due to the building generated turbulence (Letchford et al. 1993). Since the time variation of pressure cannot generally be predicted from the time variation of velocity, it is necessary for design purposes to utilize the characteristics of actual pressure fluctuations on building surfaces.

2

1.2 WIND EFFECTS ON LOW-RISE BUILDINGS

Wind pressures acting on low-rise buildings (height to width ratio less than one and mean roof height less than 20 m, NBCC (1995)) are highly fluctuating since they are located in the lower part of atmospheric boundary layer where wind turbulence and gradient of wind speed dominate. One such pressure-time trace at the roof corner of a full scale multi-span hangar is shown in Fig. 1.2, where the instantaneous pressure after subtracting its mean value, is normalized by its root-mean-square value. Suction peaks of the order of 10 to 15 times the root-mean-square pressure are noted and this is important for a realistic estimation of design loads for roofs. Note also the highly fluctuating nature of wind pressures with respect to time which is important for fatigue design of roofs.
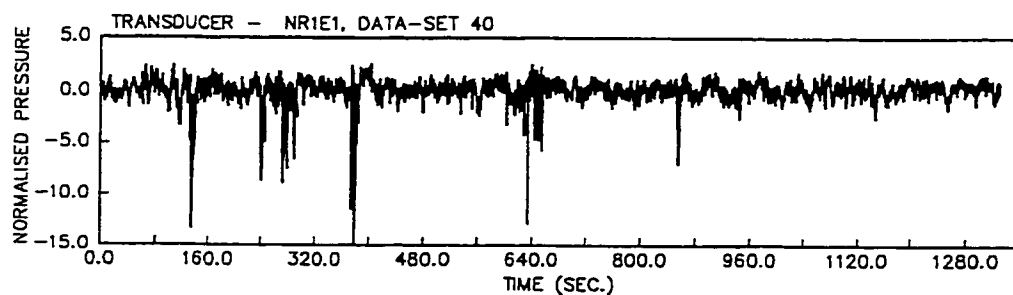
Fig. 1.2 Typical pressure time history, after Milford et al. (1992).

Damage to low-rise buildings results from aerodynamic wind pressures that develop as air flows over and around the building. External negative pressures (suctions) pull walls and roof apart; only the windward wall is subjected to positive pressure. In addition, high local suctions develop at wall corners, eaves, ridge and roof corners because of flow separation as the air particles pass the sharp corners of the building. Such local effects of wind are pictorially shown in Fig. 1.3. These local pressures tend to dislodge the roof and siding materials and cause the failure of connections between the roof and the top of the wall.

3
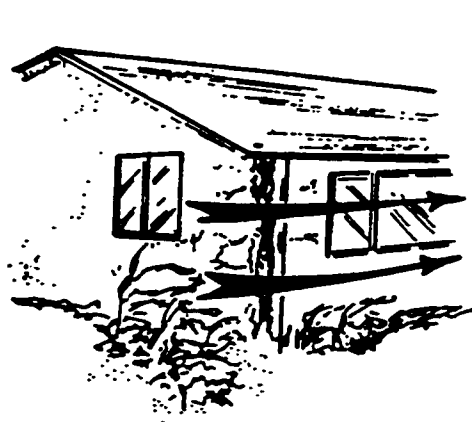
Wall Corner
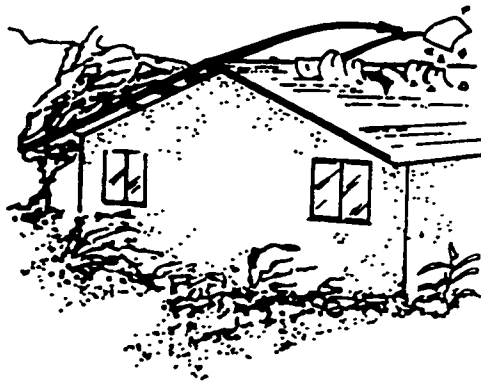
Eave

Ridge
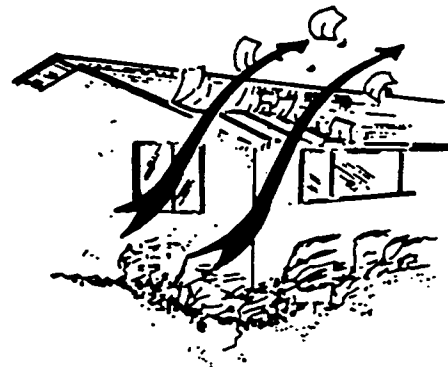
Roof Corner

Fig. 1.3 Local effects of wind, after McDonald (1985).

Reports of wind damage to low-rise buildings indicate that more serious damage occurs to roofs. A typical damage to roof is shown in Fig. 1.4 where the eaves of the building are severely damaged by the high local pressures created by the flow separation at the sharp edge between the wall and roof. Roof failure includes loss of roof covering, failure of fasteners etc. Particularly, the failure of roof due to failure of fasteners has been noticed in many cases. The failure of roofs may lead progressively to the total collapse of the building. Therefore, the roof has to be designed with utmost care.

4
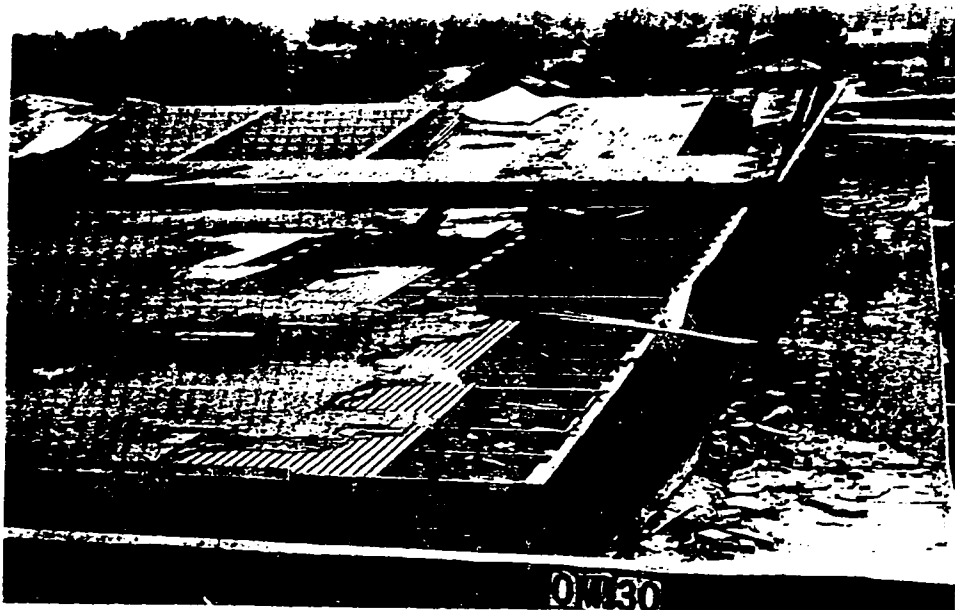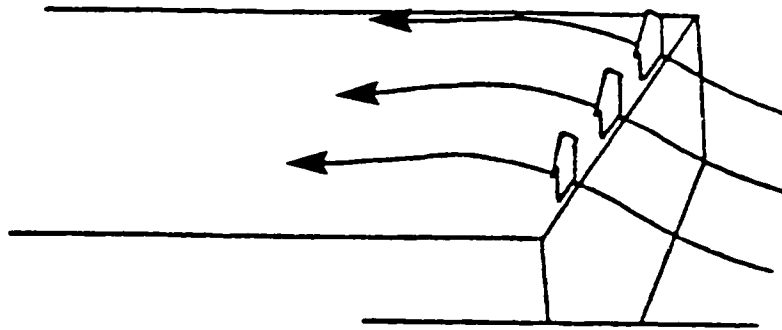
Fig. 1.4 Local roof damage induced by airflow over eaves, after Council on Low-Rise Buildings (1993).

The importance of wind pressure fluctuations on the design of low building components has been realized by researchers and designers more than three decades ago and various attempts were made to incorporate such fluctuating pressures in wind standards and building codes of practice. However, the devastative effect of long time histories of pressure fluctuations during storms has received wider attention more recently. The *ASCE*

5

Committee on Wind Tunnel Studies of Buildings and Structures (1996) notes that such fluctuating pressures acting on low-rise building roofs can create stress reversals and may lead to the failure of fasteners or cladding which is a growing concern in low-rise building industry. This was previously noted by Leicester and Reardon in 1976 and Kramer in 1985. After many years of research, the Australian wind code (AS 1170.2 1989) suggests a simple fatigue loading sequence for cyclone prone areas, while British (Cook 1990) and German (Gerhardt and Kramer 1986) recommendations propose fatigue loading sequences for temperate climatic regions where the predominant source of high wind speeds is large-scale and frequently occurring non-tropical cyclone systems. These traditional cyclic loading sequences do not represent the broadband features of actual wind pressure fluctuations (Patel and Freathy 1984). Moreover, such static proof testing methods are found to be inappropriate if the dynamic response of porous and flexible cladding systems is non-linear and frequency-dependent (Cook 1992). Therefore, it appears that the actual characteristics of pressure fluctuations on various types of buildings under different conditions are required to provide generalized guidelines for the betterment of low building design.

1.3 OBJECTIVE OF THIS STUDY

In the last four decades, boundary layer wind tunnels have been used to investigate wind pressure fluctuations on low buildings. Wind tunnel experiments are time consuming and expensive, especially in collecting several time histories of pressure fluctuations needed for extreme value analysis and fatigue design. Nevertheless, wind tunnel experiments are indeed necessary: (a) to determine wind loads on complex geometric shapes where the

analytical as well as the numerical methodology may be inadequate, and (b) to validate analytical/ numerical results. Further to wind tunnel studies, full-scale experiments can also be carried out but a comprehensive study of pressure fluctuations using full-scale measurements may not be possible since most of the parameters related to building as well as wind are practically unchangeable in a particular full-scale experiment. On the other hand, it may be better to focus one's attention to the development of a suitable analytical/empirical model, which could efficiently represent the inherent variability in pressure fluctuations under different conditions, for easy generation of several time series.

The prime objective of this study is, therefore, **to develop an efficient analytical/empirical representation for the description of true characteristics of wind pressure fluctuations on low building roofs under different conditions.** The work in this thesis concerns only with local pressure fluctuations which govern the design of roof cladding elements such as roof panels and fasteners, that are extremely vulnerable to such fluctuations. The major components of this work include experimental investigation of stochastic characteristics of wind pressure fluctuations on low building roofs, simulation of both Gaussian and non-Gaussian wind pressure fluctuations, modelling, classification and generalization of spectra of wind pressure fluctuations, and application of the simulation methodology in extreme value analysis and fatigue design.

The development of such representation appears extremely useful in simulating a number of time histories that are required to carry out extreme value as well as fatigue analysis. Furthermore, such a model can be an efficient tool to investigate the dynamic behaviour of roof cladding as well as the influence of various parameters on fatigue damage accumulation.

7

1.4 THESIS OUTLINE

This thesis consists of ten chapters, a list of references and four appendices. Digital simulation techniques are briefly reviewed in Chapter 2 with concentration on the methods that are suitable for generating Gaussian as well as non-Gaussian wind pressure fluctuations. Advantages and disadvantages are also cited in relevant cases. The necessary theoretical background for the present study is described in Chapter 3. The experimental procedure as well as the results are described in Chapter 4. In this chapter, detailed discussions about stochastic characteristics of roof pressure fluctuations in time, frequency and amplitude domains are presented.

Chapter 5 describes the simulation of Gaussian pressure fluctuations using the conventional Fast Fourier Transform (FFT) approach. The simulation of non-Gaussian pressure fluctuations are presented in Chapter 6, which includes the development of the model, the importance of stationarity of the simulated time series, as well as demonstrations showing the efficiency of the proposed model.

The simulation of wind pressure fluctuations using the proposed model requires power spectra of the corresponding fluctuations. Though the measurement of spectra is briefly addressed in Chapter 4, detailed material such as empirical modelling, classification of spectra and their generalization is discussed in Chapter 7. Furthermore, Chapter 8 presents the overall simulation methodology with elaborate demonstrations.

The application of the proposed simulation methodology in extreme value analysis and fatigue design is presented in Chapter 9 including specific illustrative examples. Finally, Chapter 10 summarizes the findings of this study. Contributions of this study as well as recommendations for the future work are also provided in this chapter.

CHAPTER 2
A BRIEF REVIEW OF DIGITAL SIMULATION TECHNIQUES

"...one of the more important areas of future development of random vibration theory is the construction of improved models for random excitations..."

S. H. Crandall and W. Q. Zhu, 1983.

This chapter briefly presents the general characteristics of wind pressure fluctuations on building envelopes. This is followed by a brief review of the state-of-the-art on digital simulation techniques suited for generating stationary univariate Gaussian as well as non-Gaussian wind pressure fluctuations.

2.1 WIND PRESSURE FLUCTUATIONS: AN OVERVIEW

Pressure fluctuations at near wall surfaces is still a hot topic of research in fluid dynamics (Simpson 1989). As far as wind engineering is concerned, wind pressure fluctuations on building surfaces are investigated generally using wind tunnel simulations or full-scale measurements. Usually, the studies are concentrated on mean, rms (root-mean-square) and peak values of the pressure time histories without providing much emphasis to other fluctuating characteristics. For instance, power spectrum, probability density functions, crossing rates etc. have received very little attention. Most recently, Computational Fluid Dynamics (CFD) provides another means to evaluate wind pressure fluctuations on building

9

surfaces (Murakami et al. 1991), though more effort is necessary for such numerical simulations, especially on turbulence models and computational efficiency.

At present, wind tunnel measurement results are found to be a comprehensive source of information as far as pressure fluctuation studies are concerned. Since many parameters are involved in the phenomenon and not all of them are fully understood, statistical descriptions of such fluctuations are indeed helpful in understanding their characteristics. Such statistical descriptions can be made in three domains, i.e., time, frequency and amplitude as shown in Fig. 2.1. The first step in statistical description of fluctuations is to confirm whether the

Single pressure time series

Time domain

Autocorrelation

Frequency domain

Power spectrum

Amplitude domain

Probability density function
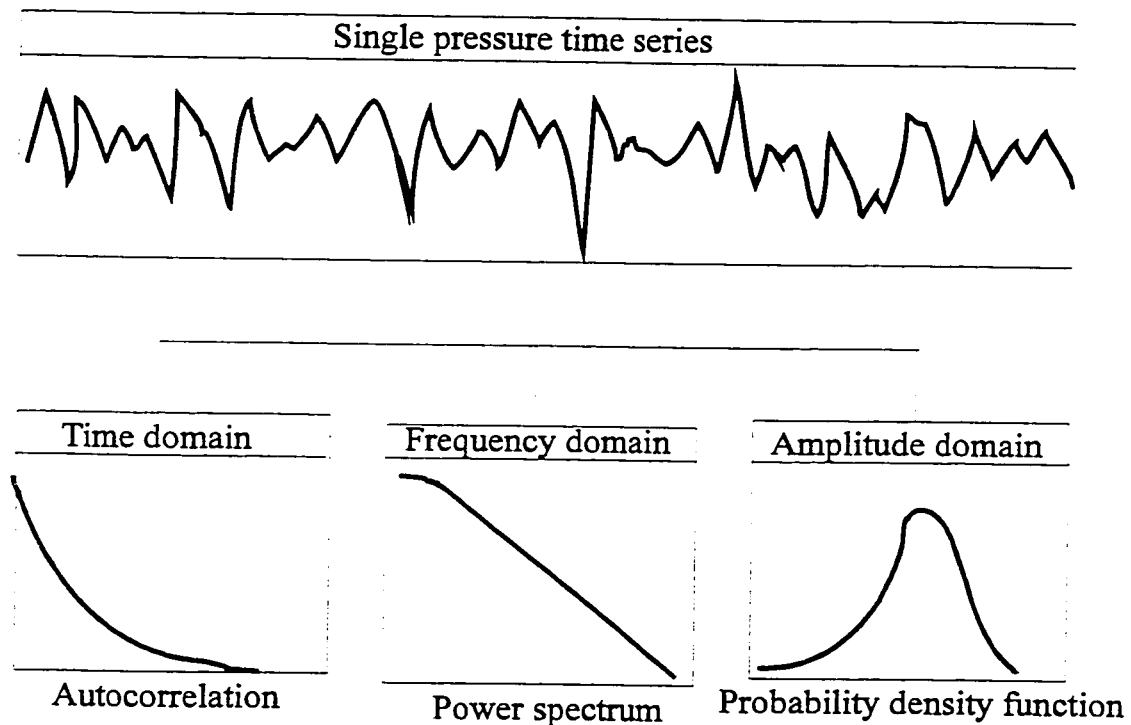
Fig. 2.1 Statistical description of wind pressure fluctuations.

process is stationary or not. In most wind engineering applications, wind velocity as well as pressures are assumed to be weakly stationary which is a reasonably good approximation deduced from experience and this postulation simplifies the mathematical theory. In non-

stationary situations the fluctuations may be transformed into stationary by using the conventional method of differencing (Box and Jenkins 1976) before any statistical descriptions can be made.

The assumption of Gaussian distribution for the Probability Density Function (PDF) is fair only for fluctuations measured on few locations of building surface. Under the Gaussian assumption a second order moment characterization is sufficient since first and second order moments uniquely define a Gaussian distribution (Bendat and Piersol 1986). However, non-Gaussian characteristics of the pressure fluctuations are noted by many researchers in their studies. Peterka and Cermak (1975) showed that probability densities for separation regions are skewed such that probability for large negative fluctuations of six standard deviations is four orders of magnitude greater than that for a Gaussian distribution. Stathopoulos (1980) noted that PDF's of wind pressures acting on low-rise buildings are positively or negatively skewed for positive and negative mean pressures, respectively. The term *skewed* means that the PDF is unsymmetrical and this measures the deviation of data points away from Gaussian density function which is symmetrical. Hence, a skewed PDF indicates the presence of high spikes in the time history of fluctuations. In practice, both Gaussian and non-Gaussian wind pressures have been observed depending on location and wind direction; mostly, non-Gaussian types are observed on corner zones and other separated flow regions (Cermak and Peterka 1975; Stathopoulos 1980). A typical non-Gaussian PDF observed on the edge pressure tap of a 5 m high gable roof building exposed to open country terrain is shown in Fig. 2.2. The dominant negative tail clearly shows that the time series is negatively skewed and this is found to be the case in almost all time series measured on the roof.
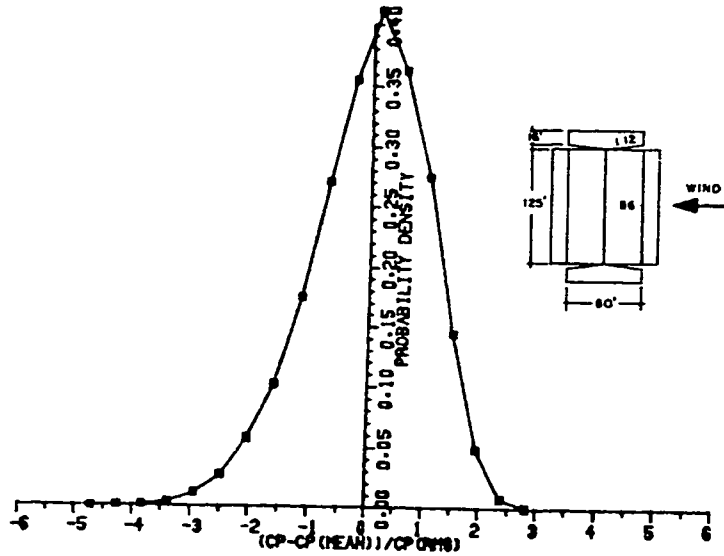
Fig. 2.2 Probability density function of pressure fluctuations, after Stathopoulos (1980).

Moreover, it is clear from the well-known equation,

$$F(t) = \frac{1}{2}\rho U(t)^2 \, Cp \, A \tag{2.1}$$

that $F(t)$ exhibits non-Gaussian properties even if $U(t)$ is Gaussian, where $F(t)$ is force experienced by the object due to wind, $U(t)$ is wind velocity, Cp is mean pressure coefficient, A is projected area of the object facing wind, and ρ is air density. Such non-Gaussian characteristics of probability distribution for dynamic windward wall pressure fluctuations, when the velocity fluctuations have a Gaussian distribution, has been analytically derived, taking account of the square-law relationship between pressure and velocity (Holmes 1981); however, the situation is complex in case of roof pressure fluctuations where building generated turbulence is involved. Thus, for the prediction of PDF and other stochastic characteristics of roof pressure fluctuations, an accurate

simulation of the time history is needed. Within this context, the various digital simulation techniques more generally used in random processes and suited for simulating wind pressure time series were reviewed and are briefly described in the following section.

2.2 DIGITAL SIMULATION TECHNIQUES

The various methods examined are aimed at simulating univariate wind pressure time series without considering cross-correlated fields. For convenience, the simulation techniques are classified into two categories, namely those for Gaussian and non-Gaussian wind pressure fluctuations.

2.2.1 Gaussian Wind Pressure Fluctuations

The possible methods that can be used for the simulation of univariate, stationary, Gaussian wind pressure time series, with specified spectral density, are divided into (1) methods based on Fourier Series (wave superposition), and (2) methods based on the application of an appropriate (analytical) filter subjected to simulated white noise process (linear filtering).

Realizations of a zero-mean Gaussian stationary process with given Spectral Density Function (SDF), have often been generated by using the wave superposition approximation of the form of the sum of evenly spaced cosine waves with weighted amplitudes and frequency range subdivided into equal intervals. The variables such as amplitude, frequency and phase used in the above basic representation denote either deterministic or random parameters. In the spectral representation method (Rice 1954), the phase is selected to be in

13

the form of independent random variables uniformly distributed in the domain [0,2π]. Further, the deterministic amplitudes are defined from the power spectrum of the process. In fact, better approximation of the discrete spectra can be achieved by summing a large number of waves indirectly providing Gaussian distribution to the time series due to the central limit theorem. In this method, deterministic frequency selection is adopted in order to employ the FFT algorithm and increase computational efficiency. However, it is known that the simulated time series using spectral representation method is periodic. In order to avoid periodicity, Borgman (1969) attempted the simulation of ocean surface elevation based on the superposition of cosine waves having constant amplitude and independent random phase angles uniformly distributed from 0 to 2π; the frequency is chosen in such a way that the amplitude of each wave is an equal portion of the spectrum. This method is inefficient due to its time consuming frequency calculations as well as its poor representation of spectral characteristics. Later, Shinozuka and Jan (1972) tried to overcome the periodicity involved in spectral representation method by introducing independent uniformly distributed random frequency fluctuations in a small interval without modifying both amplitude and phase parts, which is the so-called randomized spectral representation method. A random frequency algorithm was also developed in parallel (Goto and Toki 1969; Shinozuka 1971). It relies on independent uniformly distributed phase but the frequencies are identically distributed random variables whose PDF is related to the SDF of the process. In both cases of randomized spectral representation method and random frequency scheme, the FFT algorithm cannot be employed due to non-deterministic frequency selection and, therefore, these methods are not computationally efficient. In contrary, the spectral representation scheme is computationally efficient and produces time

series which are Gaussian and approximately ergodic (Grigoriu 1993). Gaussian signals can also be generated by inverting the Fourier coefficients constructed by linearly combining the Gaussian white noise with a prescribed target spectrum; the simulated signal attains Gaussian form due to the linearity of Fourier representation and the property of Gaussian distribution (Wittig and Sinha 1975). Similarly, Gaussian signals can be generated by inverting the complex Fourier coefficients obtained by combining the uniform random phase with deterministic amplitude constructed from a given power spectrum; this is a different version of the conventional spectral representation method and is widely used for Monte Carlo simulation. Though the FFT algorithm improves the computational efficiency of the wave superposition method, computer memory requirements may be excessive depending on the size of the problem (Kareem 1993). Li and Kareem (1993) also recommended a digital filtering scheme for synthesizing time series segments simulated using the FFT approach to obtain the desired length of time series. A detailed description of the above mentioned simulation techniques has been presented by Grigoriu (1995).

From a computational point of view, simulation using linear filters is far more efficient than the wave superposition method both in terms of computational time and computer storage (Kareem 1993). In this approach, simulated random numbers having zero mean, flat spectrum and Gaussian distribution are fed into a linear filter designed to obtain an output process with a specified spectral density. The various stages, such as model identification, parametric estimation, and diagnostic checking, involved in this iterative approach to model building have been well established for practical use (Box and Jenkins 1976; Pankrats 1983; Chatfield 1989). In addition to the wave superposition method, Borgman (1969) also used this approach for the simulation of ocean surface waves. As far as wind engineering is

15

concerned, Wyatt and May (1973) used a regressive type filter to simulate partly correlated wind forces with a specified power spectrum. Fortier and Scanlan (1979) investigated the applicability of Auto-Regressive Integrated Moving Average (ARIMA) models to fit the pressure time series around a cooling tower. More recently, researchers have attempted to simulate either pressure or wind velocity time series using ARIMA models (Reed and Scanlan 1983; Reed and Scanlan 1984; Islam et al. 1988; Mignolet and Spanos 1990; Li and Kareem 1990). A pertinent application of linear filtering techniques is the simulation of wind pressure fluctuations on monoslope roofs by using an Auto-Regressive (AR) model of order one (Stathopoulos and Mohammadian 1991; Stathopoulos et al. 1997). Despite its advantages over FFT based simulation, the difficulty remains in the selection of proper model. Moreover this method provides stationarity based on time increment while the FFT based approach provides unconditional stationarity (Brockwell and Davis 1991).

2.2.2 Non-Gaussian Wind Pressure Fluctuations

Non-Gaussian time series can be simply generated using Auto-Regressive Moving Average (ARMA) models but replacing Gaussian with non-Gaussian white noise residuals. Typical examples include Exponential Auto-Regressive (EAR), and Gamma Auto-Regressive (GAR) models (Gaver and Lewis 1980). Many studies have been undertaken to show the application of this method (Lawrence and Lewis 1985; Schiess 1986). An AR model of order one with lognormal residuals has also been applied to overcome the underestimation of peak pressure coefficients on corners of monoslope roofs caused by the Gaussian assumption; however, the improvement over the prediction of peak values was only

16

marginal (Mohammadian 1989; Stathopoulos and Mohammadian 1991). Though this method is capable of achieving target Auto-Correlation Function (ACF) as well as non-Gaussian marginal distribution, parametric control of the higher order moment properties is practically impossible. Most recently, non-Gaussian velocity time series in turbulent flows are generated using a bank of linear filters driven by non-Gaussian white noise inputs (Mengali and Micheli 1994). The filter properties are chosen based on the second-order characteristics (SDF) at filter outputs and the higher order moments are accommodated by specifying the statistical properties of the driving noises. However, the analytical solution of this formulation requires many assumptions which may not be applicable to other cases.

One of the widely recommended methods of simulating non-Gaussian time series is to generate Gaussian time series using either ARMA or FFT model followed by a nonlinear static transformation from Gaussian to non-Gaussian. Non-Gaussian vectors with specified distribution function and correlation matrix can be generated using monotonically increasing transformations (Mardia 1970). Shinozuka and Tan (1981) extended this approach to generate non-Gaussian random processes of specified marginal distribution and correlation function by mapping a zero mean unit variance Gaussian process into a non-Gaussian process. The same nonlinear transformations have been applied to generate a translation from the Gaussian process in order to study mean up-crossing rates of non-Gaussian processes (Grigoriu 1984). In another study, a simple power transformation procedure has been applied to convert non-Gaussian to Gaussian wind speed data in order to fit an AR model to the transformed data (Brown et al. 1984). In this case, an undesirable autocorrelation change after inverse transformation is inevitable. However, Yamazaki and Shinozuka (1988) proposed a novel method which first generates a Gaussian process and

17

then maps it into a non-Gaussian process with the aid of an iterative procedure matching the target spectral density. A similar transformation procedure has been attempted by Ammon (1990) where the non-Gaussian process with specified target spectra and probability distribution function is simulated by combining a linear dynamical filter system and a nonlinear static transformation using simple polynomials. Logan et al. (1988) expressed the parent distribution as a five parameter polynomial preserving prominent moments. Afterwards, the data has been transformed from parent distribution to Gaussian using probability integral transformation in order to fit an ARIMA model to the transformed data. A nonlinear instantaneous transformation procedure has also been used to generate non-Gaussian time series by Janacek and Swift (1990). In this approach, the transformation function has been expressed as an orthogonal expansion in terms of a Hermite polynomial deducing the required correlation structure of the Gaussian process to devise a linear filter to generate a Gaussian time series from normally distributed white noise. Though this method provides specific autocorrelation structure, it is agreed that certain combinations of marginal distribution and autocorrelation structure cannot be modelled as the transformation of a Gaussian process. Iyengar and Jaiswal (1993) used a similar approach to model irregularities of Indian railway tracks. In a more recent work, Hermite moment models have been used to represent non-Gaussian processes resulting from the transformation of a standardized Gaussian process (Winterstein 1988; Winterstein and Lange 1995). Using this approach, the other properties of the non-Gaussian process can be easily developed by transforming the well-known results of Gaussian process. However, practical difficulties remain in attaining the target spectral character. In a recent paper by Gurley et al. (1996), correlation distortion method based on a given target spectrum or autocorrelation as well as

18

modified direct transformation method based on a given sample time history have been presented; both the methods used Hermite polynomial transformation. Overall, the above mentioned static transformation techniques are adequate only for weakly non-Gaussian cases according to Seong and Peterka (1993). Most recently, several classes of non-Gaussian processes and their simulation procedures have been described by Grigoriu (1995).

Furthermore, a promising approach which simulates wind pressure fluctuations of non-Gaussian nature with the help of FFT and AR models has been introduced (Seong and Peterka 1993; Seong 1993). This simulation methodology is based on the following three major findings: (1) the variation of phase part does not affect the second order characteristics (variance, ACF, SDF) of the time series, (2) the spikes in the time domain, responsible for non-Gaussian nature, are strongly dependent on the phase part of the Fourier transform in the frequency domain, and (3) the spikes can be transformed from one signal to the other through the phase part of the Fourier Transform without disturbing the spectral characteristics. Consequently, the Exponential Auto-Regressive Peak Generation (EARPG) model combined with a Uniform Phase Shift (UPS) was proposed for the generation of the phase part of the Fourier coefficient. Afterwards, the time series has been simulated by inverting the generated Fourier coefficients which consist of specified amplitude and simulated phase. This model can represent broad band spectra in the frequency domain and many of the fluctuating features in the time domain. It has control over only one of the four statistics (higher order moments : skewness and kurtosis; extreme value statistics: mode and dispersion) of the target fluctuations and has been derived to model pressure fluctuations on flat roof corner zones only.

19

One of the most fundamental tools used in the analysis of any signal is the *power spectrum*. In power spectrum estimation, the signal under consideration is treated as a superposition of statistically uncorrelated harmonic components and the distribution of power among the frequency components is then estimated. It has been recognized that the power spectrum of a signal suppresses its phase part. However, the importance of phase part in producing the spiky features of a non-Gaussian signal has been confirmed in a number of studies (Kareem 1993; Seong and Peterka 1993; Seong 1993). Recent studies also show that more accurate representations of spiky features can be made through implementation of higher-order spectra, which preserve information concerning phase as well as higher order moments. For instance, the simulation of a non-Gaussian process resulting from a quadratic transformation of a Gaussian process is presented by Kareem et al. (1995). This methodology generates non-Gaussian process by inverting the Fourier coefficients after adding the second order contributions to the complex spectral amplitude components at the appropriate sum and difference frequencies. Further study in this regard is necessary in order to comment about the efficiency of this approach.

2.3 GENERAL COMMENTS

A number of methods for simulating stationary Gaussian as well as non-Gaussian time series have been discussed so far; these can be broadly classified as following into ARMA or FFT methodologies. The ARMA approach is based on the simple and well-known theory of linear difference equations and is computationally efficient. However, ARMA models cannot represent data exhibiting sudden spikes of very large amplitude at irregular intervals

20

and having negligible probability of very high level crossings (Tong 1990); therefore, these are not suitable to represent non-Gaussian time series. On the other hand, the FFT-based approach is the most widespread methodology in engineering applications due to its ease in understanding, simplicity and interaction between time and frequency domains. Although the FFT method is not as efficient as ARMA in computational aspects, recent applications of this method for the simulation of non-Gaussian pressure fluctuations as well as perpetual advancement in high speed computers provide considerable amount of optimism to continue research in this area.

Note that the capability of FFT approach in representing the stochastic properties of Gaussian as well as non-Gaussian pressure fluctuations on building envelopes is not fully explored in previous studies. Therefore, further work is required to develop a simple and efficient FFT representation for wind pressure fluctuations on low building roofs. Additional work is also required in modelling the amplitude part in the Fourier representation of pressure time series, which has been neglected in previous studies. Last but not least, generalization of the proposed model should also be investigated.

Chapter 3
Theoretical Background

"...we must welcome the future, remembering that soon it will be the past; and we must respect the past, knowing that once it was all that was humanly possible..."

Gerorge Santayana,
as quoted in Reader's Digest, Mar. 1972.

This chapter presents the necessary theoretical background for the current work. Basic Fourier transform properties of time series are highlighted. In addition, stochastic characteristics of time series such as moment properties, level crossing and peak statistics as well as extreme value statistics are also presented. For more details on this material, see Brockwell and Davis (1991) and Robson (1963).

3.1   Fourier Transform Properties of Time Series

3.1.1   Stationary Time Series

A time series is called strongly stationary, if all its moments and joint moments are time invariant (Bendat and Piersol 1986). If only the first and second moments and their joint moments are time invariant, then the time series is called weakly stationary. Note that in the case of a Gaussian time series, weak stationarity implies strong stationarity since the first and second order moments are sufficient to compute higher order moments. Time series that do not meet the requirements for stationarity are called non-stationary.

3.1.2 Spectral Representation of a Stationary Process

The spectral representation of an arbitrary discrete stationary process is as follows:

$$X_t = \sum_{k=1}^{n} A(\omega_k) e^{it\omega_k} \tag{3.1}$$

in which $-\pi < \omega_1 < \omega_2 < .....< \omega_n = \pi$ and $A(\omega_1), ..., A(\omega_n)$ are uncorrelated complex-valued random coefficients such that

$$E[A(\omega_k)] = 0 \quad , \quad k = 1,2,....,n.$$

and

$$E[A(\omega_k) \, A^*(\omega_k)] = \sigma_k^2 \quad , \quad k = 1,2,....,n.$$

where, * represents complex conjugate. In case X_t is real valued, it is necessary that $A(\omega_k)$ $= A^*(\omega_{n-k})$ for $k = 1, 2,....., n\text{-}1$. Eq. (3.1) fulfills the condition of stationarity since

$$E(X_t) = 0$$

$$E(X_{t+\tau} \, X_t^*) = \sum_{k=1}^{n} \sigma_k^2 \, e^{i\tau\omega_k}$$

where the operator E represents expectation and σ_k^2 represents variance associated with each frequency.

3.1.3 Discrete Fourier Representation of Time Series

Let $X_1, X_2,....., X_n$ be observations from a stationary time series with $\omega_k = 2\pi k/n$, $k \in F_n$, which are equally spaced n frequencies called Fourier frequencies. Note that

23

$$F_n = \{ k: -\pi < \omega_k \equiv \frac{2\pi k}{n} \leq \pi \} = \{ -[\frac{n-1}{2}], -[\frac{n-1}{2}]+1, \ldots\ldots, [\frac{n}{2}]-1, [\frac{n}{2}] \}$$

The process $\{X_t\}$ can be represented as a superposition of random sinusoids in the form

$$X_t = n^{-1} \sum_{k \in F_n} A(\omega_k) \, e^{it\omega_k} \, , \quad t = 1,2,\ldots,n. \tag{3.2}$$

The Discrete Fourier Transform (DFT) of X_t is

$$A(\omega_k) = \sum_{t=1}^{n} X_t \, e^{-it\omega_k} \tag{3.3}$$

Practically, the following DFT representation is used for computation:

$$A_k = \sum_{t=0}^{n-1} X_t \, e^{-i2\pi kt/n} \, , \quad k = 0,1,2,\ldots\ldots,n-1. \tag{3.4}$$

Similarly, the inverse Fourier representation becomes

$$X_t = n^{-1} \sum_{k=0}^{n-1} A_k \, e^{i2\pi kt/n} \, , \quad t = 0,1,2,\ldots\ldots,n-1. \tag{3.5}$$

3.1.4 Periodogram and Spectral Density Estimate

The periodogram of the time series, $\{X_t\}$, is defined by

$$I(\omega_k) = |\sum_{t=1}^{n} X_t \, e^{-it\omega_k}|^2 \tag{3.6}$$

which corresponds to the squared amplitude of the coefficients in the Fourier representation at the Fourier frequencies, $\omega_k = 2\pi k/n$, i.e.

$$I(\omega_k) = |A(\omega_k)|^2 \tag{3.7}$$

The periodogram of $\{X_t\}$ in terms of the sample auto-covariance function ($\gamma(\tau)$) can be expressed as

$$
\begin{aligned}
I(\omega_k) &= n^2 |\bar{X}|^2 && , if \ \omega_k = 0 \\
&= n \sum_{|\tau| < n} \gamma(\tau)\, e^{-i\tau\omega_k} && , if \ \omega_k \neq 0
\end{aligned}
\tag{3.8}
$$

where,

$$
\gamma(\tau) = n^{-1} \sum_{t=1}^{n-|\tau|} (X_t - \bar{X})(X_{t+|\tau|} - \bar{X})
$$

$$
\bar{X} = n^{-1} \sum_{t=1}^{n} X_t
$$

When $\{X_t\}$ is a stationary time series with mean $\bar{X}$ and the autocovariance function, $\gamma(\tau)$ is absolutely summable in the domain of infinite sequence, that is,

$$
\sum_{\tau=-\infty}^{\infty} |\gamma(\tau)| < \infty ,
$$

then a continuous spectral density of $\{X_t\}$ is given by

$$
f(\omega) = (2\pi)^{-1} \sum_{\tau=-\infty}^{\infty} \gamma(\tau)\, e^{-i\tau\omega} , \quad \omega \in [-\pi, \pi]
\tag{3.9}
$$

Thus, knowledge of the autocovariance function is mathematically equivalent to knowledge of spectral density. The striking resemblance between Eqs. (3.8) and (3.9) suggests the potential value of the periodogram for spectral density estimation.

3.1.5 Asymptotic Properties of the Periodogram

In this section, the asymptotic properties of the periodogram of the vector $(X_1, X_2, \ldots, X_n)$

when $\{X_t\}$ is a stationary time series is presented. If $\{X_t\}$ are independent identically distributed (*i.i.d*) Gaussian random variables with variance σ^2, the random variables

$$\alpha_k = \sum_{t=1}^{n} X_t \cos(\omega_k t)$$

$$\beta_k = \sum_{t=1}^{n} X_t \sin(\omega_k t)$$

$$(3.10)$$

are also *i.i.d* Gaussian random variables with mean zero and variance $\sigma^2/2$ due to orthogonality of sinusoids. Consequently, the periodogram ordinates

$$I(\omega_k) = [\alpha_k^2 + \beta_k^2]$$

$$(3.11)$$

are independent and exponentially distributed random variables, each with mean σ^2. Even for the vector $(X_1, X_2,....., X_n)$ which is an independent but not normally distributed random variable with mean zero and variance σ^2, the periodogram vector $(I(\omega_1),...., I(\omega_n))$ converges to a vector of independent and exponentially distributed random variables, each with mean σ^2, as $n \to \infty$. However, in case of correlated signal, as $n \to \infty$, the periodogram vector converges to a vector of independent and exponentially distributed random variables, the kth component of which has mean equal to $2\pi f(\omega_k)$, $k = 1, 2,..., n$.

In summary, for a Gaussian time series, each component of the periodogram vector is asymptotically independent and exponentially distributed with mean $2\pi f(\omega_k)$ or σ^2 depending on whether the time series is correlated or not.

3.1.6 The Proposed Stochastic Model

Based on the various properties of DFT discussed in previous sections, the following

26

stationary time series generation model is proposed:

$$X_t = n^{-1} \sum_{k=0}^{n-1} A(\omega_k) \, e^{it\omega_k}$$

$$= n^{-1} \sum_{k=0}^{n-1} |A(\omega_k)| \, e^{i\phi(\omega_k)} \, e^{it\omega_k} \tag{3.12}$$

where,

$$|A(\omega_k)| = \sqrt{I(\omega_k)}$$

$$= \sqrt{2\pi S(\omega_k)} \tag{3.13}$$

$$\phi(\omega_k) = \textit{Uncorrelated random phase} \tag{3.14}$$

where, spectral density $S(\omega_k)$ and periodogram $I(\omega_k)$ are deterministic. Note that the Fourier amplitude part ($|A(\omega_k)|$) is constructed from target spectral density; hence the generated time series X_t will have exactly the same given spectral characteristics regardless of the distributional property of the phase. The random phase $\phi(\omega_k)$ is an independent uniformly distributed random variable in the interval $[-\pi, \pi]$. The uncorrelated Fourier coefficients ($A(\omega_k)$) due to the uncorrelated phase part will guarantee stationarity to the simulated time series. The time series X_t follows asymptotically a Gaussian probability distribution due to the central limit theorem. However, in practice, the time series may not be exactly stationary or Gaussian as will be discussed in Chapters 4 and 6.

3.2 STOCHASTIC PROPERTIES OF TIME SERIES

3.2.1 Moment Properties of Time Series

The moment properties of time series $\{X_1, X_2, \ldots, X_n\}$ such as mean, variance, skewness

and kurtosis are related to the Fourier coefficients in the Fourier representation of each time series. The mean value $\bar{X}$ of time series $\{X_t, \ t = 1, 2, 3,...., n\}$ is determined by

$$\bar{X} = n^{-1} \sum_{t=1}^{n} X_t \qquad (3.15)$$

or by substituting Eq. (3.12) in Eq. (3.15),

$$\bar{X} = n^{-1} |A(\omega_0)| \ e^{i\phi(\omega_0)} \qquad (3.16)$$

which shows that mean of the time series is determined by the magnitude of DFT at zero frequency. The phase at zeroth frequency indicates whether the mean value is negative or positive.

The variance (σ^2) of the time series X_t is evaluated by

$$\sigma^2 = n^{-1} \sum_{t=1}^{n} (X_t - \bar{X})^2 \qquad (3.17)$$

or by substituting Eq. (3.12) in Eq. (3.17),

$$\sigma^2 = n^{-2} \sum_{k \in F_n \backslash 0} |A(\omega_k)|^2 \qquad (3.18)$$

Note that the variance of the signal is related to the amplitude part of the DFT regardless of the phase part of DFT.

The third order moment, skewness (Sk), of the pressure signal characterizes the degree of asymmetry of the distribution around its mean. Conventionally, skewness is defined as a non-dimensional number characterizing only the shape of the distribution. For example, a positive value of skewness represents a distribution with asymmetric tail extending out toward more positive x-axis. Skewness is defined as,

$$Sk = n^{-1} \sum_{t=1}^{n} [(X_t - \bar{X})/\sigma]^3 \qquad (3.19)$$

or by substituting Eq. (3.12) in Eq. (3.19),

$$Sk = \frac{n^{-3}}{\sigma^3} \sum \sum_{k \neq -l \in F_n \backslash 0} |A(\omega_k)||A(\omega_l)||A(\omega_{k+l})| \; e^{i[\phi(\omega_k)+\phi(\omega_l)-\phi(\omega_{k+l})]} \tag{3.20}$$

Thus the skewness of the time series is related to the Fourier amplitude as well as the phase part of DFT.

The fourth order moment, kurtosis (Ku), of the pressure signal is a measure of relative peakedness or flatness of a distribution. Conventionally, kurtosis is defined as a non-dimensional number related with its value for a Gaussian distribution, i.e.,

$$Ku = n^{-1} \sum_{t=1}^{n} [(X_t - \bar{X})/\sigma]^4 - 3 \tag{3.21}$$

in which, the -3 term makes Ku zero for a Gaussian distribution; however, in all calculations in this thesis, kurtosis is considered as the normalized fourth order moment excluding the term -3.

3.2.2 Estimation of Level Crossing and Peak Statistics

3.2.2.1 In time domain

Classical level-crossing and peak statistics theory are briefly reviewed here. The time series $\{X_t\}$ exhibits one x-upcrossing in time step ΔT if $X_t \leq x$ and $X_{t+1} > x$. Therefore, the average number of x-upcrossings in ΔT is $P(X_t \leq x, X_{t+1} > x)$ and the mean x-upcrossing rate of the series can be obtained from

$$N_x = \frac{1}{\Delta T} P(X_t \leq x, X_{t+1} > x) \tag{3.22}$$

Similarly, the time series $\{X_t\}$ exhibits one peak (maximum) in time step ΔT in the interval

29

dx, above the level x, if $x < X_t \leq x + dx$, $\dot{X}_t = 0$ and $\ddot{X}_t < 0$. Therefore, the average number of maxima in ΔT is $P(x < X_t \leq x + dx, \dot{X}_t = 0, \ddot{X}_t < 0)$ and the mean peak rate of the series can be obtained from

$$N_p(x) = \frac{1}{\Delta T} P(x < X_t \leq x + dx, \dot{X}_t < 0, \ddot{X}_t < 0) \tag{3.23}$$

3.2.2.2 In frequency domain

Estimation of level crossing and peak statistics using SDF is briefly reviewed in this section. For any zero-mean stationary random process, the spectral density function $(S(f))$ is defined as the Fourier transform of the autocorrelation function $(R(\tau))$ of the process, i.e.

$$S(f) = \frac{2}{\pi} \int_0^\infty R(\tau) . \cos(2\pi f \tau) d\tau \tag{3.24}$$

where, $S(f)$ is considered to be non-negative one-sided physical spectrum. The spectral moments, m_i, are defined by

$$m_i = \int_0^\infty f^i S(f) df \quad , \quad i = 0,1,2,\ldots\ldots \tag{3.25}$$

in which m_0 represents variance (σ^2) which is area under $S(f)$. The spectral moments can be used to establish level crossing rates as well as peak rates of a narrowband stationary Gaussian random process. The zero up-crossing or down-crossing rate (N_0) of the process can be estimated by

$$N_0 = [m_2 / m_0]^{1/2} \tag{3.26}$$

whilst, the positive or negative peak rate (N_p) of the process can be estimated by

$$N_p = [m_4 / m_2]^{1/2} \tag{3.27}$$

The average number of zero up-crossing as well as peaks in time T can be estimated by multiplying Eqs. (3.26) and (3.27) by T. Further, the rate of maxima, $N_p(x)$, occurring in the interval $(x, x+dx)$ for a Gaussian process can be estimated by,

$$N_p(x) = \frac{N_0 x}{2} \exp(-\frac{x^2}{2}) \left[1 + erf(\frac{\mu x}{\sqrt{2}}) + \sqrt{\frac{2}{\pi}} \frac{1}{\mu x} \exp(-\frac{\mu^2 x^2}{2}) \right] \tag{3.28}$$

where, shape factor $(\mu) = \dfrac{m_2}{\sqrt{m_0 m_4 - m_2^2}}$

Since Eqs. (3.26) and (3.27) have been developed based on narrowband assumption, they must be used with caution in case of broadband process. The broadband nature of a stationary random process can be quantified by using irregularity factor (ε) or bandwidth parameter (β). The irregularity factor (ε), a measure of distance to narrowband, can be evaluated by

$$\varepsilon = N_0 / N_p \tag{3.29}$$

The bandwidth parameter (β), a measure of the dispersion of SDF around its central frequency, can be estimated by

$$\beta = \sqrt{1 - \varepsilon^2} \tag{3.30}$$

The irregularity factor as well as bandwidth parameter range between 0 and 1. While $\varepsilon = 1$ and $\beta = 0$ represent pure narrowband process, $\varepsilon = 0$ and $\beta = 1$ represent pure broadband process. For more precise definition of terms and more details, see Vanmarcke (1983) or Nigam (1983).

31

3.2.3 Extreme Value Statistics

Extreme values of time series data are significant in various engineering applications. Therefore, special importance is provided for the statistical analysis of such extreme values. It is noted that if the probability distribution of a parent population has an exponential tail, its extreme values approach the Type-I distribution as the data increases (Gumbel 1958). It is interesting to note that the central portion of the parent distribution has little influence on the asymptotic form of the extremal distribution compared to the tail portion of the parent distribution; however, it has influence on extremal parameters. As far as wind engineering applications are concerned, the Type-I distribution is a good approximation of the extreme values though the tail of the parent population does not always follow exponential distribution (Peterka and Cermak 1975; Dalgliesh et al. 1980).

Let X_m be the random variable associated with the maximum value of the initial variate X. The Cumulative Distribution Function (CDF) of the Type-I asymptotic form for the distribution of X_m is as follows:

$$P(X_m < x) = P = F_{X_m}(x) = \exp\left(-e^{-(x-u)/s}\right) \tag{3.31}$$

where u corresponds to a characteristic largest value of the initial variate X (mode) and s corresponds to a measure of dispersion of X_m. The extremal parameters s and u can be estimated by using either Gumbel's plot or the following equations derived from the mean (μ_1) and the standard deviation (σ_1) of X_m (Gumbel 1958):

$$\begin{aligned} s &= \frac{\sqrt{6}}{\pi}\sigma_1 \\ u &= \mu_1 - 0.5772\,s \end{aligned} \tag{3.32}$$

3.2.3.1 Gumbel's plot

By taking twice logarithm on both sides, Eq. (3.31) becomes

$$\ln[-\ln \ (P)] \ = \ -\frac{(x-u)}{s} \tag{3.33}$$

which can be rewritten as

$$x \ = \ u \ + \ sy \tag{3.34}$$

where, $y = -\ln[-\ln \ (P)]$ is the reduced y-variate. The probability term P can be determined as follows: the observed extreme values are sorted into ascending order of magnitude, after which each is assigned a rank, r, where $r = 1$ for the smallest and $r = Q$ for the largest of Q values. An estimate of P corresponding to each extreme value can be calculated from their ranks using the following equation,

$$P \ = \ \frac{r}{Q+1} \tag{3.35}$$

The mode (u) and dispersion (s) can be determined from plotting Eq. (3.34) (Gumbel's plot). Mode corresponds to the x value when the reduced y-variate is zero and the dispersion is the slope of the line fitting the data.

3.3 SUMMARY

The essential Fourier transform as well as stochastic properties of time series have been presented in this chapter as a foundation for the current work. Based on the various Fourier transform properties of time series discussed in sections 3.1.1 - 3.1.5, a stochastic model is

33

suggested in section 3.1.6 for the generation of pressure time series. This model requires Fourier amplitude as well as phase for the time series generation. The Fourier amplitude can be generated either from a sample time history or from target spectra, while the Fourier phase represented by independent uniform random numbers can be easily generated. The generated time series using this model will be stationary and normally distributed. Therefore, modification of this model is required to extend its capability to represent stationary non-Gaussian time series.

It is shown in section 3.2.1 that the mean and variance of a time series are independent of the phase part but are wholly determined by the amplitude part of the DFT of time series. On the other hand, the skewness (a non-Gaussian property) of time series is related to phase as well as amplitude part of the DFT of time series. Further, as mentioned in Chapter 2, past studies showed the possibility of inducing non-Gaussian properties through the phase part of the Fourier representation of a time series without disturbing its amplitude characteristics. Therefore, Eq. (3.12) can also be used for non-Gaussian signal simulation with a different phase part. This issue will be addressed in Chapter 6.

Chapter 4
Experimental Investigation

"...Physical modelling has and continues to be the primary source of information for wind engineering applications. The capability of boundary-layer wind tunnels to simulate essential features of the atmospheric boundary layer makes this possible..."

J. E. Cermak, 1995.

The current study focuses on the development of a suitable analytical/empirical model to simulate Gaussian as well as non-Gaussian pressure fluctuations on low building roofs. To start with, systematic wind tunnel measurements are required to understand the stochastic behaviour of pressure fluctuations on roofs. The information derived from wind tunnel measurements has then formed the basis for developing an efficient model to represent the true characteristics of pressure fluctuations on roofs. This chapter addresses the methodology used in the experiments and presents the experimental results.

4.1 Experimental Procedure

This experimental study aims at acquiring a comprehensive knowledge of pressure fluctuations on various types of building roofs under different conditions. The required natural wind conditions for the measurement can be simulated in atmospheric boundary layer wind tunnels. Details associated with physical modelling and simulation of the atmospheric boundary layer are provided elsewhere (Simiu and Scanlan 1986; Cermak 1995). The roof geometry, tap location, wind attack angle, and surrounding conditions have

35

been considered in order to investigate the effect of each one of them on the fluctuating behaviour of pressures acting on roofs. A brief description of the various elements of this experimental study follows:

(a) **Wind tunnel:** The experiments were carried out in the boundary layer wind tunnel of the Centre for Building Studies (CBS) at Concordia University, Montreal, Canada. The working section of the tunnel is 12.2 m long, 1.8 m wide, and about 1.8 m high. It has an adjustable roof height to provide negligible pressure gradient in the downstream direction. More details about this wind tunnel and its simulation characteristics are given by Stathopoulos (1984a).

(b) **Approach terrain, length scale, velocity scale:** Since low-rise buildings are located at the lowest part of boundary layer where the surface roughness is comparable to the height of these buildings, the terrain conditions are expected to have influence on the fluctuating characteristics of wind-induced pressures. Further, the majority of buildings are located either in open country or in suburban terrain conditions. Therefore, these exposures were simulated in the tests of this study; their corresponding mean velocity and turbulent intensity profiles are shown in Fig. 4.1. The boundary layer scale is approximately 1:400. The wind speed at gradient height was approximately 11 m/s. The velocity scale for this study was set out to be approximately 1:3.5.

(c) **Building parameters:** Plexiglass models of common roofs such as flat, monoslope, and gable types were tested in two terrain conditions for several wind angles. The dimensions of the models used in this study are reported in Table 4.1. In the first phase of
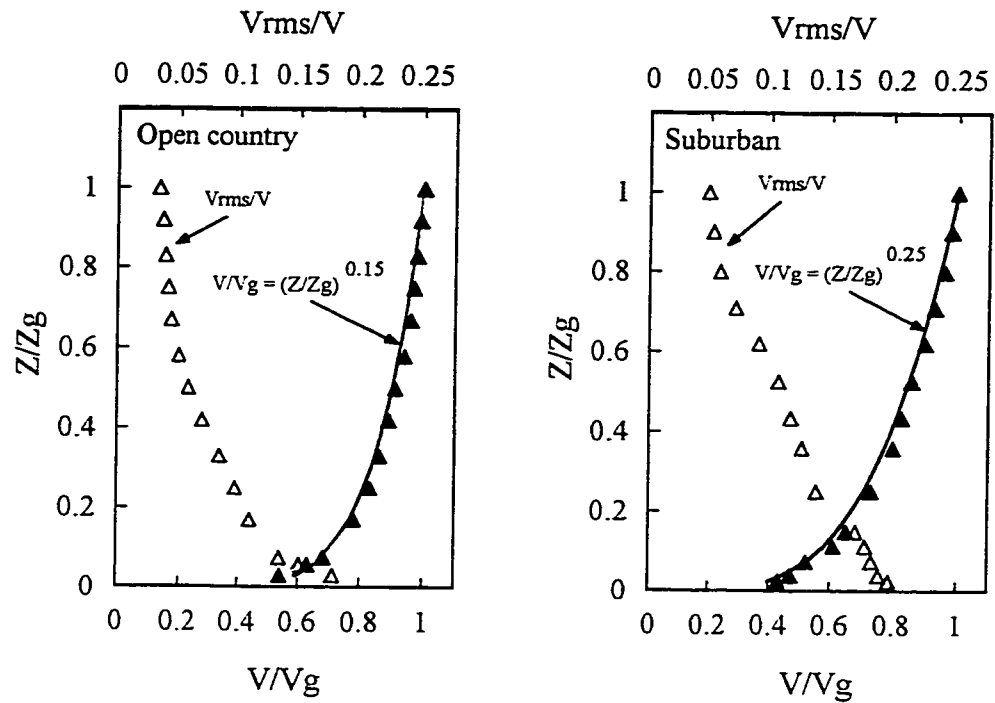
Fig. 4.1 Mean speed and turbulent intensity profiles for both terrains considered.

Table 4.1 Models used in this study.

	Dimensions		
	l	b	h_l
Monoslope Roof ($\alpha \approx 15°$)			
Full-Scale (m)	60.8	19.2	12.0
Model (mm)	152.0	48.0	30.0
Flat Roof			
Full-Scale (m)	43.2	43.2	15.0
Model (mm)	108.0	108.0	37.5
Gable Roofs ($\alpha \approx 19°$ and $\alpha \approx 45°$)			
Full-Scale (m)	60.8	39.2	12.0
Model (mm)	152.0	98.0	30.0

Note: l = length, b = width, h_l = lower eave height, α = roof angle

this study, several roof taps (Fig. 4.2 (a)) were used not to determine detailed aerodynamic behaviour but to examine variability in pressure fluctuations and possible elimination of taps from future tests. In the second phase, tests were conducted only for the selected taps (Fig. 4.2 (b)) from the first phase. The measurements were made for 7 different wind directions ($0°$, $30°$, $45°$, $60°$, $90°$, $120°$ and $180°$) in case of monoslope roof and for 5 different wind directions ($0°$, $30°$, $45°$, $60°$ and $90°$) in case of flat and gable roofs.

(d) Instrumentation: Pressure fluctuations were measured with SETRA 237 pressure transducers (0.1 psid range) using a Scanivalve. The Scanivalve was connected to pressure taps with plastic tubes that were 610 mm long and had an inside diameter of 1.6 mm. Restrictors were placed in the tubes to provide a flat frequency response up to 100 Hz. Frequencies of pressure fluctuations at most taps are expected to be below this value.

(e) Measurements: Pressure data were acquired in blocks of 8192 samples each at a sampling rate of 500 Hz using a waveform analyzer (DATA-6000) after each signal passed through a low-pass filter with cut-off at Nyquist frequency (the highest possible frequency component present in the signal, Brook and Wynne (1988)) of 250 Hz. At a length ratio of 1:400 and mean velocity ratio of about 1:3.5, the resulting time history of 16.384 seconds providing statistically stable mean and variance is equivalent to 30 minutes in full-scale. At the end of each sampling period, the measured pressure signals were converted to pressure coefficient (Cp) signals by dividing them by the reference dynamic pressure at mean roof height. Simultaneously, the pressure coefficient spectrum ($S(f)$) was also evaluated with the help of DATA 6000 analyzer. Smoothening of the spectra has been done by ensemble averaging of 16 records.
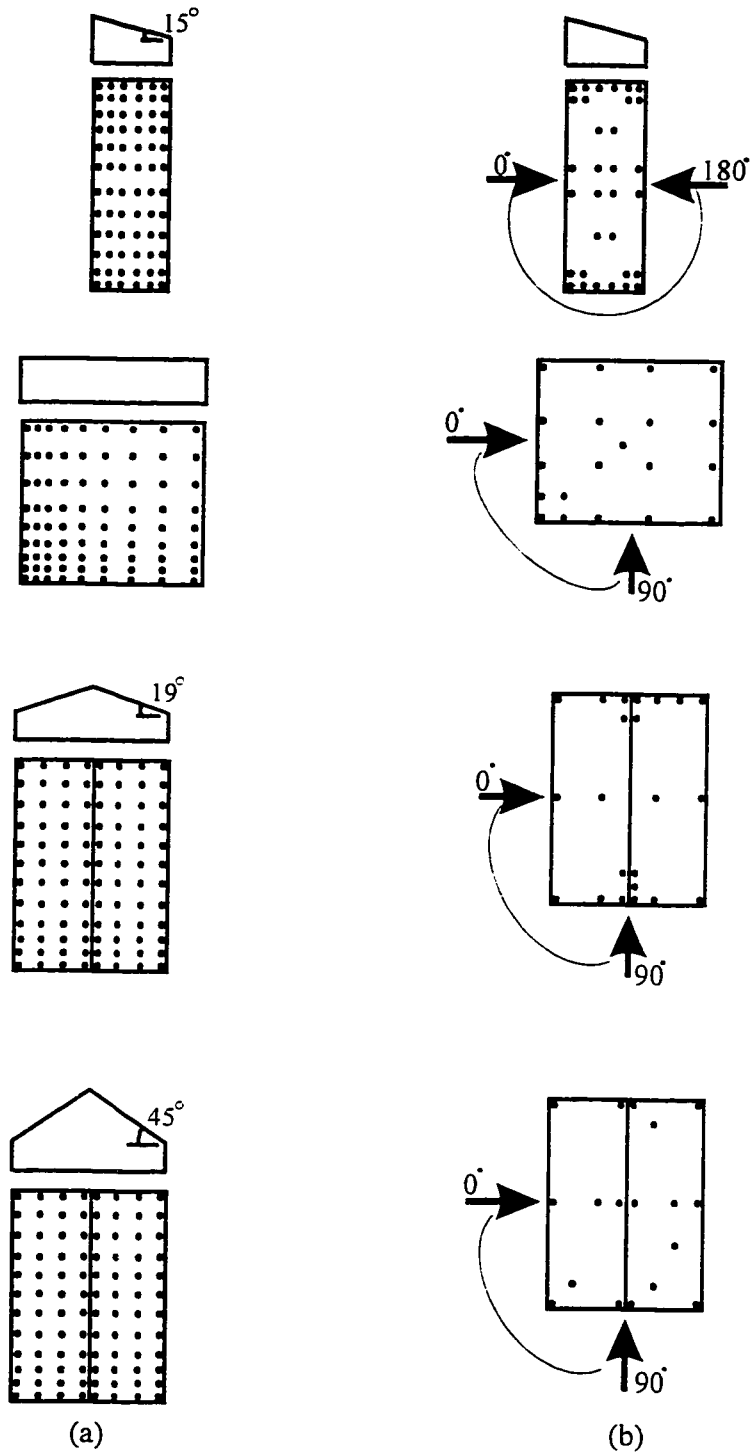
Fig. 4.2 Models and their corresponding tap locations used in the (a) first phase, and (b) second phase of the measurements.

39

4.2 EXPERIMENTAL RESULTS

A number of pressure time histories have been measured during this investigation; however, only representative samples of pressure fluctuations have been chosen for the demonstration of results reported in three conventional domains such as time, frequency and amplitude.

4.2.1 Time Domain Properties

First, the appearance of the time histories have been closely observed. Figures 4.3, 4.4, and 4.5 show the time histories of the representative samples. The statistics of the selected samples corresponding to the ensemble average of 16 records are shown in Table 4.2. The MATLAB function **MOM_ST** reported in Appendix - A is used to estimate these statistics. The observations are summarized as follows:

(a) In general, the measured pressure fluctuations on roofs have negative means and negatively going sharp spikes due to the high suction acting on roofs; however, there are exceptions. In case of sample S100 where the roof angle is 45°, the tap experiences pressure rather than suction resulting in positive mean and positively going spikes. As expected, the mean values of the fluctuations are different at various locations (see Table 4.2).

(b) The intensity of fluctuations (variance) of the time histories is sometimes quite different depending on the tap location and wind attack angle. The variances of the selected samples are provided in Table 4.2. It is noted that sample S18 has the

40
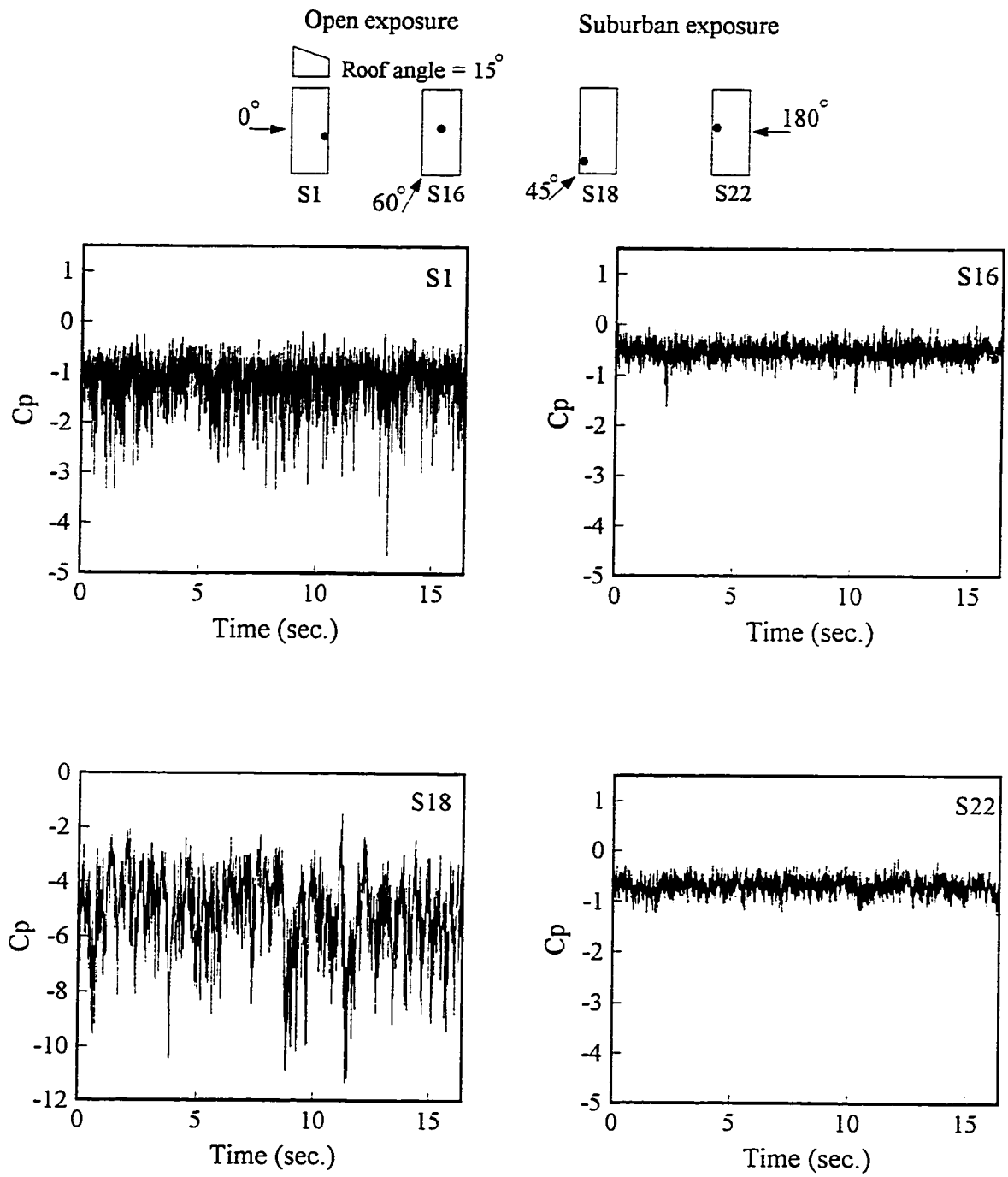
Fig. 4.3 Measured pressure time histories on a monoslope roof.
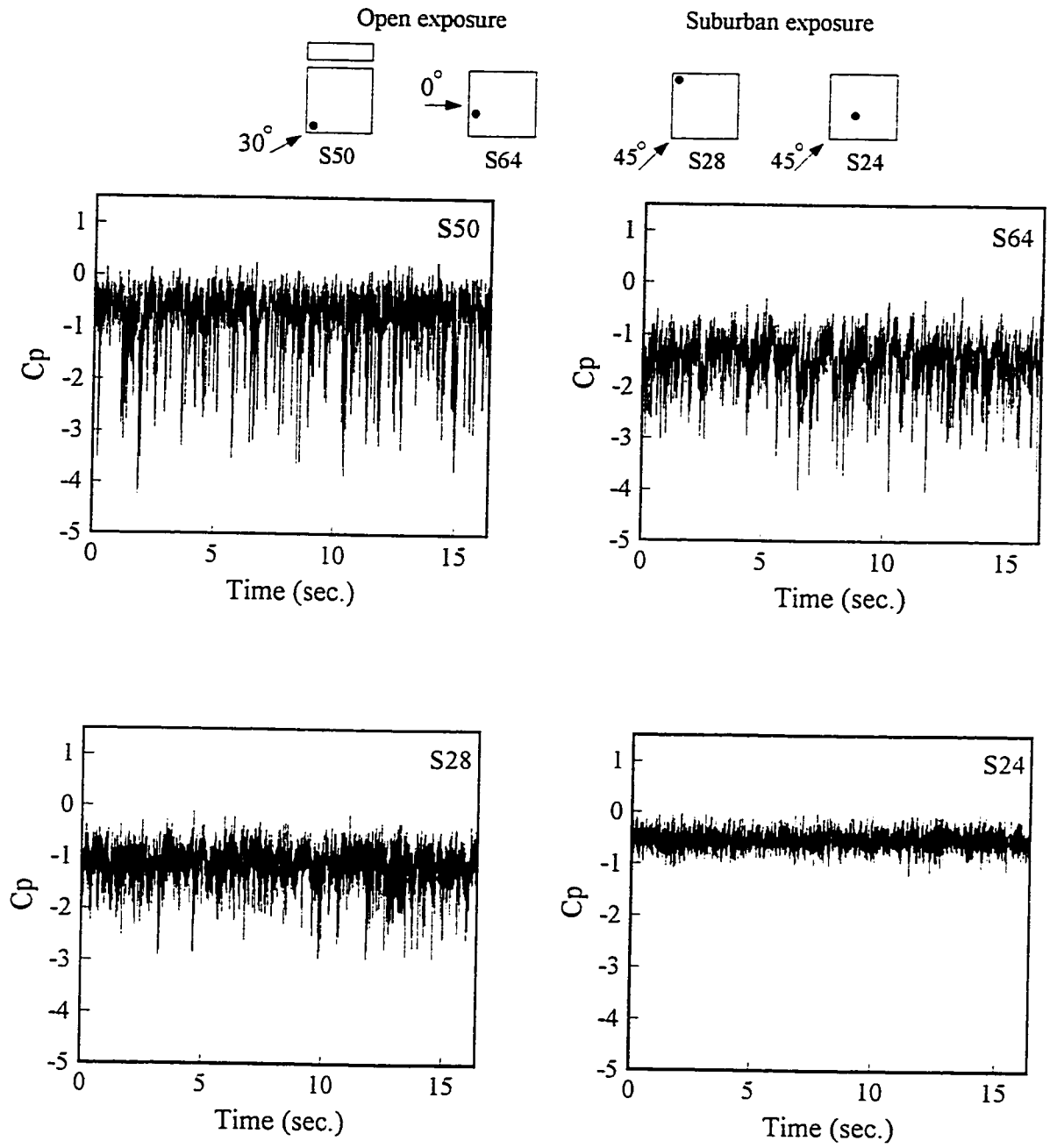
Fig. 4.4 Measured pressure time histories on a flat roof.
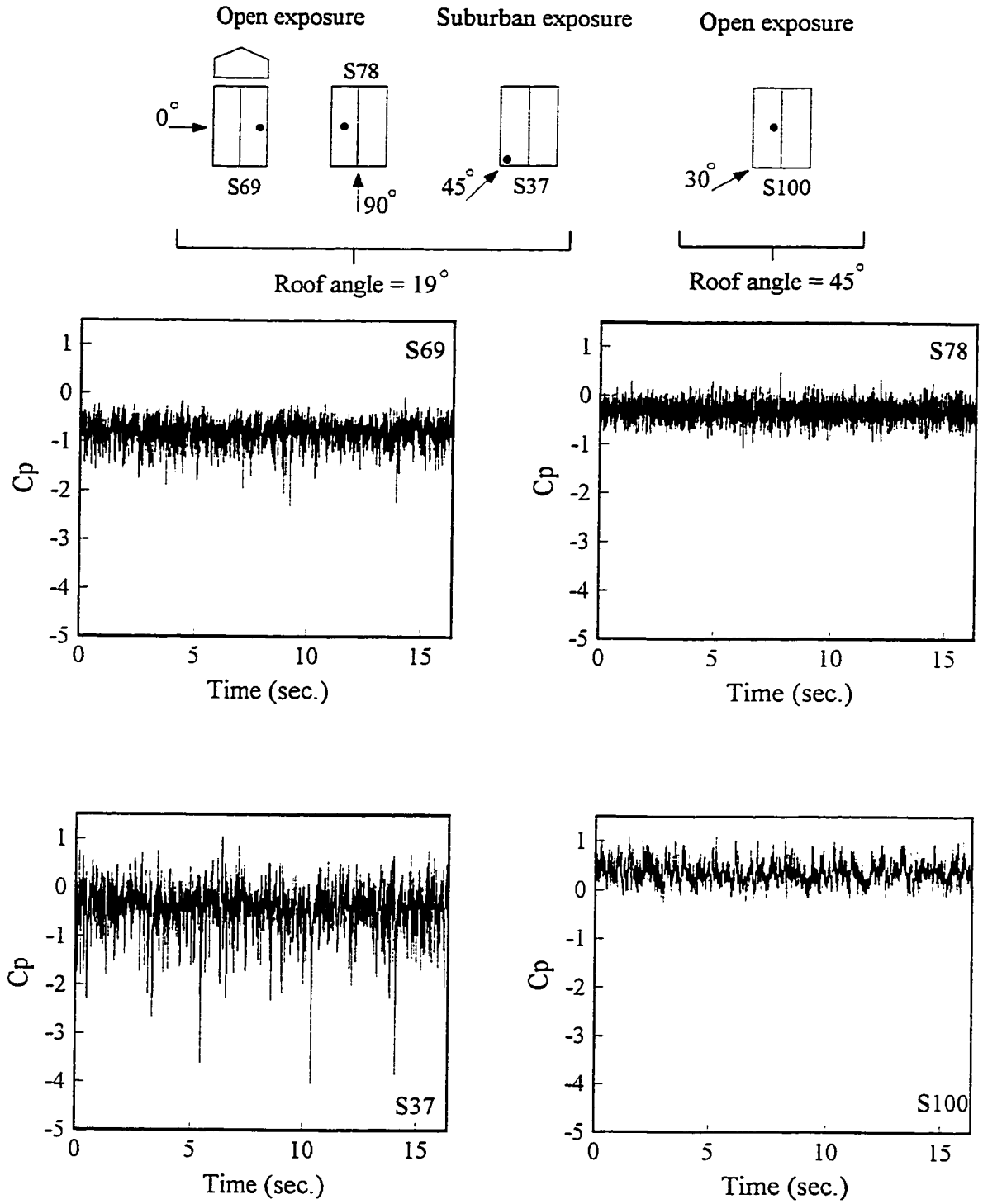
Fig. 4.5 Measured pressure time histories on gable roofs.

Table 4.2 Statistics of pressure time series data.

Sample	Mean	Variance	Skewness	Kurtosis
Monoslope Roof ($\alpha \approx 15°$)				
S1	-1.11	0.14	-1.40	7.12
S16	-0.51	0.02	-0.10	3.55
S18	-5.31	1.82	-0.67	3.56
S22	-0.68	0.02	-0.14	3.10
Flat Roof				
S50	-0.80	0.28	-2.28	9.80
S64	-1.47	0.14	-0.75	4.44
S28	-1.15	0.12	-0.86	4.89
S24	-0.53	0.02	-0.03	3.03
Gable Roofs ($\alpha \approx 19°$ and $\alpha \approx 45°$)				
S69	-0.80	0.05	-0.93	5.63
S78	-0.31	0.03	-0.07	3.32
S37	-0.38	0.17	-1.06	6.35
S100	0.37	0.04	0.31	3.02

maximum variance compared to all other signals. It can be observed from the appearance of sample S18 (Fig. 4.3) that it has patches of broad spikes rather than simply dropping sharp spikes. The unsteady behaviour of this time series is dominated by large-scale fluctuations (low-frequency fluctuations) which can be associated with the low-frequency flapping motion of the separated shear layer from the sharp edge (Seong 1993). Further, it is interesting to note that high fluctuations (variance) do not guarantee high non-Gaussianness (high skewness and kurtosis values) in a signal. For instance, though sample S18 (see Fig. 4.3) is highly fluctuating, the fluctuations are approximately evenly distributed above and below the mean and thus, it is not highly non-Gaussian. Note that samples S1, S69 and S37 are highly non-Gaussian, but they have low values of variance compared to sample S18 (see Table 4.2); while sample S50, which is highly non-Gaussian, has variance greater than the above three samples.

This shows that there is no clear evidence concerning any relation between the intensity of fluctuations (variance) and the non-Gaussianness of a signal.

(c) The commonly observed sharp spikes in pressure time series are mainly responsible for its non-Gaussian nature. A careful observation of the time histories in Figs. 4.3, 4.4 and 4.5 reveals two important characteristics of spikes. First, the frequency of spikes which varies from signal to signal depending on the different conditions of each measurement. Second, the magnitude of spikes which also varies from signal to signal. Both frequency and magnitude of spikes should be taken into account while modelling pressure fluctuations on roofs since they affect the nature of the time series. Table 4.2 shows the values of skewness and kurtosis of the selected samples. It is easy to note that some signals (samples S1, S50 and S37) are highly non-Gaussian; for instance, it is clear from Fig. 4.3 that sample S1 has more sharp spikes going in negative direction and, therefore, it must be more non-Gaussian than each of the other three samples shown in the same figure. It is interesting to note sample S50, which is one of the most highly skewed signals observed during this investigation. Samples S16, S22, S24 and S78 are close to Gaussian based on the skewness and kurtosis values given in Table 4.2.

(d) In general, the high magnitude sharp spikes in pressure fluctuations have been observed at taps located on windward edges of roofs in separated flow (azimuth 0°) as well as in vortex flow (say, azimuth 30° - 60°) conditions. A typical example of time series measured in separated flow is sample S64. This particular tap is immersed in the separation bubble formed by the sharp edge of roof. The fine sharp spikes observed in this time series reflect the flow mechanism near the surface inside this

separation bubble. The intermittent formation and breakdown of the secondary separation bubbles which are immersed in the main separation bubble might be causing such spikes (Bienkiewicz and Sun 1992). Typical examples of time series measured in vortex flow are samples S50, S28 and S37. It is well known that conical vortices form on the leading edges of a roof in vortex flow. The intensity of the conical vortices depends on many features such as roof geometry, oncoming wind turbulence, wind direction etc.; very strong conical vortices are found on flat roof edges in turbulent flow coming at an azimuth of 45° (Kawai and Nishimura 1996). The large suction fluctuations as well as the sharp spikes observed in these samples are caused by the suction induced by conical vortices (Kawai and Nishimura 1996). Note also that the intensity of the conical vortices weakens as they move far from the vertex of the roof corner. As a result, the intensity of the spikes is significantly reduced in the case of sample S28 compared with sample S50. The detailed characteristics of suction fluctuations on the leading edges of a flat roof under oblique flow are provided elsewhere (Bienkiewicz and Sun 1992; Kawai and Nishimura 1996).

Since the level-crossing and peak statistics of the signals are important in time dependent reliability problems, they have been estimated using the MATLAB functions **CROSS_ST** and **PEAK_ST** reported in Appendix - A. The results are reported in Table 4.3 where the second and third columns represent the number of mean zero down-crossings (N_0T) and the number of negative peaks (N_pT) where $T = 16.384$ s (record duration). It is clear that the number of peaks are always higher than the number of mean zero down-crossings holding a ratio of N_pT to N_0T from approximately 1.5 (sample S78)

Table 4.3 Number of mean zero down-crossings and negative peaks of pressure time series data.

Sample	N_0T	N_pT
Monoslope Roof ($\alpha \approx 15°$)		
S1	643	1523
S16	1185	1952
S18	338	1638
S22	1064	1935
Flat Roof		
S50	796	1973
S64	836	1982
S28	1186	2041
S24	1461	2030
Gable Roofs ($\alpha \approx 19°$ and $\alpha \approx 45°$)		
S69	838	1705
S78	1260	1876
S37	703	1791
S100	483	1298

to 5 (sample S18). This shows that all the selected samples are broad-banded since N_0T and N_pT are supposed to be equal or close to each other in case of narrowband process (see section 3.2.2.2). The variation of N_0T and N_pT among signals depends on the nature of fluctuations at the corresponding locations. Note the enormous difference in N_0T among signals, especially in case of samples S18 and S24; however, in case of N_pT, such huge difference is not observed. Therefore, it can be hypothesized that N_0T depends very much on the broadband nature of the signal. Table 4.4 shows the number of crossings at different levels of some of the selected samples. All calculations have been made after the signals were subtracted from their corresponding mean values and normalized by their corresponding standard deviations. For instance, the number of down-crossings at level -2 corresponds to the number of down-crossings of time series at 2σ below the mean level,

Table 4.4 Number of down-crossings at various levels of selected pressure time series data.

Sample	Level crossing below mean in terms of σ						
	0	-1	-2	-3	-4	-5	-6
S1	643	312	121	50	24	7	1
S18	338	209	66	21	6		
S50	796	227	154	91	32	9	3
S24	1461	834	166	12	1		
S78	1260	690	161	21	1		

where σ is the standard deviation of the time series. The number of downward level crossings at levels 0 to -6 are presented in Table 4.4. As expected, the number of crossings decrease as the level increases. Here, samples S1 and S50 are highly non-Gaussian which is clear from their higher level crossing nature, especially at levels -4, -5 and -6. In case of samples S18, S24 and S78, which are more or less Gaussian, there is no crossing above level -4. Even at level -4, the number of crossings are negligible compared to samples S1 and S50.

Further, when each pressure time history is inspected at a number of successive time intervals, they all have a similar appearance. Especially, the values of mean and variance of the sub-intervals of a given time history are found to be more or less constant. Such type of behaviour is idealized by saying that the process is stationary, i.e., the statistical properties are time invariant. In addition, the invariant nature of the autocorrelation functions of the measured signals with respect to uniform shift in time (τ) has been confirmed in a number of cases which further reinforces the overall stationarity of the complete second order properties of the time series. Typical autocorrelation functions provided in Fig. 4.6 support this observation.
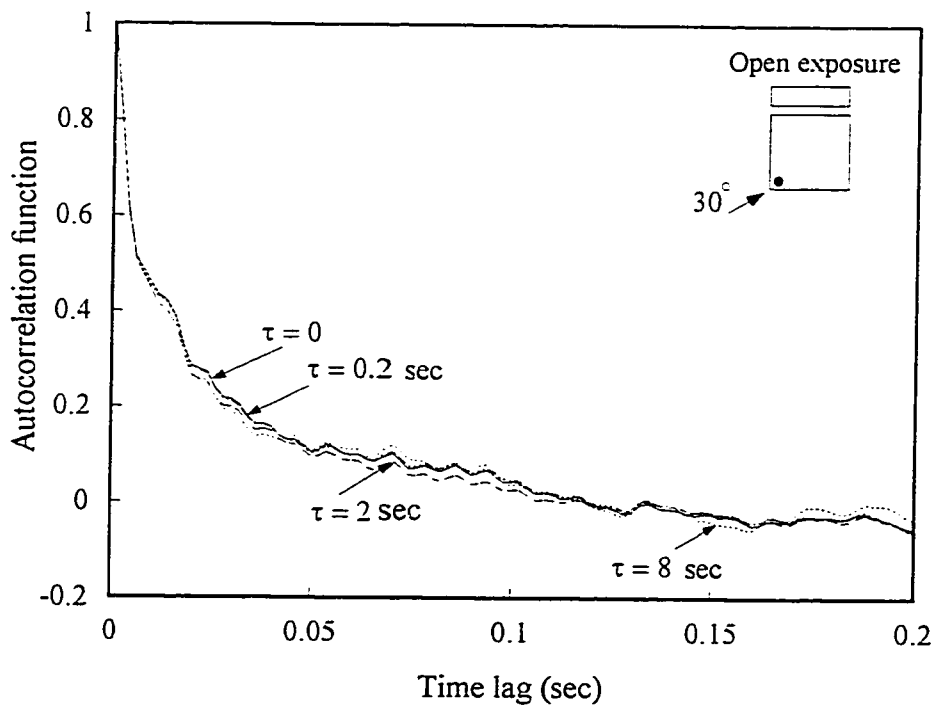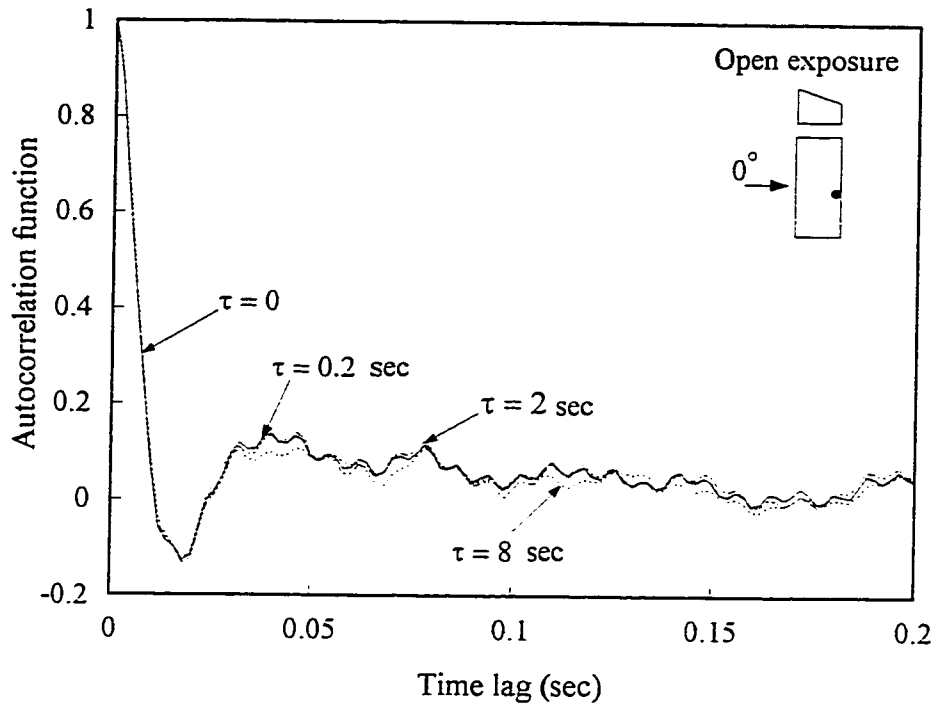
Fig. 4.6 Autocorrelation functions of pressure fluctuations subjected to uniform shift in time.

4.2.2 Frequency Domain Properties

In this section, frequency domain properties of the pressure fluctuations are discussed. Spectra are shown as a function of the independent variable during the test; the reduced frequency, $F = fh/V$, where h is a typical building dimension, say mean roof height of the building, and V is the mean velocity at mean roof height. Since most of the energy is concentrated at low frequencies, the spectrum is shown in logarithmic scale.

Figure 4.7 shows a typical sample of normalized spectra of pressure fluctuations and the corresponding longitudinal spectrum of incident wind at building height without the presence of building. The time histories corresponding to the velocity and pressure spectra have been sampled at 500 Hz with a cut-off frequency at 250 Hz. It can be seen
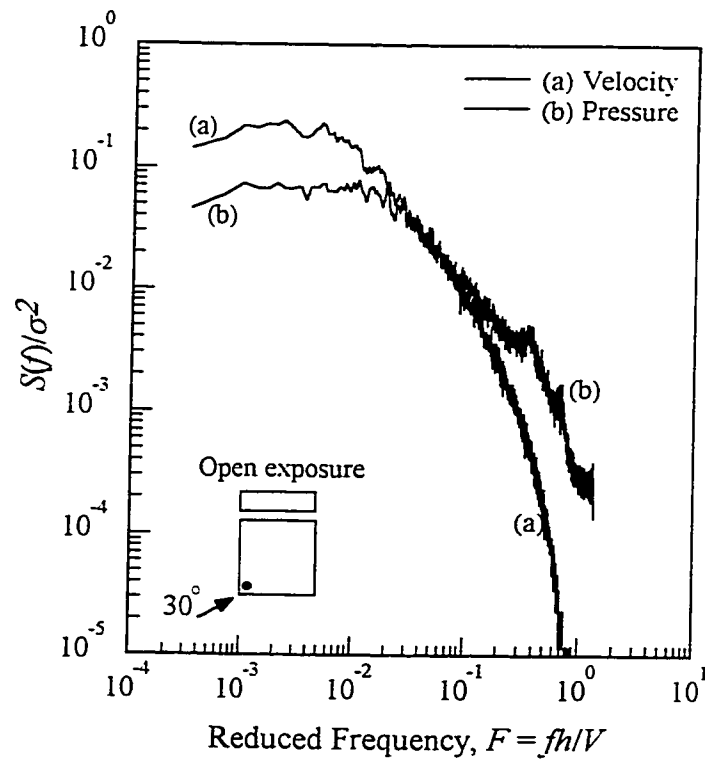
Fig. 4.7 Sample spectra of wind velocity and wind pressure.

that significant energy in the tap is distributed over a wide frequency range. In low frequency range, amplitudes of the pressure spectrum which is mainly related to the turbulence in incident flow are somewhat lower than those of the velocity spectrum. In high frequency range, pressure spectral amplitudes are significantly higher than wind spectral amplitudes. This particular observation is found to be consistent for almost all taps on roof. It is generally believed that small-scale turbulence caused by the interaction of incident wind turbulence with the building makes high frequency pressure energy significant.

Figure 4.8 shows typical comparisons between the model and full-scale wind pressure spectra. The full-scale spectra correspond to taps 50101 and 50123 of TTU building (*Texas Tech...* 1992). The full-scale time histories were sampled at 40 Hz with a cut-off frequency at 10 Hz for tap 50101 and at 8 Hz for tap 50123; the model time histories were sampled at 500 Hz with a cut-off at 250 Hz. At a length scale of 1:400 and a mean velocity ratio of about 1:3.5, the model sampling frequency and cut-off frequency were equivalent to about 4.3 Hz and 2.15 Hz in full-scale. Note that the model and full-scale cases used for this comparison are slightly different in terms of building geometry and tap location. In particular, the model height was equivalent to about 15 m in full-scale, while the full-scale building height was only 4 m. However, the comparisons show that the model spectra are in reasonably good agreement with the full-scale spectra which is encouraging. Recently, Xu (1995a) reported the higher full-scale spectral amplitudes in the higher frequency range in comparison with the lower model scale spectral amplitudes in the same region. This may be due to the differences in simulation of atmospheric turbulence between full-scale and wind tunnel (Tieleman 1992). However, it is reasonable
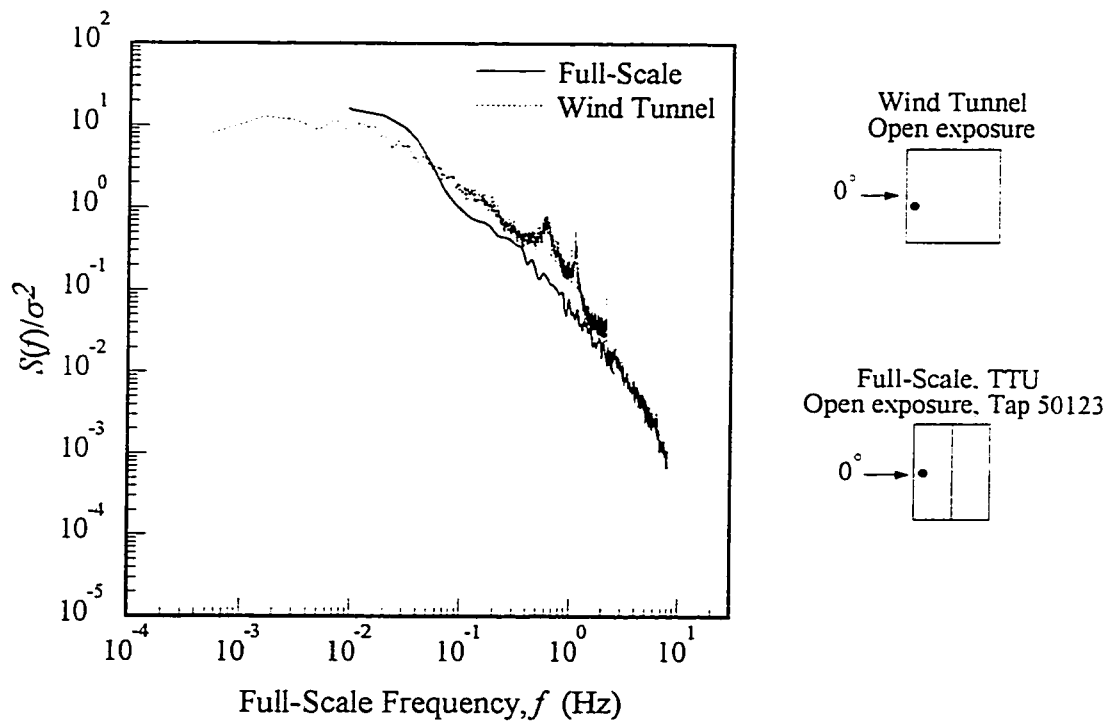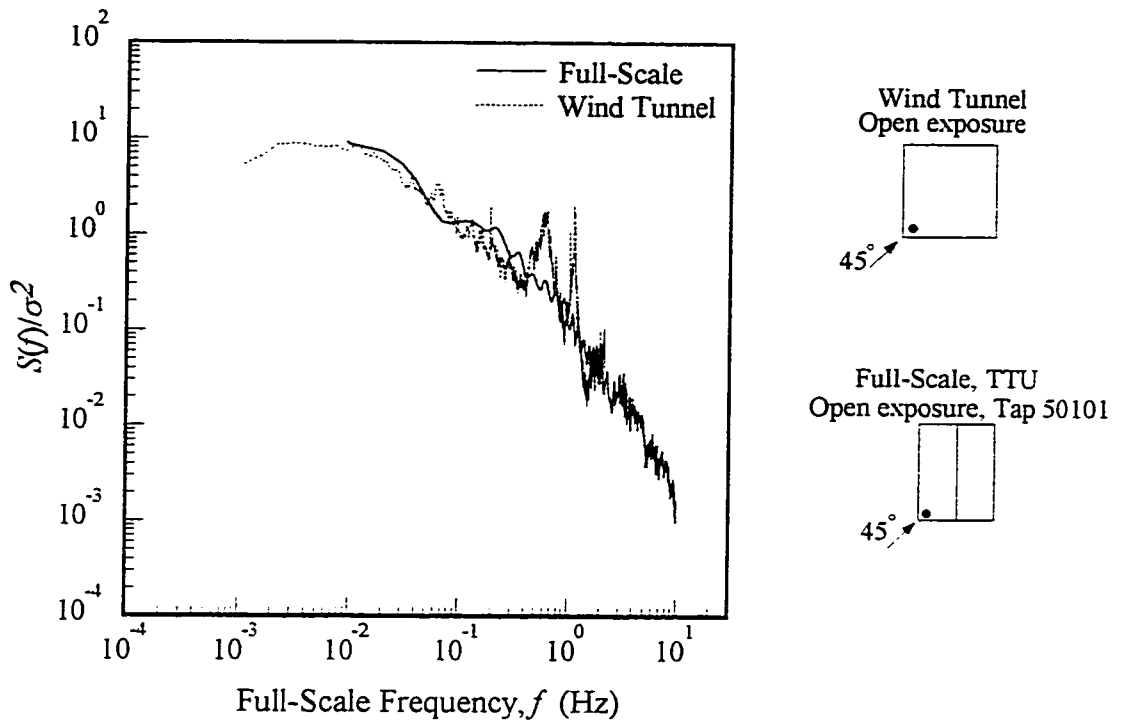
Fig. 4.8 Comparison of wind pressure spectra.

to accept that model scale spectra compare well with the full-scale spectra at least in the lower frequency range where most of the energy lies.

Figures 4.9, 4.10 and 4.11 show the measured spectra of the representative samples. As expected, spectra vary from location to location due to the nature of the physical processes that occur near the surface in boundary layer flow. The spectra measured at various locations of the roof under different conditions show that spectra have somewhat deterministic shape though some spikes occasionally appear at fan blade frequency and at harmonics of electrical frequency which can be easily cleared. For instance, samples S22, S24, S69, S78 and S100 (Figs. 4.9, 4.10 and 4.11) have some erratic spikes which are extraneous. The significance of spikes is estimated by measuring the area under the spikes. The area under the spikes in various cases is found to be within 5% of the corresponding variances. It is interesting to note that such spikes are poping out when the variance of the signal is low. For instance, in the case of sample S18 (Fig. 4.9), there are no visual spikes due to its high variance suppressing such extraneous spikes.

Though the properties of time series such as variance, the number of zero down or up-crossings (N_0T), the number of negative or positive peaks (N_pT), the irregularity factor (ε), the bandwidth parameter (β) can be deduced from spectra (see section 3.2.2.2), other properties such as mean, Gaussian or non-Gaussian nature, information about spikes etc. of the corresponding time series cannot be deduced from them. For instance, sample S1 is highly non-Gaussian while sample S22 is nearly Gaussian, as per Table 4.2; this information cannot be drawn from spectra. Furthermore, it is interesting to note that the sharp spikes present in time histories are missing in spectral information. In particular, samples S1, S50 and S37 (Figs. 4.3, 4.4 and 4.5) consist of high intensity sharp spikes;

53
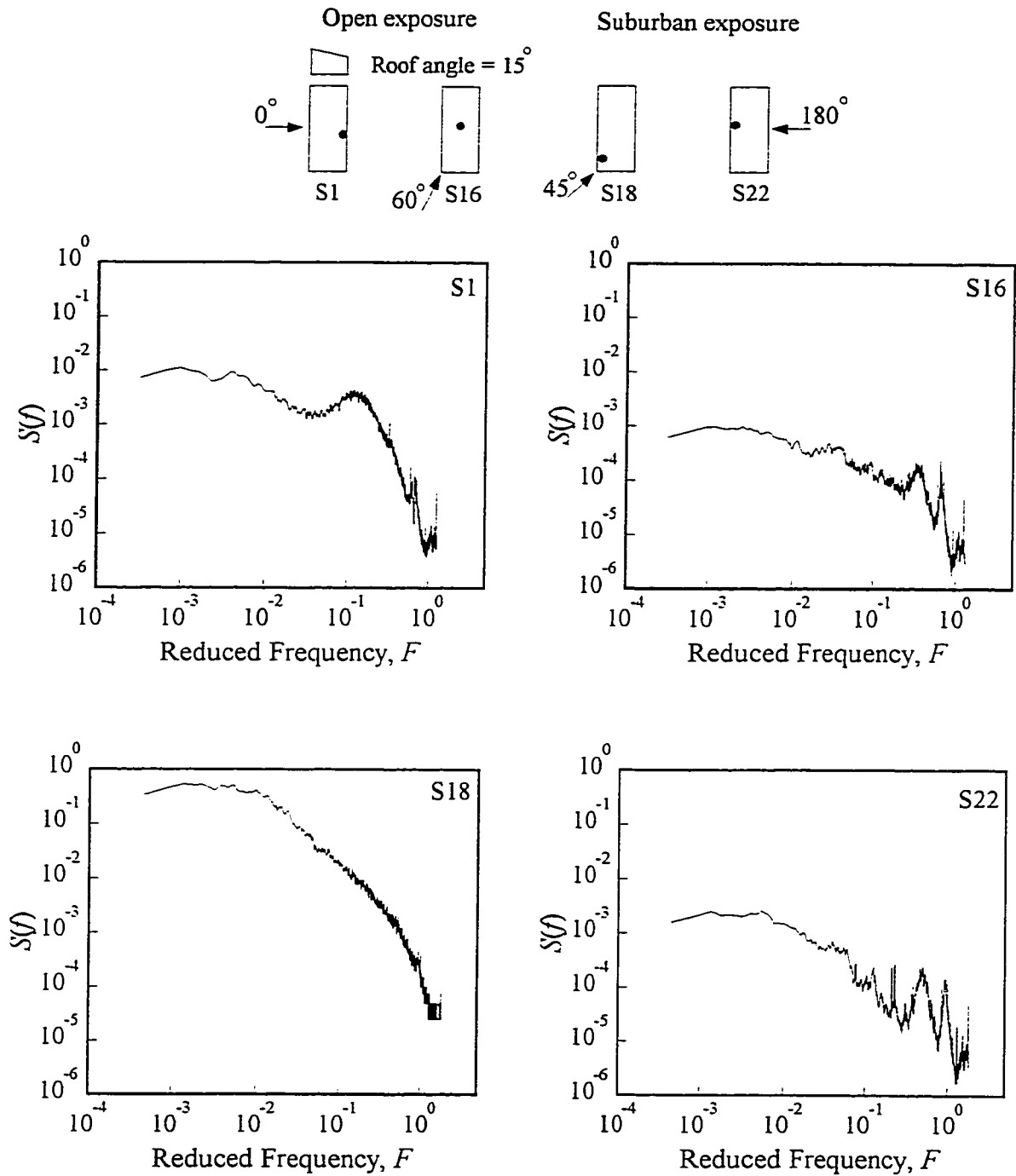
Fig. 4.9 Measured pressure spectra on a monoslope roof.
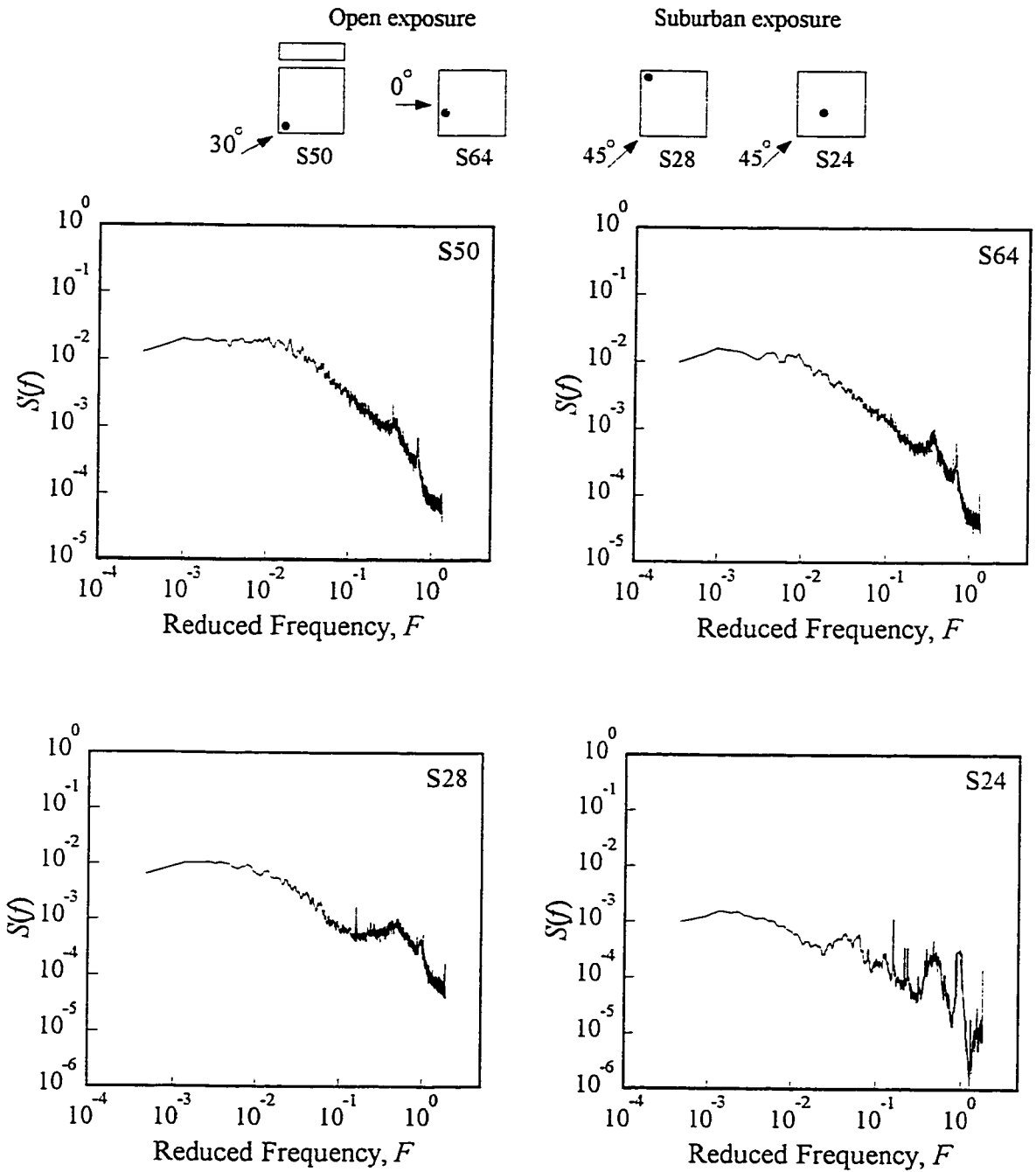
Fig. 4.10 Measured pressure spectra on a flat roof.
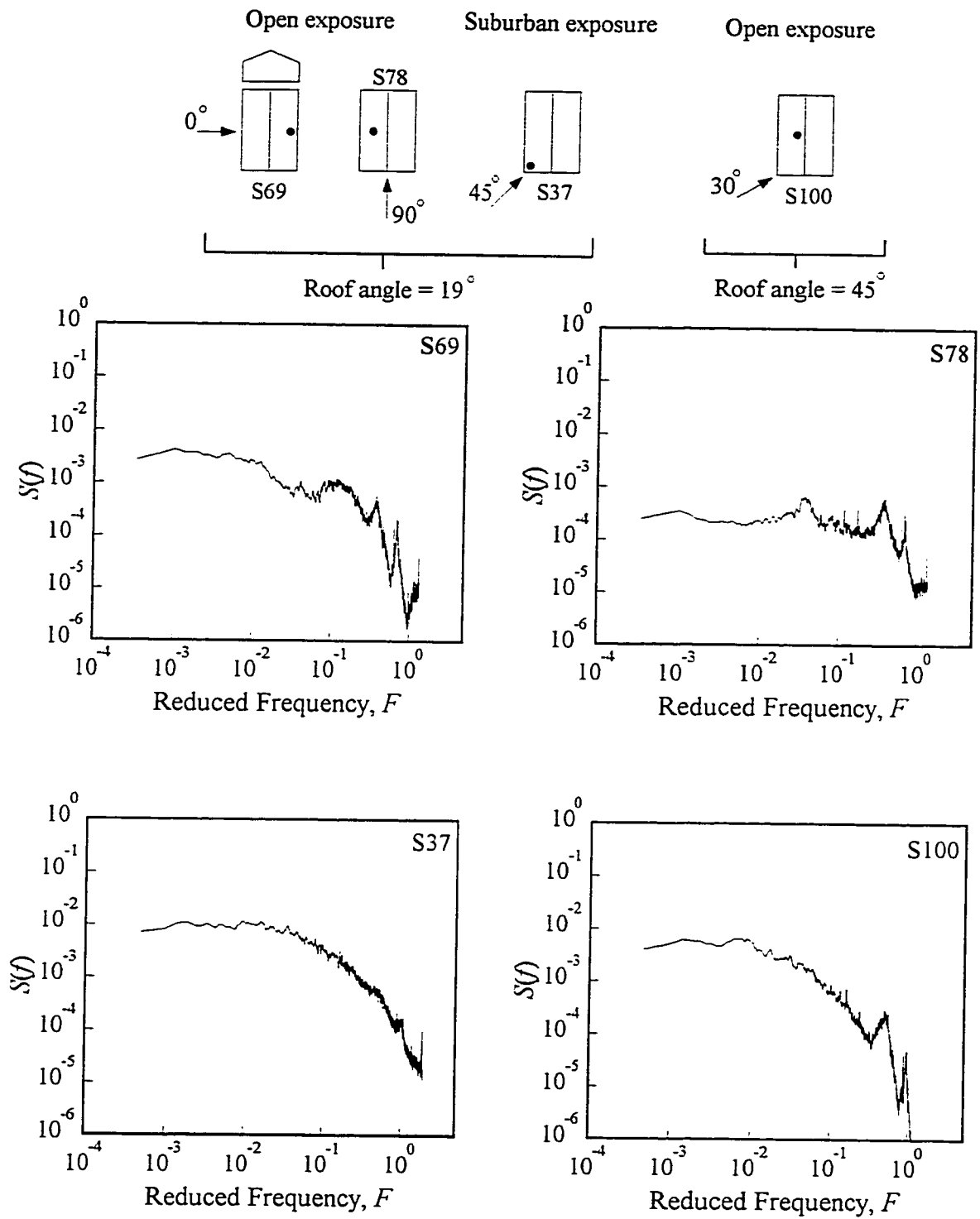
Fig. 4.11 Measured pressure spectra on gable roofs.

however, these spikes are absent in their corresponding spectra. Table 4.5 shows the

sample properties (N_0T, N_pT, ε and β) estimated from the corresponding spectra shown in

Figs. 4.9, 4.10 and 4.11. The MATLAB function **SPECM_ST** reported in Appendix - A

is used to estimate these properties. As expected, the spectra are characterized as broad-

banded from the values of ε and β (see section 3.2.2.2). This observation is common

Table 4.5 Sample properties estimated using spectra.

Sample	N_0T	N_pT	ε	β
Monoslope Roof ($\alpha \approx 15°$)				
S1	643	1750	0.37	0.93
S16	1185	2383	0.50	0.87
S18	361	1839	0.20	0.98
S22	1114	2422	0.46	0.89
Flat Roof				
S50	898	2452	0.37	0.93
S64	1002	2486	0.40	0.91
S28	1306	2549	0.51	0.86
S24	1386	2396	0.58	0.81
Gable Roofs ($\alpha \approx 19°$ and $\alpha \approx 45°$)				
S69	831	2169	0.38	0.92
S78	1343	2373	0.56	0.82
S37	742	2253	0.33	0.94
S100	494	1334	0.37	0.93

among all roof taps for all geometries tested. Further, it is noted that the number of zero

down-crossings (N_0T) as well as negative peaks (N_pT) estimated using power spectra are

mostly higher than those of the estimated using time series reported in Table 4.3. This is

possibly due to the narrowband assumption used in deriving those estimates. However,

consistency in relative terms is maintained and therefore, these estimated properties using

spectra can be used for comparison purposes. Finally, note that the difference in the value

of $N_p T$ calculated using power spectra and time series is far more than the difference in the value of $N_0 T$ calculated using both. This is possibly due to the fourth order moment involved in the estimation of $N_p T$.

4.2.3 Amplitude Domain Properties

Figures 4.12, 4.13 and 4.14 show the PDF of the selected samples where the abscissa represents normalized pressure coefficient in the form of (Cp - Cp_{mean})/Cp_{rms} (Cp_{mean} corresponds to mean pressure coefficient, and Cp_{rms} corresponds to root-mean-square pressure coefficient). The probability ordinates are shown in logarithmic scale in order to show the tail end of the PDF clearly. Further, normalized Gaussian PDF with mean zero and variance one is also plotted with a view to show the deviation of the measured PDF from the Gaussian PDF.

In general, the positive tails of the PDFs are close to those of the Gaussian distribution since the signals are not skewed in positive direction. However, the negative tails of the PDFs are significantly deviated from those of the Gaussian distribution in case of non-Gaussian fluctuations (samples S1, S50, S64, S28, S69 and S37). The curvature of deviation depends on the intensity of non-Gaussianness. A remarkable number of points are past five standard deviations from the mean, which indicates much higher probability for the larger negative pressures than a Gaussian distribution would predict. However, in case of Gaussian fluctuations (samples S22, S24 and S78), the negative tails of the PDFs do also coincide with that of the Gaussian distribution. On the other hand, in some cases
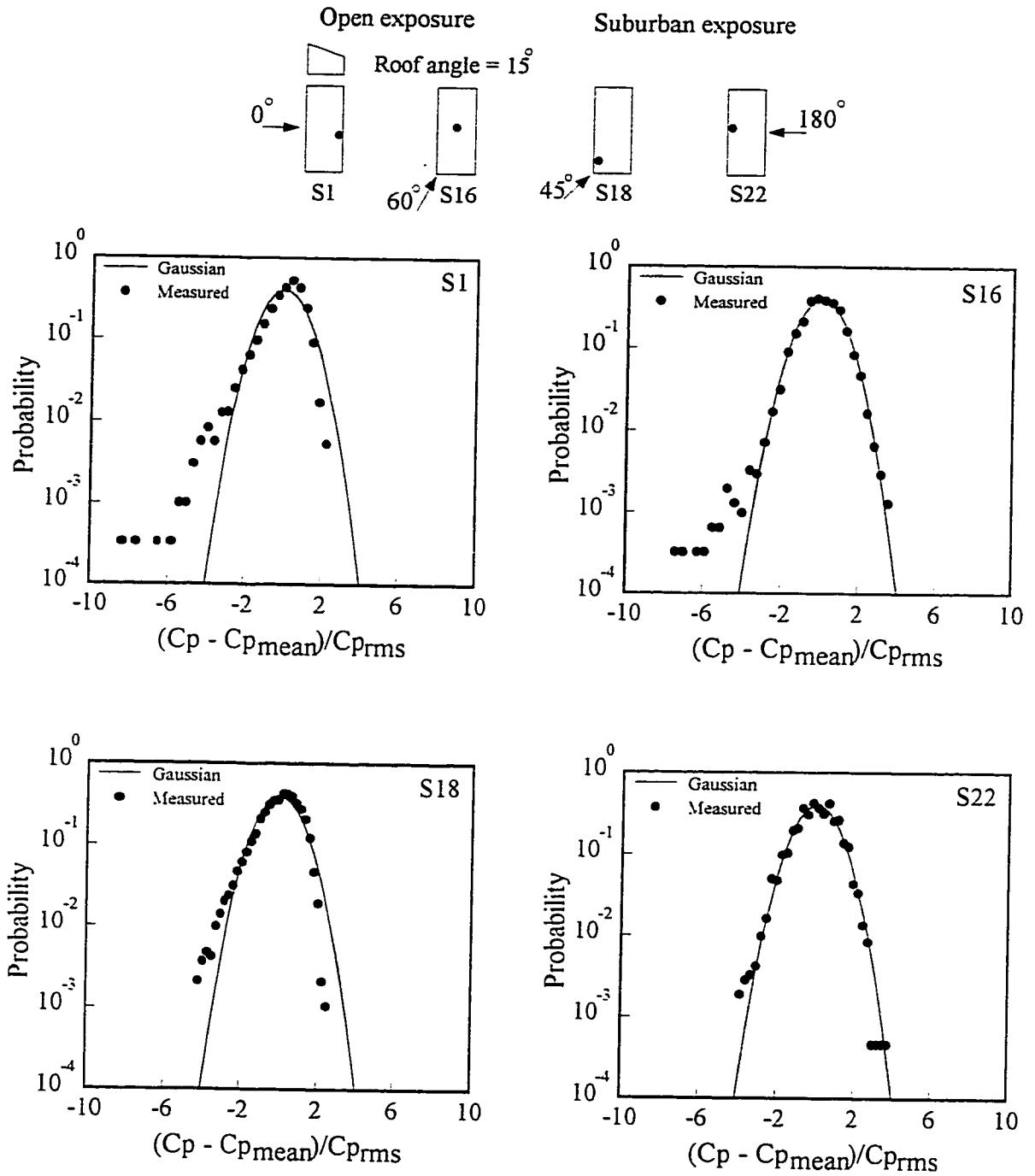
Fig. 4.12 PDFs of measured wind pressures on a monoslope roof.

59
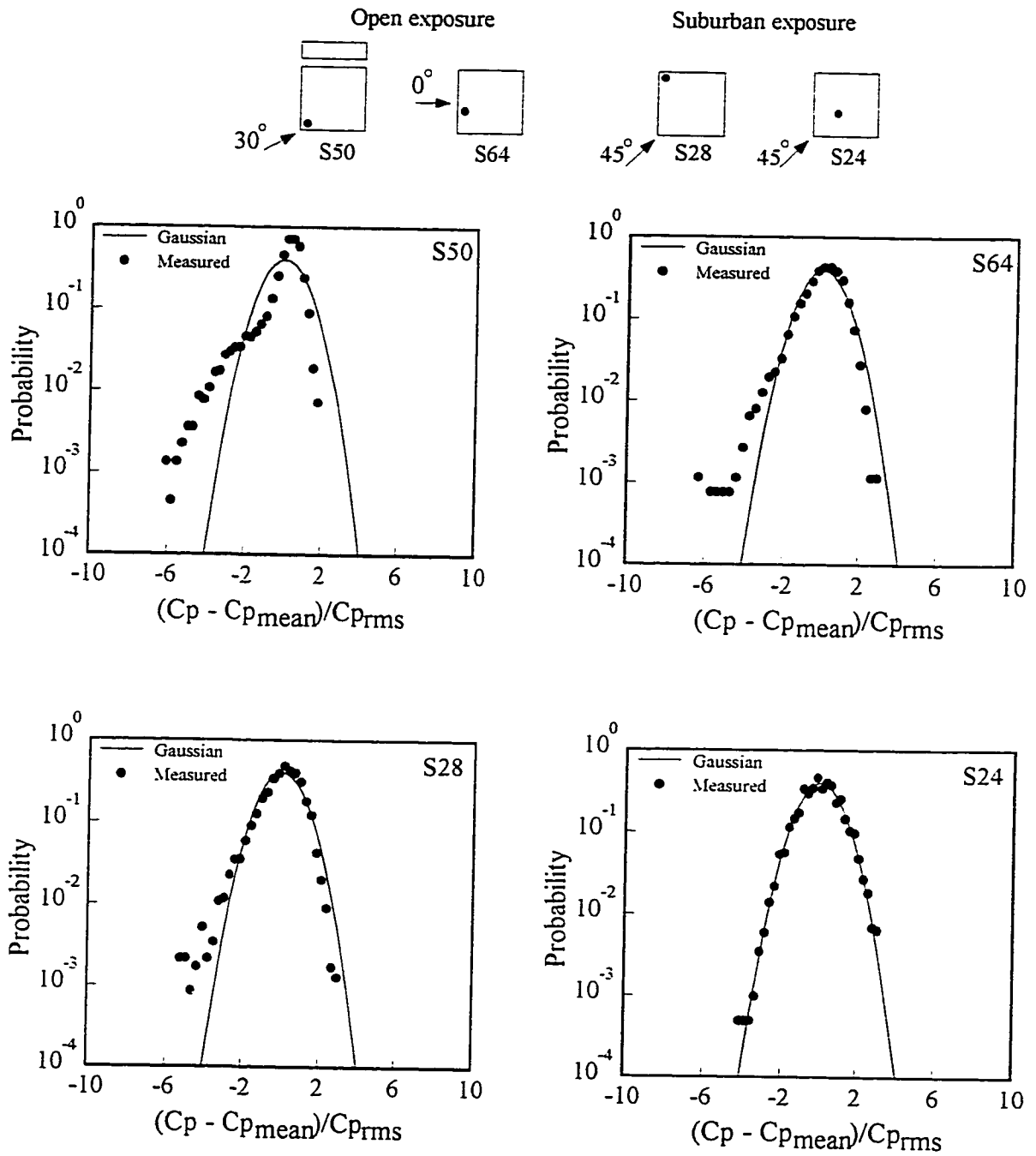
Fig. 4.13 PDFs of measured wind pressures on a flat roof.
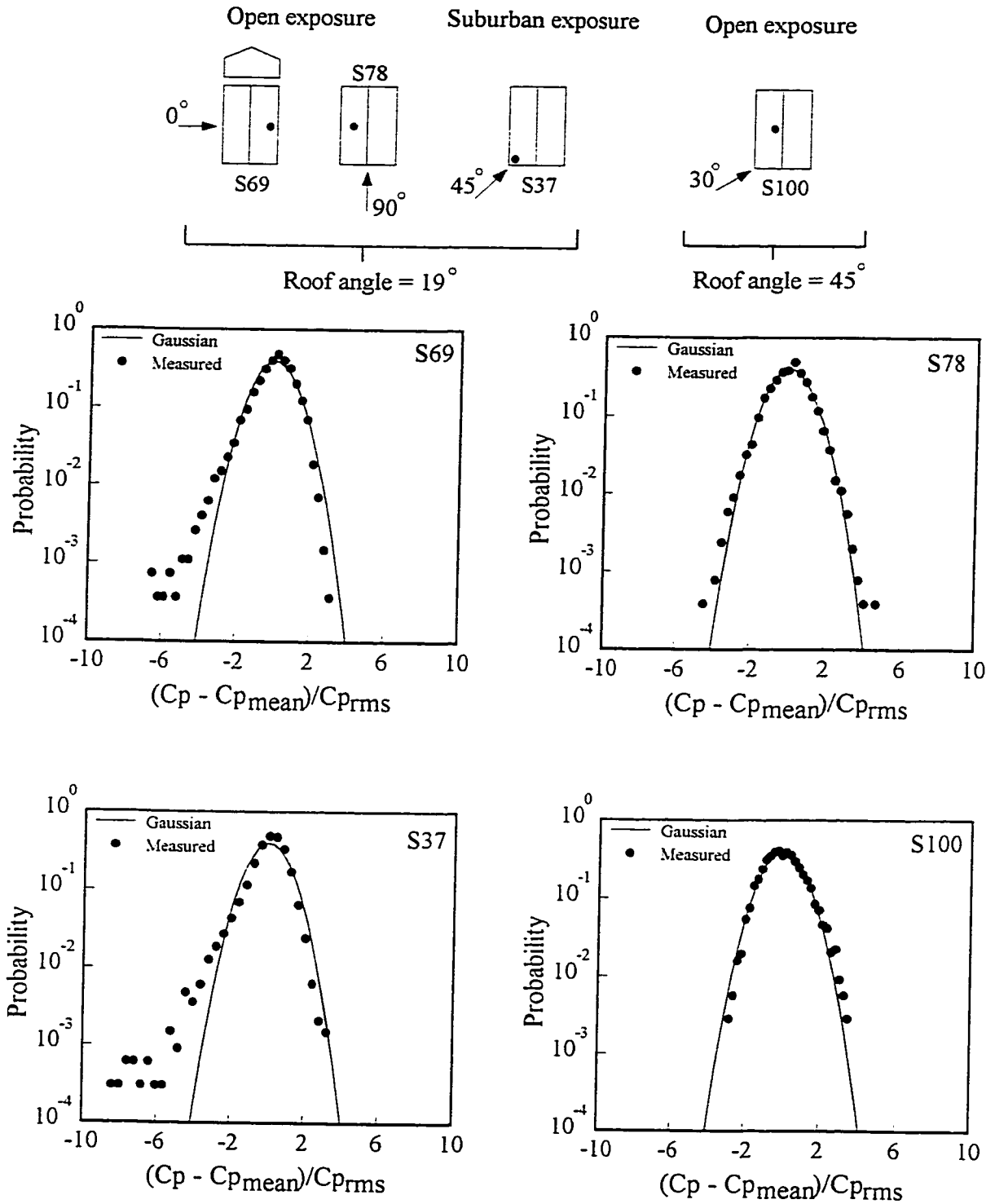
Fig. 4.14 PDFs of measured wind pressures on gable roofs.

(samples S1, S18, S50 and S64) the probability of larger positive pressures are smaller than that predicted by a Gaussian process. Similar observations were reported by Stathopoulos (1980) and Xu (1995a). Finally, it is interesting to note the peculiar shape of the PDF of sample S50 (Fig. 4.13). The pressure fluctuations corresponding to this PDF have a much higher probability of peak factor in the range around the zero peak factor. This feature is attributed to a large number of fluctuations of small suction (low amplitude high frequency fluctuations) around the mean level. It can be concluded from the preceding discussion that the PDFs of the roof pressure fluctuations follow either Gaussian or non-Gaussian distribution depending on the tap location and wind direction.

4.3 ZONES OF GAUSSIAN AND NON-GAUSSIAN PRESSURE FLUCTUATIONS

It appears that the characteristics of pressure fluctuations are dependent mainly on the tap location and wind direction. Further, Gaussian as well as non-Gaussian fluctuations have been observed on roofs. As far as modelling of pressure fluctuations is concerned, it is convenient first to classify the roof into zones of Gaussian and non-Gaussian pressure fluctuations. Within this context, the statistics of pressure fluctuations are carefully observed and the zones of Gaussian and non-Gaussian regions are identified for ranges of wind direction. A particular region is considered non-Gaussian if the absolute values of skewness and kurtosis of pressure fluctuations at various taps are greater than 0.5 and 3.5 respectively. Based on the wind tunnel measurements, the approximate Gaussian and non-Gaussian regions of monoslope, flat and gable roofs are provided in Figs. 4.15, 4.16 and 4.17; where z is assumed to be 10% of least horizontal dimension or 40% of lower
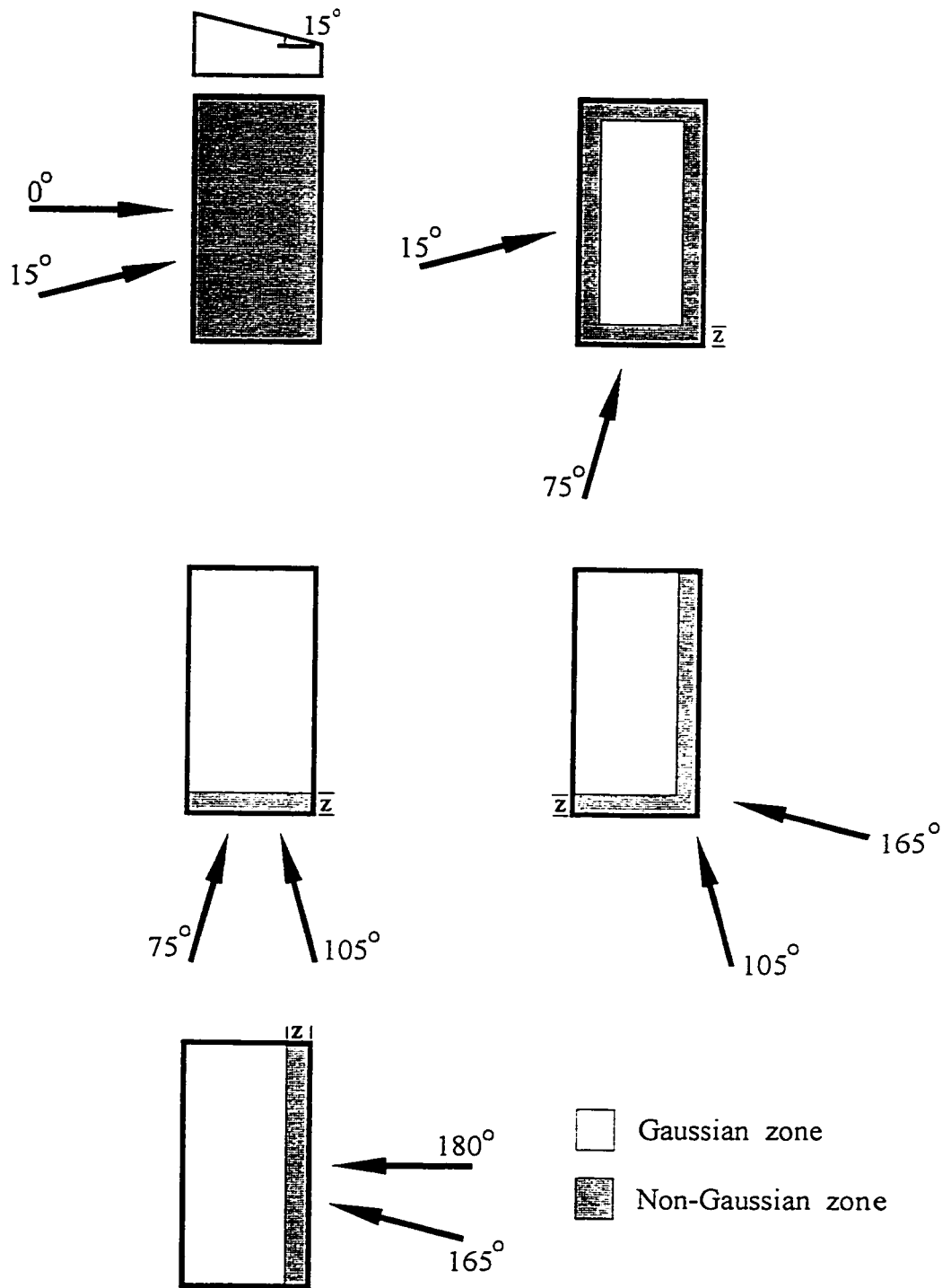
Fig. 4.15 Gaussian and non-Gaussian zones for monoslope roofs.
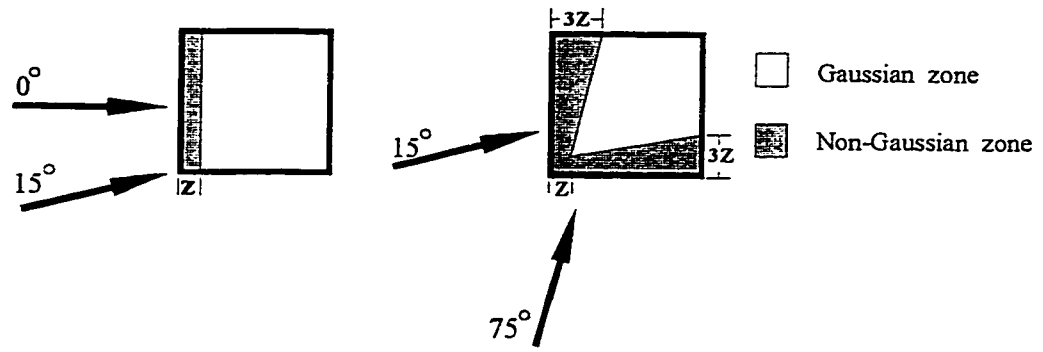
Fig. 4.16 Gaussian and non-Gaussian zones for flat roofs.
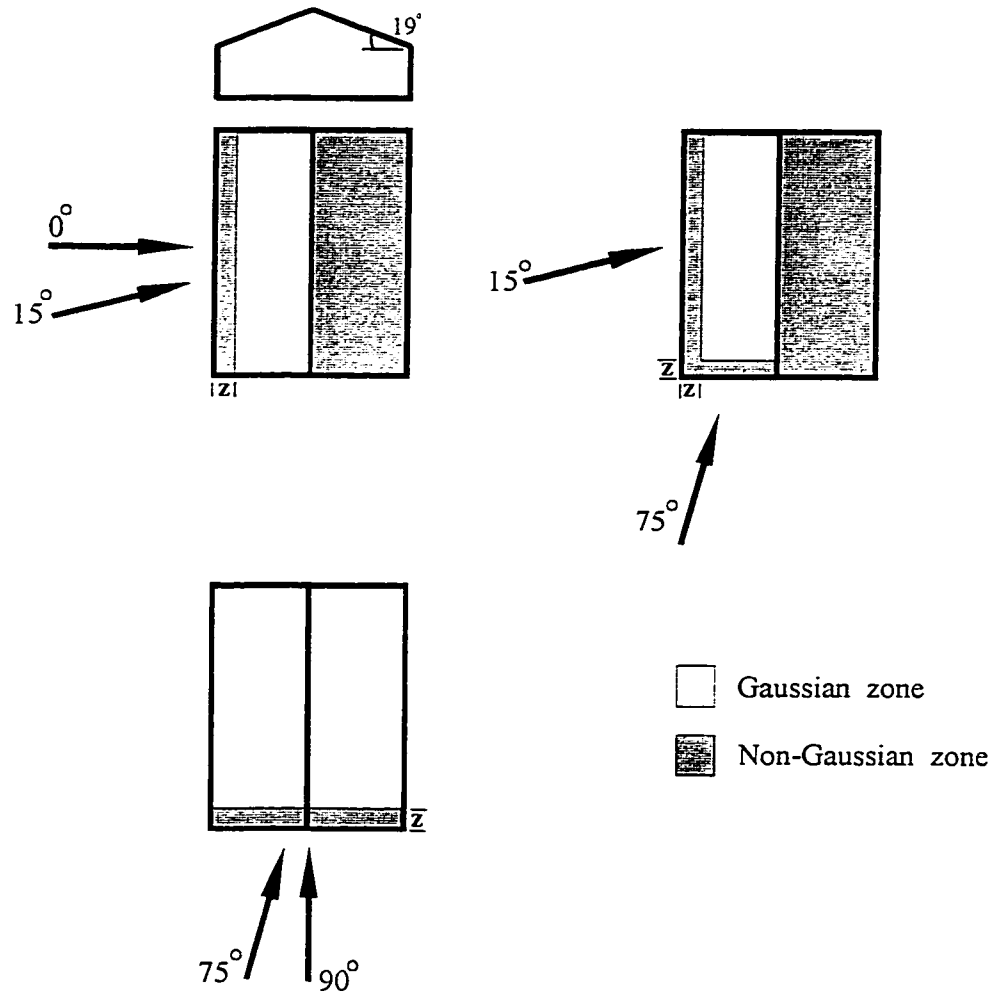
Fig. 4.17 Gaussian and non-Gaussian zones for gable roofs.

eave height, whichever is less (NBCC 1995). Figure 4.15 shows the zones of Gaussian and non-Gaussian pressure fluctuations for monoslope roofs. In general, the edges of the roof, especially windward edges, are subjected to non-Gaussian fluctuations. The middle portion of the roof except at an azimuth of 0°-15° is subjected to Gaussian fluctuations. In case of flat roof (Fig. 4.16), the windward edge is subjected to non-Gaussian fluctuations while the other portions are subjected to Gaussian fluctuations. Almost the same result prevails in the case of gable roof shown in Fig. 4.17. As far as gable roof with roof slope 45° is concerned, the pressure fluctuations are generally close to Gaussian distribution eventhough there are some isolated measurements of non-Gaussian pressure fluctuations.

Table 4.6 provides the coefficients of skewness and kurtosis of local pressure fluctuations on Gaussian and non-Gaussian zones of various roof geometries tested in two types of terrain. Note that the variation of skewness and kurtosis values among the terrains is not very significant; however, their variation among roof geometries is notable

Table 4.6 Coefficients of skewness and kurtosis of local pressure fluctuations on low building roofs.

Region	Skewness		Kurtosis	
	Open	Suburban	Open	Suburban
Monoslope Roof ($\alpha \approx 15°$)				
G	0.0 - -0.3	-0.1 - -0.4	3.0 - 3.3	3.1 - 3.4
NG	-0.5 - -1.4	-0.6 - -1.5	3.5 - 7.5	3.7 - 8.0
Flat Roof				
G	0.0 - -0.2	0.0 - -0.3	3.0 - 3.5	3.1 - 3.5
NG	-0.5 - -2.2	-0.5 - -2.3	3.5 - 9.8	3.7 - 10.0
Gable Roof ($\alpha \approx 19°$)				
G	-0.1 - -0.3	-0.1 - -0.4	3.0 - 3.3	3.1 - 3.4
NG	-0.5 - -1.0	-0.5 - -1.1	3.5 - 5.7	3.7 - 6.5

Note: G = Gaussian zone; NG = non-Gaussian zone.

in case of a non-Gaussian zone. The pressure fluctuations observed on non-Gaussian zones of flat and monoslope roofs are highly skewed compared to those of the gable roof as clearly shown in Table 4.6. On the other hand, the skewness and kurtosis values corresponding to Gaussian zones are more or less in the same range for the various roof geometries.

During this investigation, a wide spectrum of pressure fluctuations have been measured on several low building roofs at different conditions in order to draw their overall stochastic characteristics. Though the measurements have been made at many tap locations on four different roofs in two different terrain conditions for various wind directions, several other parameters which may have an effect on wind-induced pressures are not considered. It is known that wind-induced pressures on a roof also depend on roof slope, architectural features, immediate surroundings etc. (Stathopoulos 1984b). Therefore, it would be of interest to carry out further experiments considering these factors for gathering new stochastic characteristics of pressure fluctuations if any.

4.4 SUMMARY

This chapter presents the experimental procedure and results which are necessary for developing a suitable analytical/empirical representation for pressure fluctuations on low building roofs. The results of the experiments are summarized as follows:

(1)   The characteristics of fluctuations on roofs vary depending on the tap location, wind direction and roof geometry.

(2)   For all practical purposes, the measured pressure fluctuations can be considered as stationary.

(3)   The pressure fluctuations on roofs follow either Gaussian or non-Gaussian distribution depending on the tap location and wind direction.

(4)   The pressure fluctuations on roofs are broad-banded.

(5)   There are two distinct properties of spikes, namely the frequency of occurrence and the magnitude. Both should be given proper attention while modelling the time series.

(6)   With a view to simplify the modelling procedure, the zones of Gaussian and non-Gaussian pressure fluctuations have been identified for various roof geometries and wind directions. In general, the edges of the roofs are prone to non-Gaussian fluctuations.

CHAPTER 5
SIMULATION OF GAUSSIAN PRESSURE FLUCTUATIONS

"....An important special class of random process (and fields) are the normal or Gaussian processes......The importance of normal processes is because.....(ii) many real phenomena can be satisfactorily modeled by normal processes...."

S. H. Crandall and W. Q. Zhu, 1983.

A variety of techniques that have been suggested by various researchers for the simulation of Gaussian stationary random processes have been discussed in Chapter 2. The method to be favoured in terms of application of simulation studies has to satisfy the following requirements: (1) easy implementation, (2) parsimony, and (3) reasonable accuracy concerning stationarity, ergodicity, and statistical properties. The general impression obtained from the review was that conventional discrete Fourier transform (DFT) representation along with fast Fourier transform (FFT) algorithm, a method for computing DFT with minimal execution time, would be a reasonable choice satisfying all the above requirements. The stochastic properties of this model described in section 3.1.6 are revisited.

In case of Gaussian random process, the mean value and the second order properties (variance, ACF, SDF) uniquely represent the stochastic characteristics of the process (Bendat and Piersol 1986). Since ACF and SDF are Fourier transform pairs, satisfying either one of the two will guarantee the other. Further, achieving either SDF or ACF will satisfy variance. Therefore, the simulation of Gaussian pressure fluctuations aims at achieving the mean and the spectral density function.

5.1 SIMULATION METHODOLOGY

Gaussian zero-mean wind pressure time series can be generated by inverting the constructed Fourier coefficients using FFT algorithm. The simulations can be done using the following DFT equation (Brockwell and Davis 1991):

$$Z_t = n^{-1} \sum_{k=0}^{n-1} \sqrt{I_k} \; e^{i\phi_k} \; e^{i 2\pi k t / n}, \quad t = 0,1,\ldots\ldots,n-1. \tag{5.1}$$

where, Z_t corresponds to time series, n is time series length, $\sqrt{I_k}$ is amplitude, ϕ_k is phase and the term $2\pi k/n$ is the integer multiple of the fundamental frequency $2\pi/n$ known as Fourier frequency.

Knowledge of amplitude ($\sqrt{I_k}$) as well as phase (ϕ_k) are required for the proposed simulation. Power spectra can be utilized to generate the amplitude part of the Fourier coefficient (Suresh Kumar and Stathopoulos 1996a) - details are presented in Chapter 7. However, for the current simulations, the amplitude part of the DFT of target signal (X_t),

$$\sqrt{I_k} = \left| \sum_{t=0}^{n-1} X_t \; e^{-i 2\pi k t / n} \right| \tag{5.2}$$

is substituted for Fourier amplitude ($\sqrt{I_k}$). By using the amplitude part of the target signal, the various second order characteristics (variance, SDF, ACF) are satisfied automatically. The first order characteristic (mean value) can be added separately to the zero-mean simulated signal.

The phase part of the Fourier coefficient of a Gaussian signal can be represented by

independent uniform random numbers (U) ranging between $-\pi$ and π by

$$\phi_k = \begin{cases} U_k & , \quad 1 \leq k \leq \dfrac{n}{2} \\[2mm] -U_{n-k} & , \quad \dfrac{n}{2}+1 \leq k \leq n-1 \end{cases} \tag{5.3}$$

where, probability density function of U is

$$f(U) = \frac{1}{2\pi} , \quad -\pi \leq U \leq \pi \tag{5.4}$$

Theoretically, the mean as well as skewness values of the set of uniform random numbers (U) are zero, while the variance and kurtosis values of the corresponding random numbers are $\pi^2/3$ and 1.8 respectively. Such uniform random numbers (U) can be easily generated using pseudo-random number generator as will be discussed in section 5.3.

A flow chart displaying the above mentioned simulation procedure is shown in Fig. 5.1. The procedure consists of three steps: (1) generation of Fourier amplitude part of a given time history, (2) generation of Fourier phase part, and (3) simulation of the time history by inverting the Fourier coefficients, a linear combination of Fourier amplitude and phase derived from steps (1) and (2) respectively. The MATLAB function **GTIME** reported in Appendix - A is used to simulate Gaussian time series samples based on a given time history. Further, a typical simulation example is presented in Fig. 5.2. The target signal shown in this figure corresponds to the time series measured on the edge pressure tap of a monoslope roof (roof angle $\approx$ 15°) of a low-rise building for 180° azimuth in suburban terrain conditions. The skewness and kurtosis values of the signal are estimated to be -0.21 and 3.08 respectively. The appearance as well as the statistics show that this signal follows Gaussian distribution. Here, an attempt has been made to reconstruct this time series using
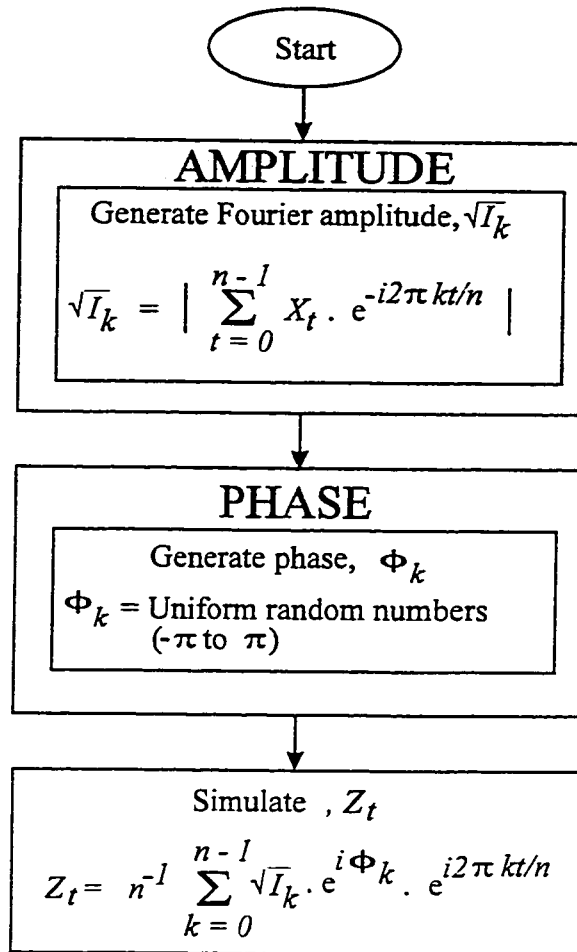
Fig. 5.1 Flow chart for synthesis of Gaussian wind pressure time series.

the procedure shown in Fig. 5.1. The amplitude part estimated using Eq. (5.2) and the estimated phase part using Eq. (5.3), where $n = 8192$, are shown in Fig. 5.2. The simulated signal also shown in Fig. 5.2, is generated using Eq. (5.1) by means of target amplitude and phase signal, whereas the mean is added separately to the zero-mean fluctuations. The general appearance of the simulated signal appears satisfactory; however, detailed demonstrations are shown in the following section.

As mentioned in section 3.1.6, the above simulation procedure provides stationarity of the time series by using independent uniform random numbers as the Fourier phase part.
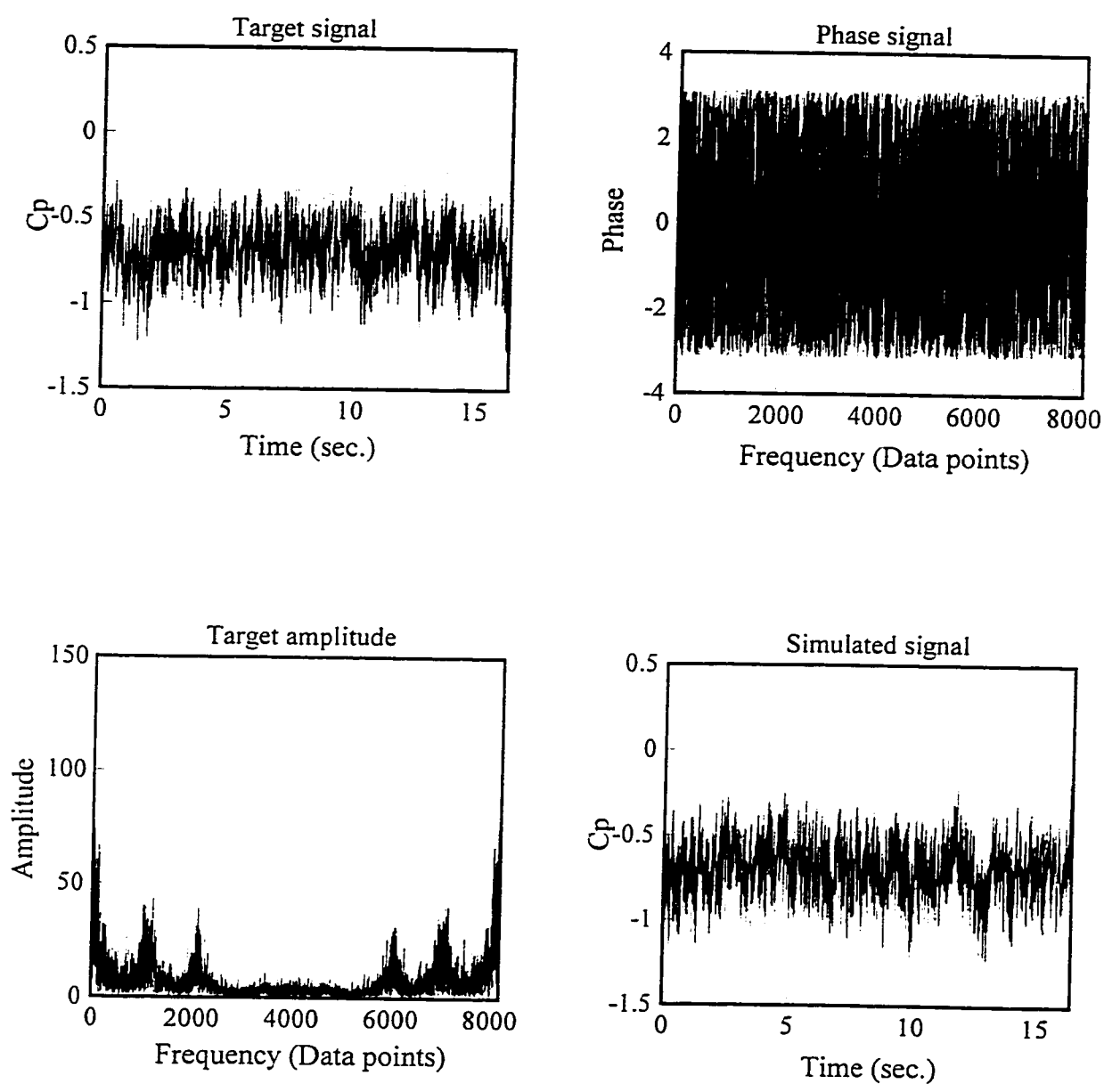
Fig. 5.2 Pictorial representation of the simulation methodology.

Therefore, in order to achieve perfect stationarity, complete lack of correlation of the set of uniform random numbers (Fourier phase part) is required. However, this requirement is almost impossible to achieve using any commonly available random number generators. On the other hand, in practice, no random process can be truly stationary and as a matter of fact, the phase processes are somewhat correlated. During this investigation, several Gaussian time series have been measured on many low building roofs at various locations for several wind attack angles. In almost all cases, the phase processes were found to be somewhat correlated; correlation values up to 6% (except at zeroth lag) have been observed. A typical example is shown in Fig. 5.3 where the autocorrelation functions of the phase process of the measured and simulated signals are comparable; the correlation value of one at zeroth lag in both cases is not shown. The low correlation values of the phase process observed at higher
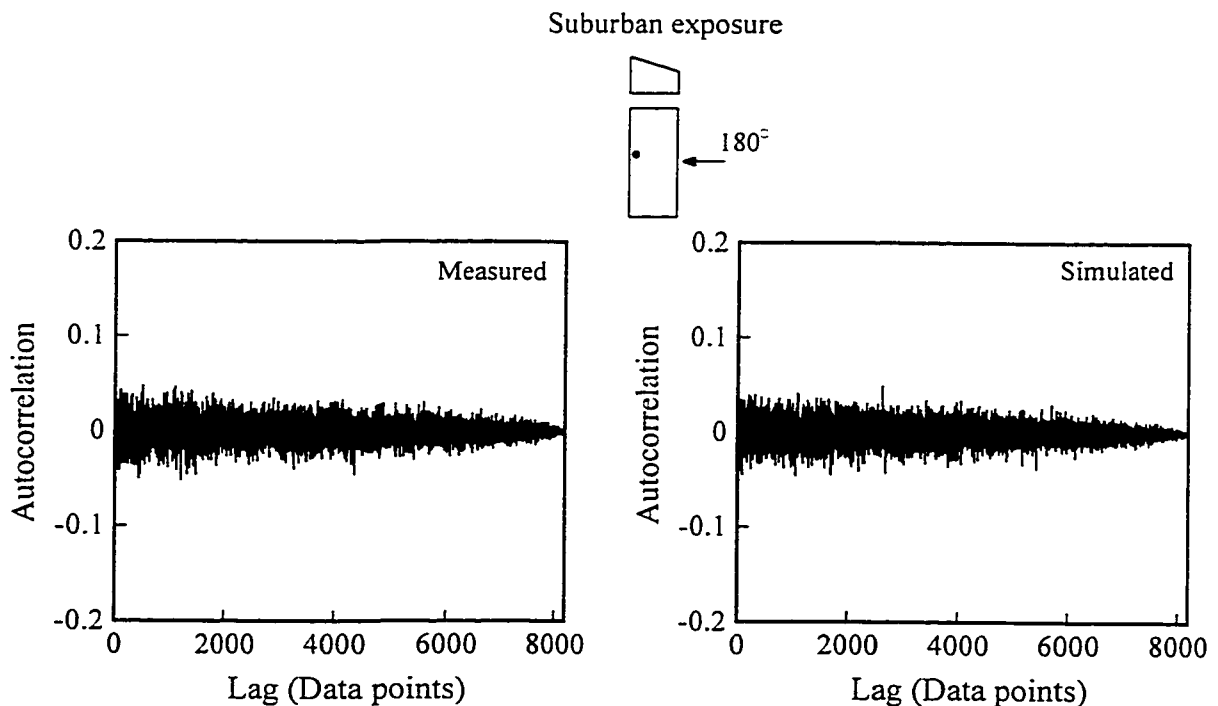
Fig. 5.3 Autocorrelation functions of the phase process of the measured and simulated signals.

lags are not expected to affect the stationarity of the time series. Furthermore, the stationarity of the simulated signals is reinforced by verifying the invariant nature of their autocorrelation functions.

5.2 EXAMPLE SIMULATIONS

Three distinct pressure time histories shown in Table 5.1 were chosen for demonstration purposes. The statistics of the time histories presented in Table 5.2 show that they are more or less Gaussianly distributed. Further these time histories are plotted in Fig. 5.4 using normplot function available in MATLAB (1994b). Normplot displays a normal probability plot of the data. The plot has the sample data displayed with the plot symbol '+'. Superimposed on the plot is a line joining the first and third quartiles of each data. The plot will appear linear if the data comes from a Gaussian distribution. Figure 5.4 shows that all

Table 5.1 Sample Gaussian pressure time series.
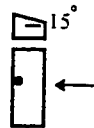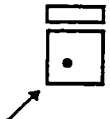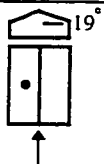
Sample	Roof type	Wind direction	Terrain condition	Orientation of model
S22	monoslope	180°	suburban	
S24	flat	45°	suburban	
S78	gable	90°	open	

74

Table 5.2 Statistics of selected samples.

Sample	Mean	Variance	Skewness	Kurtosis
S22	-0.69	0.02	-0.21	3.08
S24	-0.53	0.03	0.01	3.02
S78	-0.31	0.03	-0.07	3.39
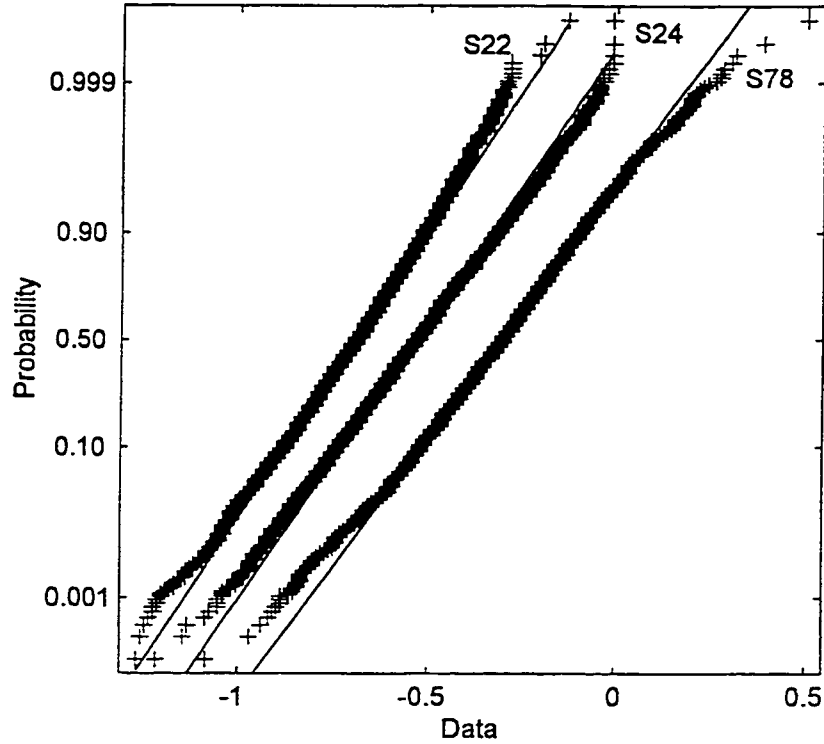
Fig. 5.4 Normal probability plot of the selected samples.

three data samples are approximately linear and therefore, can be considered as Gaussianly distributed for all practical purposes.

The above mentioned three time histories are reconstructed using the procedure discussed in section 5.1. The statistics of the simulated and target signals are compared in Table 5.3. As expected, mean and variance of the simulated signals coincide with those of the corresponding target signals. The skewness and kurtosis values of the simulated signals are

Table 5.3 Comparison between target and simulated statistics.

	Mean	Variance	Skewness	Kurtosis
Sample S22				
Target	-0.69	0.02	-0.21	3.08
Simulated	-0.69	0.02	-0.09	3.03
Sample S24				
Target	-0.53	0.03	0.01	3.02
Simulated	-0.53	0.03	-0.04	3.03
Sample S78				
Target	-0.31	0.03	-0.07	3.39
Simulated	-0.31	0.03	-0.01	3.04

closer to the expected Gaussian values of zero and three respectively. Note that the target samples S22 and S78 are not purely Gaussian; however, in simulation, there is no criteria used to satisfy their small values of skewness and kurtosis and instead, the signals are assumed to be Gaussian. This will explain the difference in skewness and kurtosis values between target and simulated signals. Both target and simulated signals as well as their PDF's and extreme values (Gumbel's plot) for each sample, are shown in Figs. 5.5, 5.6 and 5.7. Target and simulated signals are presented in the form of pressure coefficient (Cp) versus time. In case of PDF plots, the abscissa represents normalized pressure coefficient in the form of $(Cp-Cp_{mean})/Cp_{rms}$ (Cp_{mean} corresponds to mean pressure coefficient, and Cp_{rms} corresponds to root-mean-square pressure coefficient). Further, Gumbel's plots represent extreme Cp values (Cp_{peak}) as a function of reduced y-variate (see section 3.2.3.1 for details), where the extreme Cp values are obtained as follows: the 8192 simulated as well as measured data are divided into 16 segments of 512 values each and the peak value from each segment is selected. In case of sample S22, the target and simulated signal appear
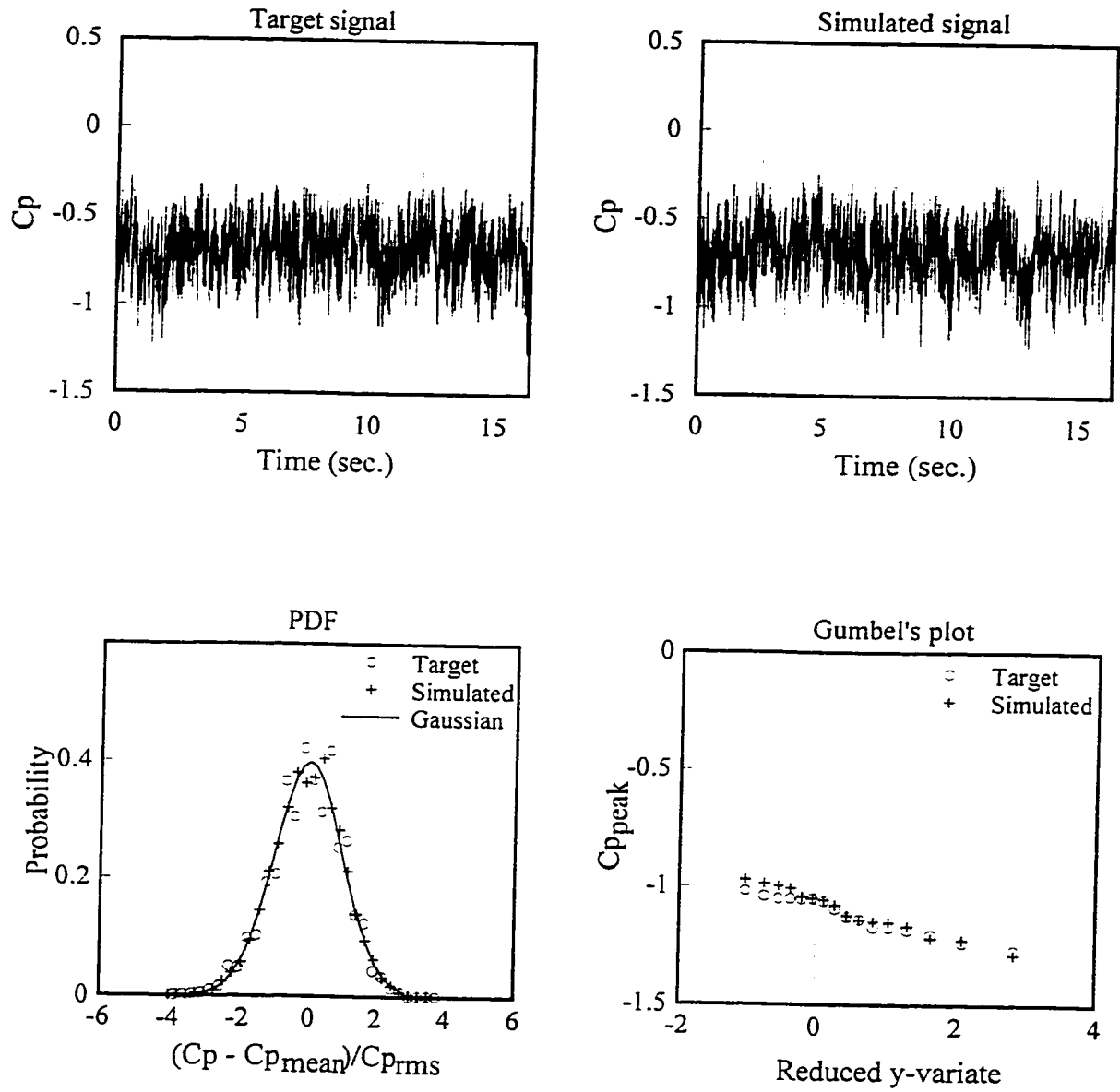
Fig. 5.5 Simulation results (sample S22).
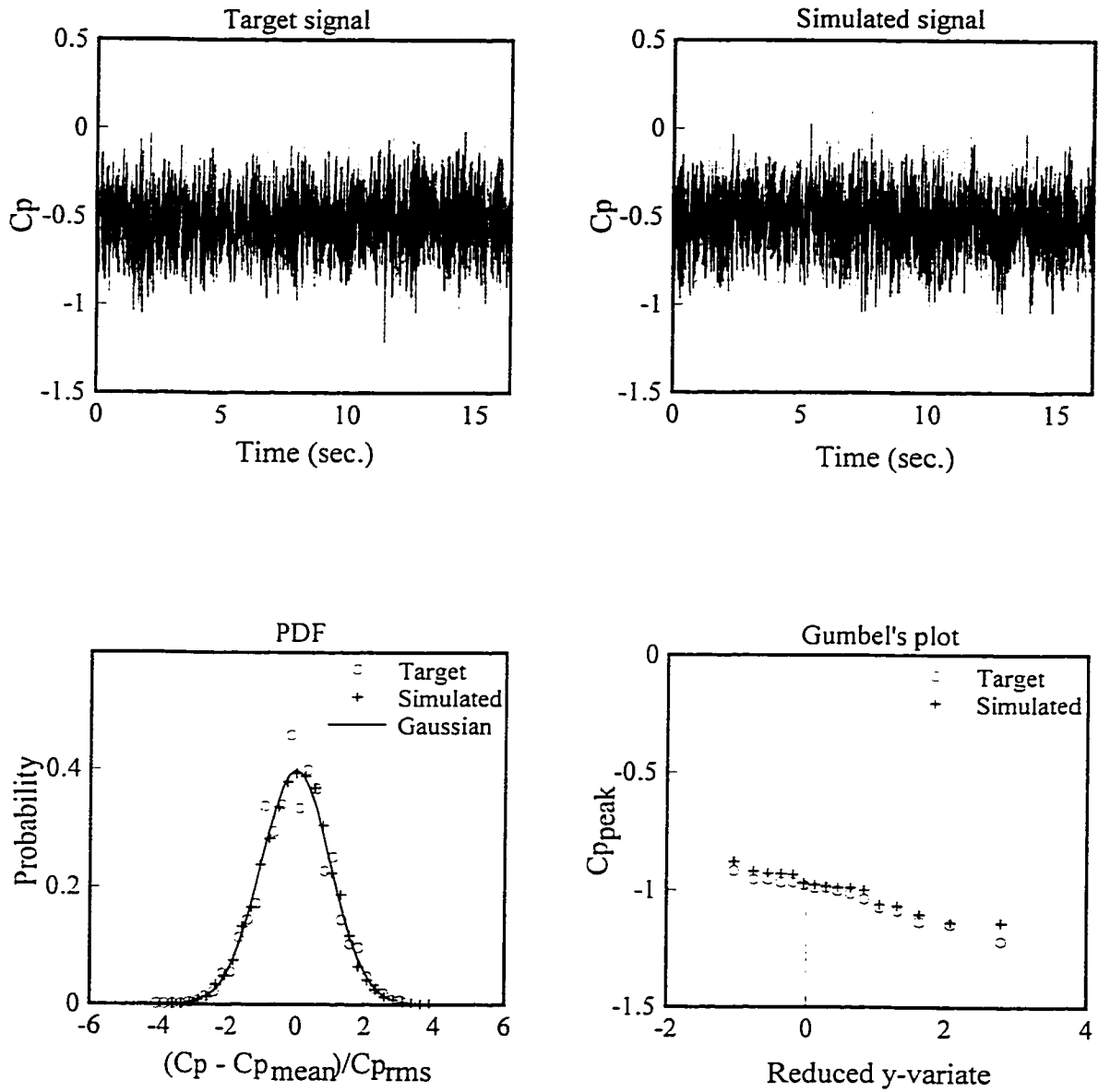
Fig. 5.6 Simulation results (sample S24).
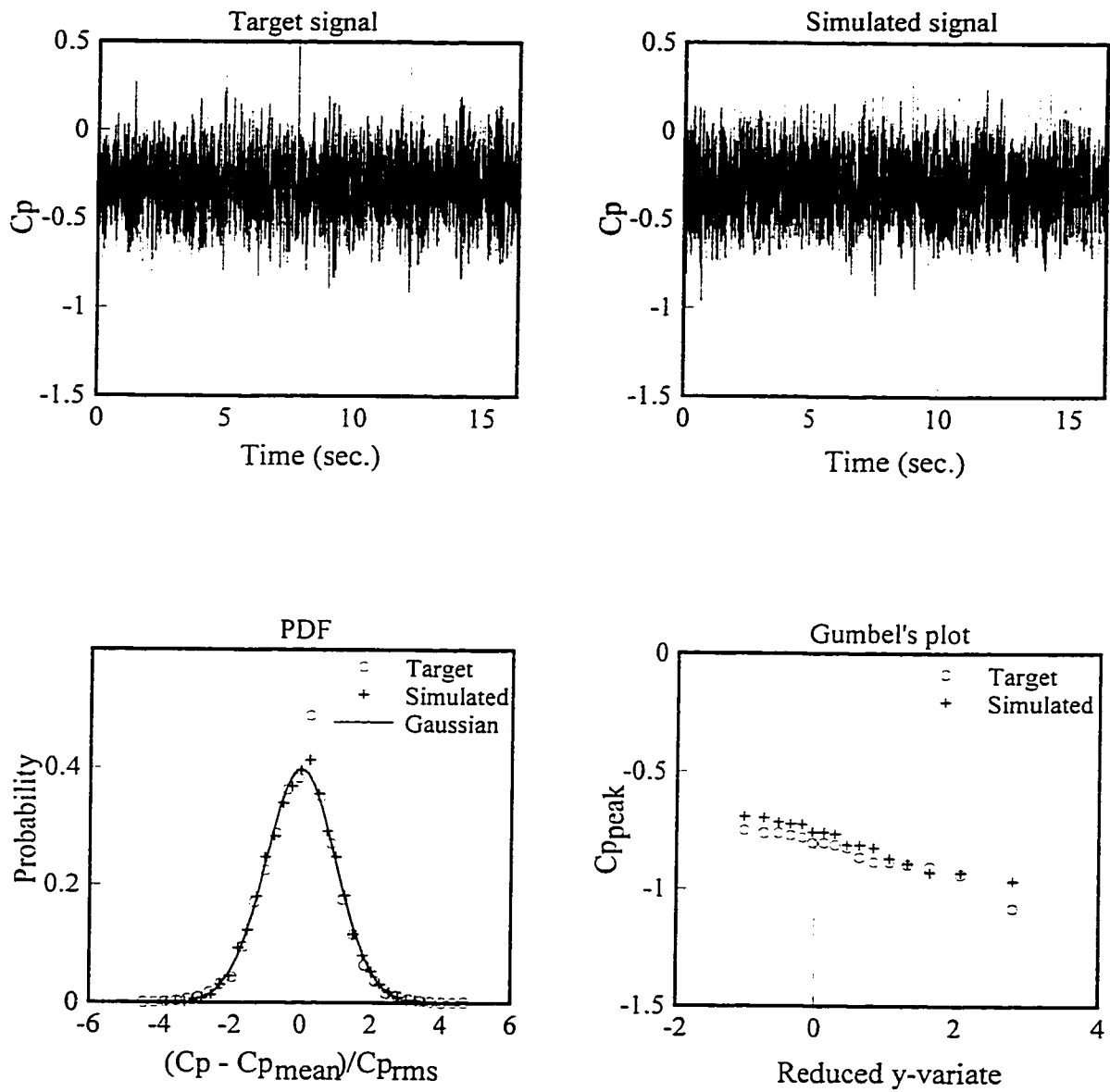
Fig. 5.7 Simulation results (sample S78).

similar. Further, the PDF as well as the Gumbel's plot of the simulated signal are in good comparison with those of the target signal. Overall, the results are repeated in case of samples S24 and S78 (see Figs. 5.6 and 5.7). The negligible discrepancies observed at the tail end of the PDF's in some cases can be attributed to the Gaussian assumption used in the simulation as previously mentioned. These three examples are representative of the several simulations that have been performed during this study.

In addition to the previous comparisons, the number of level crossings and peaks of the simulated signals have been compared with those of the corresponding target signals. Table 5.4 shows the comparison between target and simulated signals in terms of the number of negative peaks and down-crossings at various levels. All calculations have been made after the signals were subtracted from their corresponding means and normalized by their corresponding standard deviations (σ). The number of negative peaks as well as down-crossings at various levels of the simulated signals seem to be in general close with those of the corresponding target signals.

Table 5.4 Number of negative peaks and down-crossings at various levels of target and simulated time histories.

Sample		Peaks	Crossings Levels below mean in terms of σ			
			0	-1	-2	-3
S22	T	1935	1064	601	163	18
	S	1992	1060	648	132	16
S24	T	2030	1461	834	166	12
	S	2021	1441	849	169	11
S78	T	1876	1260	690	161	21
	S	1936	1278	722	136	12

Note: T = Target signal, S= Simulated signal

80

5.3 REPEATABILITY OF THE SIMULATIONS

It is now necessary to provide some comments concerning the repeatability of simulations carried out by using different random number sets. For the simulation of Gaussian signals, uniform random numbers (U) ranging between $-\pi$ and π are required to represent the phase part of the Fourier coefficients. Though various algorithms are available and listed in Knuth (1981), good random number generators are hard to find. Park and Miller (1988) presented the inadequacy of the many available random number generators along with the discussion of practical and theoretical issues concerning the design, implementation, and use of a good, minimal standard random number generator that will port to virtually all systems. They found that the linear congruential generator with proper parametric values is good in terms of accomplishing full periodicity, randomness and easy implementation. On this basis, this generator is selected for the random number generation in this study. Three quantities, i.e. a multiplier, a modulus and an initial seed value are required to generate uniform random numbers by using this algorithm. The value of multiplier and modulus equal to 7^5 and $2^{31}-1$ respectively, which provide full period, randomness and easy implementation capabilities to the generator (Park and Miller 1988), are used in this study. The initial seed value is adopted to be 931316785, the value set by MATLAB (1992) at the start of any simulation. The basic algorithm is

$U1$ = seed/(2^{31}-1),

$U = -\pi + (2\pi * U1)$,

seed = (7^5 * seed)   mod (2^{31}-1),

81

where, $U1$ corresponds to random number whose value is between 0 and 1 and U

corresponds to random number whose value is between $-\pi$ and π. Subsequent sets of

random numbers are expected to be different due to the change of initial seed value.

Therefore, an attempt has been made to examine the sensitivity of uniform random number

sequences on simulation results.

For each simulation (n = 8192), 4096 uniform random numbers ranging between $-\pi$ and π

are required (see Eq. (5.3)). One hundred distinct blocks of 4096 uniform random numbers

each have been generated and the variation of their first four moments (mean, variance,

skewness, and kurtosis) is displayed in Fig. 5.8 using boxplot. Boxplot produces a box and
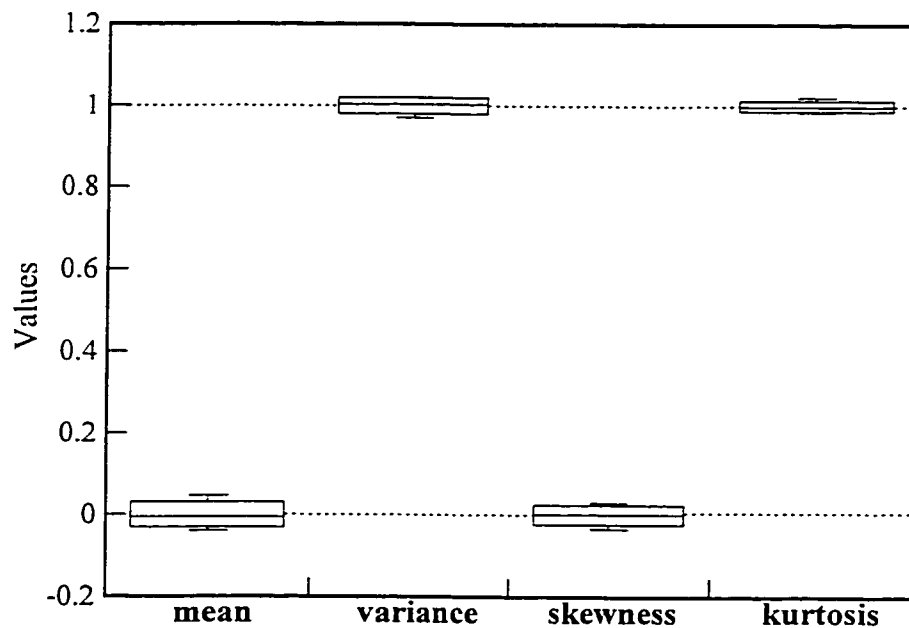
Fig. 5.8 Variation of the first four moments of the uniform random number data sets.

whisker for each data set (MATLAB 1994b). The box has lines at the lower quartile,

median, and upper quartile values. The whiskers are lines extending from each end of the

box to show the extend of the rest of the data. Mean and skewness of the random number

82

sets are supposed to be zero; however, negligible variations up to ±5% are noted. Variations in variance and kurtosis values of the random number sets are also shown in the same figure after they have been normalized with respect to their corresponding theoretical values. Again, negligible variations up to ±5% have been observed. Simultaneously, the same 100 blocks of random numbers have been used to simulate 100 corresponding time histories using the amplitude part of the sample S22. Figure 5.9 presents the variation of the first four moments of the simulated time histories in a boxplot format. Note that mean and variance of the simulated time histories are always equal to the corresponding target values of -0.69 and 0.02 respectively. This is due to the employment of the same amplitude part of the DFT of the target signal S22 in all simulations. Further, it is clear that the different random number sets (phase part) do not have an effect on the simulated means and variances. On the other hand, they do have an effect on skewness and kurtosis values of the simulated time histories. Based on the Gaussian assumption, skewness and kurtosis values of the simulated
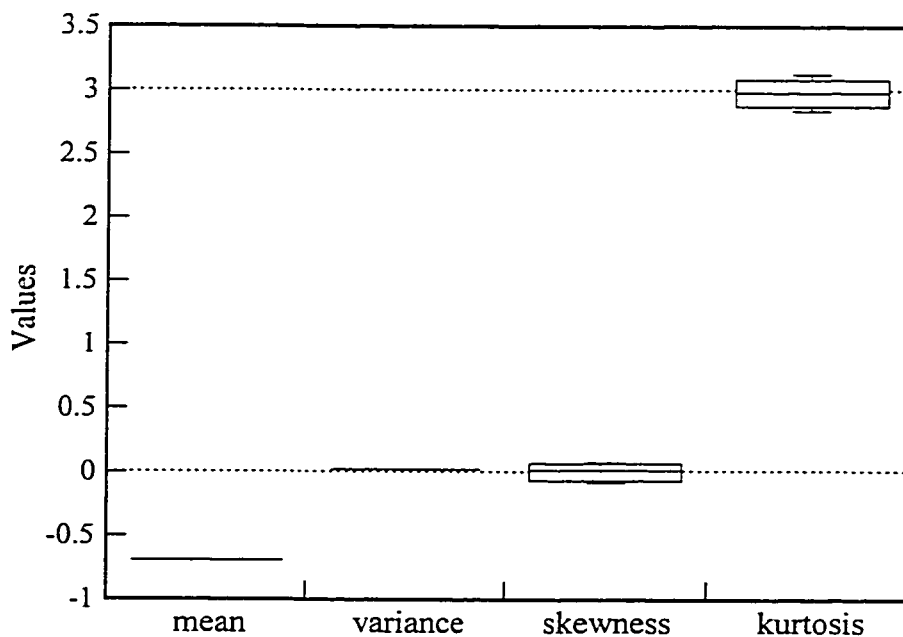
Fig. 5.9 Variation of the first four moments of the simulated time histories.

time histories are supposed to be zero and three respectively; however, due to the varying statistical properties of the random number sets, variations up to ±15% have been observed. Furthermore, since many time histories are required for extreme value analysis and fatigue analysis, the average skewness and kurtosis values among many samples are expected to be close to zero and three respectively. Overall, the performance of the used random number generator is satisfactory and the small variations noted in simulated skewness and kurtosis values can be neglected for practical applications.

5.4 SUMMARY

In this chapter, Gaussian wind pressure fluctuations are simulated by initializing complex Fourier coefficients in the frequency domain, and then inverting the Fourier coefficients back to the time domain using FFT algorithm. The amplitude part of the DFT of target signal is substituted for the Fourier amplitude part. While, the Fourier phase part, represented by independent uniform random numbers ranging between $-\pi$ and π, is simulated using a pseudo-random number generator based on the linear congruential method. Several simulations have been performed using this approach and only representative examples are presented in this chapter. The results show that the current approach is capable of simulating Gaussian wind pressure fluctuations on roofs with reasonable accuracy. Further, the sensitivity of the random number sequences on simulation results has been found to be negligible.

CHAPTER 6
SIMULATION OF NON-GAUSSIAN PRESSURE FLUCTUATIONS

"...However, because of mathematical difficulties and the lack of observed data, most generation techniques as well as analytical approaches are limited to dealing with Gaussian fields. In some situations, such a Gaussian assumption is not appropriate because the observed fields exhibit non-Gaussian characteristics.....Therefore, the development of a method for generating sample functions of non-Gaussian fields appears to have theoretical as well as practical significance....."

F. Yamazaki and M. Shinozuka, 1988.

Within the scope of the digital simulation of wind loading, it is frequently assumed that the involved process possesses Gaussian properties. Although this simplifying assumption may be justified in case of integral effects of wind load over larger areas, there are many critical regions of structures where wind load exhibits strong non-Gaussian characteristics. For instance, the local pressure fluctuations measured at corner as well as other separation flow regions of roofs of low buildings are found to be highly non-Gaussian, as mentioned in Chapter 4. The non-normality becomes of significant importance when exceedance probabilities are under investigation, i.e., the reliability of a structure is being assessed. Moreover, the non-Gaussian wind loads are found to induce increased fatigue damage compared to Gaussian loads (Lynn and Stathopoulos 1985; Reed 1993; Suresh Kumar and Stathopoulos 1996b, 1997d). Though plenty of simulation tools are available for the generation of Gaussian wind pressures, efficient simulation of non-Gaussian wind pressures is still problematic. In light of the importance of the non-Gaussian loads and unavailability of efficient simulation tools for their generation, further work on the representation and

simulation of non-Gaussian wind loads would be useful.

Within this context, this chapter presents a novel simulation methodology, based on FFT approach, for the generation of univariate non-Gaussian wind pressure fluctuations on low building roofs. Modelling of the phase part of the Fourier coefficient of a signal is the key issue addressed in this chapter. Comprehensive background on the role of phase part in inducing non-Gaussian characteristics in a signal is provided at the beginning. This is followed by the description of Seong and Peterka's (1993) model for phase. Thereafter, the simulation methodology is described. The development of a new model for phase is discussed and the proposed model for phase, parametric estimation criteria, demonstration of the methodology are presented. The stationarity of the simulated time series is examined. Finally, elaborate demonstrations have been made and the repeatability of simulation has been discussed.

6.1 BACKGROUND

Some of the important properties of Fourier coefficients in the Fourier representation of a non-Gaussian signal, noted previously by Seong (1993), are revisited in this section in order to provide a comprehensive foundation for the proposed model. A pressure time series measured on the edge pressure tap of a monoslope roof (roof angle $\approx 15°$) of a low-rise building for $0°$ azimuth (sample S1 in Fig. 4.3) is used as the target non-Gaussian signal for all demonstrations.

6.1.1 The Role of Phase Part

The effect of phase part on the non-Gaussian characteristics of a signal is demonstrated in this section. Figure 6.1 shows the phase part of the target signal (only half of the phase part is shown due to symmetry) as well as the independent uniform random numbers distributed on the interval $-\pi$ to π (random phase signal). It seems that both phase part of the
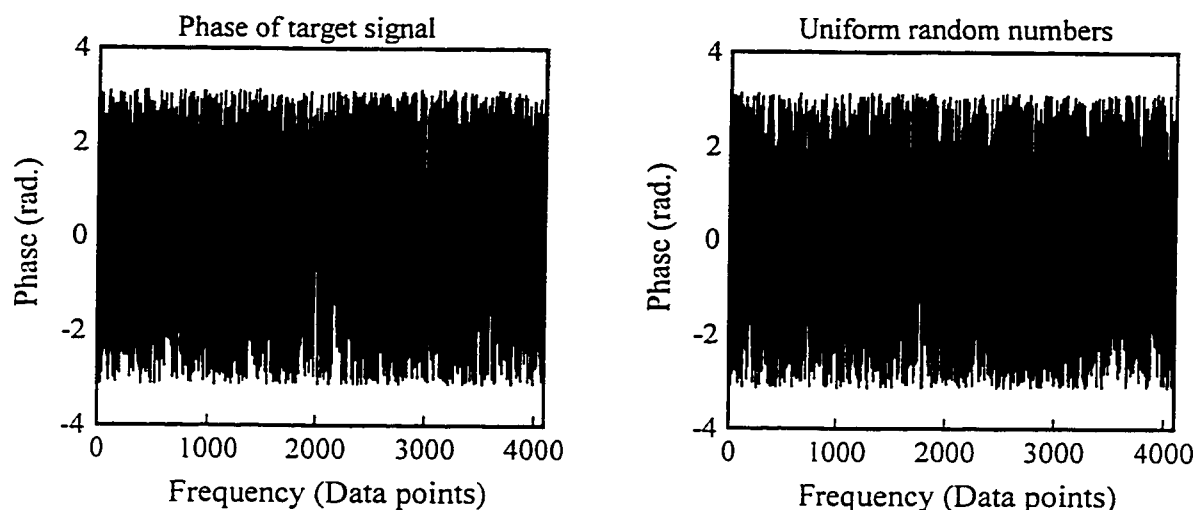
Fig. 6.1 Phase part of DFT of target pressure signal and uniformly distributed random numbers on the interval $-\pi$ to π.

target signal and random phase signal are identical. Figure 6.2 shows the autocorrelation functions of the phase part of the target signal as well as random phase signal. Though the autocorrelation amplitudes of the phase part of target signal are slightly higher than those of the random phase signal, both target phase signal and random phase signal are uniformly distributed and have almost the same statistics as shown in Table 6.1. Further, several measurements revealed that the phase part of non-Gaussian signals is uniformly distributed between $-\pi$ and π. Therefore, it was decided to use the random phase signal as a substitution for the phase part of the target signal in the Fourier representation of time series. Following
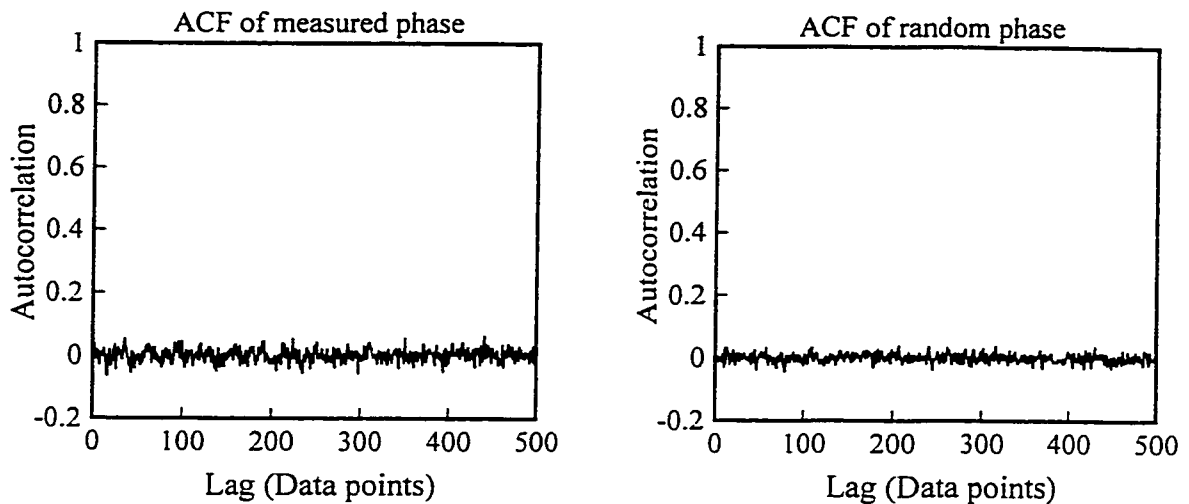
Fig. 6.2 Autocorrelation functions of the phase of DFT of the target signal and random phase signal.

Table 6.1 Comparison of statistics between (a) the phase part of DFT of the target signal and (b) the random phase signal.

	Mean	Variance	Skewness	Kurtosis
(a)	0.0004	3.3312	0.0000	1.7861
(b)	0.0003	3.2352	-0.0000	1.8231

the procedure provided in Fig. 5.1, the signal is reconstructed using the amplitude part of the target signal and the random phase shown in Fig. 6.1 (only half of the phase part is shown due to symmetry). The simulated signal presented in Fig. 6.3 shows a dramatic change in the characteristic spike features in comparison with the target signal, i.e. all the negatively skewed sharp spikes present in the target signal disappear and, as a result, the overall distribution becomes symmetric and close to Gaussian. However, it should be noted that the simulated signal shown in Fig. 6.3 has exactly the same spectral character, the same autocorrelation, and the same mean and variance by using the identical amplitude part. The difference in phase part resulted in significantly different features in the time history. This demonstration illustrates that the uniformly distributed phase process of a measured non-
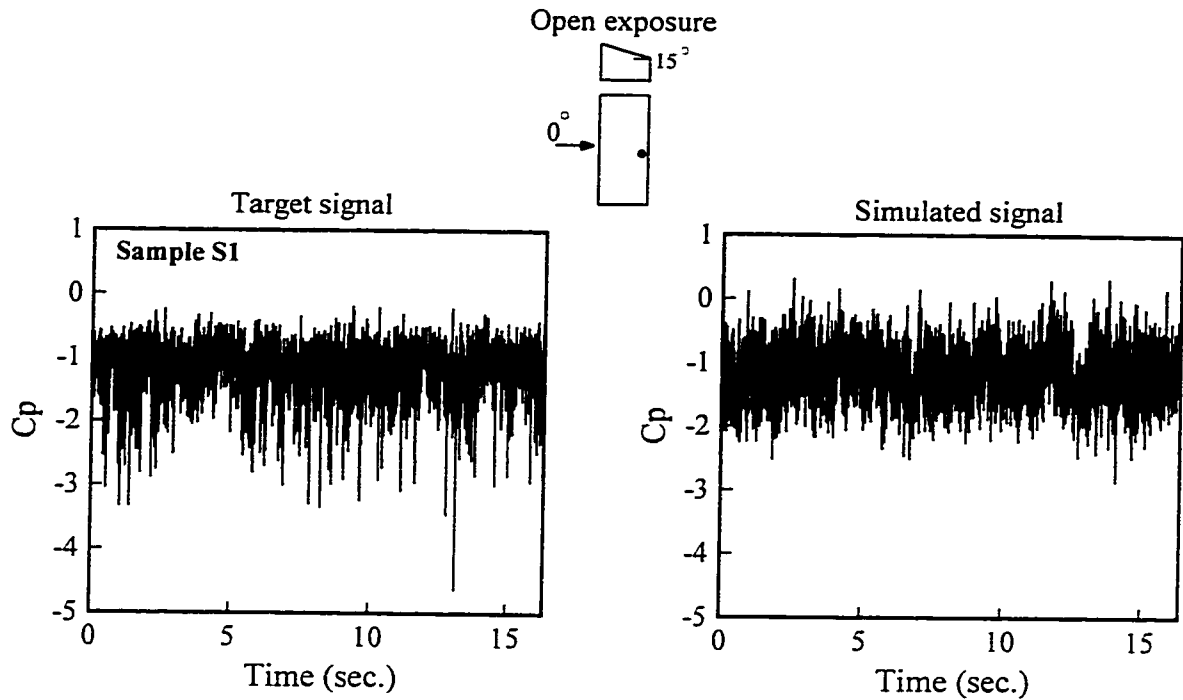
Fig. 6.3 Target and simulated signals.

Gaussian time history is somewhat correlated. The correlation of the phase part seems to be the major source of providing non-normality in time series.

In addition to this, Seong (1993) showed that the magnitude and pattern of spikes is not sensitive to the change of the spectrum shape in the low frequency range (below 10 Hz). Clearly, the phase part of the DFT in the Fourier representation plays a major role in forming the spike features in the time series rather than the amplitude part of the DFT.

6.1.2 Inducing Spike Characteristics

Based on the previous discussion, it has been decided to replace the phase part of the DFT in Fourier representation of the measured pressure signal by the phase part of the DFT of a single spike test signal and reconstruct the signal by inverse Fourier transform for further investigation. Here, the mean of the simulated signal is considered zero for convenience.

89

Figure 6.4 shows the single spike test signal and its phase part of DFT. The simulated signal in Fig. 6.4 is obtained by inverting the modified complex Fourier coefficients which consist of amplitude part of the DFT of the target signal (see Fig. 6.3 for the time series) and the phase part of the DFT of the test signal. The simulated signal displays the sharp single spike at the same location as the test signal but with different magnitude. As previously shown in section 3.2.1, the variance of a signal is only related to the Fourier amplitude part of the signal regardless of the phase part. Therefore, the simulated signal must have the same variance as that of the target signal since identical amplitude part of the DFT of the target signal has been used in the simulation. As a result, the magnitude of the spike is scaled to achieve the target variance. Thus the magnitude of spikes in the simulated signal is not affected by the magnitude of spikes in the test signal but it is dictated by the amplitude of DFT of the target signal. On the other hand, the location of spikes in the simulated signal is controlled by the phase part of the test signal. The autocorrelation of the phase part presented in Fig. 6.4 has a relatively organized pattern and very high amplitude. It appears that such highly correlated phase is required to provide a single spike in the simulated signal. Further, it can be conjectured that this spike is the result of the addition of many sinusoids arranged carefully using organized phase so that their crests coincided to form this sharp spike.

In another attempt, two more spikes are inserted into the previous test signal and the same procedure is repeated using the same target signal. The test signal, its phase, and the corresponding simulated signal are shown in Fig. 6.5. The simulated signal has its main spikes exactly at the same locations as those of the test signal along with some additional erratic spikes at other locations. However, further investigation revealed that the magnitude
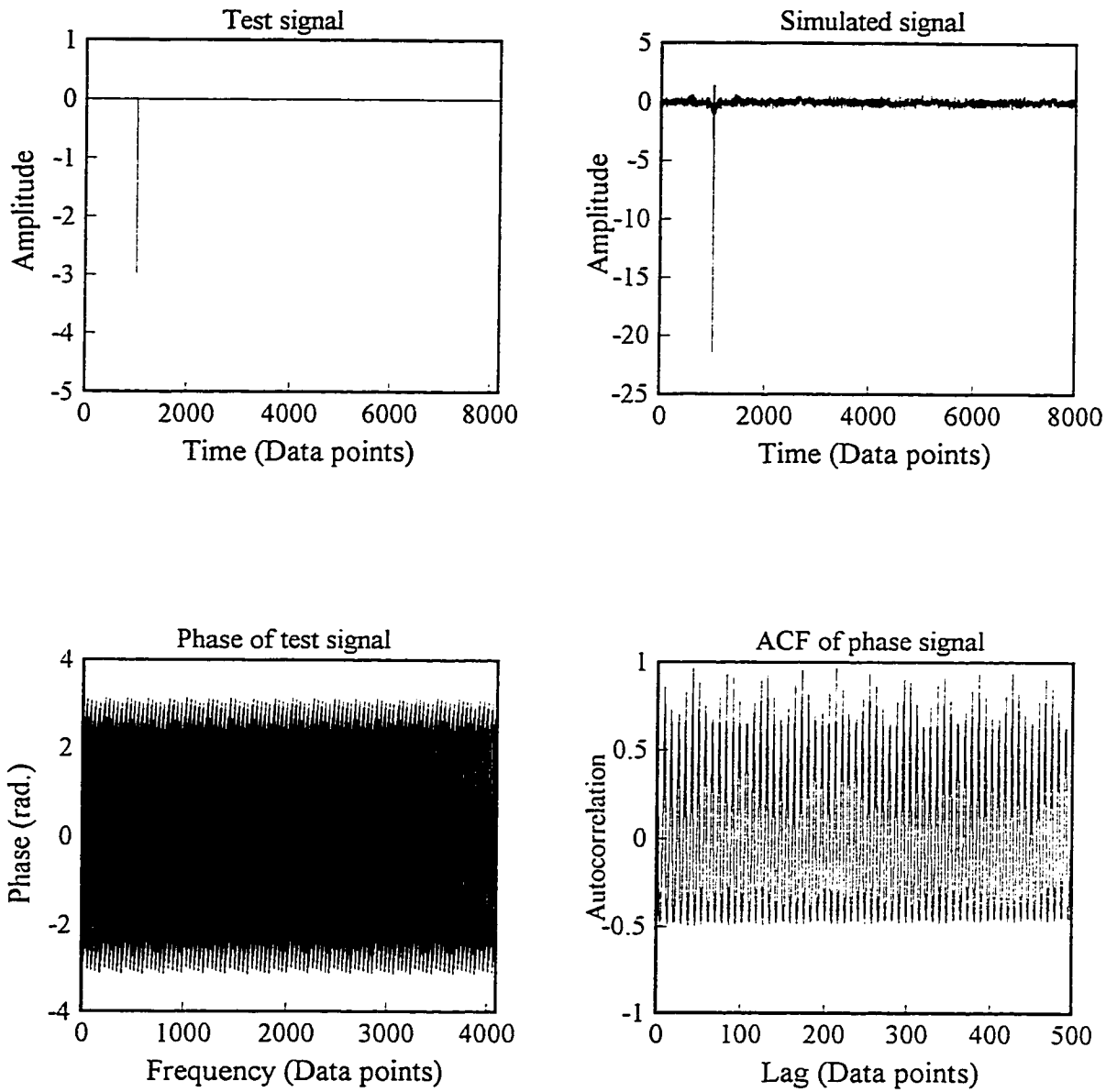
Fig. 6.4 Synthesis of a signal using the target amplitude and phase of DFT of a single spike test signal.
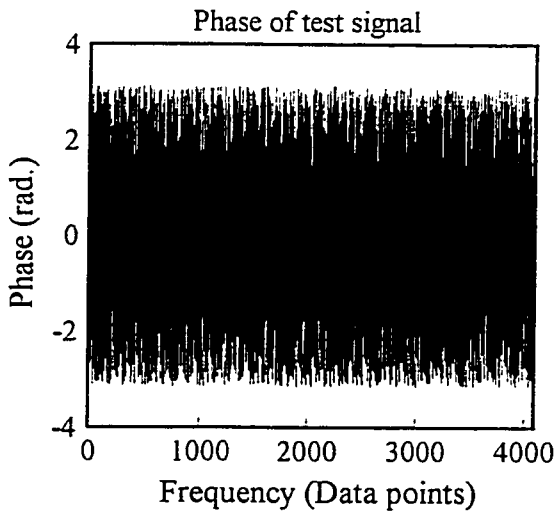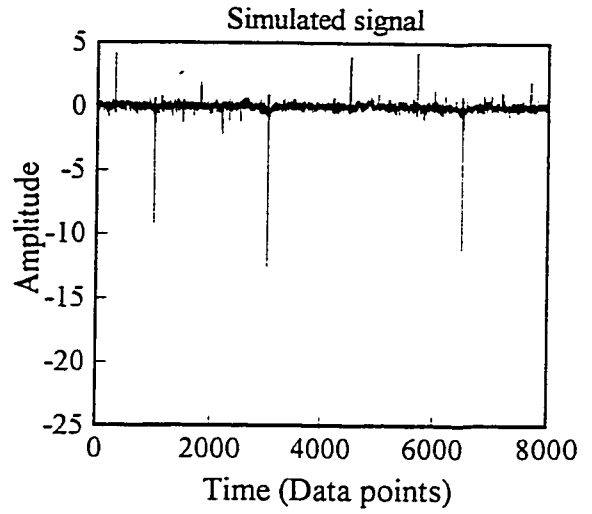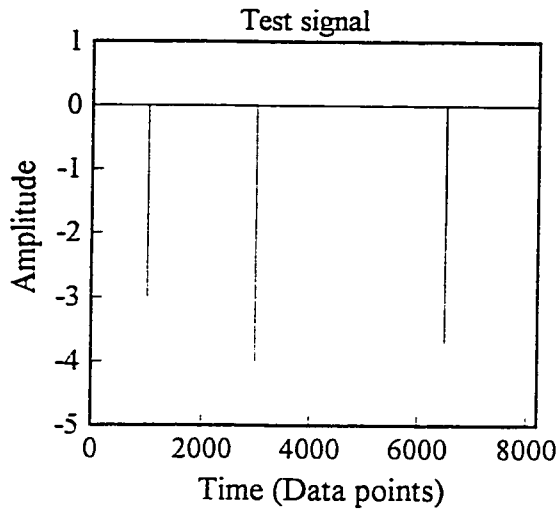
Fig. 6.5 Synthesis of a signal using the target amplitude and phase of DFT of a three spike test signal.

of such erratic spikes in a simulated signal reduces as the number of spikes increases in the test signal. The simulated signal appears to be formed primarily by superimposing small amplitude fluctuations whereas the large magnitude sharp spikes originate from the test signal and transferred through the phase part of DFT. Similar to the case shown in Fig. 6.4, the simulated signal has the same variance as that of the target signal. On the other hand, note that as the number of spikes in a test signal increases, the magnitude of spikes in the simulated signal decreases. In this particular case, the magnitude of spikes is automatically reduced since many spikes are present in the signal to achieve the target variance. This shows that the magnitude of spikes in simulated time series depends not only on the amplitude part of the DFT of the target signal but also on the number of spikes in test signal. Moreover, it is interesting to note the irregular pattern of the phase part compared to the phase of the single spike test signal. Clearly, as the number of spikes increases in a test signal, the regularity as well as the autocorrelation of phase decreases and correspondingly, the magnitude of the spikes in simulated signal decreases as well.

In summary, the phase part of DFT strongly controls the spike features in a signal. The spike features of the test signal can be transferred to the simulated signal through the phase part of its DFT with the help of target amplitude part. Thus, the overall pattern of spikes and their locations in the simulated signal can be controlled by parametrically controlling the spike features in test signal.

As mentioned in Chapter 4, the measured pressure fluctuations on low building roofs, in general, have several such simply dropping sharp spikes. The frequency as well as magnitude of these spikes seem to vary depending on the flow condition above roof. Therefore, there is a need to control the frequency as well as magnitude of spikes

parametrically while modelling these time histories. Within this context, the previously described role of phase in inducing spike features can be utilized to develop a suitable representation for phase. One such attempt by Seong and Peterka (1993) is described in the next section.

6.1.3 Seong and Peterka's (1993) Model for Phase

After an extensive investigation, Seong (1993) concluded that for modelling the phase of non-Gaussian signals, both the autocorrelation function as well as the spike character of the target signal must be reproduced. Based on this idea, a stochastic model (EARPG) along with a uniform phase shift parameter d was suggested for the generation of phase. The EARPG model takes the form,

$$Y_t = \begin{array}{ll} aY_{t-1} + 0 & , with\ probability\ b \\ aY_{t-1} + E_t & , with\ probability\ 1-b, \quad 0 \le b \le 1 \end{array} \qquad (6.1)$$

where, Y_t is known as preliminary signal, a is an autoregressive parameter which represents the correlation features of the target signal, b is a probability parameter which controls the magnitude as well as the frequency of spikes in a signal, and E_t represents exponential random variables. The noise term on the right side of the addition can be considered as intermittent or discontinuous exponential random variables whose properties are addressed in Appendix - B. The phase part,

$$\phi_k = \begin{array}{ll} \zeta_k + d & for \quad 1 \le k \le \dfrac{n}{2} \\ \zeta_k - d & for \quad \dfrac{n}{2}+1 \le k \le n-1 \\ \pi & for \quad k = 0 \end{array} \qquad (6.2)$$

94

is generated by applying a phase shift d on the phase part of the DFT of the preliminary signal (ζ_k) to provide a natural shape of spikes. For the simulation, the selection of parameters b and d is based on any one of the desired non-Gaussian characteristics (skewness, kurtosis, mode or dispersion); 3-dimensional figures showing a non-Gaussian property of simulated signal as a function of b and d are used for such selection.

A typical simulation example is provided in Fig. 6.6 using this model. The Fourier amplitude part of sample S1 (see Fig. 6.3) is used for this simulation. Figure 6.6 shows the test signal (preliminary signal) whose parameters are taken from Seong and Peterka (1993). The test signal is generated using Eq. (6.1). Using Eq. (6.2), the phase shift d is applied on the phase part of the DFT of Y_t to obtain a modified phase part. The simulated signal is obtained by inverting the complex Fourier coefficients consisting of the amplitude part of sample S1 and the modified phase part. The simulated signal has several spikes approximately at the same locations as those of the test signal but with different magnitude. Compared to the cases described in Figs. 6.4 and 6.5, the magnitude of spikes in the simulated signal is reduced dramatically; this clearly shows the dependence of the magnitude of spikes in a simulated signal on the frequency of spikes in a test signal. The autocorrelation of the phase part presented in Fig. 6.6 seems to have high correlation structure which violates the general requirement of a stationary process. Further, the potential simplification of this model, the adequacy of the model for other building zones and flow characteristics and the possibility of achieving more than one non-Gaussian properties have not been explored in Seong and Peterka's study (1993). The skewness and kurtosis values of the simulated signal provided in the same figure have been used for comparison in section 6.3.

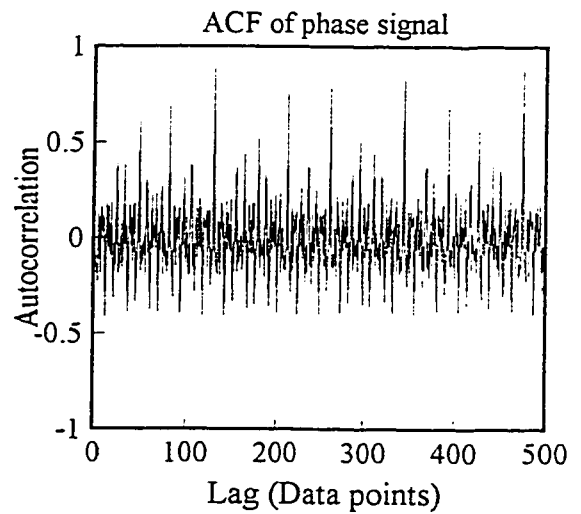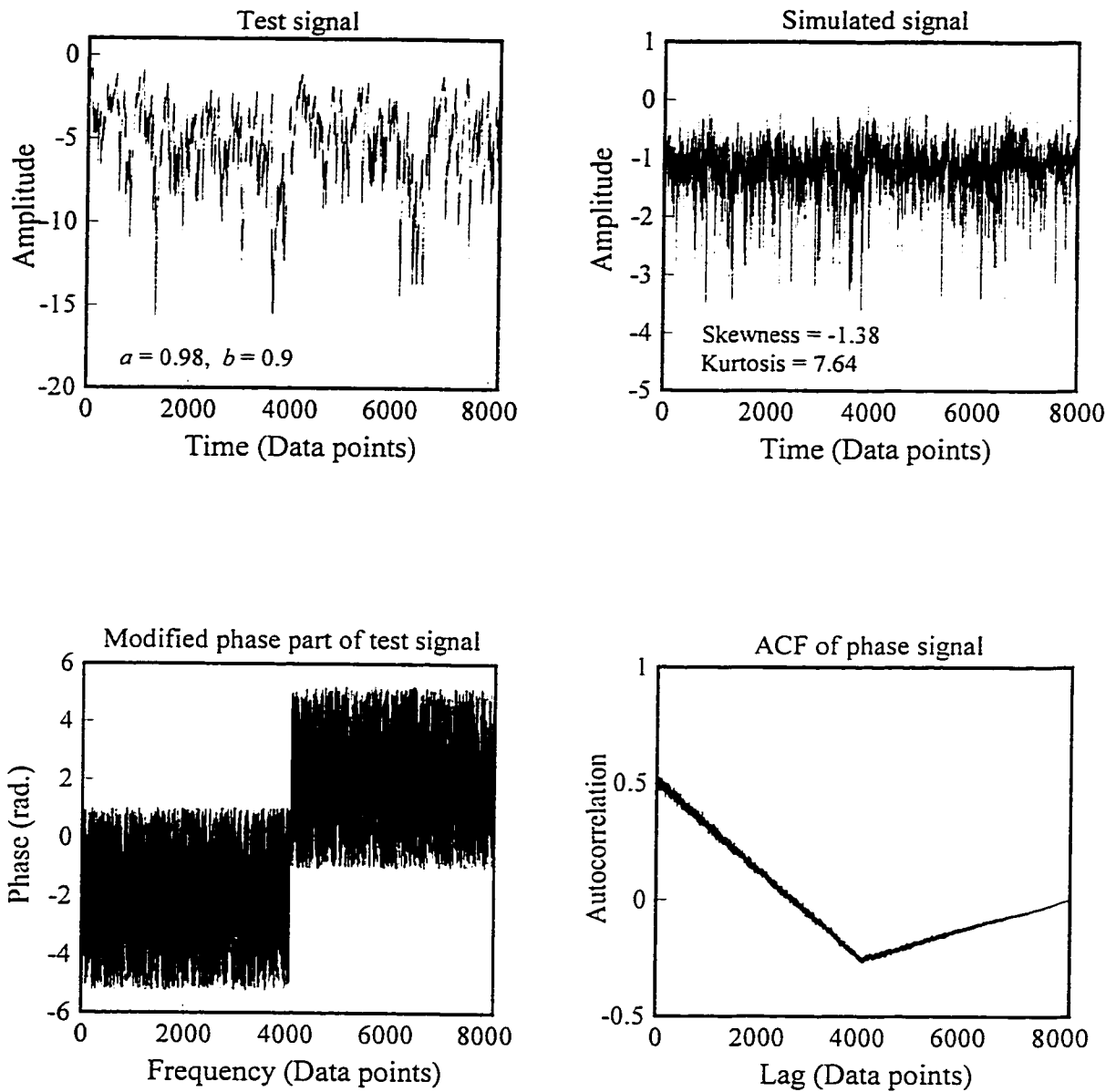**Fig. 6.6** Synthesis of a signal using the target amplitude of sample S1 and EARPG model with phase shift, $d = -2.09$ rad. (the model parameters are taken from Seong and Peterka (1993)).

6.2 SIMULATION METHODOLOGY

The present work focuses on the development of a novel simulation methodology based on FFT approach for the simple and efficient generation of univariate stationary non-Gaussian wind pressure fluctuations on various low building roofs. The proposed technique is aimed at achieving the second order characteristics (variance, ACF, SDF) through the amplitude part of the Fourier transform and the spike features by properly tailoring the phase part of the signal. These spike features which induce the non-Gaussian character to the distributional characteristics of the signal are the key issue in this current investigation.

Univariate non-Gaussian zero-mean wind pressure fluctuations can be generated by inverting the properly selected Fourier coefficients with the help of the FFT algorithm. The discrete Fourier transform (DFT) equation (Brockwell and Davis 1991) used for such simulation is described by:

$$Z_t \; = \; n^{-1} \sum_{k=0}^{n-1} \sqrt{I_k} \; e^{i\phi_k} \; e^{i2\pi kt/n}, \quad t = 0,1,\ldots,n-1. \tag{6.3}$$

where, Z_t corresponds to time series, n corresponds to time series length, $\sqrt{I_k}$ corresponds to amplitude, ϕ_k corresponds to phase and the term $2\pi k/n$ is the integer multiple of the fundamental frequency $2\pi/n$ known as Fourier frequency.

The above simulation procedure requires knowledge of amplitude ($\sqrt{I_k}$) and phase (ϕ_k) in order to simulate a signal (Z_t). The amplitude part of the signal can be easily generated from known spectra. Wind tunnel measurements show the possibility of modelling spectra of pressures acting on roofs of low buildings empirically and this will eventually simplify the whole simulation process (Suresh Kumar and Stathopoulos 1996a, 1997e). In this chapter, thrust is given in simulating the phase part assuming that the amplitude is known.

For all simulations, the amplitude ($\sqrt{I_k}$) is taken as the amplitude part of the DFT of target signal (X_t) which is in the form,

$$\sqrt{I_k} = |\sum_{t=0}^{n-1} X_t \; e^{-i2\pi kt/n}|$$

(6.4)

Since the target amplitude is used for the reconstruction of signal, the synthesized signal reproduces the various second order characteristics of the target signal. Here, the zero frequency component of the amplitude part representing the first order characteristics of fluctuations (mean) has been kept zero for convenience. The mean of the corresponding fluctuations can be added separately to the simulated zero-mean signal.

The phase part of the Gaussian time series, represented by independent uniformly distributed random numbers between $-\pi$ to π (Rice 1954), can be easily generated using commonly available algorithms. However, in the case of non-Gaussian time series, the phase part cannot be replaced by uniform random numbers, as previously discussed. In light of the unavailability of a simple and efficient model for the generation of phase, further work on this area is required. The model should induce various stationary non-Gaussian characteristics with minimum number of parameters along with an efficient parametric estimation technique. Moreover, the efficiency of this methodology should be demonstrated for various building zones and flow characteristics.

6.3 DEVELOPMENT OF THE MODEL FOR PHASE

During the development stage of an efficient model for phase, the phase shift parameter d of the EARPG model has been identified as the main source for the highly correlated phase.

On this basis, it was decided to remove the parameter d from the EARPG model and carry out the simulation. As a result, the phase part of the Y_t is used for the simulation, where Y_t is generated using Eq. (6.1). The same simulation procedures corresponding to Fig. 6.6 have been repeated excluding the phase shift operation and results are provided in Fig. 6.7. The Fourier amplitude part of sample S1 (see Fig. 6.3) is used for this simulation. It is interesting to note the stunning autocorrelation structure of the phase part where the autocorrelation amplitudes are extremely low compared to the case provided in Fig. 6.6. This shows that the parameter d is responsible for the peculiar shape of the autocorrelation structure of the phase part observed in Fig. 6.6. Further, it is interesting to note the reduction in the frequency as well as magnitude of spikes and the non-Gaussian properties (skewness and kurtosis) of the simulated signal in comparison with the case shown in Fig. 6.6. However, it may be possible to raise the magnitude of non-Gaussian properties by adjusting the number of spikes in a test signal through the parameter b.

Seong (1993) introduced parameter a in order for the simulated signal to have closely similar fluctuating features of the preliminary signal. However, further investigation revealed that the parameter a is not very important either in inducing non-Gaussian properties or in changing the properties of spikes. In fact, it was found in this study that approximately the same fluctuating features of the test signal can be transferred to the simulated signal even without using the parameter a in phase generation. Therefore, as a next step, the parameter a was assumed to be zero and b was the only parameter used in the simulation of phase part. A typical simulation is carried out under these conditions and the results are provided in Fig. 6.8. In this case, the same simulation procedures corresponding to Fig. 6.7 have been repeated with the Fourier amplitude of sample S1; the only difference

99
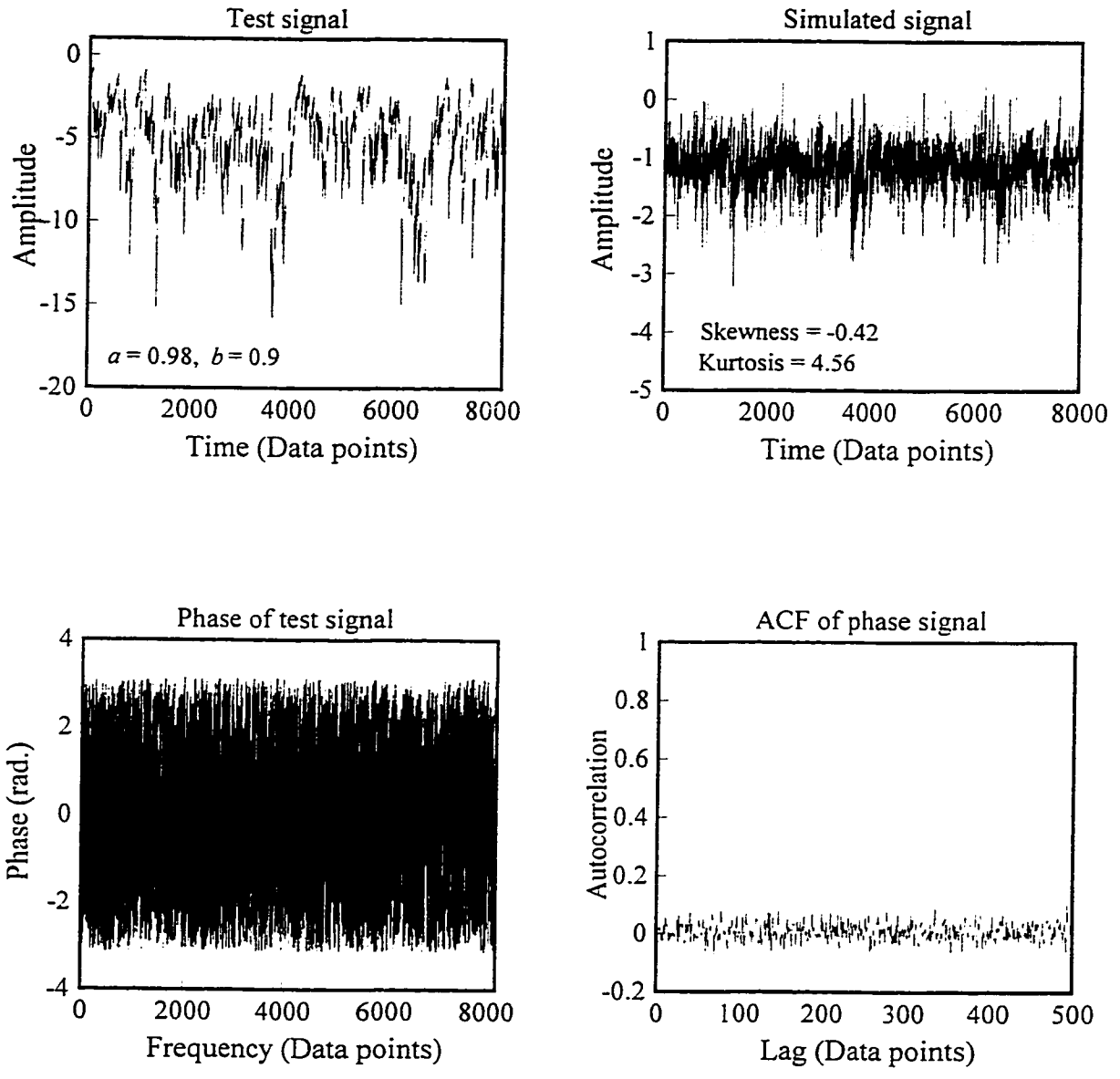
Fig. 6.7 Synthesis of a signal using the target amplitude of sample S1 and EARPG model without phase shift.
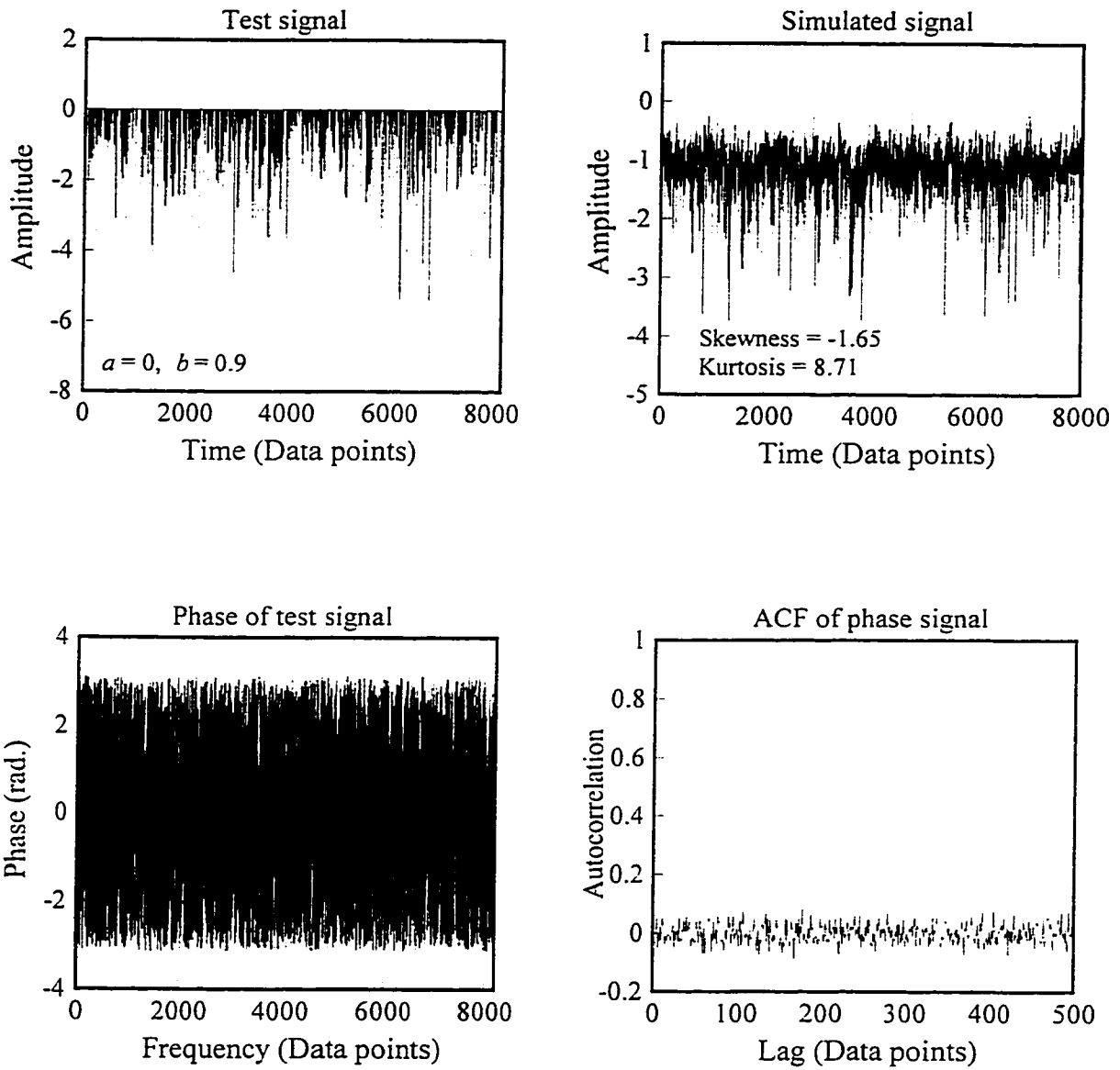
Fig. 6.8 Synthesis of a signal using the target amplitude of sample S1 and EARPG model with $a = 0$ and $d = 0$.

was in the generation of skeleton signal. The test signal in this case is indeed very different from those of the previous two cases shown in Figs. 6.6 and 6.7. The test signal of Fig. 6.8 seems to be chopped at zero; this is due to the absence of parameter a in its construction. This test signal depends on parameter b and exponential random numbers. In this study, exponential random numbers are constructed by logarithmic transformation of uniform random numbers ranging between 0 and 1, as will be described later in section 6.7. As a result, the upper limit of exponential random numbers is $\log(1) = 0$; this seems to be the chopped limit for the test signal shown in Fig. 6.8. Further, due to the autocorrelation property (or the parameter a) of the test signals in Figs. 6.6 and 6.7, the number of spikes is higher in both cases compared to the test signal shown in Fig. 6.8. Fortunately, there is no major change in the autocorrelation structure of the phase part compared to Fig. 6.7. Note also the similar spike characteristics of the test signal and simulated signal. Higher non-Gaussian properties (skewness and kurtosis) are induced in this case in comparison with the cases shown in Figs. 6.6 and 6.7. This is due to the increment in the magnitude of spikes in the simulated signal corresponding to the decrement in number of spikes in the test signal. These demonstrations show that the EARPG model is unnecessarily based on three parameters; only one is really important for simulating non-Gaussian properties.

6.3.1 Exploration of the EARPG Model when $a = 0$, and $d = 0$

Since the EARPG model with $a = 0$ and $d = 0$ appears to be promising in the representation of phase part of the non-Gaussian signals, some of its properties were further explored. Figure 6.9 shows the effect of parameter b on the frequency as well as magnitude of spikes
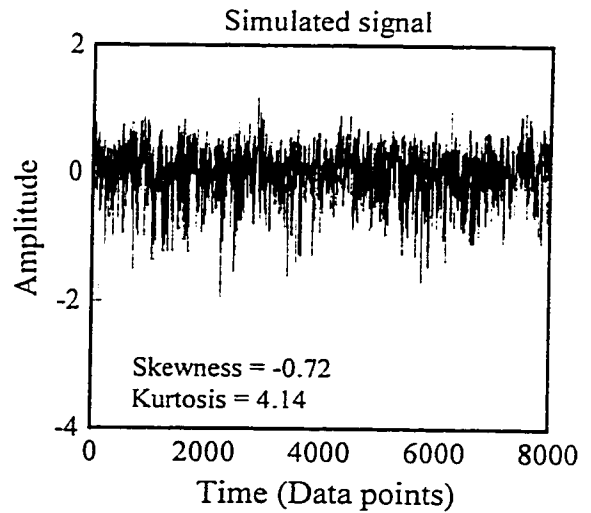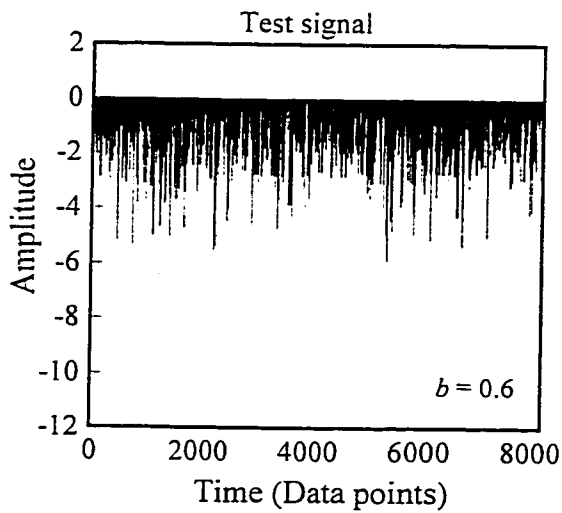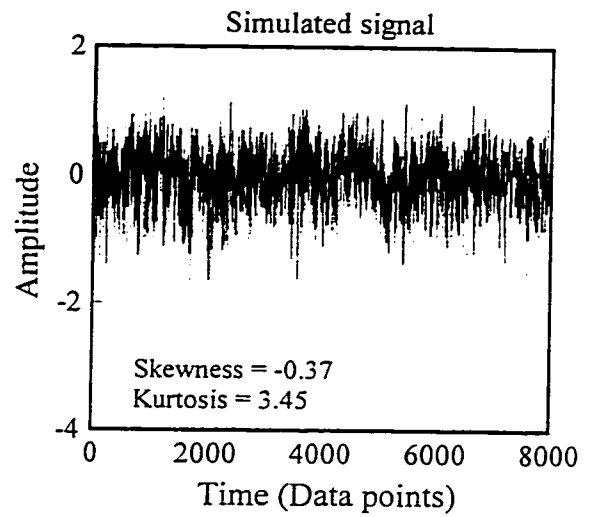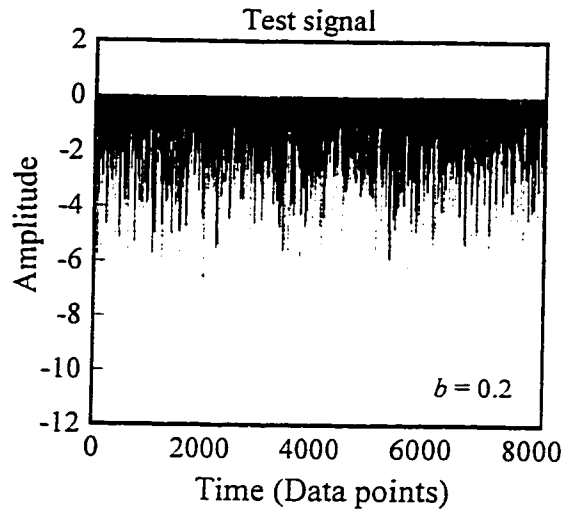
Fig. 6.9 The test signal of EARPG ($a = 0$, $d = 0$) for different values of b and the corresponding simulated signal using the target amplitude of sample S1 (without considering the mean) and phase of the test signal.

103

Fig. 6.9 Continued.

104
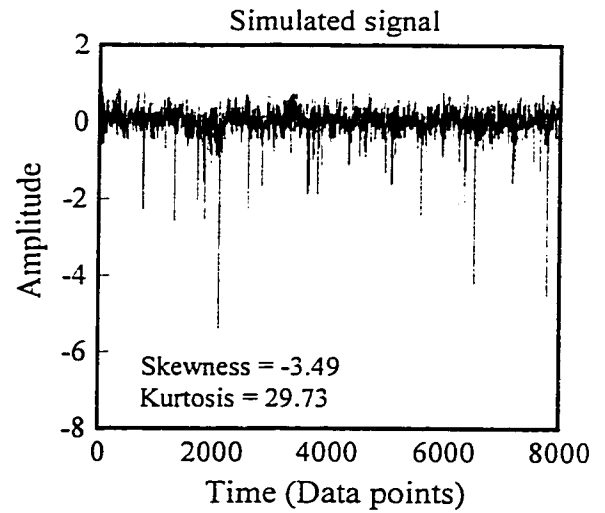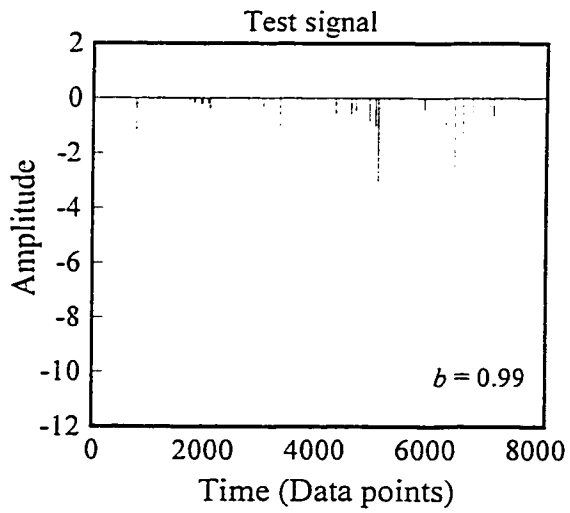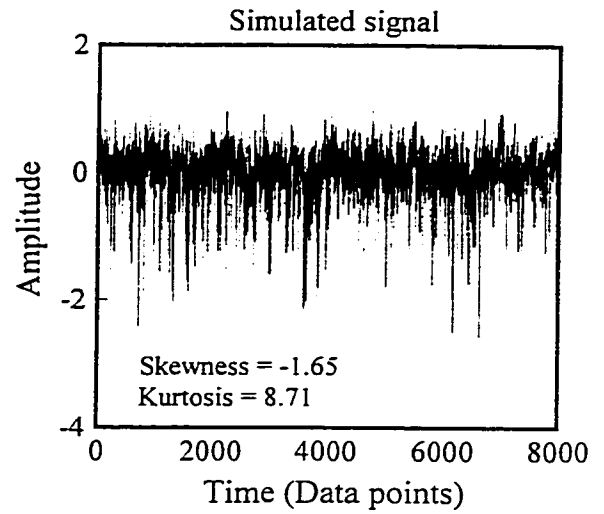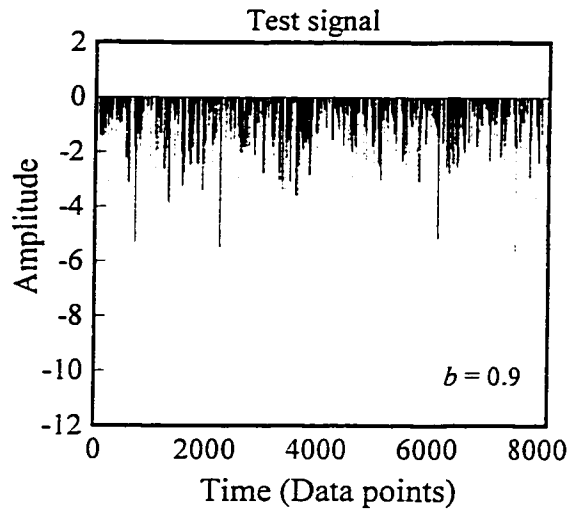
and correspondingly on the non-Gaussian properties of simulated signal. The figure clearly shows that as the parameter b increases, the frequency as well as magnitude of spikes in test signal decreases, as expected. The smaller the number of spikes in test signal, the higher the magnitude of spikes in simulated signal and correspondingly, the higher the magnitude of the non-Gaussian characteristics. Note the wide range of skewness and kurtosis values covered corresponding to the variation of b between 0.2 and 0.99. This shows that the model has great flexibility to control a wide range of non-Gaussian properties. The probability density function of the simulated signals is shown in Fig. 6.10 along with standard Gaussian PDF. The abscissa represents normalized amplitude (mean of the amplitudes is subtracted from the amplitude and then divided by the root-mean-square value of the amplitudes). Clearly, as b increases, the negative tail of the PDF of the simulated signal deviates more from that of the Gaussian PDF.
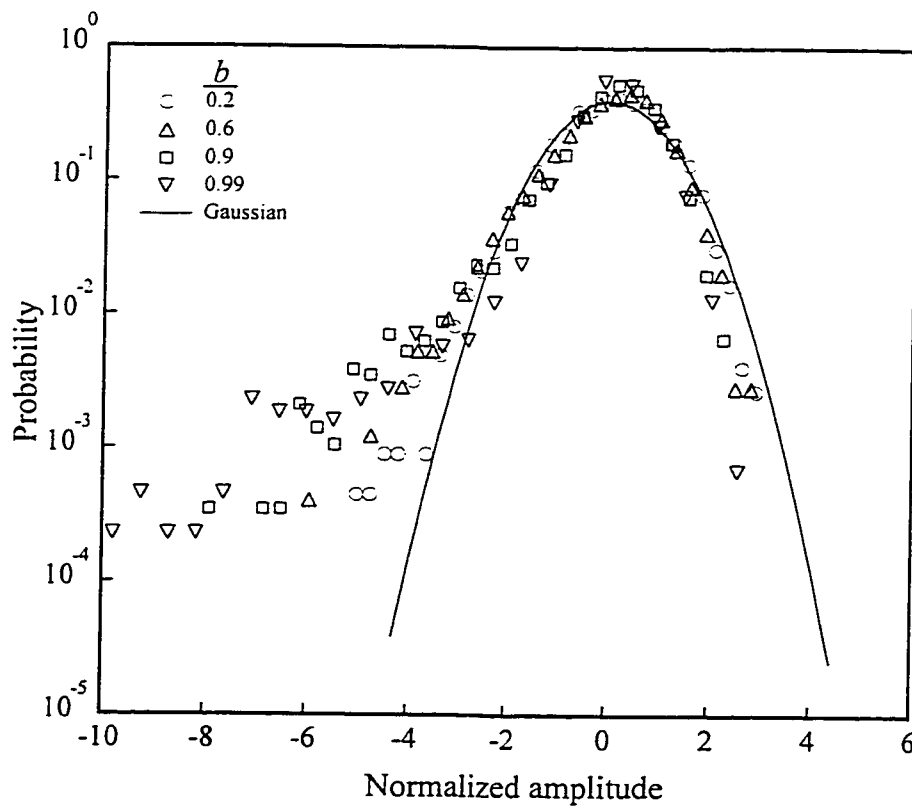
Fig. 6.10 Probability density functions of the simulated signals shown in Fig. 6.9.

Figure 6.11 shows the autocorrelation functions of the phase processes of the simulated signals shown in Fig. 6.9. It appears that as the parameter b increases the autocorrelation amplitudes of the phase process also increase. When $b = 0.99$, the autocorrelation amplitudes are quite predominant; however, the increment in autocorrelation amplitudes as b raises from 0.2 to 0.9 appears negligible. Though this model reduces the phase correlation substantially in comparison with the actual EARPG model described in section 6.1.3, the correlation observed when $b = 0.99$ is still not acceptable for the simulation of a stationary process. On the other hand, it appears that the skewness and kurtosis values of the simulated signal for $b = 0.99$ are really high compared to those of the highly non-Gaussian measured fluctuations, as mentioned in Chapter 4. These observations lead to further thoughts concerning the range of b by which the desired stationary non-Gaussian characteristics of the target signal can be achieved. This issue is addressed later in this chapter.

6.4 PROPOSED MODEL FOR PHASE

Based on the previous discussion, an extreme case of the EARPG model, by fixing $a = 0$ in Eq. (6.1) and removing parameter d, is proposed here to generate the phase. After the elimination of parameters d and a, the only condition remaining in the selection of the model for phase is the parametric control of the non-Gaussian statistics. Furthermore, this methodology takes advantage of the DFT property allowing to transfer the characteristics of spikes from an arbitrary signal to the simulated signal through its Fourier phase using a specified amplitude. Here, the arbitrary signal, named as skeleton signal, represents the distribution of spikes with arbitrary magnitudes. In other words, the skeleton of target signal only represents the distributional characteristics of spikes. It may be reasonable to assume

106
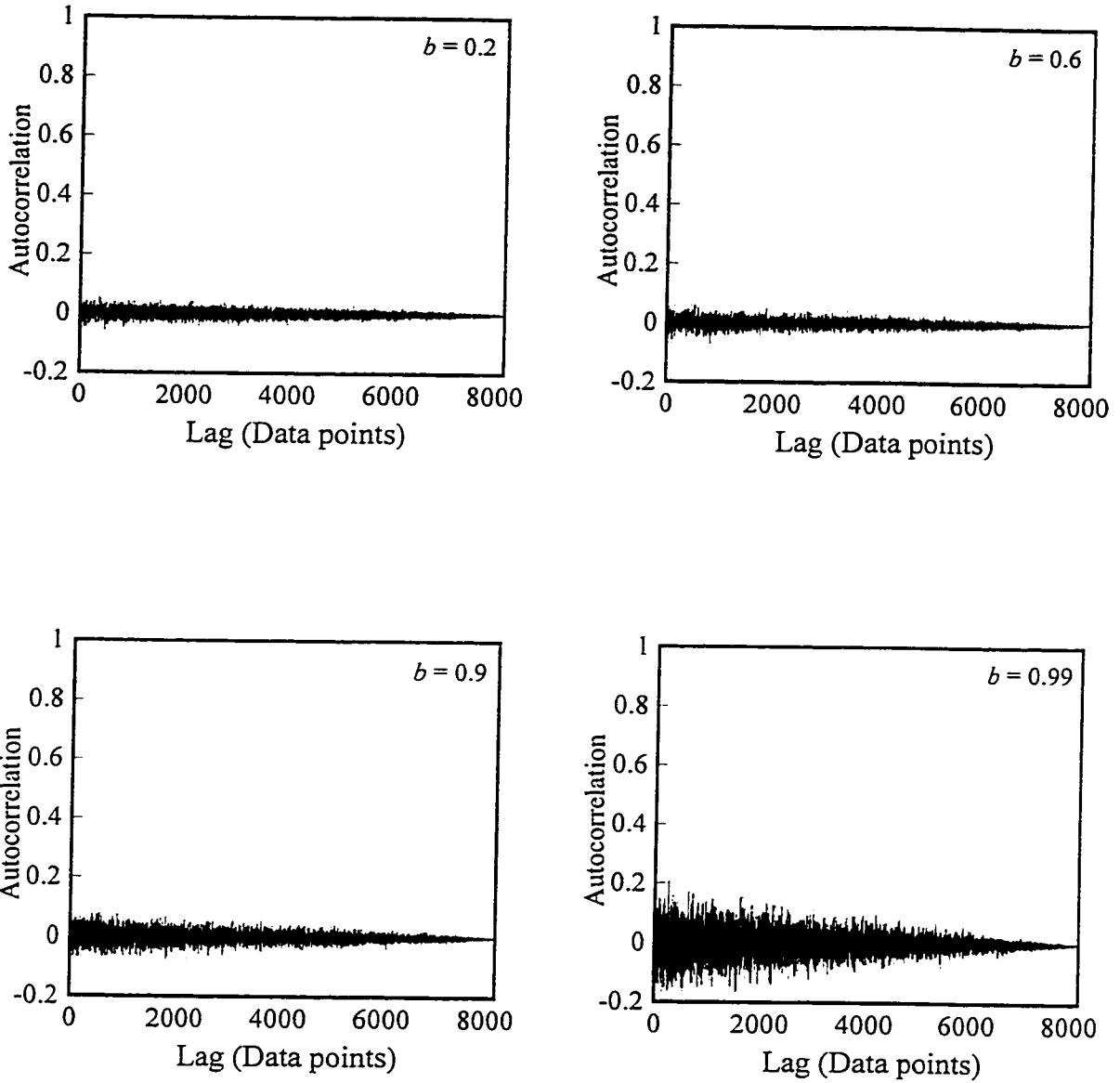
Fig. 6.11 Autocorrelation functions of the phase of the DFT of the test signals shown in Fig. 6.9.

that the PDF of the skeleton signal is exponential based on the fact that the spikes in wind pressure signals are invariably associated with exponentially decaying tails of its PDF. This is further supported by the observations made by Dalgliesh (1979), whereby an exponential distribution has been proposed to represent pressure spikes observed in cladding of tall buildings. On the other hand, note the discontinuous occurrence of spikes in pressure signals. This suggests that their intermittent occurrence can be better represented by using an intermittent exponential PDF for the generation of skeleton signal; however, other PDF's with exponentially decaying tails may also be appropriate.

6.4.1 Exponential Peak Generation (EPG) Model

The EPG model is proposed for the generation of skeleton signal from which the required phase can be drawn. The EPG model takes the form,

$$
Y_t = \begin{array}{l} 0 \quad, \textit{with probability } b \\ E_t \;, \textit{with probability } 1-b \qquad 0 \le b < 1 \end{array}
$$

(6.5)

where, Y_t corresponds to skeleton signal, b is the probability parameter which controls the magnitude as well as the frequency of spikes in the skeleton signal, and E_t is the exponential random variable. The skeleton signal Y_t represents intermittent exponential random variables (ε_i). This can be regarded as the multiplication of the $i.i.d$ sequence of exponential random variables, E_t and the $i.i.d.$ sequence I_t in which $P\{I_t = 1\} = 1 - P\{I_t = 0\} = (1-b)$ whose properties are discussed in Appendix - B. The Fourier phase (ϕ_k) required for the simulation in Eq. (6.3) can be obtained by taking the phase part of the DFT of skeleton signal (Y_t) by

$$\phi_k = \arctan \cfrac{-\sum\limits_{t=0}^{n-1} Y_t \ sin(2\pi kt \ / \ n)}{\sum\limits_{t=0}^{n-1} Y_t \ cos(2\pi kt \ / \ n)} \qquad (6.6)$$

where, the result of the mathematical operation *arctan* representing four-quadrant inverse tangent will lie in the interval -π to π which is the same for phase angles of a signal. This is in contrast with the result of simple inverse tangent which is limited to the interval -π/2 to π/2 (MATLAB 1992).

The magnitude of spikes in a simulated signal depends on the number of spikes produced in the skeleton signal and hence partly on the parameter b. When b is close to one, few spikes will be created in the skeleton signal and, consequently, few spikes at the corresponding locations will be induced in the simulated signal but in order to achieve the target variance, the magnitude of spikes will be high. Such high magnitude spikes will be reduced as b decreases and as a result skewness and kurtosis will also get reduced.

6.4.2 Estimation of Parameter b

In the parametric estimation stage, a signal with specified target amplitude is generated using Eq. (6.3) with the help of Eqs. (6.5) and (6.6) for each value of b selected from the defined range, 0 to 1. Thereafter, skewness and kurtosis of the simulated and target signals are compared before selecting the next value of b. This procedure will be continued until the optimum value of b is found. For convenience, a computer code is written to draw the optimum value of parameter b from the range, 0 to 1, to satisfy the desired non-Gaussian statistics in least square sense. The Sum of the Squared Errors (SSE) in skewness and kurtosis are calculated for each value of b and the value which gives the least SSE is chosen

as the optimum one. The advantage of this estimation procedure is its ability to achieve both desired non-Gaussian properties (skewness and kurtosis) in the best way possible from this modelling approach.

As a typical example to illustrate the parametric estimation scheme, an attempt has been made to obtain the optimum value of b for the pressure time series (sample S1) shown in Fig. 6.12. The MATLAB function **PAR_EST** reported in Appendix - A is used to estimate the parameter b. The value of b was found to be 0.87 which gives the least SSE based on target skewness and kurtosis of -1.38 and 6.90 respectively. The variation of SSE with respect to b is also shown in Fig. 6.12 where the SSE is normalized by sum of the squares of the target skewness and kurtosis. It is noted that the value of SSE increases steeply as b exceeds 0.90. Further, Fig. 6.12 shows the variation of skewness and kurtosis of a simulated signal using the target amplitude of sample S1 as a function of parameter b. The absolute values of skewness and kurtosis increase as b increases, in fact drastically for $b > 0.90$. This shows that when b approaches unity, the number of spikes in skeleton signal will be drastically reduced and thereby spikes in the simulated signal will be very high to attain the target variance. In low ranges of b, say $b < 0.5$, skewness as well as kurtosis appear to have very small variation. As expected, the optimum value of b induces skewness and kurtosis values close to the target values. Note also that this variation of skewness and kurtosis with respect to the parameter b depends, to some extent, on the Fourier amplitude. Therefore, the magnitude of variation of skewness and kurtosis may change in case of different signals.

During this investigation, a number of pressure time series have been measured on various locations of monoslope, flat and gable roofs of low rise buildings exposed to open and suburban terrain conditions. The measurements have been made for 7 different wind directions ($0°$, $30°$, $45°$, $60°$, $90°$, $120°$ and $180°$) in case of monoslope roof and for 5 different wind directions ($0°$, $30°$, $45°$, $60°$ and $90°$) in case of flat and gable roofs. The

Open exposure
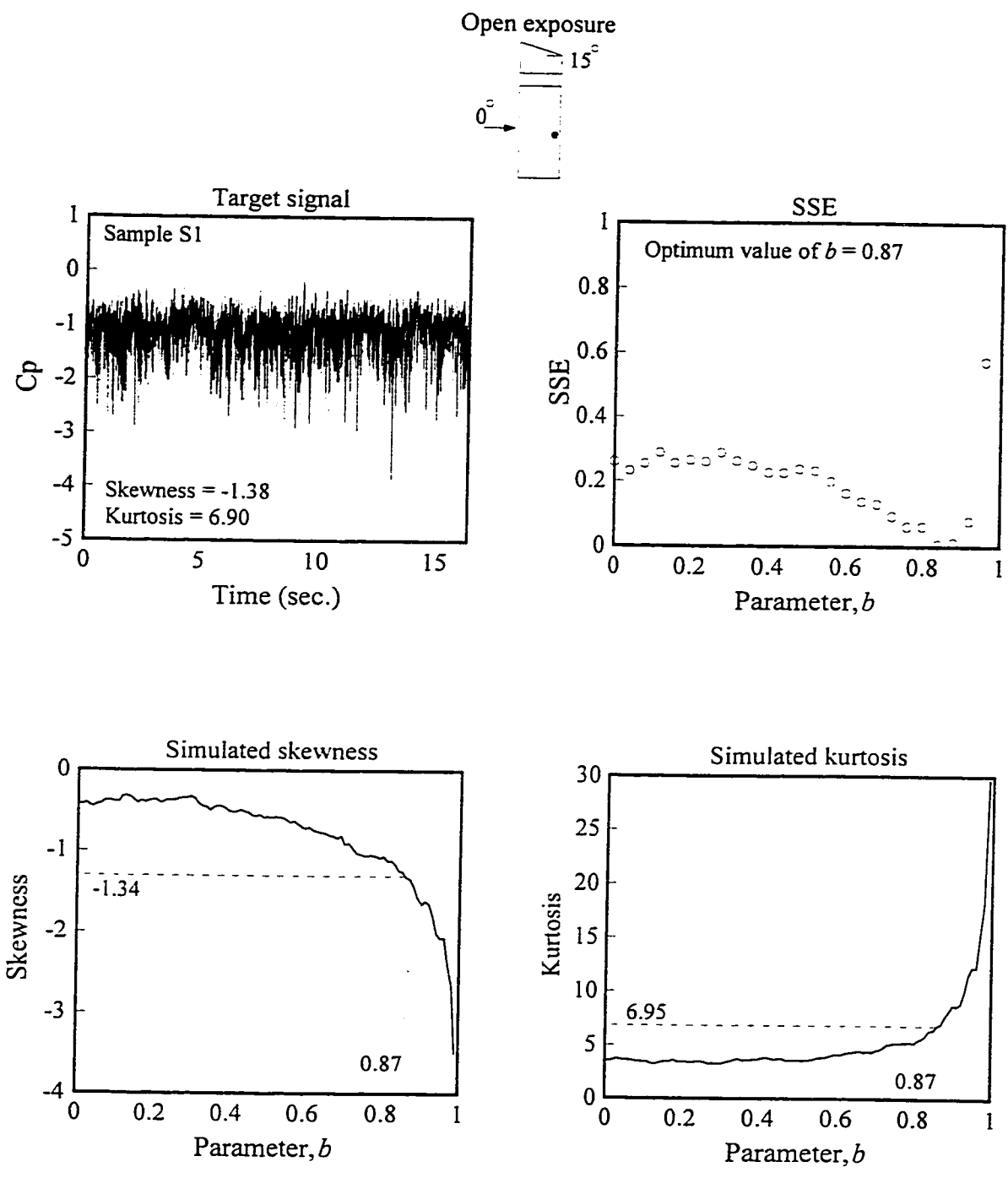
Fig. 6.12 Parametric estimation (sample S1).

111

measured time histories have subsequently been classified into Gaussian and non-Gaussian based on their skewness and kurtosis values. A particular time series is considered non-Gaussian if its absolute values of skewness and kurtosis are greater than 0.5 and 3.5 respectively. Figure 6.13 shows the skewness and kurtosis values of all the measured non-
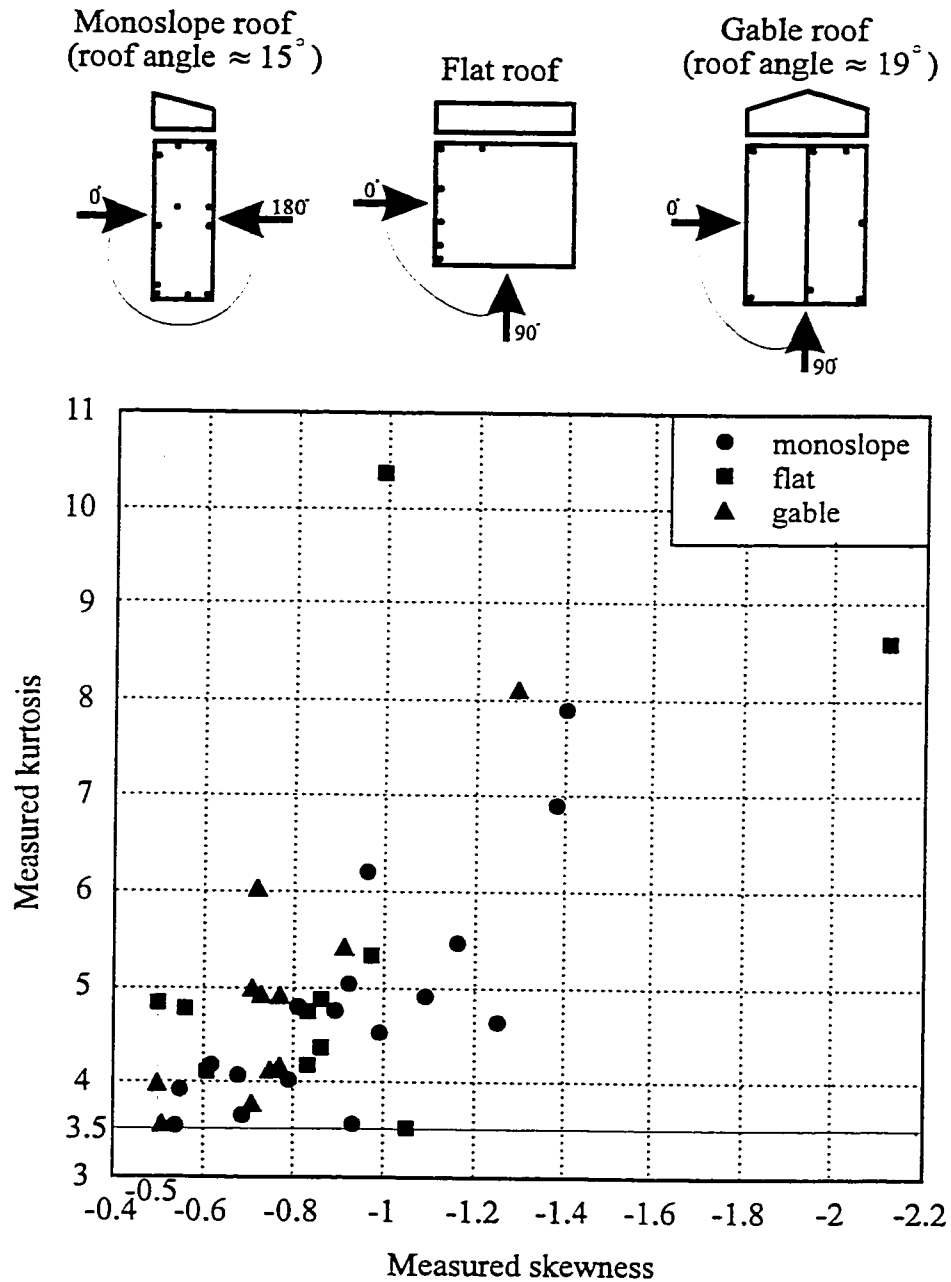
Fig. 6.13 Skewness and kurtosis values of measured non-Gaussian time histories.

Gaussian time histories. Note that the maximum skewness and kurtosis values of the many measured pressure fluctuations are -2.15 and 10.4 respectively. Note also that such high values of skewness and kurtosis rarely occur. Further, the parameter b has been estimated using the previously described procedure for the corresponding cases noted in Fig. 6.13. The estimated values of b are plotted against the corresponding simulated skewness values in Fig. 6.14. The value of b required to achieve the target skewness and kurtosis of a
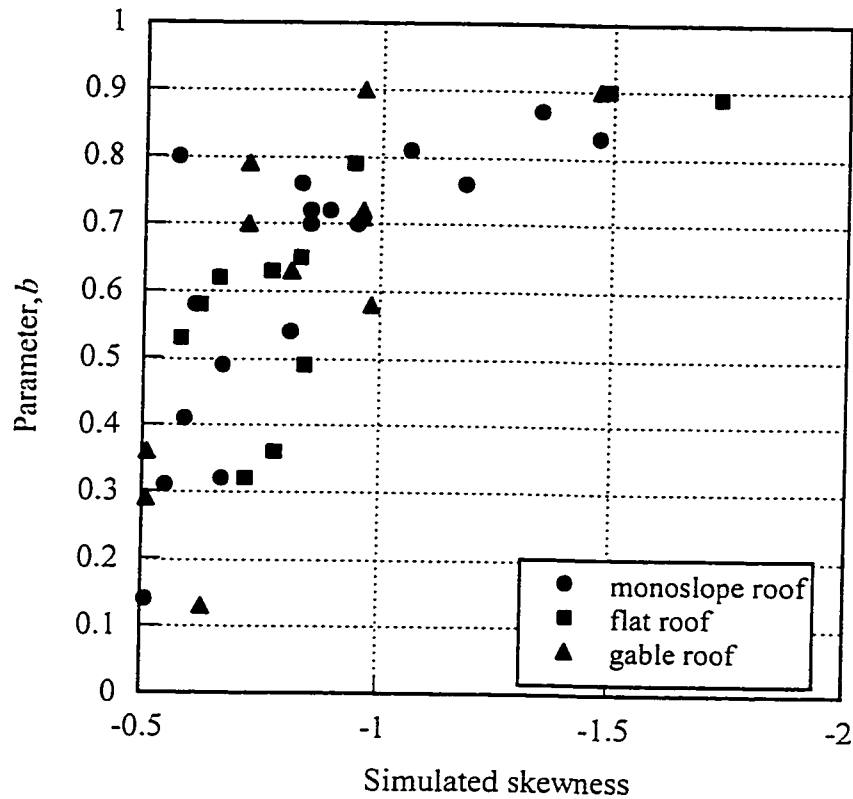
Fig. 6.14 The variation of parameter b for several different cases.

spectrum of non-Gaussian pressure fluctuations is found to be less than or equal to 0.9. Note also that the same value of b can provide different non-Gaussian characteristics (say, skewness) depending on the Fourier amplitude characteristics of the signal, as previously mentioned.

113

6.4.3 Simulation of Pressure Fluctuations

The previously established parameter b can be used to simulate time series samples having the same target stochastic properties. To demonstrate the overall simulation procedure, the equations provided in sections 6.2 and 6.4.1 have been organized in the form of a flow chart. Figure 6.15 shows a typical flow chart for the simulation of a non-Gaussian signal, where the Fourier amplitude is taken as the amplitude part of the DFT of target signal. Non-Gaussian signals can be generated by inverting the Fourier coefficients which consist of target amplitude and phase that are generated via the EPG model controlled by a single parameter b. In this process, exponential random numbers are generated followed by the generation of skeleton signal (b is known from parametric estimation) from which the Fourier phase can be extracted using Eq. (6.6). The MATLAB function **NGTIME** reported in Appendix - A is used to simulate non-Gaussian time series samples based on given time history. For illustrative purposes, the pressure time series shown in Fig. 6.12 has been reconstructed and the step by step procedures are pictorially shown in Fig. 6.16. The target signal is negatively skewed due to the presence of a large number of negatively going spikes, as expected from wind-induced pressures on the roof of any low-rise building. The estimated target amplitude using Eq. (6.4) is also shown in Fig. 6.16 where the value at zero frequency (first data point) is assumed to be zero, for convenience. The skeleton signal generated using Eq. (6.5) with $b = 0.87$ (known from parametric estimation) is also presented in the form of arbitrary amplitude versus number of data points; however, this represents the distributional characteristics of spikes. The estimated phase is derived from skeleton signal using Eq. (6.6). The simulated signal shown in Fig. 6.16 is generated using

114

Start

AMPLITUDE

Generate Fourier amplitude ($\sqrt{I_k}$)

$$\sqrt{I_k} = \left| \sum_{t=0}^{n-1} X_t \cdot e^{-i2\pi kt/n} \right|$$

PHASE

Generate exponential random numbers, E_t

Generate skeleton signal, Y_t
$Y_t = 0$, with probability b
E_t, with probability $1\text{-}b$

Generate phase signal (Φ_k)

$$\Phi_k = arctan \frac{-\sum_{t=0}^{n-1} Y_t \cdot sin\,(2\pi\,kt/n)}{\sum_{t=0}^{n-1} Y_t \cdot cos\,(2\pi\,kt/n)}$$

Simulate, Z_t

$$Z_t = n^{-1} \sum_{k=0}^{n-1} \sqrt{I_k} \cdot e^{i\Phi_k} \cdot e^{i2\pi\,kt/n}$$
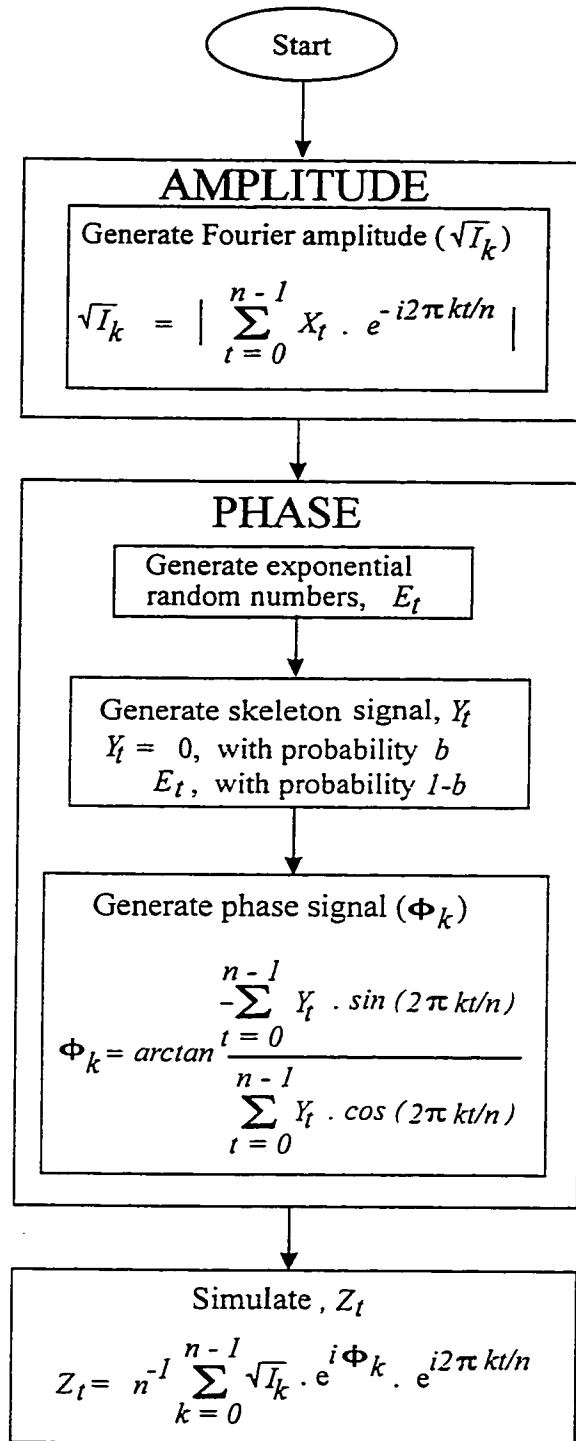
Fig. 6.15 Flow chart for synthesis of non-Gaussian wind pressure time series.

115
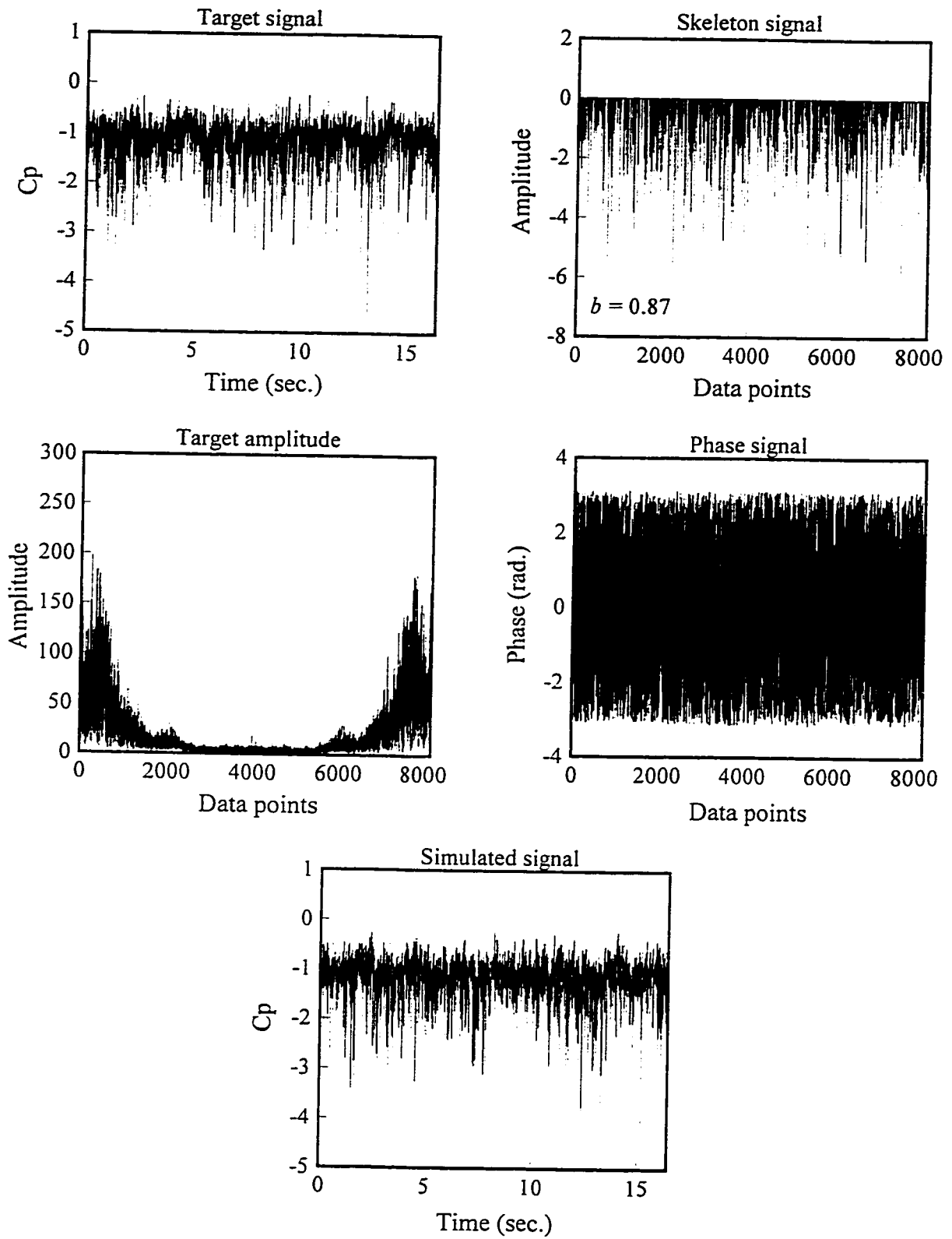
Fig. 6.16 Pictorial representation of the proposed simulation methodology.

Eq. (6.3) by means of target amplitude and phase signal, whereas the mean is added separately to the zero-mean fluctuations. Target and simulated signals appear similar; detailed simulation results and comparisons are provided later in this chapter.

6.4.4 Comparison between EPG and EARPG Models

This section is devoted to carry out a direct comparison between the performance of EPG and EARPG model in the simulation of pressure fluctuations on low building roofs. The target signal (sample S1) shown in Fig. 6.12 is again adopted for this demonstration and the procedure described in Fig. 6.15 is used for all simulations except in case of EARPG simulation where the skeleton signal is simulated using Eq. (6.1). In addition, a phase shift d is applied on the phase part of the DFT of the skeleton signal using Eq. (6.2). The parameter found in Fig. 6.12 is used for EPG simulation whereas the parameters required for EARPG simulation are estimated as follows (Seong 1993): (1) the parameter a is determined considering the autocorrelation of the target signal, (2) after deciding the major target non-Gaussian property as skewness, the parameters b and d are selected by investigating the 3-dimensional variation of skewness versus parameters b and d. Figure 6.17 shows skeleton signals simulated using EARPG and EPG models. Thereafter, these skeleton signals have been used with the target amplitude of sample S1 to generate corresponding simulated signals which are also presented in Fig. 6.17.

A significant difference in skeleton signals generated by EARPG and EPG models has been observed. Note that more intermittent spikes appear in skeleton signal simulated using EARPG model, irrespective of the value of b, due to its autocorrelation property. Here, the

117
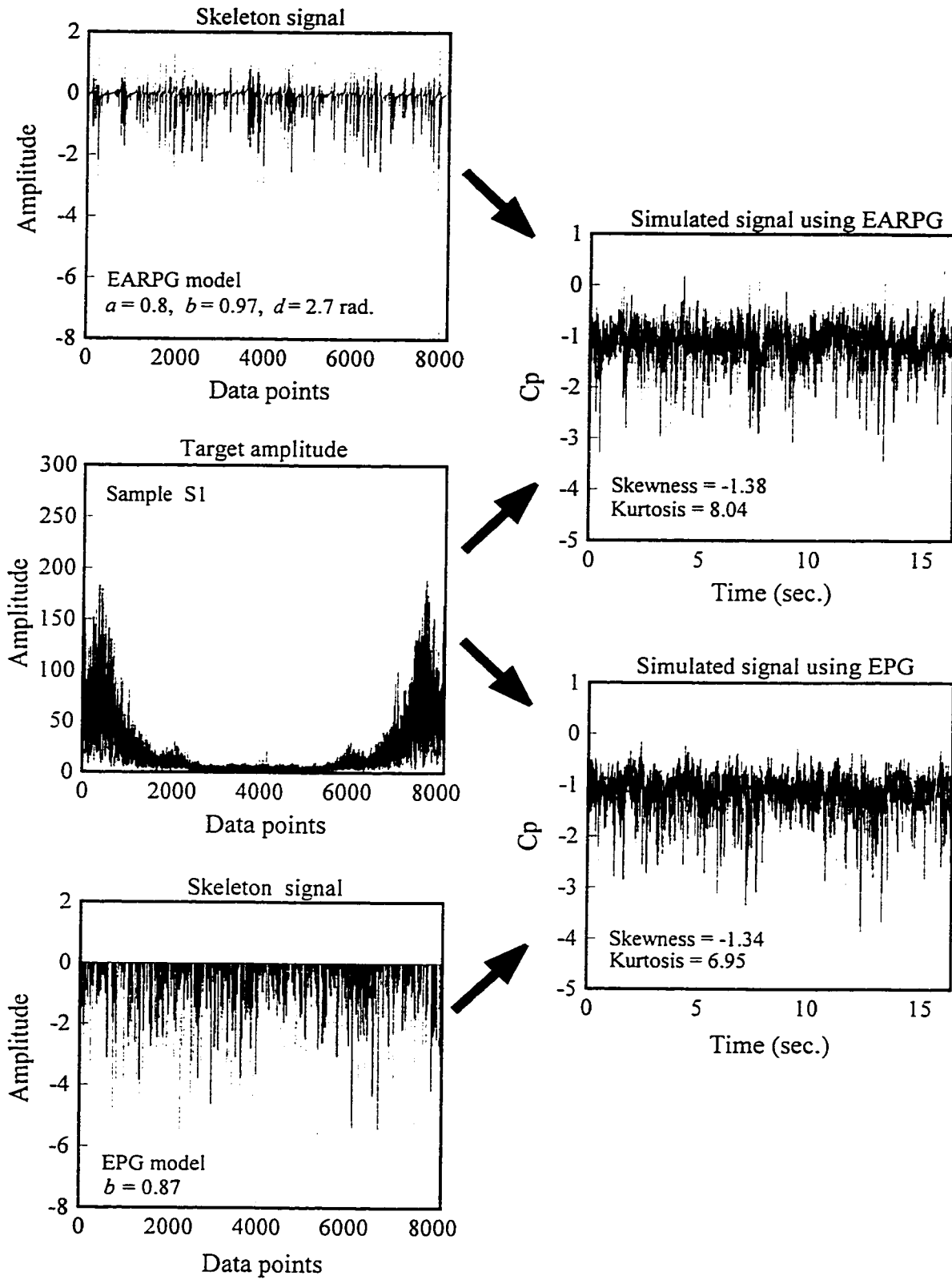
Fig. 6.17 Simulations using EPG and EARPG models (sample S1).

118

parameters b and d are selected with a view to achieve target skewness only. Though the target skewness is achieved, the kurtosis value is away from the target value. Such discrepancies of the EARPG model have also been observed in the example provided by Seong and Peterka (1993) which is summarized in Table 6.2. The target signal corresponds to Tap.50501 on TTU model building for $240°$ azimuth, while the simulated signal is based on the Fourier amplitude of the target signal and the phase generated using EARPG model with parameters $a = 0.98$, $b = 0.9$ and $d = -2.09$ rad. In this particular case, the parameters b and d were determined based on the 3-dimensional variation of a target non-Gaussian property, mode of the extremes. As a result, mode was achieved; however, the fundamental characteristics of a non-Gaussian signal such as skewness and kurtosis were not achieved. Clearly, the inefficiency of the EARPG model in achieving more than one desired non-Gaussian properties is noted. On the other hand, Fig. 6.17 shows that the simulated signal using EPG model efficiently represents the spike features as well as the non-Gaussian characteristics (skewness and kurtosis) of the target signal S1. The simple EPG model with the parametric estimation scheme introduced in this chapter overcomes the various limitations of the EARPG model. Table 6.3 briefly summarizes the advantages of EPG model over EARPG model. Overall, these considerations reinforce the applicability of EPG model as a replacement of the EARPG model.

Table 6.2 Comparison of target and simulated statistics (Seong and Peterka 1993).

	Target	Simulated
Mean	-0.80	-0.81
RMS	0.43	0.42
Skewness	-1.19	-0.63
Kurtosis	4.95	3.93
Mode	-2.88	-2.89
Dispersion	0.30	0.27

Table 6.3 Comparison between EARPG and EPG models.

Description	EARPG model	EPG Model
(1) Number of parameters involved	three	one
(2) Parametric estimation	Not efficient; uses cumbersome 3-dimensional figures	Efficient; uses computational algorithm
(3) Accuracy	Achieves only one of the non-Gaussian characteristics (mode, dispersion, skewness, kurtosis)	Achieves two non-Gaussian characteristics (skewness and kurtosis)
(4) Stationarity of the simulated time series	The phase part is highly correlated and therefore this property is questionable	Good; see details in section 6.5
(5) Adequacy of the model in all roof zones	Not known	Good; verified for many different cases.

6.5 STATIONARITY OF THE SIMULATED TIME SERIES

As previously noted in Chapter 5, the phase processes of the DFT of measured pressure signals are somewhat correlated. During this investigation, several non-Gaussian time series have been measured on many low building roofs at different conditions as previously mentioned and in all cases, the phase processes are somewhat correlated. A typical example provided in Fig. 6.18 shows the autocorrelation of the phase process of the measured sample S1 excluding zeroth lag. Correlation values are below the 10% level for both measured and simulated processes. Figure 6.19 shows the histogram of the absolute maximum phase correlation values (excluding zeroth lag) of all the measured non-Gaussian

120
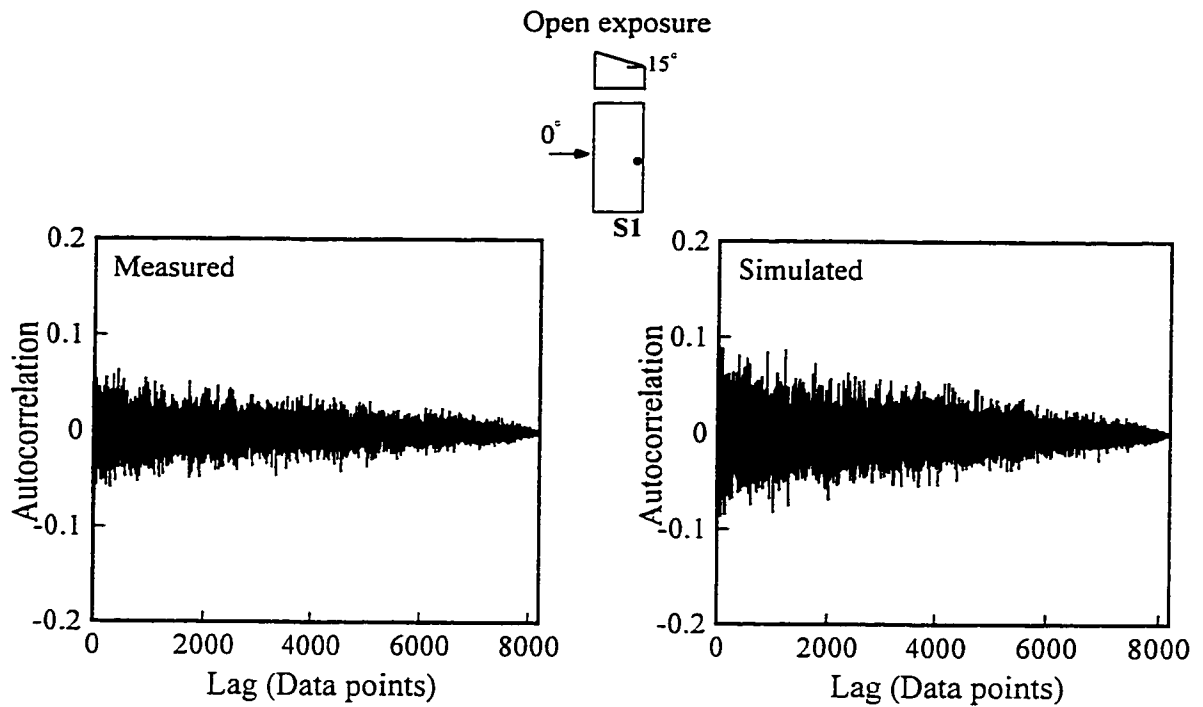
Fig. 6.18   Autocorrelation function of the phase process of the measured and simulated signals.
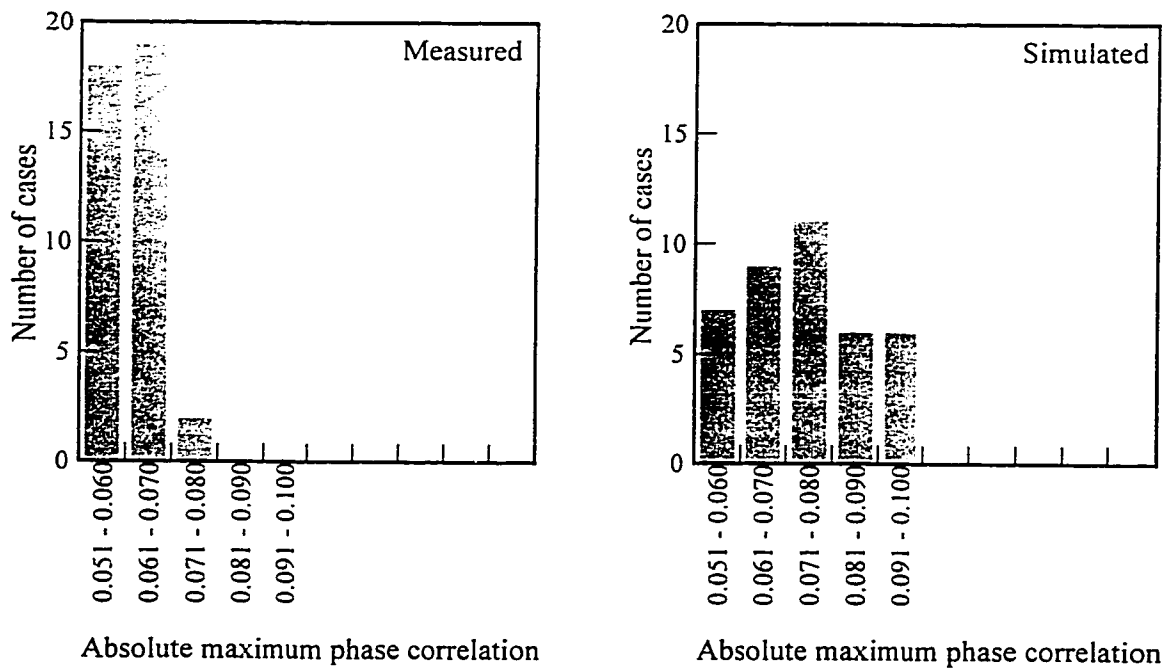
Fig. 6.19   Absolute maximum phase correlation values of measured and simulated time histories.

121

signals, where the estimated phase correlation values are arranged in bins with their corresponding frequencies of occurrence. Note that the absolute maximum phase correlation values of measured time series range between 0.05 and 0.08.

During the simulation of non-Gaussian time series, the non-Gaussian properties were induced through the Fourier phase part generated using Eqs. (6.5) and (6.6). It was found that the produced phase process is uniformly distributed but somewhat correlated. The correlation of the phase part seems to be the source of providing non-normality in time series. However, the use of correlated phase for the simulation is against the general requirement of a stationary process. Note, however, that though the phase process (Eq. (6.6)) is correlated, the magnitude of correlation really depends on the value of parameter b, as shown clearly in Fig. 6.20. The ordinate refers to the absolute maximum phase correlation (excluding zeroth lag) corresponding to various values of b. As the parameter b
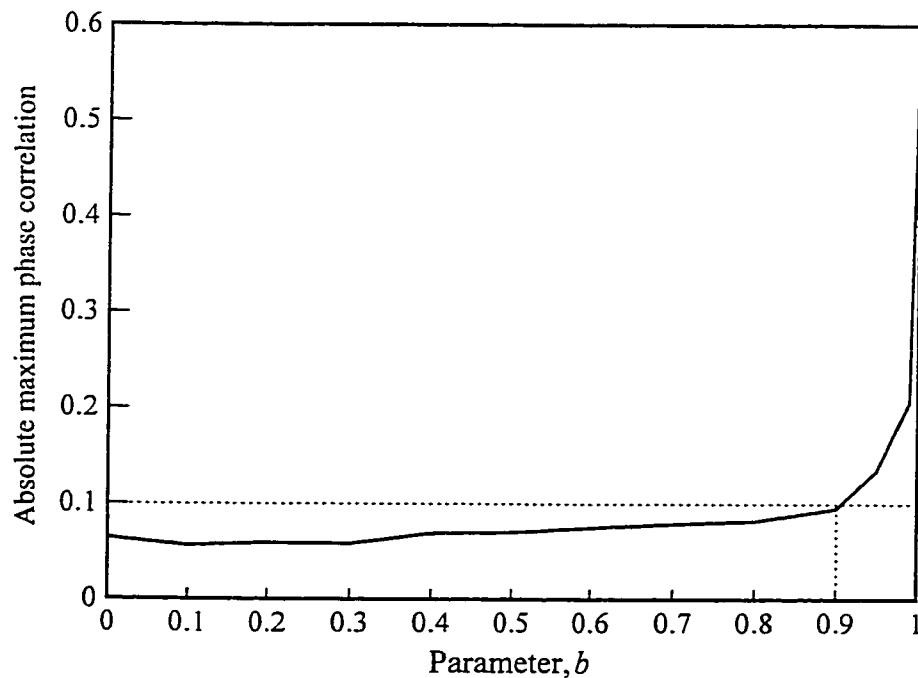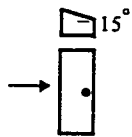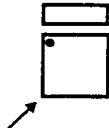
Fig. 6.20 Variation of absolute maximum phase correlation values (excluding zeroth lag) with respect to parameter b.

increases, phase correlation value also increases but only marginally as b rises from 0 to 0.9. When $b > 0.9$, phase correlation increases exponentially and this would be problematic for the simulation of a stationary process. Note however that the very high skewness and kurtosis values induced for high values of b seemed to be unrealistic based on many wind tunnel measurements of pressure time series on low building roofs. In fact, Figs. 6.13 and 6.14 show that values of $b > 0.9$ are not obtained even when modelling highly non-Gaussian pressure fluctuations. This in association with the low phase correlation values observed when $b \leq 0.9$ is encouraging. The histogram of the absolute maximum phase correlation of the simulated time histories corresponding to the measured cases shows that the phase correlation values of the former range between 0.05 and 0.10 compared to those of the latter ranging between 0.05 and 0.08, as previously mentioned - see Fig. 6.19. Finally, the invariant nature of the autocorrelation functions of the simulated signals with respect to uniform shift in time has been verified in several cases. This further reinforces the reasonable accuracy concerning the stationarity of the time series simulated using this methodology.

6.6 EXAMPLE SIMULATIONS

For demonstration purposes, two distinct non-Gaussian time series have been selected and listed in Table 6.4. Figure 6.21 displays normal probability plot of the samples. The deviation of the data away from straight line (samples follow straight lines if they are normally distributed) towards negative tail end displays how far the data is away from normal distribution. Both selected time histories are reconstructed using the amplitude part

123

Table 6.4 Sample non-Gaussian pressure time series.

Sample	Roof type	Wind direction	Terrain condition	Orientation of model
S1	monoslope	0°	open	
S28	flat	45°	suburban	
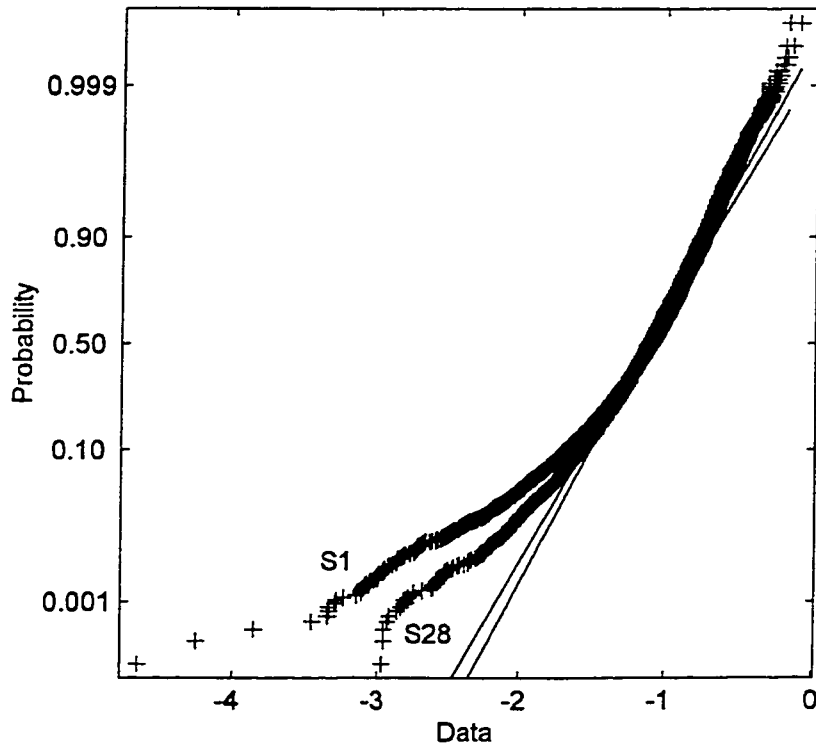
Fig. 6.21 Normal probability plot of the selected samples.

of the DFT of their target counterpart and phase generated using the EPG model. The parameter of the EPG model has been estimated based on target skewness and kurtosis as previously discussed. Here, the comparison has been made between simulated and target characteristics.

124

The statistics of target and simulated data are compared in Table 6.5. The first and second moments (mean and variance respectively) of the simulated signals coincide with those of the corresponding target signals, as is always the case. One common feature of target signals is that they are negatively skewed but with varying intensity. In general, the skewness and kurtosis values of the simulated signals are close to their corresponding target values. This

Table 6.5 Comparison between target and simulated statistics.

	b	Mean	Variance	Skewness	Kurtosis
Sample S1					
Target		-1.16	0.16	-1.38	6.90
Simulated	0.87	-1.16	0.16	-1.34	6.95
Sample S28					
Target		-1.14	0.11	-0.83	4.74
Simulated	0.49	-1.14	0.11	-0.84	4.76

shows that by properly choosing the value of parameter b (shown in Table 6.5) for each case, the desired skewness and kurtosis can be achieved. The same trend is also observed in other cases. Further, the decrement in b is noted corresponding to the decrement in skewness and kurtosis. Both target and simulated signals as well as their PDF's and extreme values (Gumbel's plot) for each sample, are shown in Figs. 6.22 and 6.23. The simulated and target signals are presented in the form of pressure coefficient (Cp) versus time. In case of PDF plots, the abscissa represents normalized pressure coefficient in the form of (Cp-Cp_{mean})/Cp_{rms} (Cp_{mean} corresponds to mean pressure coefficient, and Cp_{rms} corresponds to root-mean-square pressure coefficient). Further, Gumbel's plots represent extreme Cp values as a function of reduced y-variate (see section 3.2.3.1), where the extreme Cp values are obtained as follows: the 8192 simulated as well as measured data are divided into
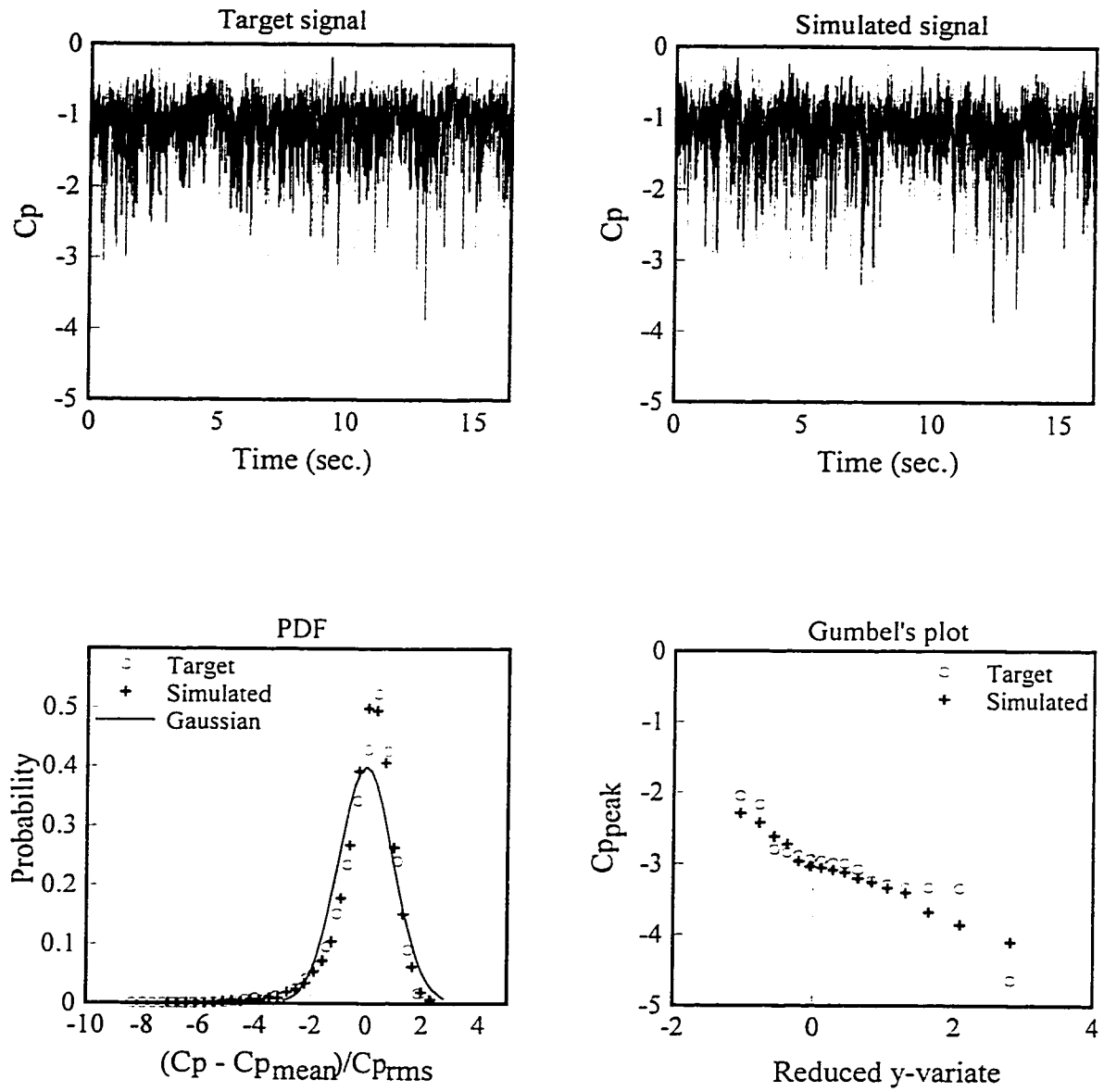
Fig. 6.22 Simulation results (sample S1).
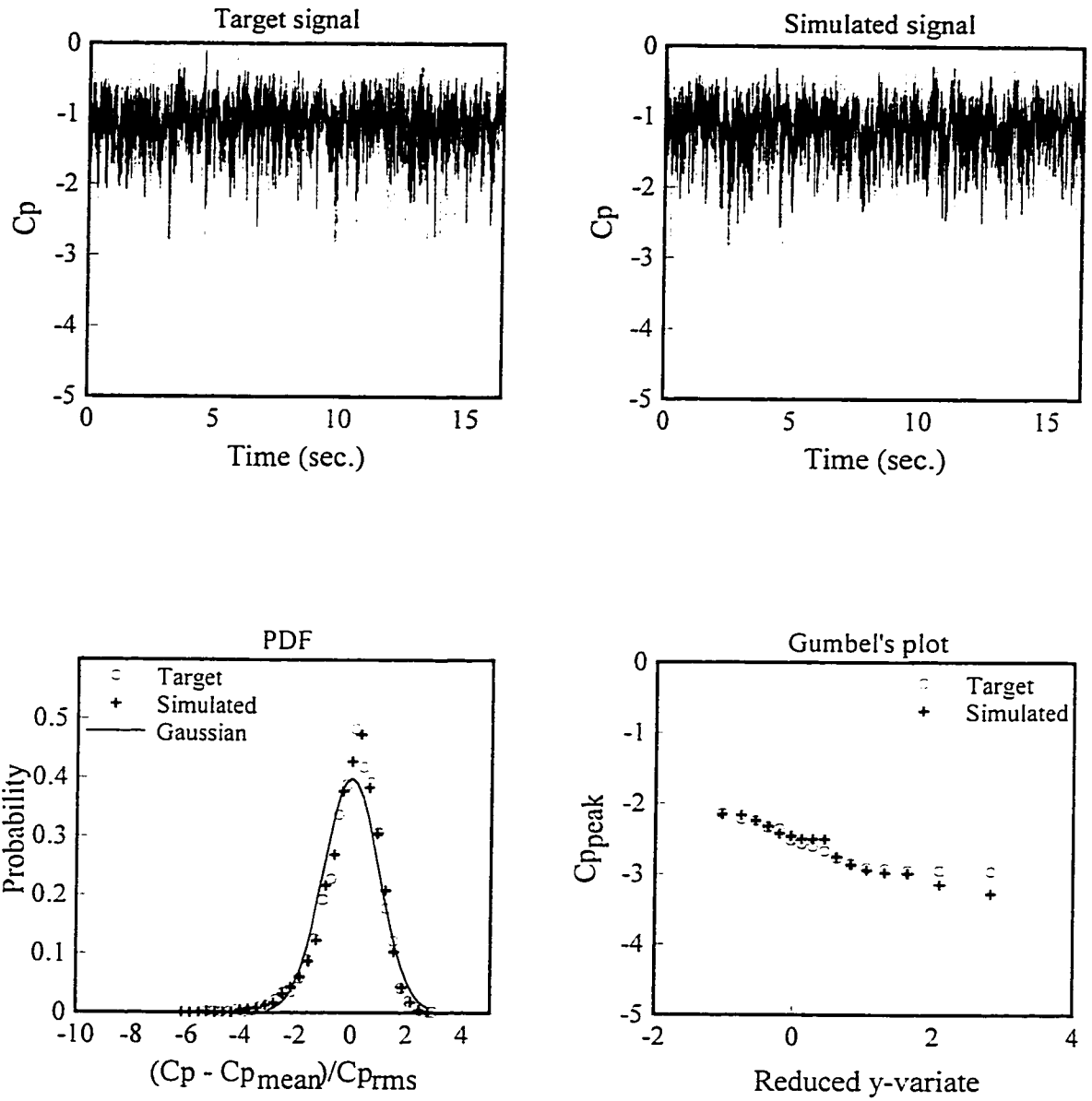
Fig. 6.23 Simulation results (sample S28).

127

16 segments of 512 values each and the peak value from each segment is selected. In case of sample S1, the target and simulated signals appear similar. Both signals seem to have high negatively going spikes which induce high skewness. The PDF's of both target and simulated signals shown in Fig. 6.22 match well except negligible discrepancies at the negative tail end. This is due to the difference in intensity of spikes between the target and simulated signals. Gaussian PDF shown in the same plot makes it clear that the sample S1 is highly non-Gaussian due to the highly skewed negative tail end. The extreme values of the signals are also compared in Fig. 6.22. The mode (Cp_{peak} corresponding to zero reduced y-variate) of the target and simulated signals is fairly close; however, dispersions (slopes of data lines) of the corresponding signals seem to be slightly different possibly due to the difference in number of crossings of the spikes at different levels. The simulation results for sample S28 are presented in Fig. 6.23. Compared to the sample S1, clear reduction in magnitude of spikes is observed. The similarity between the target and simulated signals in terms of time series, PDF's and extreme values seems to be good. It should be noted that these examples are representative samples of several simulations performed during this investigation with similar results.

In the present study, the criterion for successful modelling is set up as the reproduction of the first four moments and the spectral density function. The efforts involved in finding a non-Gaussian model are further justified if it can reflect the level crossing and peak statistics of the measured data better in comparison with the simpler Gaussian model. In Table 6.6, the number of negative peaks and down-crossings of the target signals have been compared with those of the simulated signals based on non-Gaussian and Gaussian models. All calculations have been made after the signals were subtracted from their corresponding

Table 6.6 Number of negative peaks and down-crossings at various levels of target and simulated time histories.

Sample		Peaks	Crossings Levels below mean in terms of σ						
			0	-1	-2	-3	-4	-5	-6
S1	T	1523	643	312	121	60	24	7	1
	SNG	1469	642	295	136	62	31	11	5
	SG	1500	662	387	89	7	1		
S28	T	2041	1186	579	208	59	24	6	
	SNG	2049	1159	649	249	71	17	8	1
	SG	2077	1218	702	139	13	1		

Note: T = Target, SNG = Simulated non-Gaussian, SG = Simulated Gaussian

means and normalized by their corresponding standard deviations (σ). The number of peaks is more or less close to the target values irrespective of the model used. However, it is observed that the non-Gaussian model is consistently better than the Gaussian model in case of level crossings, especially at higher levels.

6.7 REPEATABILITY OF THE SIMULATIONS

Some comments concerning the repeatability of the simulations are provided here. For the simulation of non-Gaussian time series, intermittent exponential random number sequence is required (see section 6.4.1). On the other hand, generation of exponential random numbers is essential for the generation of intermittent exponential random numbers. Many algorithms are currently available to generate exponential random numbers (Knuth 1981; Clark and Holz 1960). For the present study, logarithmic transformation of uniform random numbers is employed for the generation of exponential random numbers. This is the most

129

widely used algorithm. The intermittent exponential random number sequence, controlled by the parameter b is generated using the following algorithm:

if $(0 < U1(i) < b)$, $\varepsilon_t(i) = 0$

if $(b \le U1(i) \le 1)$, $\varepsilon_t(i) = \log(U2(i))$

where, $U1$ and $U2$ are two independent sets of uniform random numbers whose values are between 0 and 1. ε_t represents intermittent exponential random numbers whose upper limit is obviously zero but its upper limit varies. This algorithm is coded in MATLAB function **NGTIME** given in Appendix - A. Subsequent sets of intermittent exponential random numbers are expected to be different due to the change of initial seed value used in the generation of uniform random numbers. Therefore, an attempt has been made to examine the sensitivity of intermittent exponential random number sets on simulation results.

For each simulation, 8192 intermittent exponential random numbers are required. One hundred distinct sets of 8192 intermittent exponential random numbers each have been generated using $b = 0.87$ (the parameter estimated for sample S1). For each set, the first four moments (mean, variance, skewness and kurtosis) have been computed and then normalized with respect to their corresponding theoretical values estimated using the equations provided in Appendix - B. The variation of their normalized moments is displayed in Fig. 6.24 using boxplot. It is clear from the figure that the variation of the statistics is higher than those in the case of uniform random numbers shown in Fig. 5.8. The mean, variance and skewness of the sequences vary up to ±15%, while the kurtosis values vary up to ±25%. It is suspected that this high variation in statistics is due to the presence of very small values

130
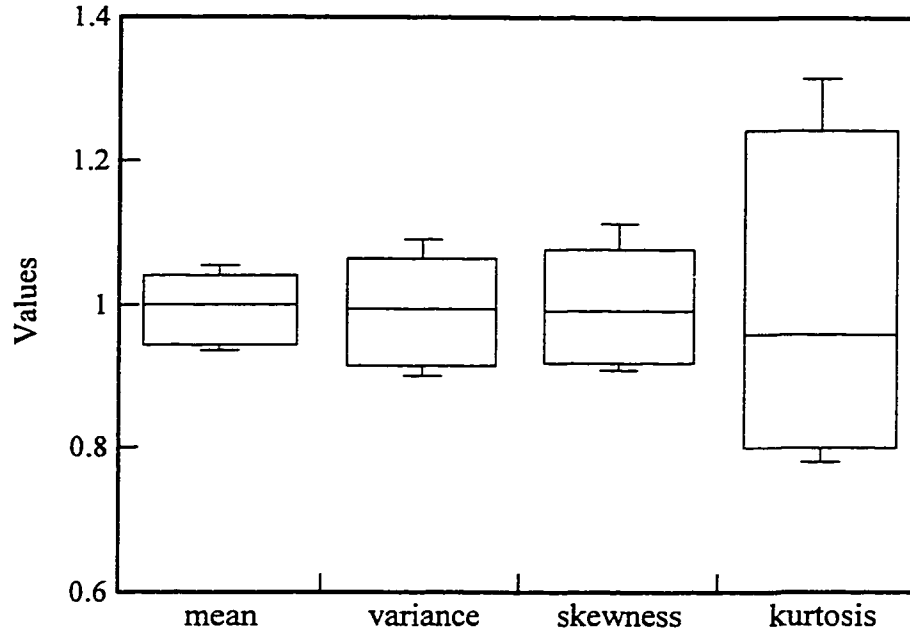
Fig. 6.24 Variation of the first four moments of the intermittent exponential random numbers.

close to zero in some of the sets of uniform random numbers. This can change the statistics

of the exponential random numbers drastically since the logarithm of those values are high.

Since this variation in statistics is suspected to be due to the transformation of uniform random

numbers, other algorithms not using the transformation of uniform random numbers have

been attempted. For instance, the algorithm provided by Clark and Holz (1960) and some of

the algorithms provided by Knuth (1981) were applied but, no significant improvement over

the present method was observed. On this basis, the present method is used in this study.

Simultaneously, the same 100 blocks of random numbers have been used to simulate 100

corresponding time histories using the amplitude part of the sample S1. Figure 6.25 presents

the variation of skewness and kurtosis of the simulated time histories in a boxplot format.

Variations up to ±25% have been observed in both quantities and this high variation is due to

the highly varying statistical properties of the intermittent exponential random number

131
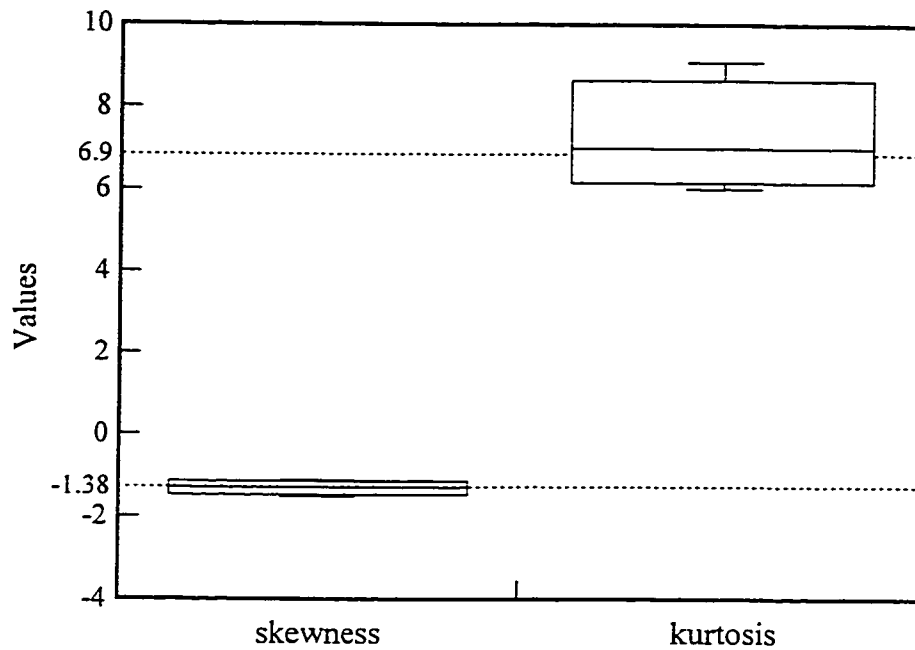
Fig. 6.25 Variation of skewness and kurtosis values of the simulated time histories.

sets shown in Fig. 6.24. On the other hand, the noted high variation in skewness and kurtosis of the simulated signal can be reduced by averaging them for a number of samples. Moreover, this scenario seems practical since several time histories are required for carrying out extreme value analysis and fatigue analysis. A typical example provided in Fig. 6.26 shows the average skewness as well as kurtosis values against the number of simulations. The time histories previously simulated for Fig. 6.25 have been used for this demonstration. For instance, the skewness value at the 50th number of simulation represents the average skewness value of the first 50 simulated time histories. As the number of simulations increases, the average skewness as well as kurtosis stabilize. After 100 consecutive simulations, the target skewness and kurtosis are achieved within 5%. Overall, the performance of the used random number generation is satisfactory. Nevertheless, further research is required to develop a good exponential random number generator which would produce independent random number sets with stable statistics.

132
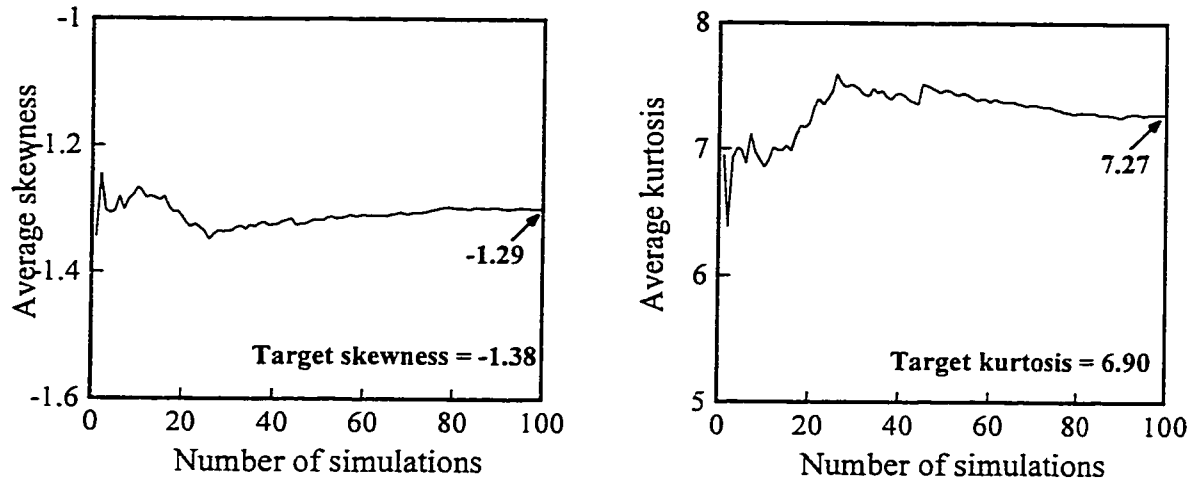
Fig. 6.26 Variation of average skewness and kurtosis values with respect to number of simulations.

6.8 SUMMARY

In this chapter, a novel simulation methodology has been developed for the digital generation of non-Gaussian wind pressure fluctuations on low building roofs whose amplitude part is known. The method based on FFT approach is set to preserve the first four moments (mean, variance, skewness and kurtosis) and spectra of the time series. A simple stochastic model (EPG) based on a single parameter b is suggested for the simulation of phase part which induces non-normality in simulated time series. The model parameter has been estimated by minimizing the sum of the squared errors in skewness and kurtosis. Several computer experiments dealing with the simulation of pressure time series on low building roofs of various geometries have been carried out in order to demonstrate the efficiency of the new approach for various building zones and flow characteristics. The results indicate that the proposed methodology can represent fluctuations of diverse nature.

133

The repeatability of the simulation has also been verified.

In comparison with the EARPG model, the EPG model in describing the phase part of a non-Gaussian process appears to be quite effective, especially in conjunction with increasing simplicity by reducing the number of parameters involved, elevating flexibility by introducing an efficient parametric estimation procedure and enhancing accuracy by achieving two non-Gaussian properties. Further, stationarity of the simulated time series is justified for $b \leq 0.9$.

The proposed simulation technique is capable of generating the data required for extreme value analysis as well as fatigue analysis. As a result of the successful simulation of a number of different pressure time histories, generalization of the simulation methodology in terms of building geometry, terrain conditions and surroundings may be possible. This would help the user to simulate an unlimited amount of data on any type of roof under various conditions without the need of extensive experimental measurements. Moreover, the proposed simulation methodology can be utilized in other engineering problems encountering random processes of similar nature where the first few moments and the PSD function are the only available information about the process. Generation of the amplitude part from target spectra, generalization of the simulation methodology and applications of the methodology are discussed in the following chapters.

CHAPTER 7
SPECTRA OF WIND PRESSURES ON LOW BUILDING ROOFS

"...The response of structures to random excitation is of wide engineering interest. The vibration environment may be generated by such diverse sources as atmospheric turbulence, ocean waves in a rough sea, or ground motion due to earthquakes.... A frequency domain approach using power spectral density functions to describe excitation and response, and a transfer function to characterize the system, has proved to be very useful..."

E. H. Vanmarcke, 1972.

Spectrum (SDF) of wind pressure fluctuations on low building roofs, which is required for the simulation of pressure time series, is the basic description of the probabilistic nature of the wind loads acting on them. As previously mentioned, the Fourier amplitude part in the proposed simulation methodology can be constructed from the given spectrum. This chapter summarizes a study in which several wind pressure spectra were measured at various tap locations on the roofs of several low building models placed in two types of terrain in order to determine their characteristic shape and derive a suitable empirical representation.

In the past there have been several studies on quantifying wind velocity spectra which is essential for the theoretical analysis of wind loads on buildings (Panofsky and McCormick 1954; Davenport 1961). Most recently, Tieleman (1995) presented unified spectral methods for the three-component velocity fluctuations in wind-tunnel generated shear flows and in the atmospheric boundary layer. In contrast with the many studies that have been conducted with respect to the wind velocity spectrum, wind pressure spectra have received only limited attention due to their complex nature. Wind pressure spectrum representing energy content in pressure fluctuations receives contributions not only from mechanical turbulence but also from

building generated turbulence which makes it complex especially in separation as well as roof corner zones. As a result of this, only isolated measurements have been made for specific cases in many studies. However, the classification of spectra of space-averaged pressures over flat roof panels (Stathopoulos et al. 1981) and the more recent attempt to describe the basic shapes of spectra (Kasperski and Koss 1996) are notable exceptions. Since the literature shows that there is no systematic information available on spectra of wind pressures acting on low building roofs, an extensive investigation has been carried out on this area.

This chapter describes the overall characteristics of pressure spectra acting on low building roofs under various conditions with the help of wind tunnel measurements. The measurement details as well as some preliminary results have been reported in Chapter 4. An empirical model for the description of spectra of wind pressures on low building roofs is suggested. Thereafter, the construction of Fourier amplitude part from synthetic spectra is provided. This is followed by the demonstration showing the efficiency of the fitted spectra in time series simulations. An attempt has also been made to classify SDF's complex pattern on roof after they have been appropriately normalized. Finally, the various zones of the roof and their corresponding spectral shapes in terms of their parameters are provided for various roof geometries. Some of these results were reported in Suresh Kumar and Stathopoulos (1996a, 1997c, 1997e).

7.1 CHARACTERISTICS OF PRESSURE SPECTRA

Typical samples of measured pressure spectra are shown in Figs. 7.1 and 7.2. A common feature found in all measurements is that, in general, the amplitude of pressure spectrum dies out as the frequency increases. However, a small growth in spectral amplitudes at
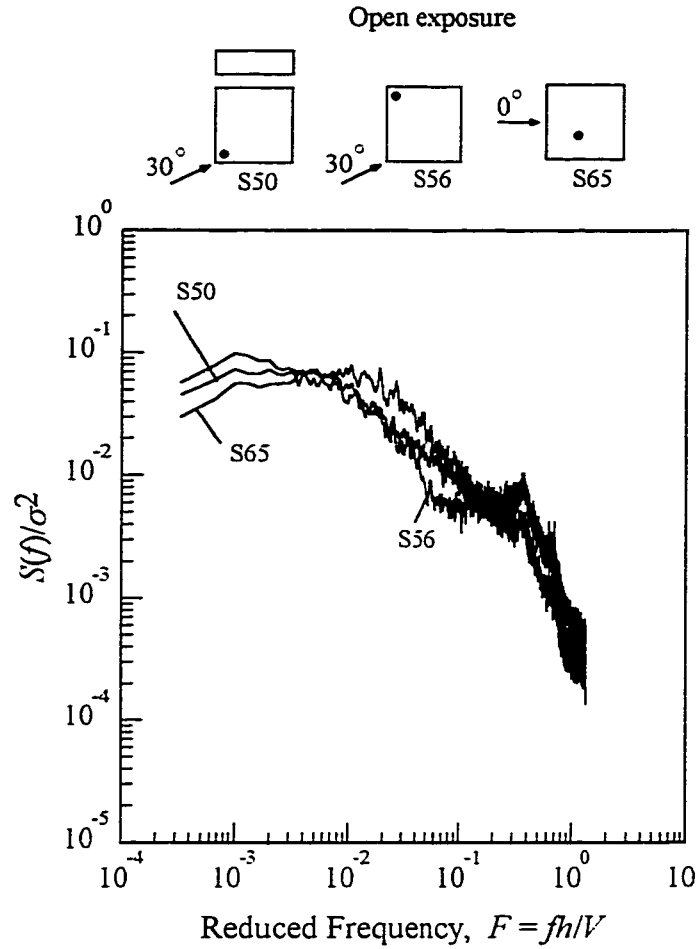
Fig. 7.1 Sample wind pressure spectra on flat roof.

dimensionless frequencies (F) between 0.1 and 0.2 $(f \approx 20$ to 40 Hz) has been observed at taps located in farwind as well as leeward regions of the roof due to the increase in contribution from small scale turbulence in those regions. Note that farwind region represents the windward edge region away from the windward corner in case of oblique wind angle. Typical samples are shown in Figs. 7.1 and 7.2 for flat (sample S56) and sloped roofs (samples S69 and S1). In Fig. 7.1, sample S56 which corresponds to the tap located in farwind region has small growth between the corresponding frequency range as previously mentioned. However, such growth is predominant in case of taps located in leeward regions of gable and monoslope roofs
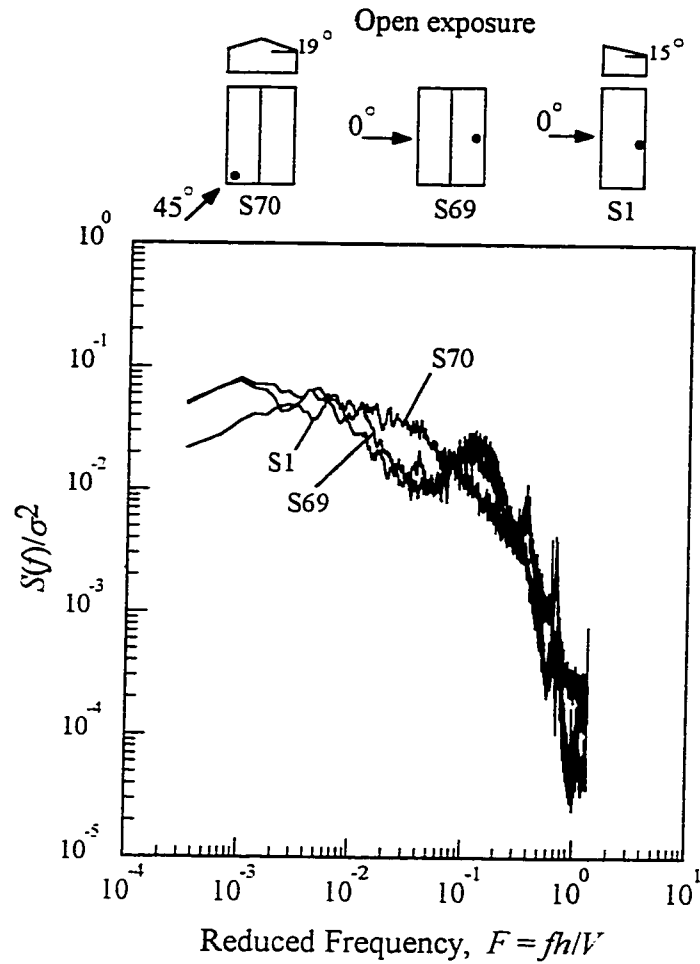
Fig. 7.2 Sample wind pressure spectra on gable and monoslope roofs.

as shown in Fig. 7.2. Further, the evolution of the above mentioned two spectral shapes and the transition from one to the other are clearly shown in Figs. 7.3 and 7.4. While Fig. 7.3 demonstrates the evolution of spectral shapes in case of a flat roof building in open terrain exposure, Fig. 7.4 demonstrates this in case of a monoslope roof building in open terrain exposure. It is clear from the figures that the spectral hump appeared in case of tap located in leeward region of a monoslope roof building is predominant compared to that in case of tap located in farwind region of a flat roof building. This has been attributed to the increasing contributions from small scale turbulence in case of monoslope roof possibly due to the tap
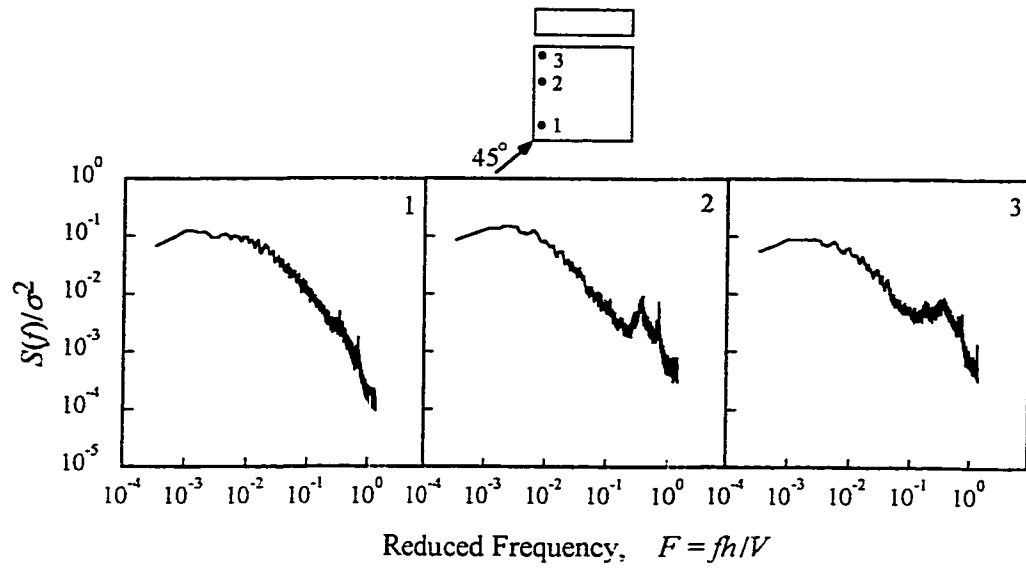
Fig. 7.3 Evolution of spectral shapes (flat roof).
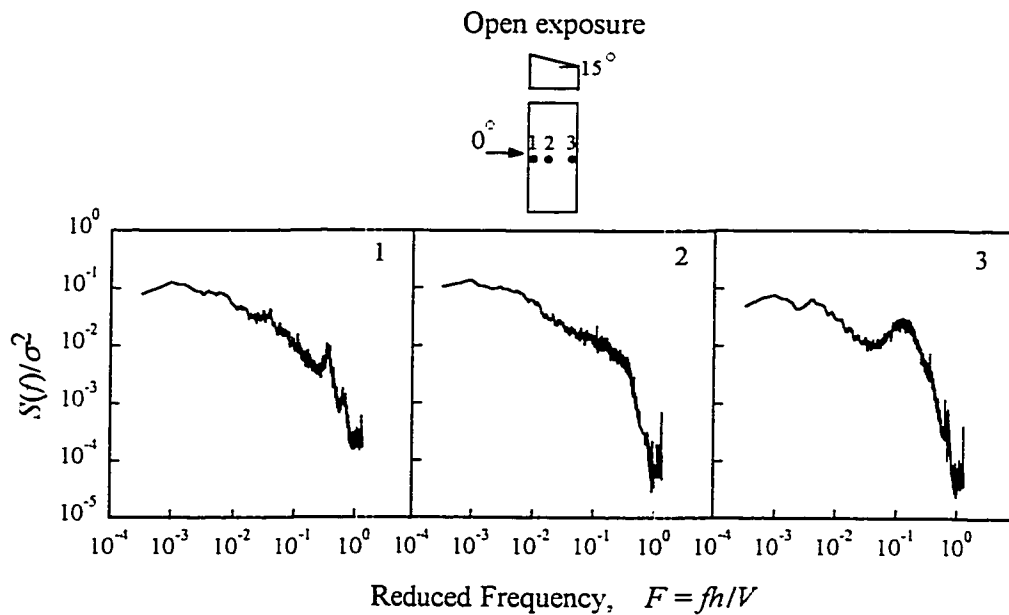
Fig. 7.4 Evolution of spectral shapes (monoslope roof).

location and roof slope. Figure 7.5 compares two spectra measured at the same location on a flat roof in open country and suburban terrain conditions. Eventhough the variances are different due to the variation in incident turbulence, the normalized spectra appear to be similar.
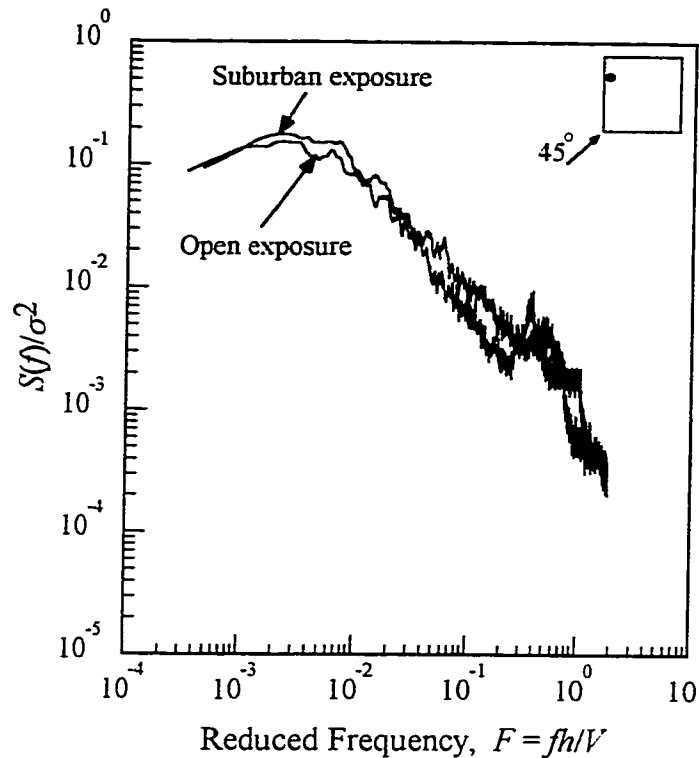
Fig. 7.5 Comparison of wind pressure spectra at different terrain conditions.

The same characteristics are also found at other locations. Following the inspection of various spectra on roof, a number of qualitative conclusions can be drawn and summarized as follows:

(a) Though the spectra change in shape and magnitude depending on the geometry of roof, terrain conditions, wind attack angle and tap location, they can be classified into two categories: (1) spectra which die out as the frequency increases and (2) spectra which die out up to a certain frequency and then grow to have another hump prior to their dying. The growth in the second type of spectra is attributed to the additional contribution from pressure fluctuations in the separation layer.

(b) The variance of the fluctuations (area under $S(f)$) appears to be different for different conditions. For comparison purposes, all spectra have been normalized with respect to

140

their variance and many normalized spectra seem to be similar in shape and magnitude. This is a favourable element for the analytical description of spectral curves.

(c)   The normalized pressure spectra corresponding to the same tap at open and suburban terrain conditions seem to be similar, though the variance is greater in case of suburban conditions, as expected.

Since normalized spectra measured at various locations of the roof under different conditions show similarities, there is a possibility to draw an empirical expression to represent spectral curves which is discussed in more detail in the following section. Standard spectral shapes may be proposed for different zones of the roof. The actual pressure spectra at the corresponding location can be obtained by simply multiplying the standard shape by the corresponding variance.

7.2 REPRESENTATION OF SPECTRA

As previously discussed, spectral curves can be represented by empirical equations and thereby Fourier amplitude can be generated in a synthetic manner. Though spectra of pressure fluctuations at various taps appear generally similar in shape, the spectral amplitudes vary depending on the variances of the corresponding fluctuations. In order to simplify the empirical modelling as well as to get standard spectral shapes, all spectra have been normalized by their variance. Thereafter, several traditional curve fitting techniques have been employed to extract a suitable empirical equation for spectra. Because of the initial lack of success, a different approach by using trial and error was attempted.

The organization of the curve fitting technique used in this study is shown in Fig. 7.6. The

141
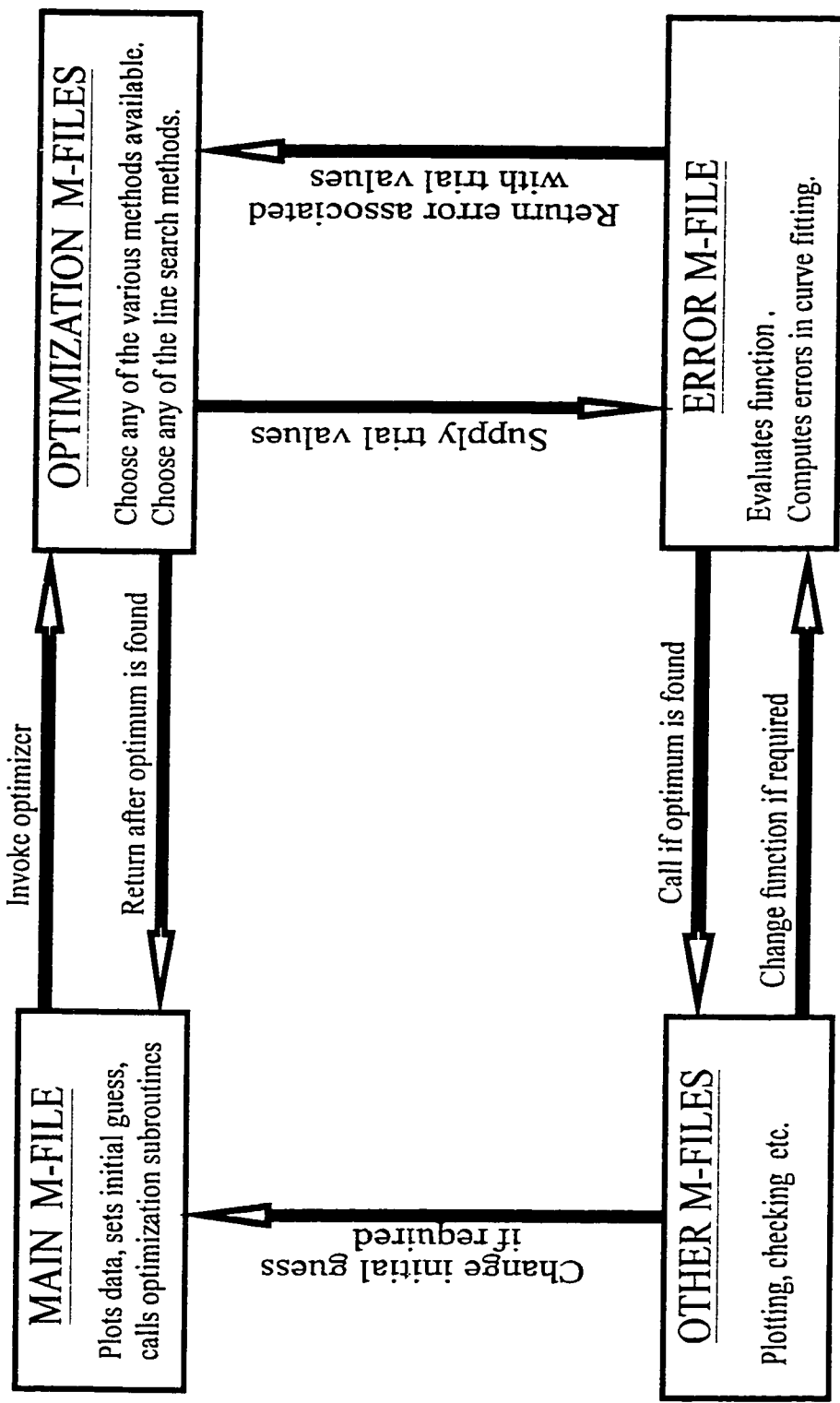
Fig. 7.6 Flow chart showing empirical fitting of pressure spectra.

procedure is distributed in four M-files (M-file is a default editor in an empty MATLAB window allowing one to create a new program) and is self explanatory. The code is written in MATLAB environment with the help of available built-in functions. In this procedure, the inputs to the program are data set, initial values of parameters and the function to be fitted. The program uses traditional optimization methods to estimate the optimum parametric values iteratively by minimizing the sum of the squared residuals. In this case, the data set consists of independent variables (f) and dependent variables $(S(f)/\sigma^2)$. Optimum results can be obtained in minimal computer time (of the order of 10 seconds) by choosing good trial values which could be changed in subsequent trials to obtain optimum values quickly. The least-square error criterion, minimization of the sum of the squared residuals, i.e. minimization of the sum of the square of the difference between the fitted spectral ordinates and the measured spectral ordinates, was used in error M-file for the selection of the optimum parameters. This M-file keeps the value of the previous smallest error and returns immediately to the optimization M-file if the error is larger. Several traditional optimization methods such as Steepest Descent, Simplex search, Gauss-Newton etc., and line search strategies such as mixed polynomial and cubic polynomial methods are provided in optimization M-files, and the user is free to select a suitable optimization method and a line search method (MATLAB 1994a). In this study, the Levenberg-Marquardt algorithm known for its robustness along with cubic polynomial interpolation line search method has been used to carry out least-square optimization (MATLAB 1994a).

Several functions representing approximately the same shape as the target spectra have been tried. SDF's monotonic decay in amplitude with increasing frequency (a straight line decay in logarithmic scale) indicates that a power function of the form f^α where, α is the power index

143

and f is the frequency might be suitable but not for low frequencies where most of the energy lies. Moreover, the hump that is noticed in several spectra cannot be represented by this function. After an extensive investigation, an exponential function has been found to be more appropriate. Moreover, under general conditions, the periodogram ordinates (linearly proportional to the spectrum ordinates) at any set of frequencies are asymptotically independent exponential random variables (Brockwell and Davis 1991) which reinforces the suitability of this function. The proposed function is

$$S(f)/\sigma^2 = a_1 e^{-c_1 f} + a_2 e^{-c_2 f} \qquad (7.1)$$

where, $S(f)$ is the spectral ordinate, σ^2 corresponds to variance, f corresponds to frequency, a_1 & a_2 are the position constants and c_1 & c_2 are the shape constants. The position constants control the location of the spectra, whilst the shape constants control their dying out shape. The proposed function consists of two exponential functions; $a_1 e^{-c_1 f}$ represents the amplitudes at high frequency range, while $a_2 e^{-c_2 f}$ represents the amplitudes at low frequency range. The four parameters (a_1, a_2, c_1 and c_2) corresponding to a particular data set can be estimated using the procedure described in Fig. 7.6. Here, the initial guesses are made only for c_1 and c_2 since the other two parameters (a_1 and a_2) can be easily found out using Eq. (7.1) written in the matrix form,

$$\begin{matrix} (mx1) & (mx2) & (2x1) \\ [S(f)/\sigma^2] = [e^{-c_1 f} \quad e^{-c_2 f}] [a_1 \ a_2]^T \end{matrix} \qquad (7.2)$$

Then,

$$[a_1 \ a_2]^T = [e^{-c_1 f} \quad e^{-c_2 f}] \backslash [S(f)/\sigma^2] \qquad (7.3)$$

144

is the solution in the least-squares sense to the overdetermined system of Eq. (7.2) computed by Gauss elimination where, the symbol '\' represents the matrix left division operator (MATLAB 1992). It is known that

$$\int_0^\infty \frac{S(f)}{\sigma^2} df = 1 \tag{7.4}$$

Further, the substitution of Eq. (7.1) in Eq. (7.4) would result in

$$\frac{a_1 c_2 + a_2 c_1}{c_1 c_2} = 1 \tag{7.5}$$

By using Eq. (7.5), one of the spectral parameters can be determined by knowing the other three. Therefore, SDF can be simulated by knowing any three parameters.

An example of the measured and fitted wind pressure spectra is shown in Fig. 7.7. The MATLAB functions **FIT** and **FUNFIT** (see Appendix - A) based on the procedure shown in Fig. 7.6 have been used for the fitting of pressure spectra. The fitting has been done as follows: first, the MATLAB function **FIT** is initialized by calling its name. Then, the data to be fitted (format of the data is $[f \ S(f)/\sigma^2]$) and the initial guesses for c_1 and c_2 are provided. Next, a suitable optimization method and a line search method are chosen from a list provided by the program. Finally, the program will provide the fitted curve and its corresponding parameters as well as the error. The spectral fit shown in Fig. 7.7 appears satisfactory; the spectral statistics (N_0, N_p, ε and β - details are provided in section 3.2.2.2) of the fit is closer to the corresponding target values (see Table 7.1). Satisfactory performance of the proposed empirical expression has also been observed in a variety of other cases. Though the fit is based on minimizing the squared residuals (i.e. square of the difference between the fitted spectral
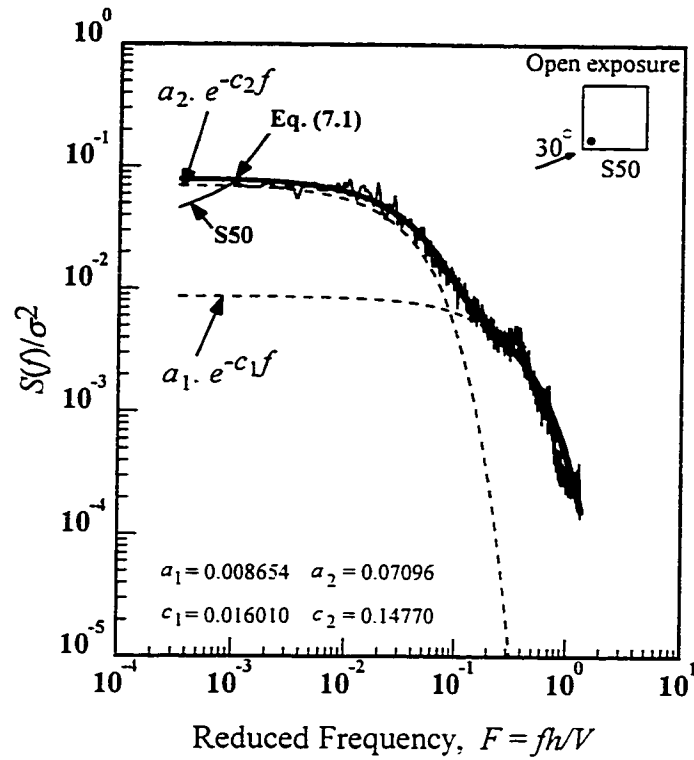
Fig. 7.7 Measured and fitted wind pressure spectra (flat roof).

Table 7.1 Spectral statistics of measured and synthetic spectra.

Sample	N_0	N_p	ε	β
Measured (Fig. 7.7)	55	150	0.37	0.93
Synthetic (Fig. 7.7)	57	150	0.38	0.92
Measured (Fig. 7.8)	75	154	0.49	0.87
Synthetic (Fig. 7.8)	73	146	0.50	0.87

amplitudes and the measured spectral amplitudes), it is decided to quantify the level of accuracy of the fit based on four spectral statistics (N_0, N_p, ε and β) with a view to provide a physical meaning to the error caused by the fit. During this investigation, a number of case studies showed that the above spectral statistics can be obtained within 10% using this fitting procedure which is reasonable for practical applications.

Further, the evolution of the fitted curve is shown in Fig. 7.7 by plotting $a_1 e^{-c_1 f}$ and

$a_2 e^{-c_2 f}$ separately. It is clear that the term $a_1 e^{-c_1 f}$ controls the position and shape of spectra at higher frequency region, while the term $a_2 e^{-c_2 f}$ controls the position and shape of spectra at lower frequency region. The term $a_1 e^{-c_1 f}$ shifts the ordinate of the spectra to the right side and thereby represents the additional growth noted in some cases. It is interesting to note that the parameters obtained in the previous fitting are all positive and therefore, the derivative of Eq. (7.1) at any point is a negative quantity which reveals the fact that the fitted curve does not have an upward slope. As a result, this function represents only mild growth in spectra and needs modifications to fit the predominant spectral growth observed in some cases such as samples S69 and S1 shown in Fig. 7.2. In such cases, spectra show a clear hump and the proposed Eq. (7.1) requires an additional term $a_3 e^{-c_3 f}$ to fit the data efficiently; the modified function is

$$S(f) / \sigma^2 = a_1 e^{-c_1 f} + a_2 e^{-c_2 f} + a_3 e^{-c_3 f} \tag{7.6}$$

The parameters a_3 and c_3 can be established using the fitting procedure as previously shown in Fig. 7.6 with some minor modifications in the program; these include the addition of new term $a_3 e^{-c_3 f}$ in Eq. (7.1), the corresponding changes in Eqs. (7.2) and (7.3) and the incorporation of c_3 in the list of initial guesses. Figure 7.8 demonstrates a typical example where the spectral growth at certain frequencies is predominant. Note the negative value obtained in case of parameter a_2 by which the upward slope in fitting is established to represent the hump. The efficiency of this fitting process is once again demonstrated using the appearance of the fit shown in Fig. 7.8 and the spectral statistics shown in Table 7.1.

Finally, it is noted that Eq. (7.1) can efficiently represent spectra in most of the locations of

147
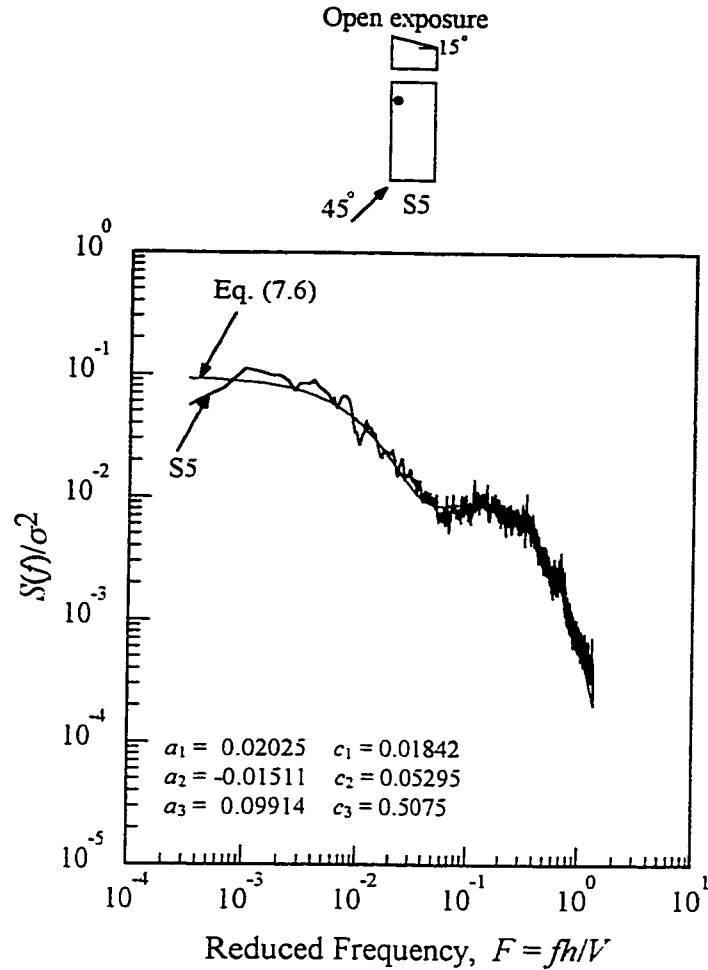
Fig. 7.8 Measured and fitted wind pressure spectra (monoslope roof).

various roof geometries for various azimuths; however, Eq. (7.6) is required to represent the predominant spectral growth observed in few cases. These cases will be specified in later part of this chapter.

A typical example providing the sensitivity of spectral parameters is shown in Fig. 7.9, in terms of the variation of spectral statistics with respect to the variation of spectral parameters. The spectral fit shown in Fig. 7.7 is used for this demonstration. Each time, one of the spectral parameters is varied around its optimum value and the corresponding variations of spectral statistics are plotted. It is clear from Fig. 7.9 that the spectral statistics is highly sensitive only to

148
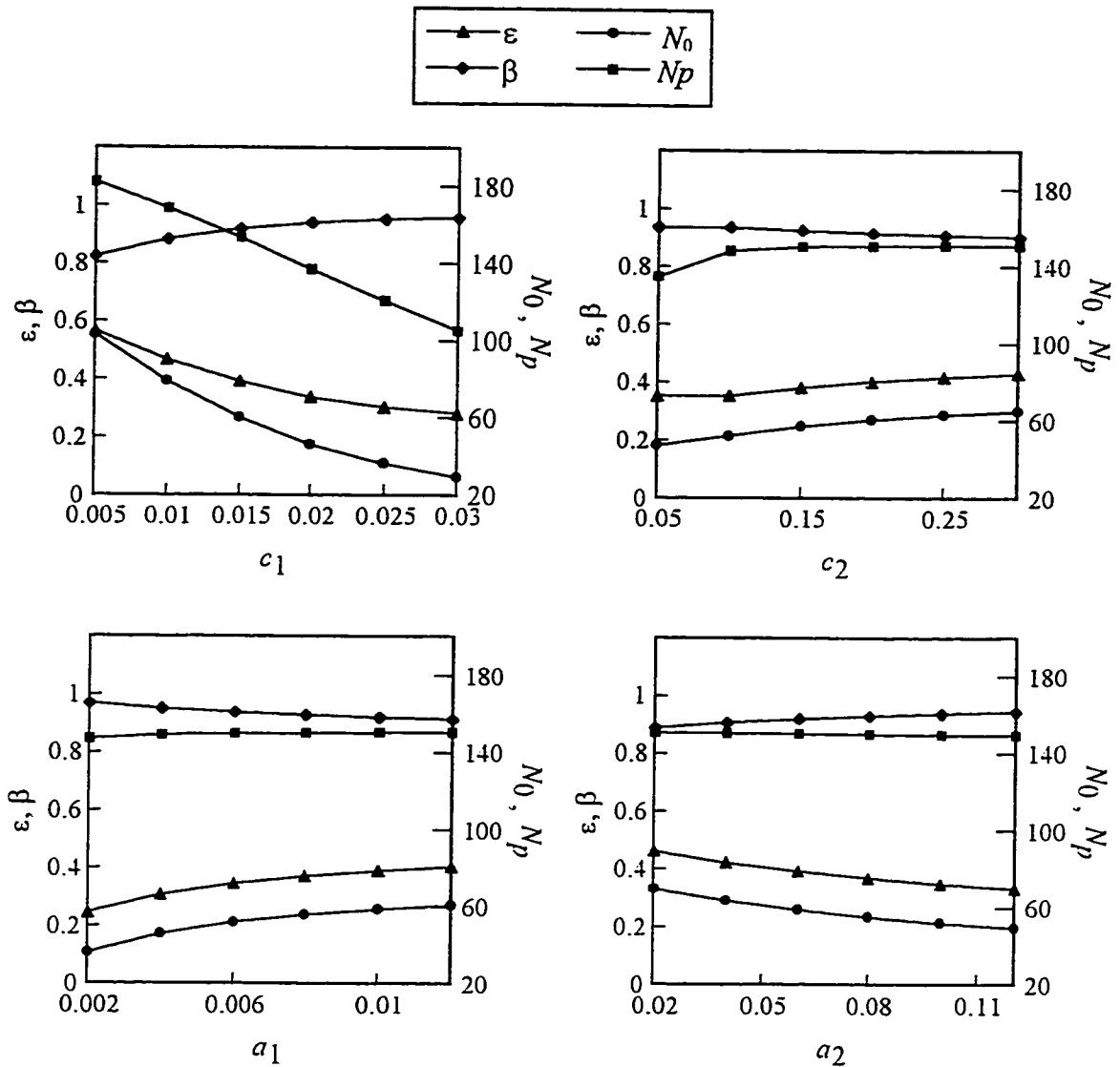
Fig. 7.9 Sensitivity of spectral parameters (case - Fig. 7.7).

c_1, when varied around its optimum value of 0.01601 - see Fig. 7.7. Note that c_1 determines the dying out rate at high frequency range representing the energy content in small scale turbulence generated by the building. Note that the spectral statistics is not highly sensitive to parameters a_1, a_2, and c_2 in comparison with c_1. In case of parameters a_2 and c_1, the spectral statistics such as ε, N_0, and N_p reduce with increasing parameter values, while β increases with increasing parameter values. However, in case of parameters a_1 and c_2, the spectral statistics such as ε, N_0,

and N_p increase with increasing parameter values, while β reduces with increasing parameter values. Note that as ε increases, β decreases and vice versa which is expected from Eq. (3.30). Moreover, as ε decreases, N_0 also decreases and vice versa. This is because as ε decreases, the process tends to become broad-banded and consequently, the number of zero up-crossings are expected to be reduced. Similar trends are observed in other spectra.

7.3 Construction of Fourier Amplitude Part of DFT ($\sqrt{I_k}$)

The function which is proposed to generate pressure spectra is expressed in a discrete form as

$$S_p(f_k) / \sigma^2 = a_1 e^{-c_1 f_k} + a_2 e^{-c_2 f_k} \; ; \quad f_k = k\Delta f \, , \quad 1 \le k \le n/2 \tag{7.7}$$

where, $S_p(f_k)$ is the spectral ordinate, σ^2 corresponds to variance, f_k corresponds to frequency, Δf corresponds to frequency resolution (i.e, inverse of the period of time series $= f_s/n$; $f_s =$ sampling frequency, $n =$ number of samples), a_1 & a_2 are the position constants and c_1 & c_2 are the shape constants. Eq. (7.7) corresponds to physical spectrum that computes only the first half of the spectral amplitudes in the positive frequency range and $\Delta f = 500/8192$ is used as the frequency resolution. However, the mathematical spectrum ($S_m(f_k)$), symmetric about the midpoint and ranging both in the positive and negative frequencies, is required for computational purposes. The desired format of mathematical spectra can be estimated by,

$$
\begin{aligned}
S_m(f_k) = \; & S_p(f_k)/2 \; ; \quad f_k = k.\Delta f \, , \quad && 1 \le k \le \frac{n}{2} \\
& S_p(f_k)/2 \; ; \quad f_k = (n-k).\Delta f \, , \quad && \frac{n}{2}+1 \le k \le n-1 \\
& 0 \qquad \; ; \quad f_k = 0
\end{aligned}
\tag{7.8}
$$

Then, the Fourier amplitude ($\sqrt{I_k}$) can be evaluated using,

$$\sqrt{I_k} = n.\sqrt{S_m(f_k)\,\Delta f} \qquad (7.9)$$

Detailed explanations of the above formulation (Eqs.(7.8) and (7.9)) can be found elsewhere (Bendat and Piersol 1986).

It is appropriate at this point to present an application of the proposed empirical function for spectra of pressure fluctuations acting on low building roofs. The spectral fit shown in Fig. 7.7 is used for this demonstration. A typical example of the construction of Fourier amplitude part from synthetic spectra is pictorially shown in Fig. 7.10. The normalized spectrum is generated using Eq. (7.7) with the help of the parameters established in Fig. 7.7. Physical spectrum is obtained by multiplying the ordinates of the normalized spectrum by the variance of the corresponding pressure fluctuations (0.28 in this case). Eq. (7.8) is used to construct the mathematical spectrum from physical spectrum. Finally, the Fourier amplitude is constructed from mathematical spectrum using Eq. (7.9). In summary, once the spectral parameters (a_1, a_2, c_1 and c_2) are provided, the Fourier amplitude part required for time series simulation can be easily generated with the help of variance of the corresponding pressure fluctuations. Figure 7.11 shows the simulation of the corresponding time history using the synthetic Fourier amplitude part from Fig. 7.10. The skeleton signal and its corresponding phase shown in Fig. 7.11 are generated based on the description provided in Chapter 6. The simulated signal is obtained by inverting the Fourier coefficients which are a combination of Fourier phase and Fourier amplitude. In order to find the efficiency of synthetic spectra in time series simulation, it was decided to compare the statistics of the simulated signal using target spectra (Simulation-I) with that of the simulated signal using synthetic spectra (Simulation-II). Though Simulation-I

151
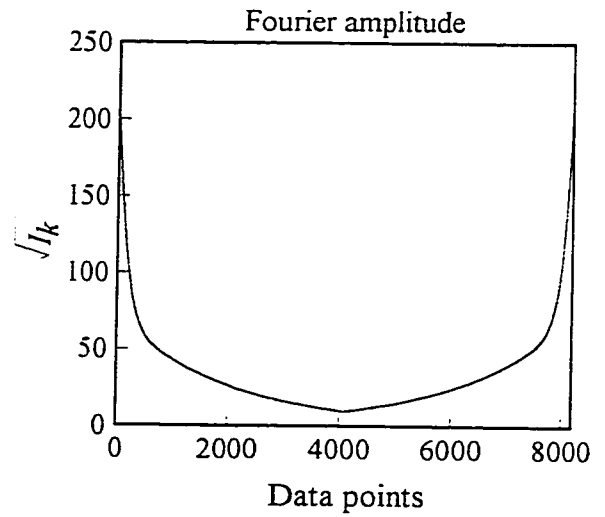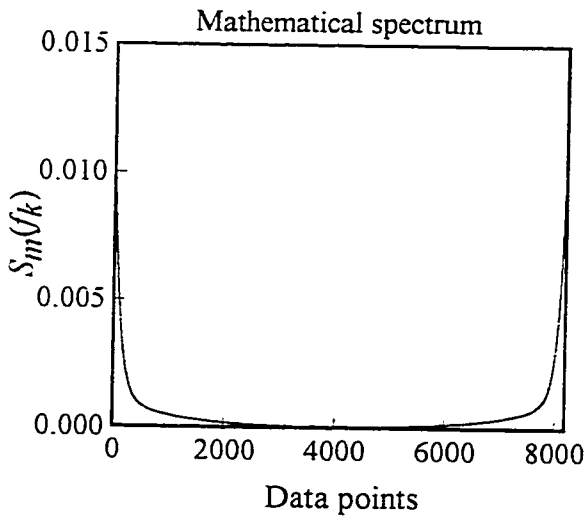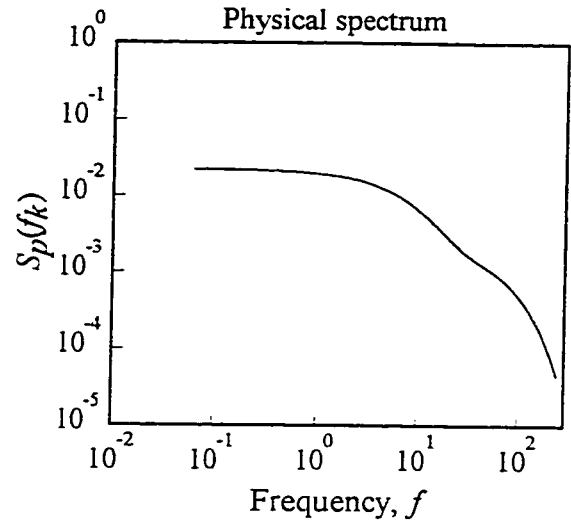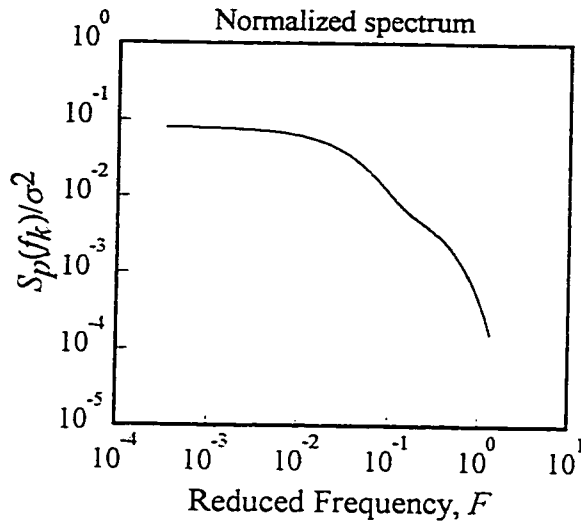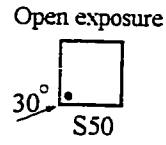
Fig. 7.10 Construction of Fourier amplitude (case - Fig. 7.7).
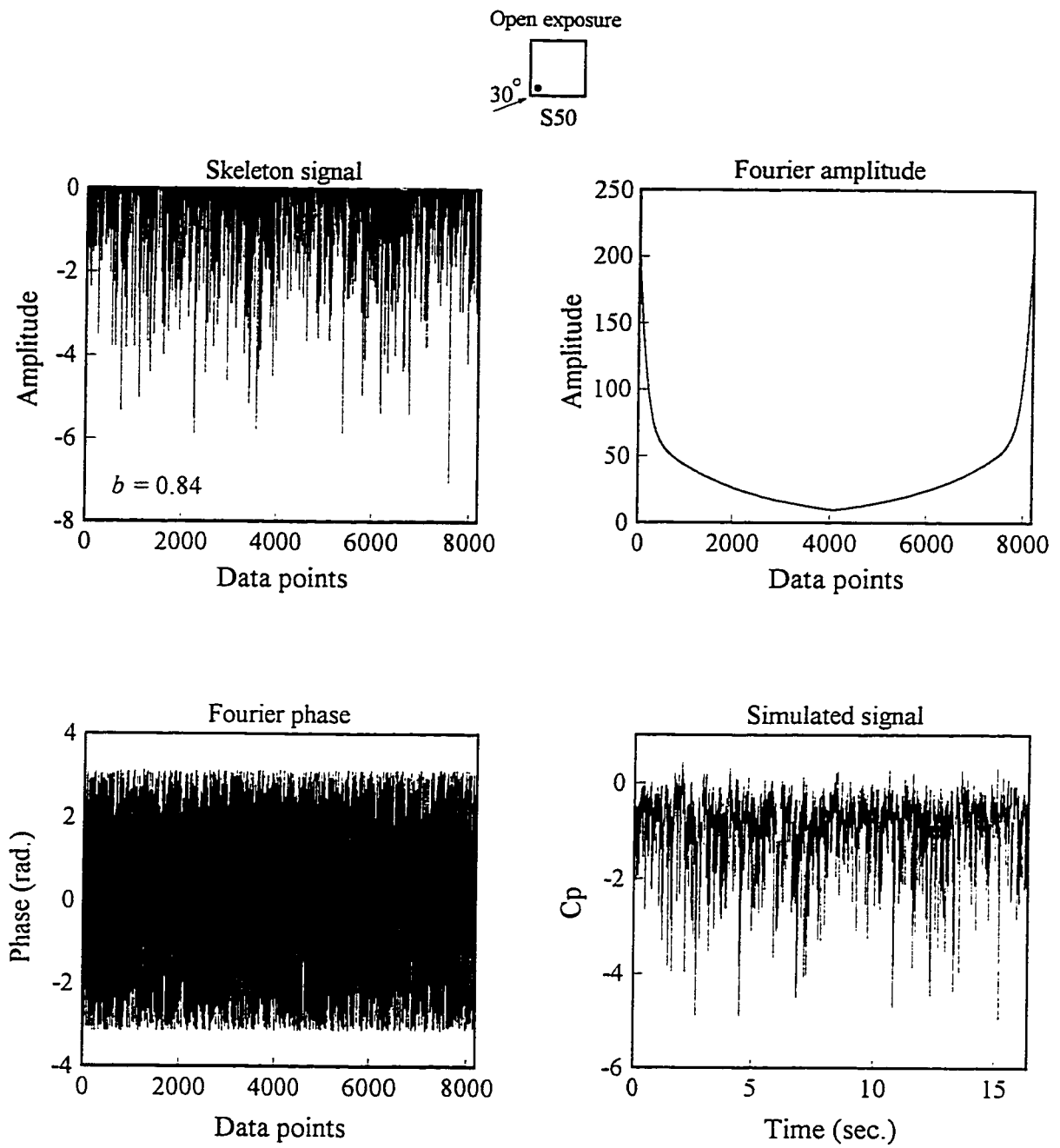
Fig. 7.11 Simulation of pressure time series using synthetic spectra (Simulation - II).

153

is not pictorially shown, the same procedure as Simulation-II was adopted for Simulation-I. The same Fourier phase from Simulation-II was used in Simulation-I; the only difference was in Fourier amplitude part which was constructed from target spectra shown in Fig. 7.7 using Eqs. (7.8) and (7.9). While Table 7.2 compares the first four moments (mean, variance, skewness and kurtosis) of the simulated signals, Table 7.3 compares the number of negative peaks and down-crossings of the simulated signals. The corresponding values of both signals are close and the same result is observed in other cases.

Table 7.2 Statistics of simulated signals.

	Mean	Variance	Skewness	Kurtosis
Simulation-I	-0.8	0.28	-1.92	9.87
Simulation-II	-0.8	0.28	-1.96	10.22

Table 7.3 Number of negative peaks and down-crossings at various levels of simulated signals.

Sample	Peaks	Crossings						
		Levels below mean in terms of standard deviation						
		0	-1	-2	-3	-4	-5	-6
Simulation-I	1854	617	362	189	100	43	22	12
Simulation-II	1939	629	374	193	100	45	25	12

7.4 GENERALIZATION

As previously discussed, it is possible to group normalized spectra of pressures acting on roofs due to their similarities. Further, it is of practical interest to categorize all types of spectra on roofs into certain limited number of groups. Since the simulation methodologies used for

154

Gaussian and non-Gaussian time series simulations are different, it would be better to classify the zones of Gaussian and non-Gaussian regions prior to the grouping of spectra at the respective regions. The zones of Gaussian and non-Gaussian pressure fluctuations have already been identified for various roof geometries and reported in Chapter 4 (section 4.3). Following this, an attempt has been made to group the spectra at previously identified Gaussian and non-Gaussian zones separately.

Generally, the spectra observed on Gaussian regions appear to have more erratic spikes due to their low variance; however, normalized spectra seem to be similar irrespective of location and wind direction. For instance, Fig. 7.12 shows the normalized spectra measured at different
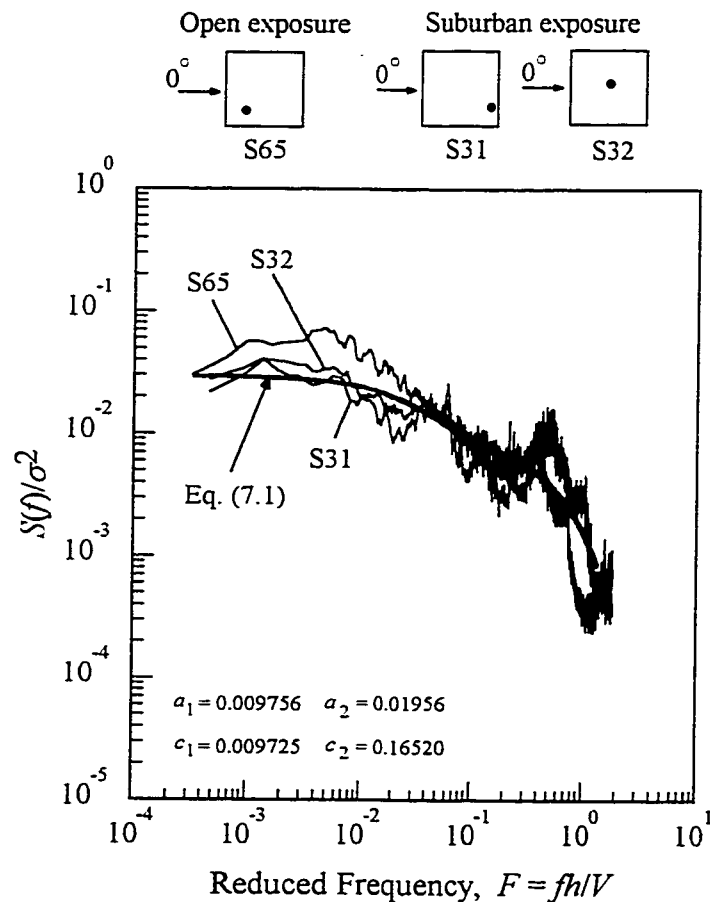
Fig. 7.12 Measured and fitted wind pressure spectra (flat roof, Gaussian zone).

locations on a flat roof at different terrain conditions for zero wind direction. The spectra appear to have more or less similar shapes. This has been noted at several locations of a flat roof for other wind directions. Since their shapes are similar, pressure spectra are averaged to obtain the most probable spectra for that region. Thereafter, the proposed empirical function is fitted in accordance with the procedure shown in Fig. 7.6. Statistics of the fitted spectra is compared with those corresponding to the observed in Table 7.4. Note that this fitting is based on twelve measured spectra from this Gaussian region. In most of the cases, the spectral statistics is obtained within 20% and this discrepancy is due to the averaging of several spectra.

Table 7.4 Comparison of spectral properties (flat roof, Gaussian zone).

Sample	N_0	N_p	ε	β
Fit	94.9	169.8	0.56	0.83
S65	70.2	143.9	0.49	0.87
S31	88.5	153.5	0.58	0.82
S32	80.1	144.7	0.55	0.83

In the case of non-Gaussian region, two types of spectra have been found; the first dies out as frequency increases on windward regions and the second has another hump prior to its dying out on the farwind or leeward regions. Based on this, the non-Gaussian region is again divided into two zones. Figure 7.13 shows normalized spectra selected from farwind non-Gaussian regions of the flat roof building in open and suburban conditions. Such spectra appear similar and they have been averaged and fitted by the empirical expression. The statistics of the fitted and observed spectra are given in Table 7.5 which shows that fitted spectrum is a good representative of the observed spectra.

This procedure has been carried out for monoslope as well as gable roofs. In the case of monoslope roof, two types of spectra in Gaussian zone have been observed; the first type lies

Open exposure   Suburban exposure

S56 S62   S28
S61   S26

45°   45°

Eq. (7.1)

S26   S61

S28   S56

S62

$a_1 = 0.008162$ $a_2 = 0.1205$
$c_1 = 0.010840$ $c_2 = 0.3823$

Reduced Frequency, $F = fh/V$
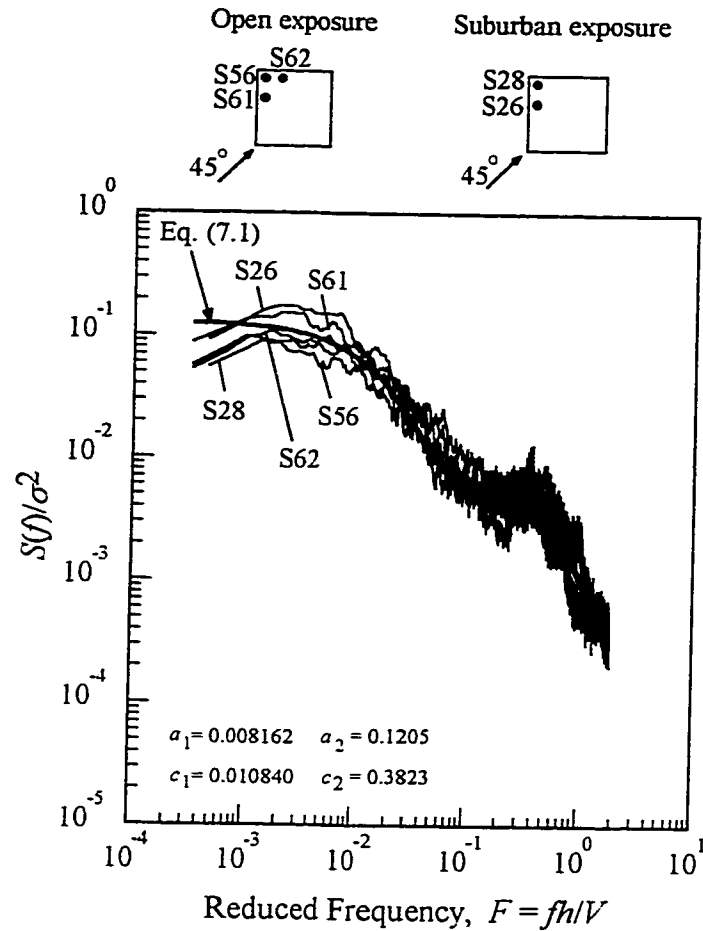
Fig. 7.13 Measured and fitted wind pressure spectra (flat roof, non-Gaussian zone).

Table 7.5 Comparison of spectral properties (flat roof, non-Gaussian zone).

Sample	N_0	N_p	ε	β
Fit	80.2	166.7	0.48	0.88
S56	78.5	155.4	0.50	0.86
S61	70.8	160.2	0.44	0.90
S62	75.7	163.7	0.46	0.89
S26	64.9	154.9	0.42	0.91
S28	79.5	155.4	0.51	0.86

on interior and the other type lies on the edges of the roof. In farwind as well as leeward non-Gaussian regions of monoslope roof, spectra seem to indicate a clear hump. In this particular case, Eq. (7.6) is required to fit the data efficiently. A typical example provided in Fig. 7.14
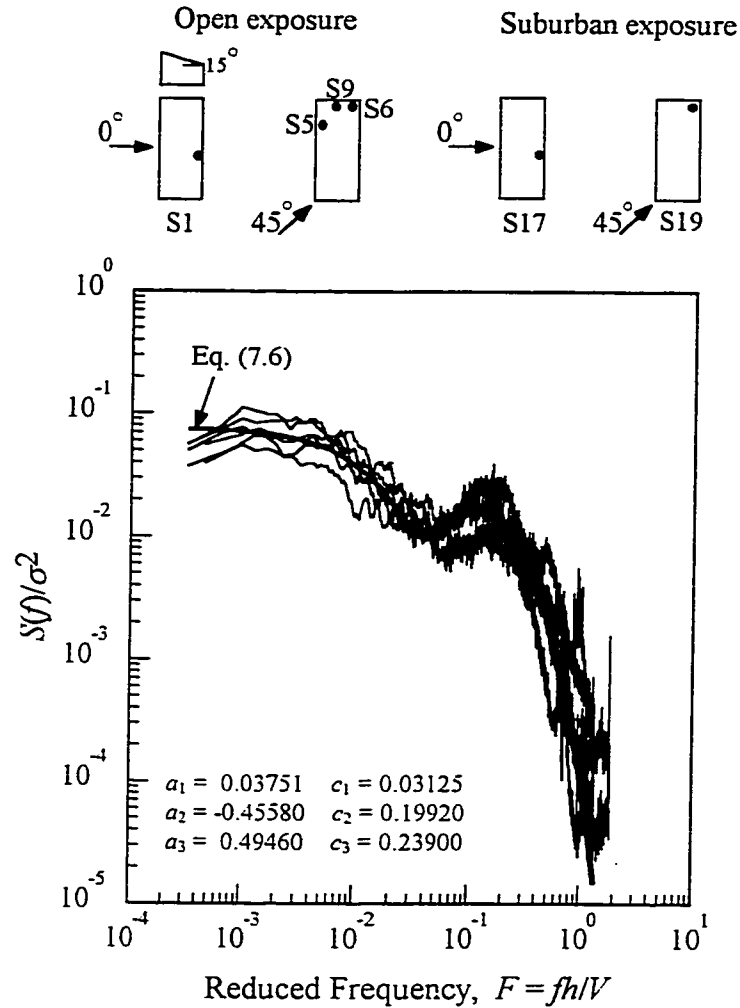
Fig. 7.14 Measured and fitted pressure spectra (monoslope roof, non-Gaussian zone).

shows several normalized spectra from the corresponding regions of monoslope roof ($\alpha \approx 15°$) and the fitted curve. In the case of gable roof ($\alpha \approx 19°$), the normalized spectra in Gaussian zone are found to be identical with those in Gaussian zone of flat roof; therefore, the same spectral parameters have been adopted. In the case of gable roof with roof angle 45°, the normalized spectra from various regions for various wind angles appear similar and therefore, a single representative spectrum is proposed.

The grouping of spectra has been carried out for various roof geometries. Results are summarized in Figs. 7.15, 7.16 and 7.17, where the standard SDF shapes associated with
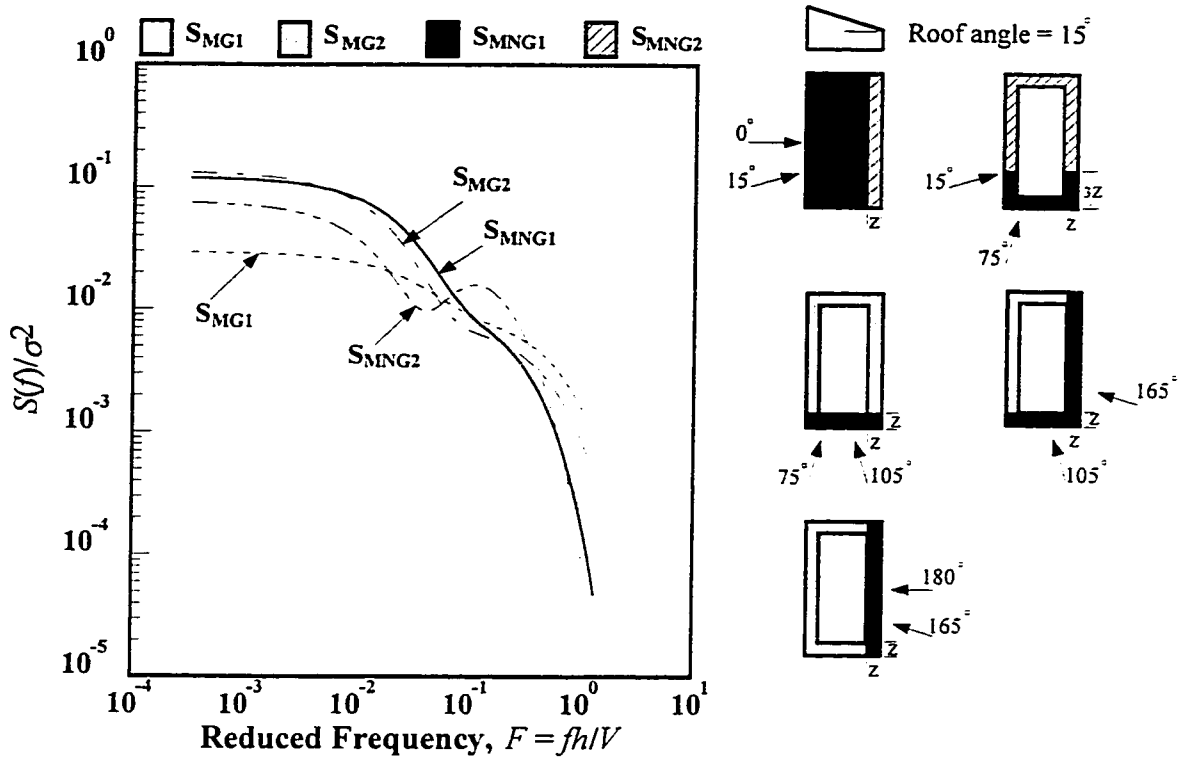
Fig. 7.15 Standard spectral shapes for monoslope roof.
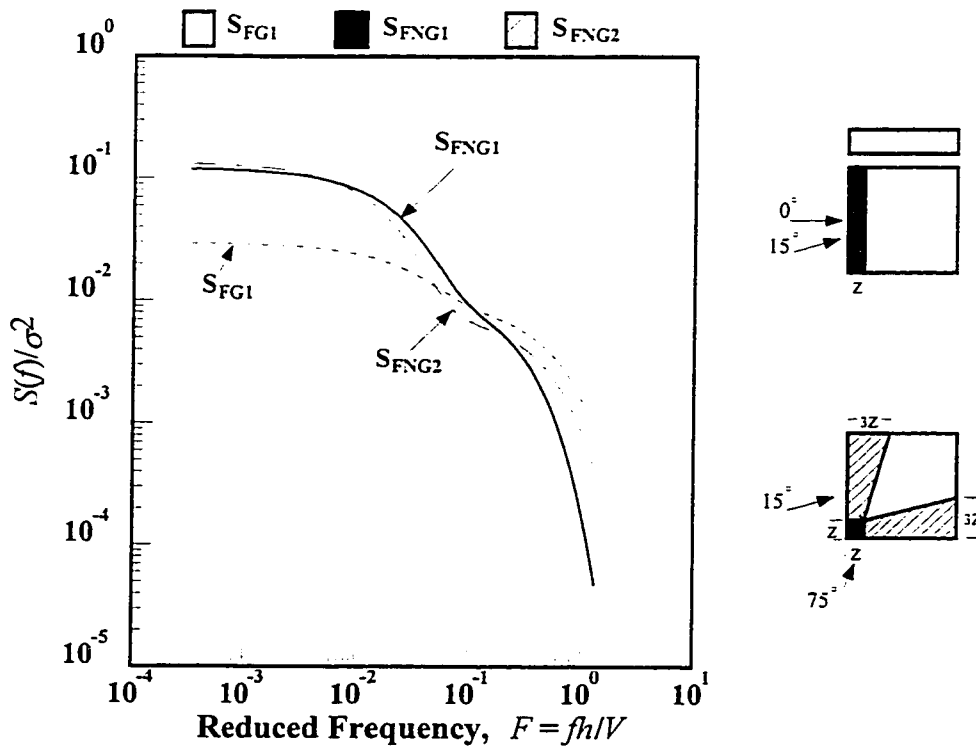
Fig. 7.16 Standard spectral shapes for flat roof.

159
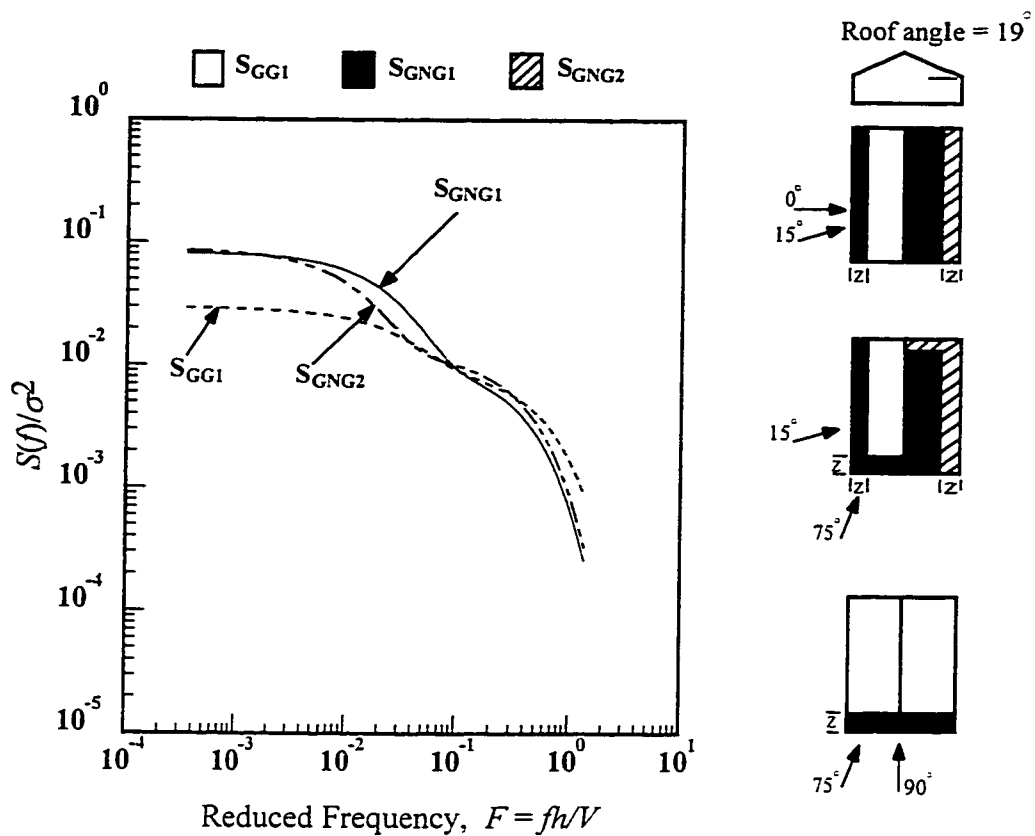
Fig. 7.17 Standard spectral shapes for gable roof.

different regions of the roofs are provided for various roof geometries. Each spectra is assigned a subscript where the first letter stands for the type of roof, G stands for Gaussian zone, NG stands for non-Gaussian zone and the number stands for the type of spectra in that zone. Since the normalized spectra found in Gaussian regions (S_{FG1}, S_{GG1}, S_{MG1}) are somewhat similar irrespective of the roof geometry, tap location, wind direction and terrain conditions, they have been averaged and fitted by the empirical expression. As a result, Figs. 7.15, 7.16 and 7.17 show identical spectra at the corresponding regions. The comparison between the first type of spectra observed on non-Gaussian regions (S_{FNG1}, S_{GNG1}, S_{MNG1}) among various roof geometries provided in Figs. 7.15, 7.16 and 7.17 respectively shows that their shapes are somewhat similar. However, there are variations among SDF shapes in the case of second

type of spectra observed on non-Gaussian regions among the various geometries tested. Data available may not be sufficient to group the spectra among various geometries; however, the provided SDF shapes can be used to establish actual spectra corresponding to a particular tap of a specific geometry by multiplying the appropriate SDF shape by the corresponding variance. Parameters of SDF shapes are provided in Table 7.6. Note that the position constant, a_2 corresponding to spectra from Gaussian regions is lower than that of spectra from non-Gaussian regions which reveals that the spectra from non-Gaussian regions are located above spectra from Gaussian regions in low frequency range. Similarly, the shape constants (c_1 and c_2) corresponding to spectra from Gaussian regions are lower than those of spectra from non-Gaussian regions; this shows that the dying out rate of spectra from Gaussian regions is

Table 7.6 Proposed spectral parameters.

	Parameters (x 10^{-2})					
	a_1	a_2	a_3	c_1	c_2	c_3
Monoslope Roof ($\alpha \approx 15°$)						
S_{MG1}	0.9756	1.9560		0.9725	16.5200	
S_{MG2}	0.8203	12.4900		1.2020	32.9600	
S_{MNG1}	1.2220	10.8000		2.2230	24.0400	
S_{MNG2}	3.7510	-45.5800	49.4600	3.1250	19.9200	23.9000
Flat Roof						
S_{FG1}	0.9756	1.9560		0.9725	16.5200	
S_{FNG1}	1.2070	11.6100		1.9770	30.1500	
S_{FNG2}	0.8162	12.0500		1.0840	38.2300	
Gable Roof ($\alpha \approx 19°$)						
S_{GG1}	0.9756	1.9560		0.9725	16.5200	
S_{GNG1}	1.0620	7.1800		1.4990	22.1600	
S_{GNG2}	1.2920	7.4560		1.4730	44.1200	
Gable Roof ($\alpha \approx 45°$)						
	2.4560	17.6900		4.1050	49.5300	

generally lower than that of spectra from non-Gaussian regions. The effects of such variations of parameters on SDF shapes is clear from Figs. 7.15, 7.16 and 7.17. The detailed results are provided in Appendix - C in the form of envelopes of the measured spectra along with fitted spectra for various roof zones for several roof geometries.

Though the results provided are based on limited measurements, it is believed that a large database of measurements in the future could improve the proposed zoning as well as the associated spectral parameters, and include spectral parameters for various other geometries.

7.5 SUMMARY

Spectra of wind pressures acting on low building roofs vary with respect to location, wind direction, roof geometry and terrain conditions. The results show that spectra have a low frequency concentration of energy for taps on windward roof regions, whilst they show a growth between certain frequencies for taps on the farwind and leeward roof regions. Based on the similarities between appropriately normalized spectra measured under different conditions, an empirical relationship between the normalized spectral amplitude and the frequency has been suggested for the generation of normalized spectra. Thereafter, normalized SDF's are classified based on whether the region of interest experience Gaussian or non-Gaussian fluctuations. Finally, the standard spectral shapes associated with various zones of each roof and their parameters are provided for the synthetic generation of spectra; this is useful in establishing Fourier amplitude part in the simulation of Gaussian and non-Gaussian wind pressure fluctuations on low building roofs.

162

CHAPTER 8
SIMULATION OF PRESSURE TIME SERIES ON LOW BUILDING ROOFS

"...In designing structural systems reliably, effects of adverse natural environments must often be considered....An exact deterministic prediction of the loads generated by these natural phenomena often requires precise global models of the atmosphere, the seas, and the ground motions. In this regard, many concurrent factors that render the exact physical modeling practically impossible must be considered. Thus, the designer is led to use either simplified deterministic representations or realizations of stochastic processes. In the latter case, the natural loads are described by means of stochastic processes whose characteristics such as probability densities and power spectra have been estimated from available data..."

P. D. Spanos and M. P. Mignolet, 1988.

This chapter presents schematic diagrams and brief descriptions of the overall simulation methodology for Gaussian and non-Gaussian pressure fluctuations. Further, a number of distinct simulation examples have been provided to demonstrate the efficiency and practicality of the proposed methodology in representing the wind pressure fluctuations on low building roofs.

8.1 OVERALL SIMULATION METHODOLOGY

It is necessary at this point to describe the overall simulation methodology and demonstrate its efficiency. Since the details of the proposed simulation methodology have been described at various occasions in Chapters 5, 6 and 7, the focus here is only on the overall methodology. First, the simulation of Gaussian pressure time series is discussed. The schematic of the simulation of Gaussian time series using a sample Gaussian time history (X_t) is shown in Fig. 8.1. Using this procedure, a number of samples of similar time series
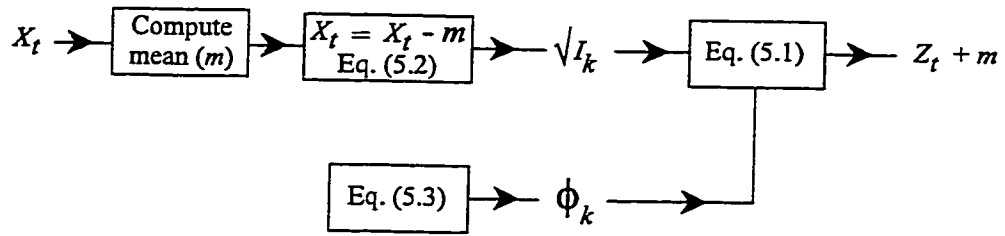
Fig. 8.1 Schematic of the simulation of Gaussian pressure time series using a sample time series.

having the same spectral density function, variance and mean can be generated. The MATLAB function **GTIME** (see Appendix - A) can be used to simulate realizations of Gaussian time series by providing a sample time series. The Gaussian time series samples can also be simulated by providing a power spectra of the fluctuations and the procedure is schematically shown in Fig. 8.2. The MATLAB function **GSPEC** (see Appendix - A) can be used for this simulation, in which the physical spectrum $(S_p(f_k))$ and mean (m) of the pressure fluctuations are provided as inputs. $S_p(f_k)$ can be either a measured spectrum or a synthetic spectrum. The previously established standard shapes of spectra for various zones of the roofs can be used to generate synthetic spectra with the help of variance of pressure fluctuations.
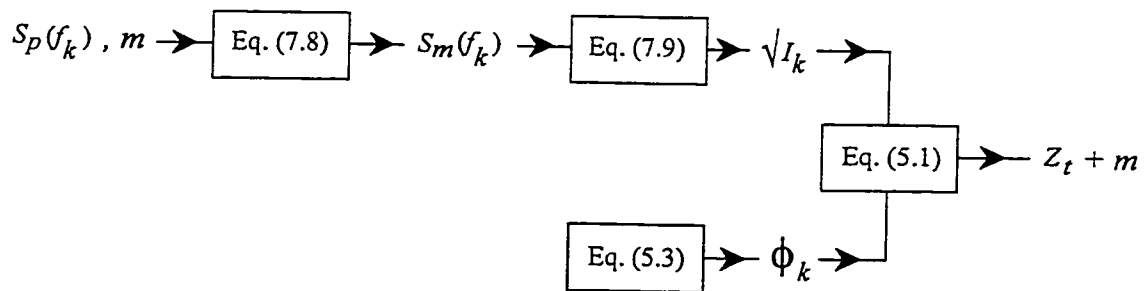
Fig. 8.2 Schematic of the simulation of Gaussian pressure time series using power spectra.

Contrary to the simulation of Gaussian fluctuations, the simulation methodology for non-Gaussian fluctuations provides the required emphasis on the generation of phase part of the

DFT which induces the non-normality in time series. Figure 8.3 shows a schematic of the simulation of non-Gaussian time series using a sample non-Gaussian time series. The estimation of parameter b, which induces the required skewness as well as kurtosis, is included in this sketch along with the simulation of time history. The MATLAB function **PAR_EST** can be used for parametric estimation, while **NGTIME** can be used for the simulation of non-Gaussian time series using a sample non-Gaussian time series (see
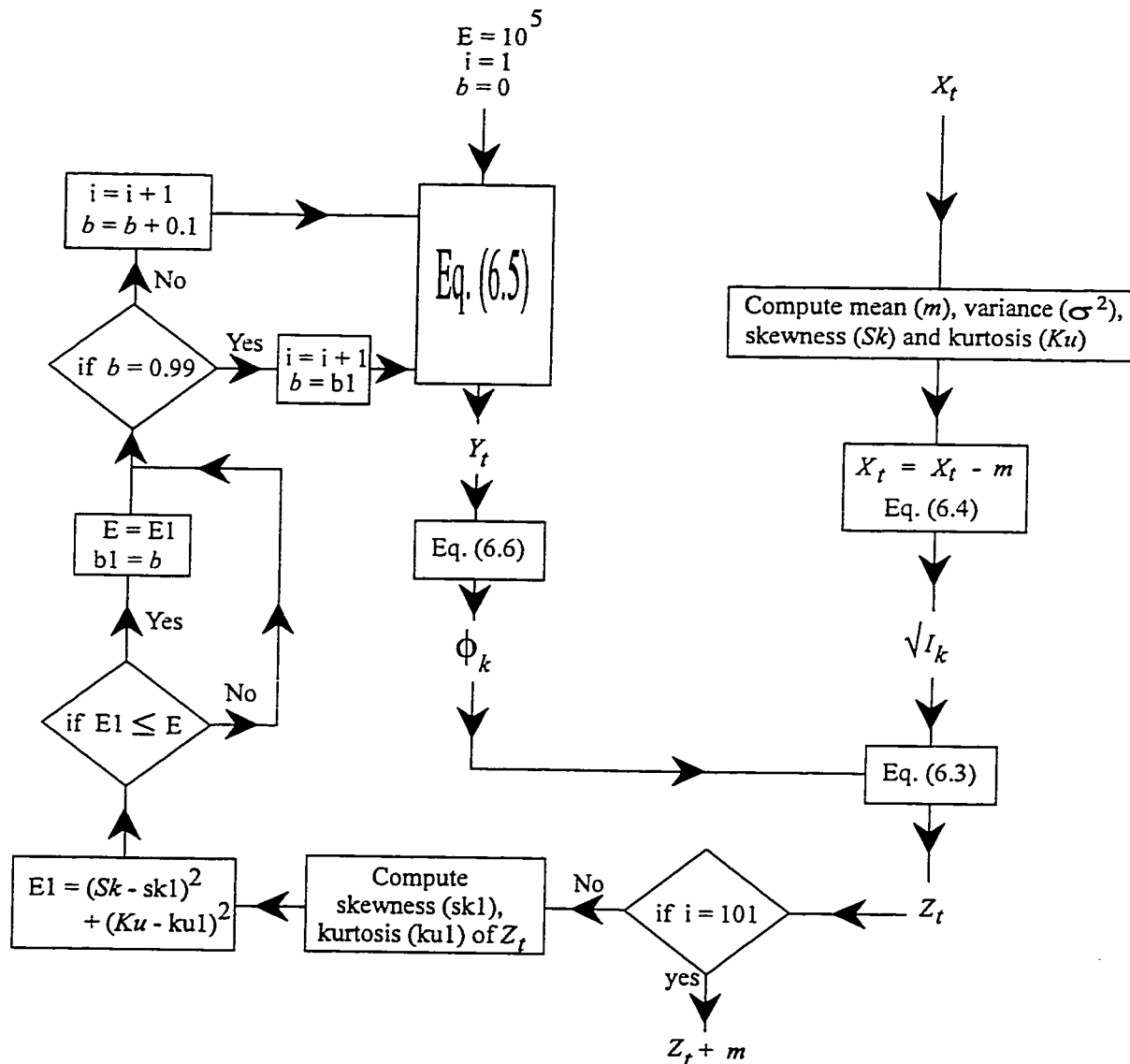
Fig. 8.3 Schematic of the simulation of non-Gaussian pressure time series using a sample time history.

165

Appendix - A). The details of the estimation of parameter b as well as simulation of non-Gaussian time series have already been presented in Chapter 6. The non-Gaussian time series can also be simulated by providing a physical spectrum ($S_p(f_k)$), mean (m), skewness (Sk) and kurtosis (Ku) of the pressure fluctuations to be achieved. Figure 8.4 shows the schematic of this simulation procedure. The generation of the phase part of the DFT is exactly the same as that of Fig. 8.3; the only difference is in the generation of amplitude
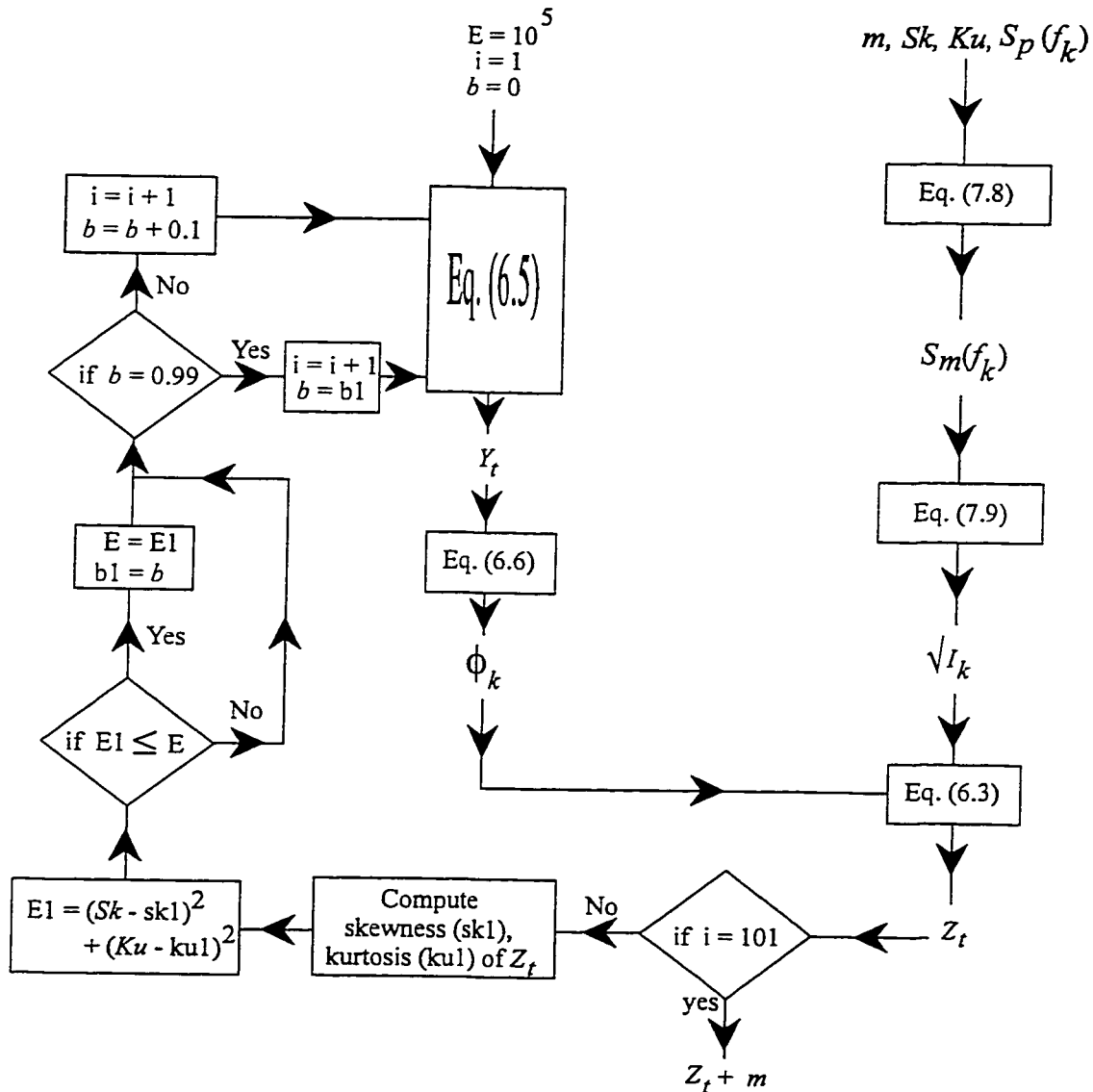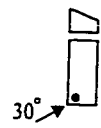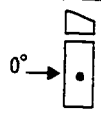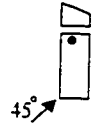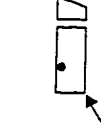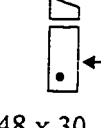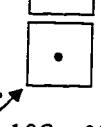
Fig. 8.4 Schematic of the simulation of non-Gaussian pressure time series using power spectra.

part of DFT. The MATLAB function **PAR_EST** can be used for parametric estimation, while **NGSPEC** can be used for the simulation of time history (see Appendix - A).

8.2 SIMULATION OF PRESSURE TIME HISTORIES
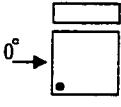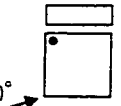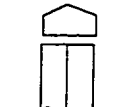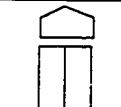
A number of distinct simulation examples are provided in this section in order to show the efficiency of the proposed simulation methodology using generalized parameters. Table 8.1 shows typical simulation results regarding the pressure fluctuations acting on low building roofs. Twelve distinct cases are provided with details. All the simulations have been carried out using the standard spectral shapes associated with the corresponding tap locations. The parameter b required for the simulation of non-Gaussian time series has been estimated based on the target skewness and kurtosis. The statistics (mean, variance, skewness and kurtosis) as well as peak (maximum suction) of the simulated and target signals are compared in Table 8.1. Note that the statistics of target and simulated signals are based on 16 records, while each peak value corresponds to the maximum suction of the corresponding 16 simulated or measured records. Results indicate the capability of the proposed methodology to represent the most pertinent statistics in a simple manner. Considering the sensitivity of the peak values compared to statistics, simulated and measured peak values are rather close. Furthermore, the corresponding target (T) and simulated (S) signals are shown in Fig. 8.5. In general, the target and simulated time series appear similar. Figure 8.6 displays the similarities between target (T) and simulated (S) PDFs; their deviation from Gaussian PDF is also shown. Overall, the proposed simulation methodology is promising; however, note the negligible discrepancies in some simulations

Table 8.1 Typical simulation results.

Sample	Geometry and Orientation l x b x h_l(mm), α	b	Spectra	Description	Target (T)	Simulated (S)
S2	30° 152 x 48 x 30, 15° Monoslope roof Open terrain	0.81	S_{MNG1}	mean variance skewness kurtosis peak	-1.75 0.19 -1.31 7.21 -6.76	-1.75 0.19 -1.43 7.36 -6.74
S3	0° 152 x 48 x 30, 15° Monoslope roof Open terrain	0.59	S_{MNG1}	mean variance skewness kurtosis peak	-0.95 0.05 -0.82 4.67 -2.90	-0.95 0.05 -0.93 4.84 -2.81
S9	45° 152 x 48 x 30, 15° Monoslope roof Open terrain	0.56	S_{MNG2}	mean variance skewness kurtosis peak	-1.07 0.13 -1.05 4.95 -3.85	-1.07 0.13 -1.12 5.38 -4.10
S12	120° 152 x 48 x 30, 15° Monoslope roof Open terrain		S_{MG2}	mean variance skewness kurtosis peak	-0.65 0.01 -0.07 3.03 -1.19	-0.65 0.01 -0.01 3.01 -1.07
S49	180° 152 x 48 x 30, 15° Monoslope roof Open terrain		S_{MG1}	mean variance skewness kurtosis peak	-0.38 0.02 -0.01 3.04 -1.16	-0.38 0.02 -0.00 3.01 -1.01
S60	45° 108 x 108 x 37.5 Flat roof Open terrain		S_{FG1}	mean variance skewness kurtosis peak	-0.47 0.02 -0.01 3.00 -1.10	-0.47 0.02 -0.00 3.01 -1.10

Note: l = length, b = width, h_l = lower eave height, α = roof angle, b = model parameter

Table 8.1 Continued.

Sample	Geometry and Orientation l x b x h$_l$(mm), α	b	Spectra	Description	Target (T)	Simulated (S)
S29	108 x 108 x 37.5 Flat roof Suburban terrain	0.48	S$_{FNG1}$	mean variance skewness kurtosis peak	-1.78 0.31 -0.83 4.20 -5.79	-1.78 0.31 -0.87 4.64 -6.17
S27	108 x 108 x 37.5 Flat roof Suburban terrain	0.41	S$_{FNG2}$	mean variance skewness kurtosis peak	-0.51 0.04 -0.74 5.48 -2.85	-0.51 0.04 -1.05 5.42 -2.27
S56	108 x 108 x 37.5 Flat roof Open terrain	0.0	S$_{FNG2}$	mean variance skewness kurtosis peak	-1.22 0.13 -0.93 4.69 -4.00	-1.22 0.13 -0.89 4.85 -4.11
S37	152 x 98 x 30, 19° Gable roof Suburban terrain	0.63	S$_{GNG1}$	mean variance skewness kurtosis peak	-0.38 0.16 -1.06 6.35 -3.66	-0.38 0.16 -1.31 6.56 -4.54
S75	152 x 98 x 30, 19° Gable roof Open terrain	0.13	S$_{GNG2}$	mean variance skewness kurtosis peak	-1.19 0.10 -0.83 4.18 -3.64	-1.19 0.10 -0.94 4.96 -3.92
S78	152 x 98 x 30, 19° Gable roof Open terrain		S$_{GG1}$	mean variance skewness kurtosis peak	-0.31 0.03 -0.07 3.32 -1.27	-0.31 0.03 -0.00 3.01 -1.08

Note: l = length, b = width, h$_l$ = lower eave height, α = roof angle, b = model parameter

169
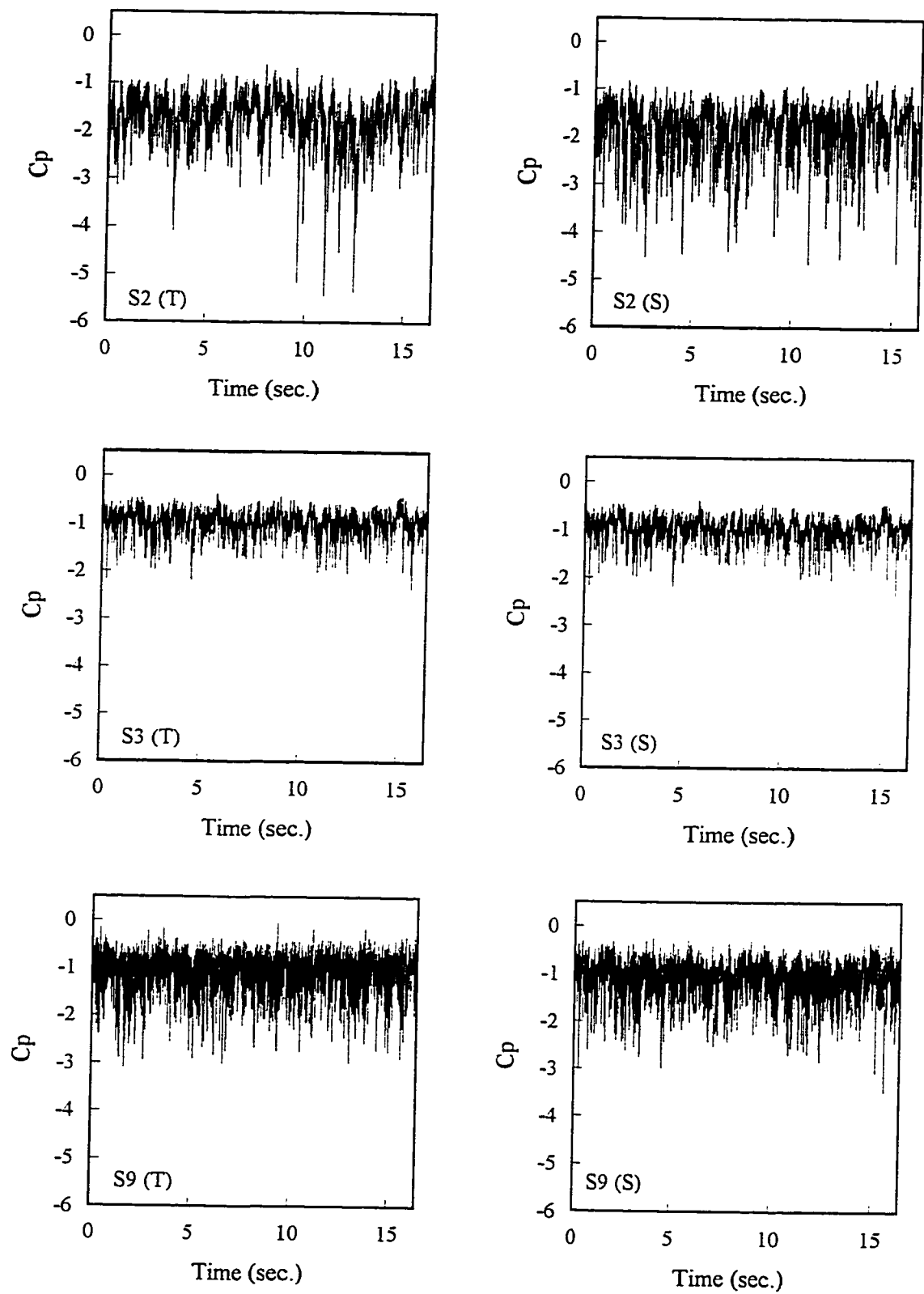
Fig. 8.5 Target and simulated pressure time histories (cases - Table 8.1).

170

Fig. 8.5 Continued.

171

Fig. 8.5 Continued.

172

Fig. 8.5 Continued.

173
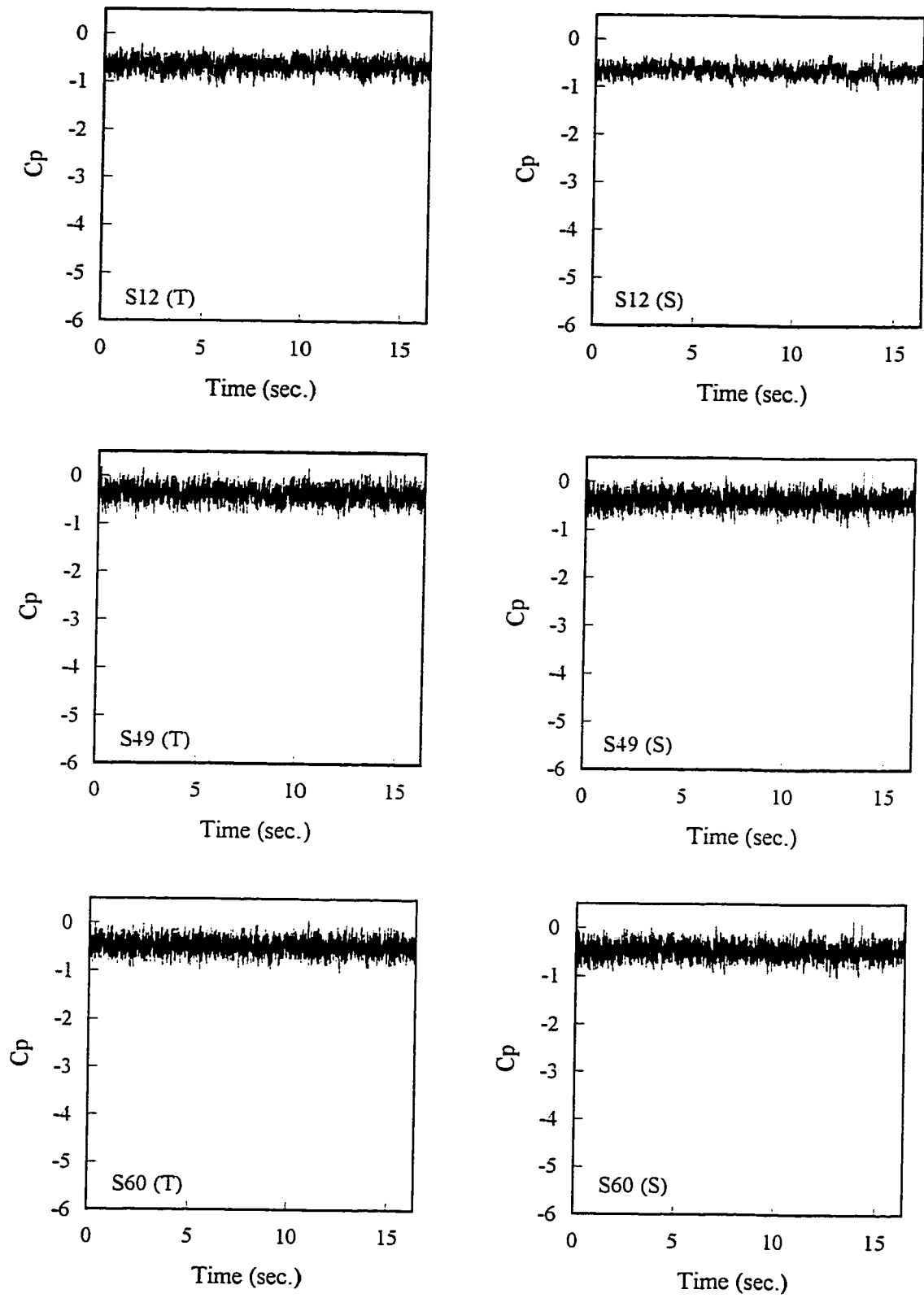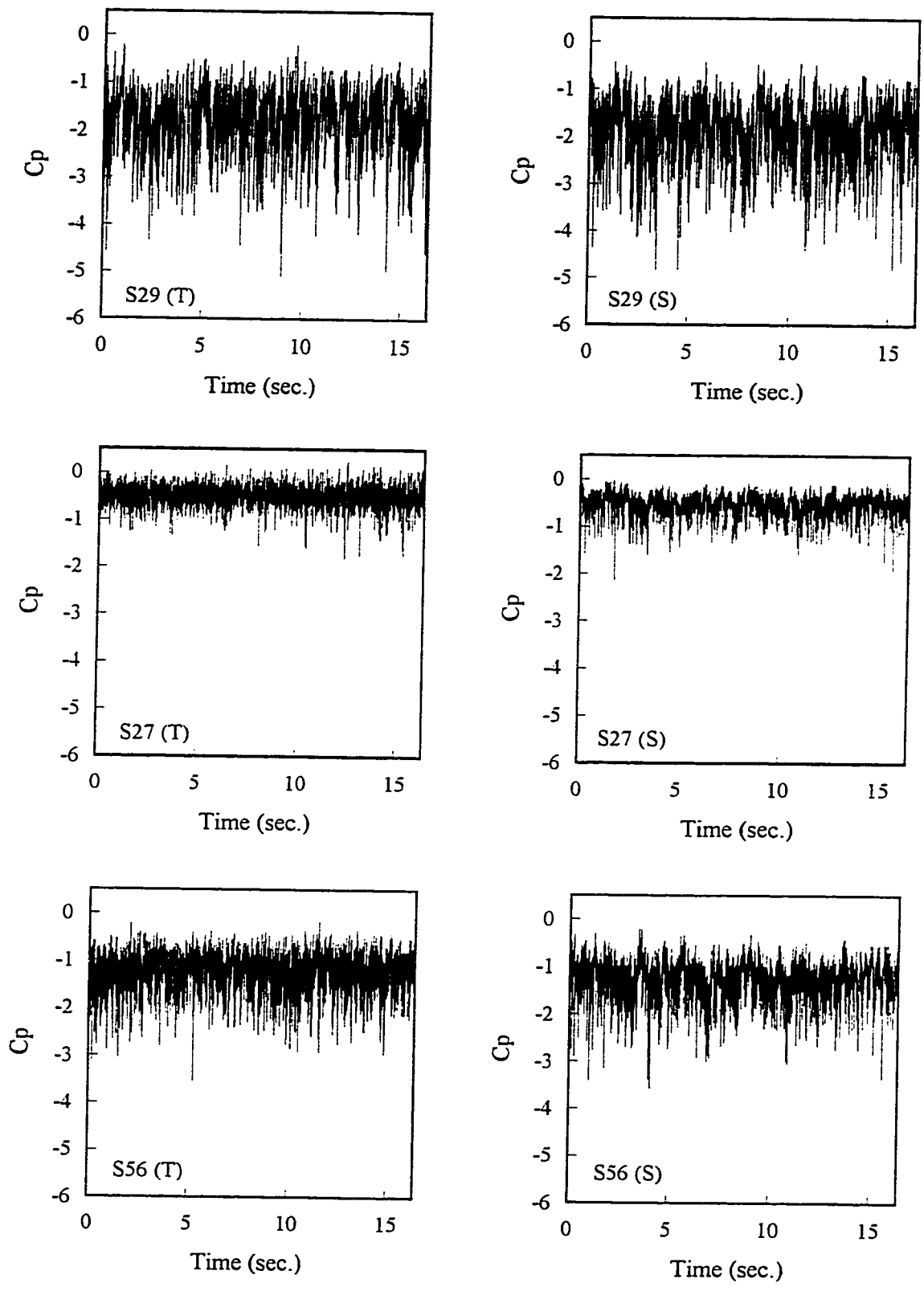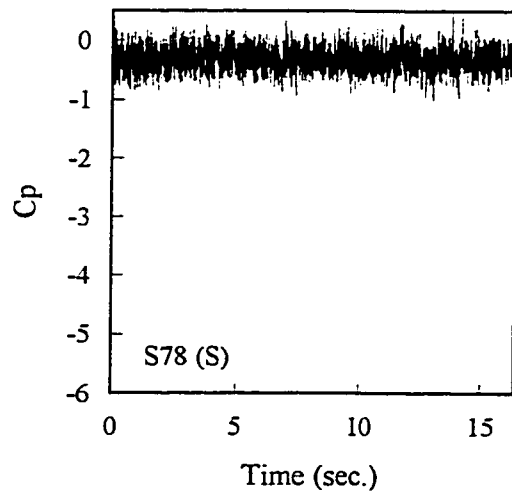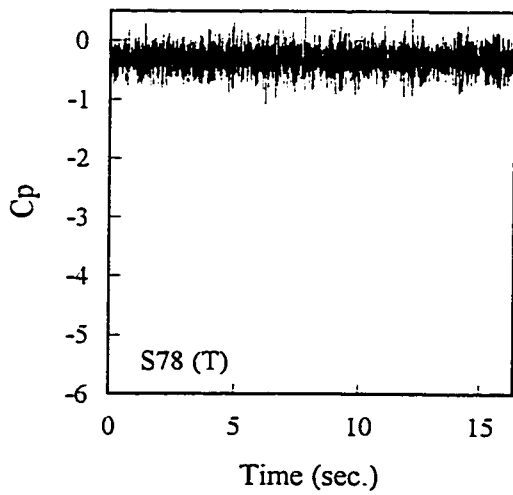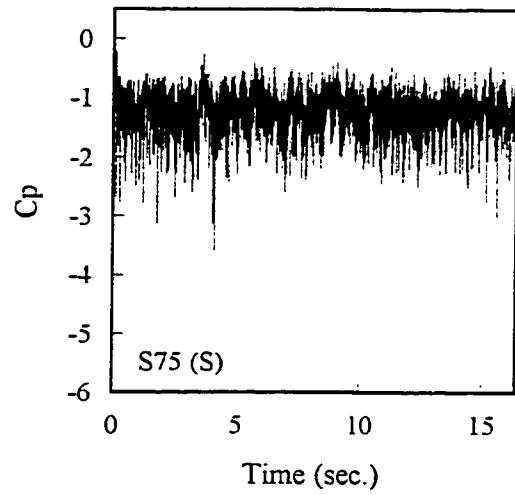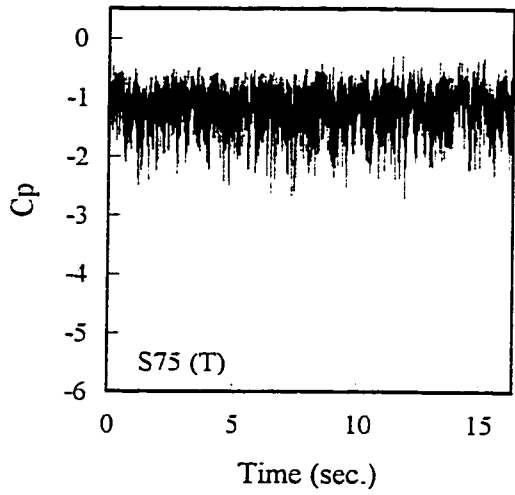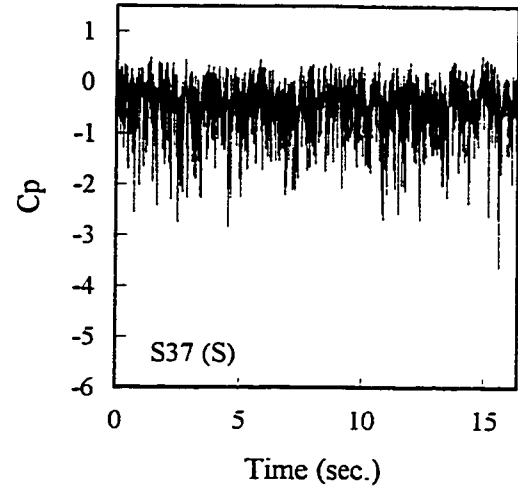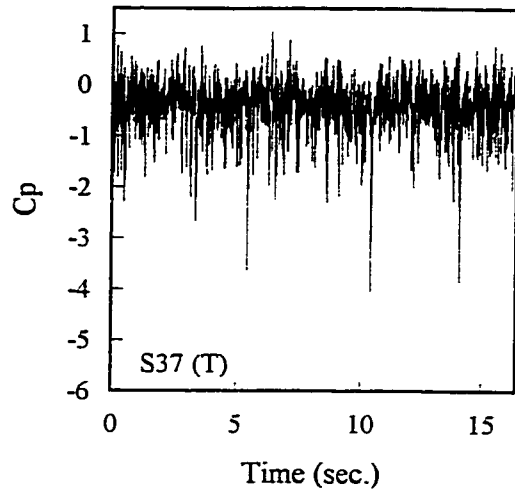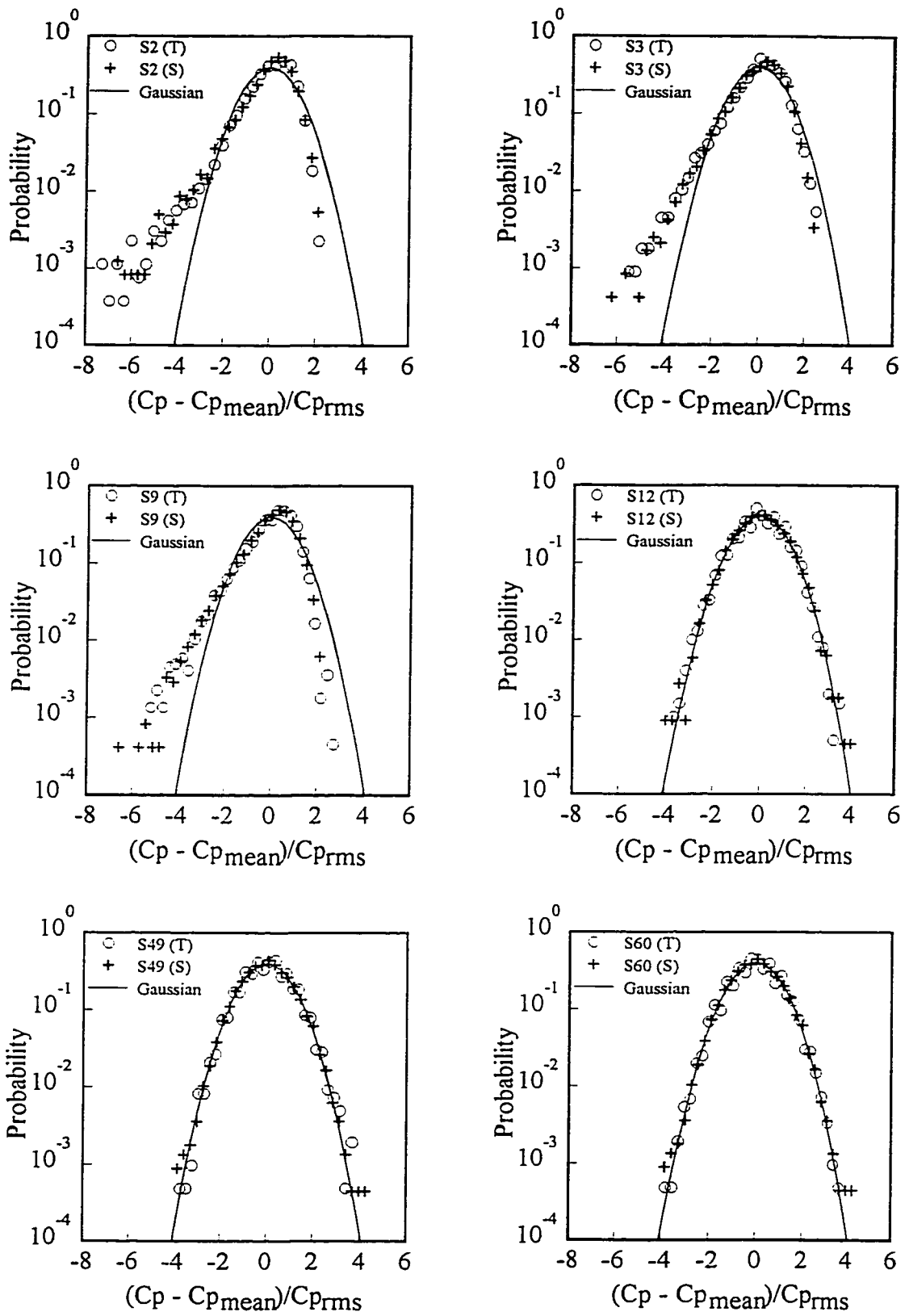
Fig. 8.6 PDFs of target and simulated pressure time histories (cases - Table 8.1).

Fig. 8.6 Continued.

175
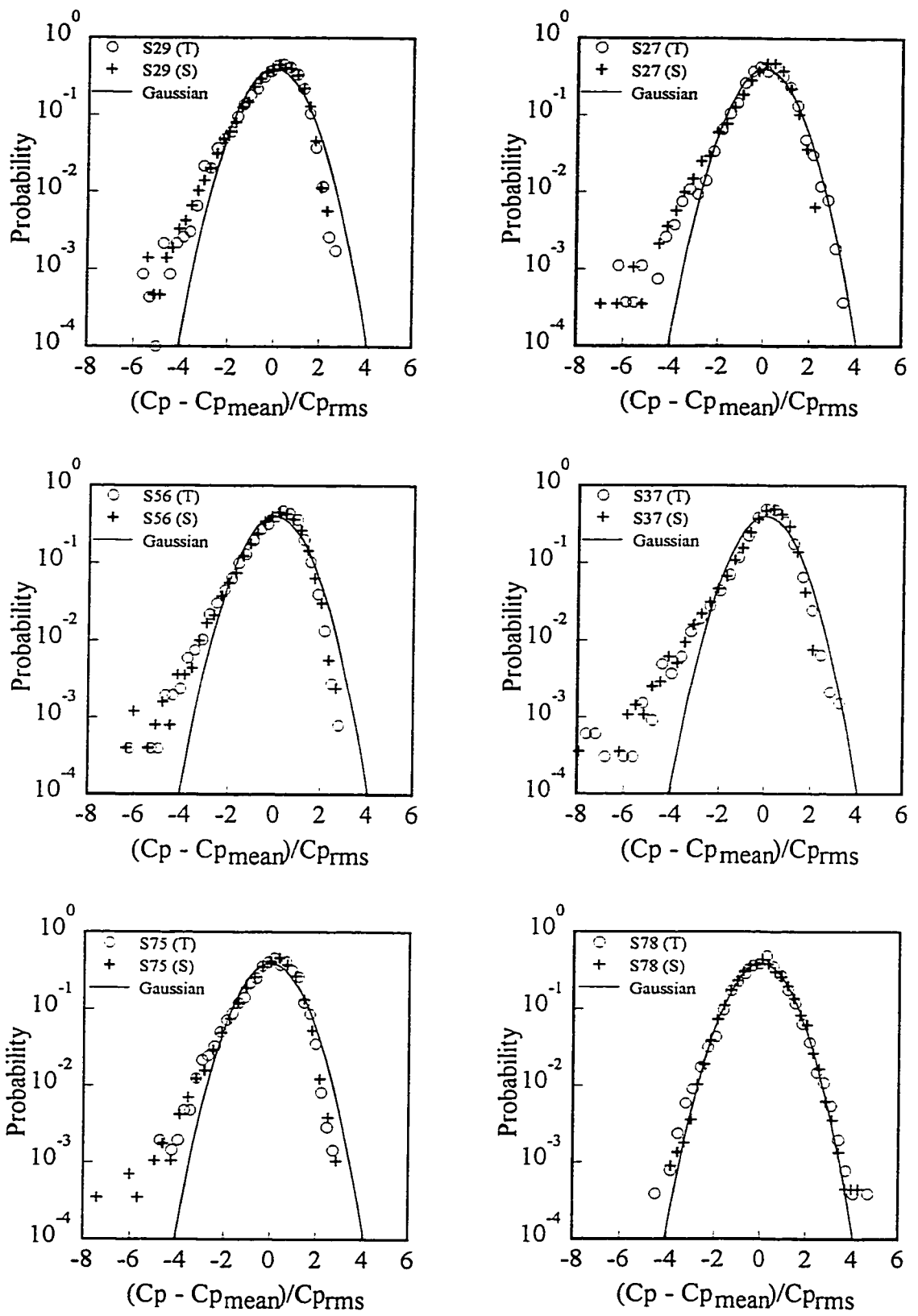
in terms of difference in statistics, time series and PDF's. These are possibly due to (1) the difference in spectra between the target (spectra at a particular location) and the simulated (generalized spectra of that roof zone) and (2) the difference in statistics of random number sets in subsequent simulations.

8.3 GENERAL COMMENTS

In these demonstrations, the statistics (mean, variance, skewness and kurtosis) of the time series are known from wind tunnel experiments. However, in practice some of these statistics can be obtained from literature. For instance, the values of mean and variance of pressure fluctuations on different locations of common roof geometries for various conditions can be obtained from past studies. On the other hand, the skewness and kurtosis values of pressure fluctuations are seldom known; however, these values can be established by conducting wind tunnel measurements. Once the mean, variance, skewness, and kurtosis of pressure fluctuations acting on a particular roof location are known, the desired time series at specific locations can be generated with the help of standard spectral shapes provided in this study. Furthermore, this methodology can be integrated with the wind tunnel experiments to develop an automated pressure generating system without the need of sophisticated expensive instrumentation.

CHAPTER 9
POTENTIAL APPLICATIONS OF THE PROPOSED SIMULATION

"...Experience suggests that unserviceability due to repeated loading effects is a more likely occurrence than unserviceability or collapse from the single application of an exceptionally large load. The action of repeated loading by wind can cause a variety of forms of structural unserviceability. The first of these is fatigue damage..."

A. G. Davenport, 1968.

This chapter presents potential applications of the proposed simulation methodology in low building roof design. The developed simulation methodology can be used to derive the desired number of peaks necessary to carry out an extreme value analysis. This analysis results in producing peak pressure coefficients versus probability of exceedance, i.e. design risk level. Such representation which is important for reliability-based design, is currently lacking in most codes of practice. The methodology can also be used to generate time histories necessary to carry out fatigue analysis either analytically or experimentally; this is elaborated in this chapter.

9.1 EXTREME VALUE ANALYSIS

The peak values (extremes) observed in pressure time histories are important for the design of building components. They vary from sample to sample. However, this random variation of peak values can be quantified statistically by constructing either a PDF of the pressure

177

signal or PDF of the extremes from different samples. The PDF of the pressure signal, called parent distribution, needs a large sample for its construction. The main drawback of the parent distribution is the lack of a microscopic view of the data and, as a result, the tails of the distribution are the most poorly defined parts (Siddall 1983). On the other hand, the PDF of the peak values focuses only on the extremes. This approach shows a magnified view of the extremes compared to parent distribution. Following the results of several studies, Type-I distribution is widely accepted in wind engineering as the PDF of extremes (Peterka 1981).

The proposed simulation methodology can be used to conduct extreme value analysis. Long time histories of data can be simulated in order to derive several peaks necessary to carry out this analysis. Finally, the peak pressure coefficients can be plotted with a specified risk level, i.e. probability of exceedance. Since there is no adequate information provided in the wind codes for reliability-based design of buildings, such results will indeed be quite useful and can be suggested for codification. The efficiency of the present methodology in the prediction of peaks has already been noted in many cases; however, an extensive comparison has been provided in this section.

The simulation examples provided in section 8.2 have been revisited here. The simulation of time histories has been carried out using the proposed methodology with the help of generalized spectra from the corresponding zones as explained in section 8.2. Figure 9.1 shows peak pressure coefficients (Cp_{peak}) for various cases. In the analysis, simulated peak pressure (suction) coefficients have been obtained as follows: 16 records of 8192 values each were simulated and the peak value from each record was selected and plotted against the relevant risk level; measured data was also obtained in the same format. The probability

178
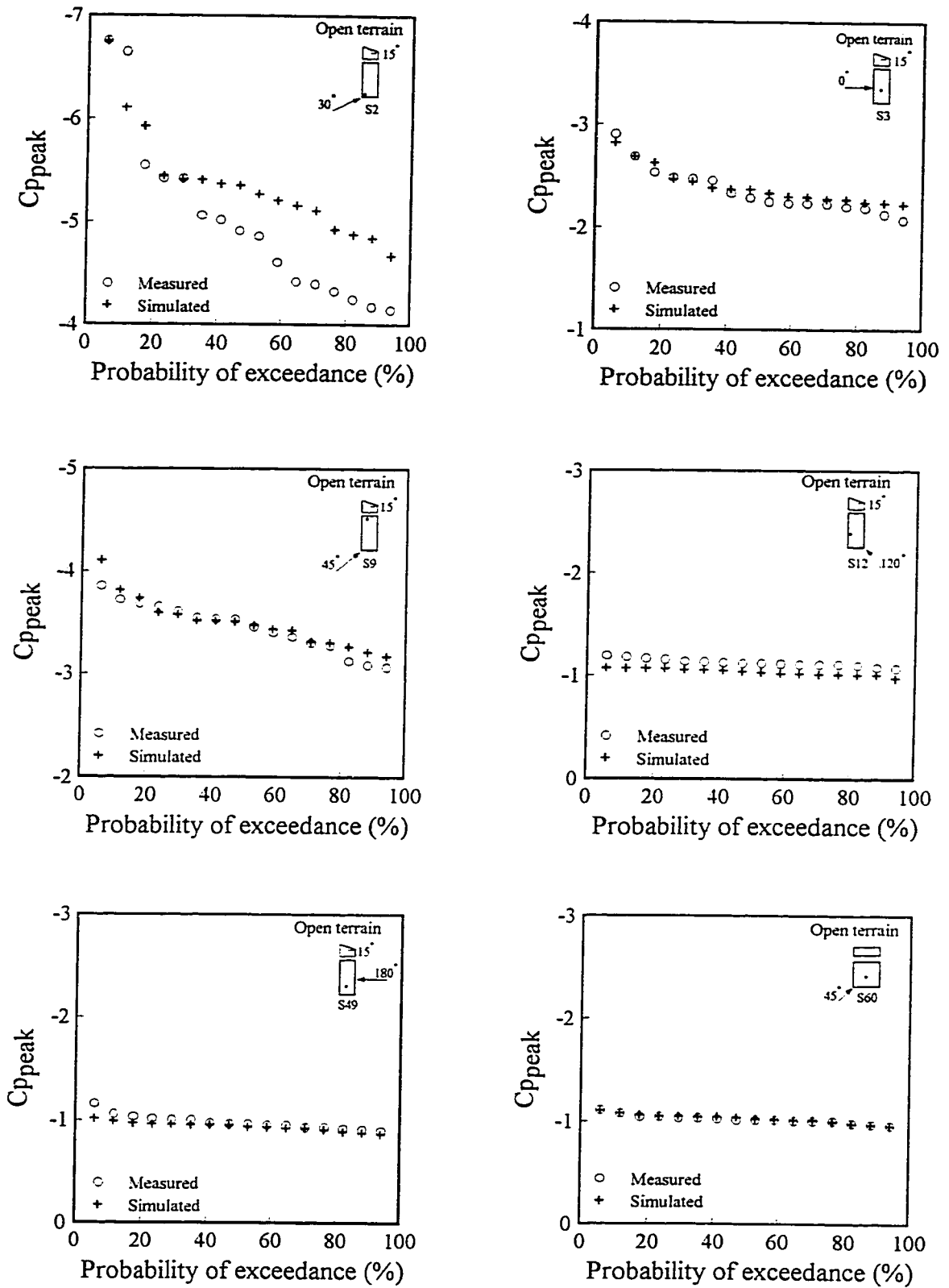
Fig. 9.1 Extreme values of pressure coefficients, Cppeak, for cases shown in Table 8.1.
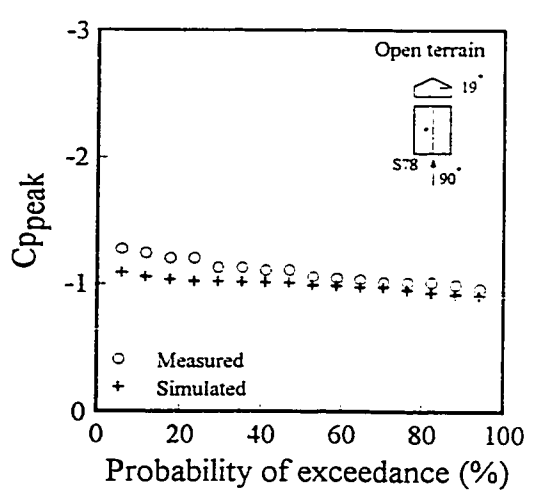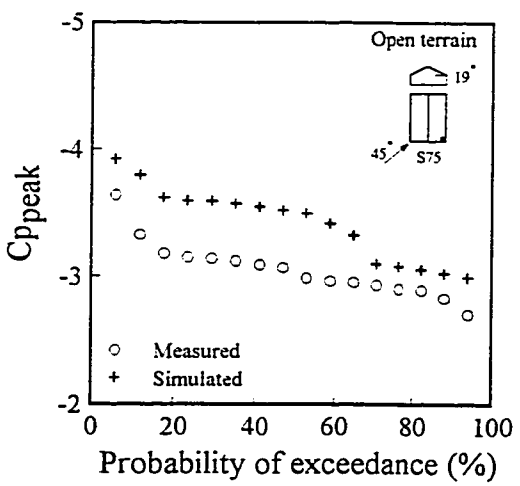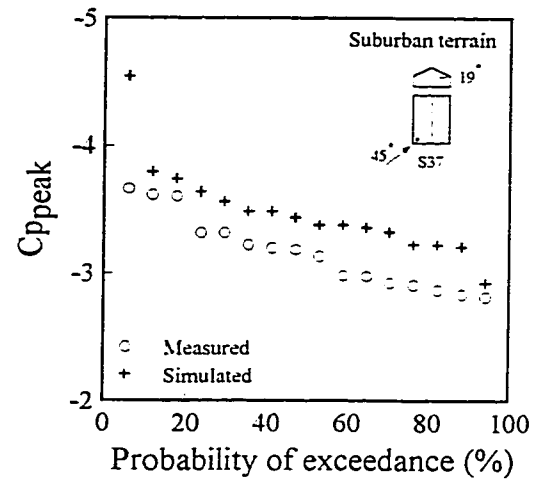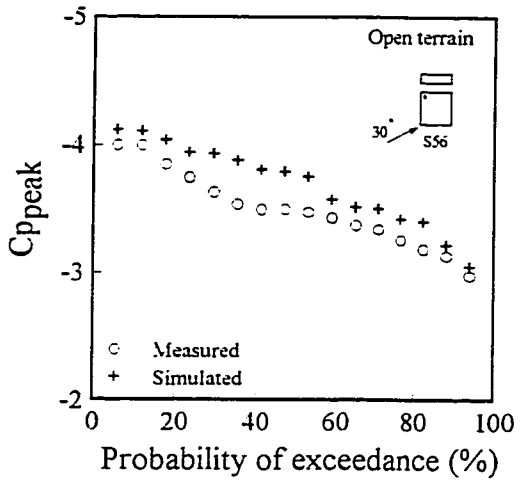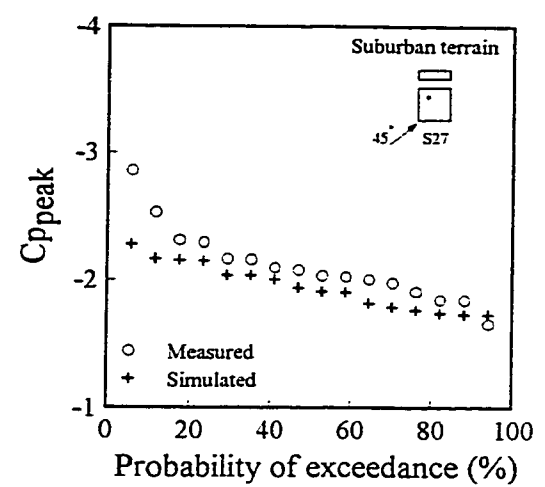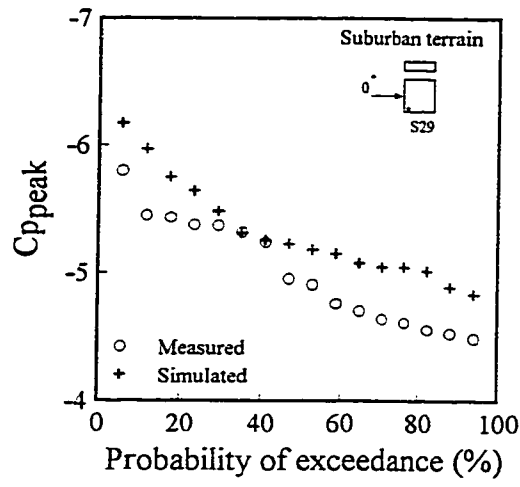
Fig. 9.1 Continued.

of exceedance (risk level) of each peak value has been evaluated using Eq. (3.35) - see section 3.2.3.1 for details. The comparison shows that the simulated suction peaks are somewhat closer to the measured values. However, differences up to ±20% have been found in some cases. This discrepancy is possibly due to (1) the difference in spectra between the target (spectra at a particular location) and simulated (generalized spectra of that roof zone) and (2) the difference in statistics of random number sets in subsequent simulations. Considering these issues, the comparison of peaks is satisfactory; the small differences observed in some cases can be tolerated for practical applications. Diagrams such as that of Fig. 9.1 can be used to establish design-pressure coefficients according to any desirable risk level, presumably consistent with reliability-based design.

9.2 FATIGUE ANALYSIS

9.2.1 Background

Low buildings have generally been designed for static wind loading. However, the failure at relatively low wind speeds of building components, which are actually rated to sustain high wind speeds by static design, has received wider attention more recently. Fatigue due to repetitive sequences of high pressure fluctuations has been identified as the main reason for the extensive damage to building components in many violent storms (Walker 1975; *Assessment of damage*..... 1993). For the first time, DABM (1976) incorporated provisions for proof-testing of roof systems against wind-induced fatigue based on the subsequent field investigations and laboratory tests carried out after the severe damage caused by the cyclone

Tracy in Darwin, Australia (Walker 1975). Thereafter, a series of investigations by Morgan and Beck (1977), Melbourne (1977), and many others led to the development of new recommendations such as TR440 (1978), AS 1170.2 (1989) etc. where wind-induced load cycle distributions are proposed for cyclone prone areas. While, British (Cook 1990) and German (Gerhardt and Kramer 1986) recommendations proposed load cycle distributions for temperate climatic regions where the predominant source of high wind speeds is large-scale and frequently occurring non-tropical cyclone systems. Despite the allowance provided in some codes and standards for proof-testing of building components against wind-induced fatigue, damages during storms are still common. This shows the need for further investigation in this area.

In the past two decades, several researchers have investigated wind-induced fatigue using either wind tunnel or full-scale measurements - see Xu (1993). More recently, Xu (1993) and Letchford and Norville (1994) investigated wind-induced fatigue of roof cladding using measured pressure fluctuations on a full-scale building. Regarding analytical studies, Davenport (1966) proposed a method to estimate wind-induced fatigue damage by assuming the wind loading as a broadband Gaussian process. Later, Lynn and Stathopoulos (1985) improved the predictions by including the effect of non-normality by using a mixed Gaussian-Weibull extremum model. The suggested model to evaluate the mean life time ($\bar{T}$) is,

$$\bar{T} = \left[\int_0^\infty \frac{N_p(g)dg}{N(g)} \right]^{-1} \tag{9.1}$$

in which $N_p(g)dg$ is the number of maxima per unit time with magnitudes between g

182

and $g + dg$; and $N(g)$ is the required number of cycles to failure at level g. The suggested

model for the rate of maxima ($N_p(g)$) is

$$N_p(g) \;=\; \sqrt{2\pi}\, N_0 \exp\!\left\{-\left[\frac{g}{c}\right]^k\right\} \left\{\frac{k(k-1)}{c^2}\left[\frac{g}{c}\right]^{k-2} - \left[\frac{k}{c}\right]^2\left[\frac{g}{c}\right]^{2k-2}\right\} \tag{9.2}$$

when the dimensionless peak factor (g) is greater than 2.5; the approximate range of

Weibull parameters c and k was provided by Stathopoulos (1980). In case of g less than or

equal to 2.5, the rate of maxima corresponding to Gaussian process, Eq. (3.28), has been

used. N_0 is the cycling rate which represents the rate at which pressure exceeds the mean

value. Both Eqs. (3.28) and (9.2) are based on the assumption that the process is broad-

banded. In case of narrowband Gaussian process, the rate of maxima $N_p(g)$ can be

estimated using the familiar Rayleigh form (Nigam 1983):

$$N_p(g) \;=\; N_0\, g \exp\!\left(\frac{-g^2}{2}\right) \tag{9.3}$$

Later, Winterstein (1988) derived Hermite moment models to predict fatigue damage rates;

these models use moments (skewness and kurtosis) to form non-Gaussian contributions.

The developed ratio of actual non-Gaussian to Gaussian damage rate is

$$\gamma \;=\; \frac{E[D_{ng}]}{E[D_g]} \;=\; \left(\frac{\sqrt{\pi}\,M}{2\,V_R!}\right)^{m_1} \frac{(m_1\,V_R)!}{\left(\frac{m_1}{2}\right)!} \tag{9.4}$$

where,

$$V_R \;=\; \sqrt{\frac{4(1+h_4+\tilde{h}_4)-\pi}{\pi}}$$

$$M = (1 + 2\tilde{h}_3^2 + 6\tilde{h}_4^2)^{-1/2}$$

$$h_4 = \frac{Ku - 3}{24}$$

$$\tilde{h}_4 = \frac{\sqrt{1 + 1.5(Ku - 3)} - 1}{18}$$

$$\tilde{h}_3 = \frac{Sk}{4 + 2\sqrt{1 + 1.5(Ku - 3)}}$$

where, Sk and Ku represent skewness and kurtosis values of the time series and m_1 corresponds to the slope of the S-N curve of the material under consideration. The three inputs required to compute Eq. (9.4) are Sk, Ku and m_1. This model is based on the assumption that the process is narrow-banded; however, according to Winterstein (1988), the damage ratio is not affected much by the bandwidth effects and therefore, is usually conservative with respect to the rainflow counting assumption.

Recently, analytical models have been incorporated into computer programs to simulate fatigue behaviour of roof cladding during the passage of a tropical cyclone (Jancauskas et al. 1994). This approach included a number of tasks such as deriving the time history of wind speed and direction for a design cyclone event of five hour duration, integration with wind tunnel data and calculation of fatigue damage. Mahendran (1994) applied a different treatment for the simulation of cyclonic wind forces on roof cladding by providing a random block loading, which is more realistic than the usual cyclic loading, based on fatigue wind loading matrices obtained from wind tunnel testing and computer modelling. Further, Mahendran (1995) suggested a new fatigue loading sequence for codification after considering the wind speed as well as wind direction variation during a tropical cyclone.

Note that the previously suggested analytical models such as Eqs. (3.28), (9.2), (9.3) and (9.4), which were derived based on linear random vibration theory, represent the number of cycles present in a time history. Unfortunately, these models cannot reproduce the effects of spikes, sequences etc. present in actual time history. Furthermore, these analytical models are based on the peak cycle counting method; this method is not suited for counting cycles in the case of wind pressure fluctuations on low building roofs that are broad-banded and non-Gaussian. Therefore, it appears that time history of loading and more accurate cycle counting method are required for the meaningful prediction of wind-induced fatigue.

Several studies in the past showed that it is reasonable to assume that pressure fluctuations on building envelopes are stationary random processes. Therefore, the theory of stochastic processes can be used to quantify such loadings. For instance, the power spectra of the pressure fluctuations may help in the simulation of representative sample time histories. Thereafter, an appropriate cycle counting technique such as the rainflow algorithm, and a damage accumulation hypothesis such as Miner's rule can be used to obtain fatigue life estimates (Fuchs and Stephens 1980; Osgood 1982). Goodman's method can be employed to approximately account for the effect of mean load; however, the conventional damage hypothesis cannot take into account the sequence effects present in actual wind pressure fluctuations. As a matter of fact, the simulated wind pressure fluctuations can be applied directly on a roof with the help of facilities like BRERWULF (Cook et al. 1988) in order to represent the actual effects of wind pressure fluctuations on cladding elements.

Though the above mentioned procedure is simple, it may have a number of limitations which must be addressed before it can successfully be used. For instance, the conventional simulation of a time history based on power spectra assumes that the process is Gaussian.

However, both Gaussian and non-Gaussian wind pressures have been observed depending on roof point location and wind direction; mostly, non-Gaussian wind pressures are observed on corner zones as well as on other separated flow regions as previously noted in Chapter 4. Therefore, the new simulation scheme which can generate both Gaussian as well as non-Gaussian pressure fluctuations (Suresh Kumar and Stathopoulos 1996a, 1997b) and whose efficiency has been verified for a number of cases can be used. The evaluation of fatigue life estimates using this simulation scheme has been first attempted in the framework of the present study.

The main objective of this section is therefore to address the application of the simulated pressure fluctuations in predicting the fatigue behaviour of roof cladding using rainflow algorithm, Miner's rule and Goodman's method. The rate of fatigue damage accumulation both under Gaussian and non-Gaussian wind pressure loadings has been investigated. Furthermore, the long-term wind climate was integrated with the simulated fatigue characteristics of roof pressures to evaluate total fatigue loading on roof cladding of low buildings located in temperate regions. Simulated results were compared with existing models such as Rayleigh, Gaussian and Weibull extremum models in terms of fatigue mean life time, while they were compared with the German and British recommendations in terms of cycles of fluctuating pressures for fatigue design. A few preliminary results were reported in Suresh Kumar and Stathopoulos (1996b, 1997d).

9.2.2 Methodology
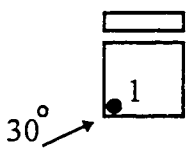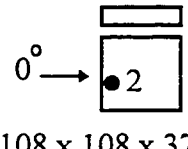
9.2.2.1 Simulation of pressure fluctuations

Time histories of Gaussian and non-Gaussian local roof pressures can be generated with the help of discrete Fourier transform equation as described in Chapters 5, 6, 7 and 8. Fourier

amplitude as well as phase are required for this simulation. The Fourier amplitude can easily be constructed from power spectra of the pressure fluctuations. A simple stochastic model with a single parameter b, inducing non-normality in time series has been suggested for the simulation of phase. In the case of Gaussian wind pressure fluctuations, phase is represented by independent identically distributed uniform random numbers ranging from $-\pi$ to π. Many successful simulations have been performed at various locations of the roof by using synthetic spectra derived from several wind tunnel measurements. The same procedure has been adopted in this study to simulate wind pressure fluctuations on roof cladding for fatigue evaluation.

Fatigue characteristics of pressure fluctuations have been investigated at few locations over flat and monoslope roof buildings although only two representative examples have been provided in this thesis. Pressure taps have been selected in zones of very high energetic fatigue loading of a 15 m high flat roof building and the simulation details are provided in Table 9.1. Statistics of the simulated fluctuations provided in Table 9.1 show that both

Table 9.1 Simulation details of time series.

Sample	Geometry and Orientation l x b x h₁ (mm)	b	Spectra	Description	Simulated
S50	30° 108 x 108 x 37.5 Flat roof, Open terrain	0.84	S_{FNG1}	mean variance skewness kurtosis	-0.80 0.28 -1.86 9.57
S64	0° 108 x 108 x 37.5 Flat roof, Open terrain	0.54	S_{FNG1}	mean variance skewness kurtosis	-1.47 0.14 -0.85 4.46

187

samples are non-Gaussian and sample S50 is highly non-Gaussian compared to S64. The importance of the inherent non-normality of the samples in fatigue damage accumulation can be demonstrated by comparing the damage caused by the actual non-Gaussian loading with that of the corresponding simulated loading based on Gaussian assumption. Within this context, Gaussian counterparts for both cases were also simulated using their corresponding spectra.

9.2.2.2 Damage estimation

Wind-induced fatigue damage, D, can be estimated using the well-known damage accumulation hypothesis of Miner's rule:

$$D = \sum_{i=1}^{k} \frac{n_i}{N_i} \qquad (9.5)$$

in which n_i = total number of cycles in the ith block of constant pressure range, S_{ri}; N_i = number of cycles to failure under S_{ri}; and k = total number of blocks. Failure occurs when D = 1. More details about the various models including Miner's rule that designer's use to predict fatigue under variable amplitude and random loading are provided elsewhere (Wirsching and Light 1980; *ASCE Committee on Fatigue* ...... 1982).

As previously mentioned, the wind pressure fluctuations are broad-banded and sometimes non-Gaussian too; therefore, the description as well as counting of load cycles are not easy as in the case of a narrowband Gaussian process. Dowling (1972) summarized several cycle counting methods and showed the superiority of rainflow count method over others in estimating the number of cycles present in a broadband non-Gaussian process. The

ASCE Committee on Fatigue and Fracture Reliability (1982) also recommended the rainflow count method in case of broadband non-Gaussian process. In this study, the recent standardization of rainflow method by Amzallag et al. (1994) has been adopted to count the number of cycles, n_i, present in pressure fluctuations. This method is presented in Appendix - D. The number of cycles to failure N_i is obtained from the constant amplitude S-N curve of the corresponding roof cladding material (Xu 1995b). By applying Goodman's simplification to estimate the pressure range equivalent to nonzero mean pressure (Fuchs and Stephens 1980), the conventional S-N relationship becomes

$$N_i = K \left[\frac{S_{ri}}{1 - \frac{S_{mi}}{S_u}} \right]^{-m_1}, \quad S_{ri} \geq S_{th} \qquad (9.6)$$

where, S_{ri} = pressure range associated with mean pressure S_{mi}, S_u = ultimate pressure of roofing components, S_{th} = threshold pressure below which there is no damage to roof, and K and m_1 are constants representing intercept and slope respectively of the constant-amplitude S-N curve plotted on a log-log graph. The parameters S_u, K and m_1 for any particular roofing material can be established by conducting conventional constant-amplitude tests (Xu 1995b). Further, two common roof types used in Australia have been chosen from Xu (1995b) to demonstrate the fatigue damage caused by the simulated pressure fluctuations; their constant-amplitude test results are provided in Table 9.2.

Table 9.2 Constant-amplitude test results of typical roofing sheets.

	K	m_1	S_u (kPa)
Trapezoidal roofing	6.248×10^5	3.008	9.2
Ribbed roofing	2.088×10^5	2.531	7.6

9.2.3 Fatigue Characteristics of Roof Pressures

The number of data in each record of the simulated and measured pressure time histories is 8192, corresponding to a duration of 16.384 s in model scale. The results of rainflow method in terms of the maximum pressure cycle range (Cp_{rmax}), the number of load cycles in model scale (N_m), and full-scale (N_p) of the corresponding time histories are listed in Table 9.3. The MATLAB function **RFLOW** (see Appendix - A) was used for this

Table 9.3 Typical results of rainflow counting method.

Sample	Type	Cp_{rmax}	N_m	$N_p = \bar{n}$
	NG	5.30	1803	180
S50	G	4.25	1882	188
	M	4.40	1974	197
	NG	3.12	1817	181
S64	G	3.01	1882	188
	M	3.70	1983	198

Note: NG - Simulated (non-Gaussian), G - Simulated (Gaussian) ,
M - Measured

computation. While applying rainflow algorithm, no hysteresis threshold limit has been used to eliminate small cycles since it was decided to use such threshold in the estimation of total fatigue loading and corresponding damage. Note that each sample of Table 9.3 depicts the rainflow results of the simulated non-Gaussian time series (NG), their Gaussian (G) counterparts and the corresponding measured non-Gaussian time series (M). As expected, the maximum pressure cycle range of simulated non-Gaussian time history is greater than its corresponding Gaussian counterpart; however, the difference between the two depends on the intensity of non-normality. For instance, the difference between the maximum

pressure cycle range corresponding to the simulated non-Gaussian time series and its Gaussian counterpart in case of S64 is less than that of S50 since sample S64 is not highly non-Gaussian (see Table 9.1). On the other hand, the Cp_{rmax} of simulated non-Gaussian time series is different from the corresponding measured non-Gaussian time series. This is because the simulations are based on generalized spectra of that zone and moreover, Cp_{rmax} is sensitive to peaks which vary from sample to sample. Note that the total number of cycles in model scale corresponding to both samples are close, though they usually vary according to tap locations.

For actual damage estimation, the number of cycles corresponding to model scale has to be converted to full-scale. Additional information required for this conversion is the relationship between the wind speed and the number of cycles. In the present study, the similarity equation associated with the Strouhal number which provides the linear relationship between number of cycles and wind speed (Lynn and Stathopoulos 1985; Xu 1993; Jancauskas et al. 1994) has been used to evaluate the number of cycles per hour per one m/s of mean hourly wind velocity at building height in full-scale (N_p) provided in Table 9.3. The number of cycles in both full-scale and model scale wind pressures, counted by the rainflow method, are expected to approximately satisfy the similarity equation,

$$N_p = N_m \frac{L_m}{L_p} \frac{V_p}{V_m} \frac{T_p}{T_m}$$
(9.7)

where, N is number of cycles, L is geometric length, T is time, V is hourly mean wind velocity at building height, and the indices p and m stand for prototype and model respectively. The number of cycles per hour per one m/s of hourly mean wind velocity at

building height, $N_p = \bar{n}$, is evaluated with the help of corresponding N_m's and by taking $L_m/L_p = 1/400$, $V_p = 1$ m/s, $V_m = 5.5$ m/s, $T_p = 3600$ s, and $T_m = 16.384$ s; $\bar{n}$ corresponding to various cases is provided in Table 9.3. Later, the total pressure cycles in full-scale corresponding to a particular wind velocity for a period of time in hours can be evaluated by multiplying N_p by the corresponding wind velocity and period.

The distribution of pressure cycles over both cycle ranges and mean levels provided by rainflow count method can be displayed using the three-dimensional cycle histogram. Figures 9.2, 9.3, 9.4 and 9.5 display typical cycle histograms of the simulated and measured samples. The vertical axis shows the ratios of the number of cycles in each cell to the total number of cycles. The two horizontal axes refer to the range and mean level of cycles expressed as a ratio of the maximum pressure cycle range of the corresponding simulated time history obtained from rainflow counting method. Low cycle ranges have been included. Clearly, the low level cycle ranges corresponding to low cycle mean levels are filled with more cycles and this is typical for most cases; however, various patterns of distribution of cycles have been noted depending on the location of the tap on the roof and the wind direction. For instance, compared with sample S64 (Figs. 9.4 and 9.5), the cycles corresponding to sample S50 (Figs. 9.2 and 9.3) are more or less concentrated on the cells of lowest mean cycle levels. The cycles of S64 are more uniformly distributed compared with those of S50. It is also noted that the maximum pressure cycle range of a time series is consistently greater than the maximum pressure cycle mean level for the cases studied. In general, the cycle histogram of simulated pressure fluctuations corresponding to S50 and S64 are similar to those of the corresponding measured pressure fluctuations. This similarity of cycle histograms and the number of cycles between the simulated and the measured cases
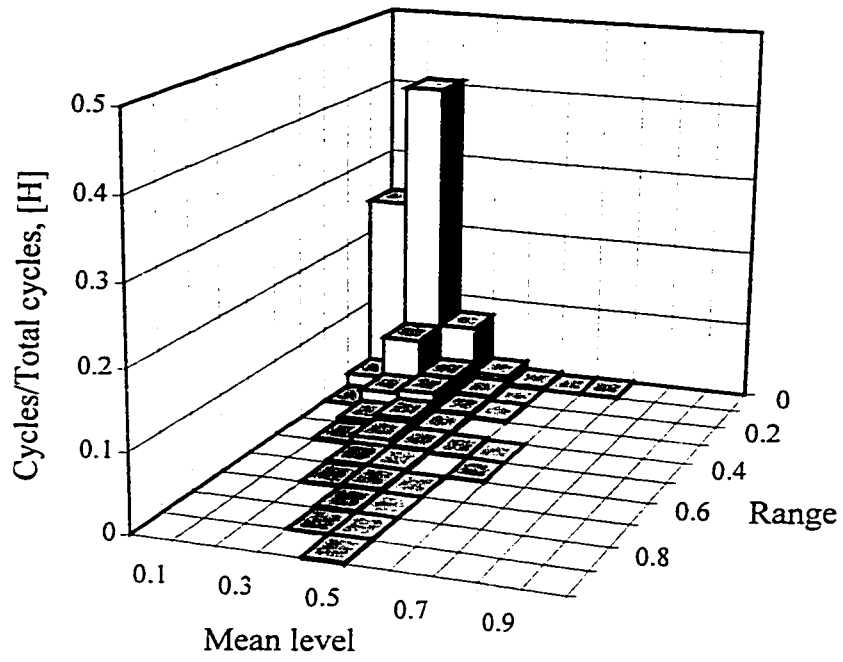
Fig. 9.2 Cycle histogram of S50 (Simulated).
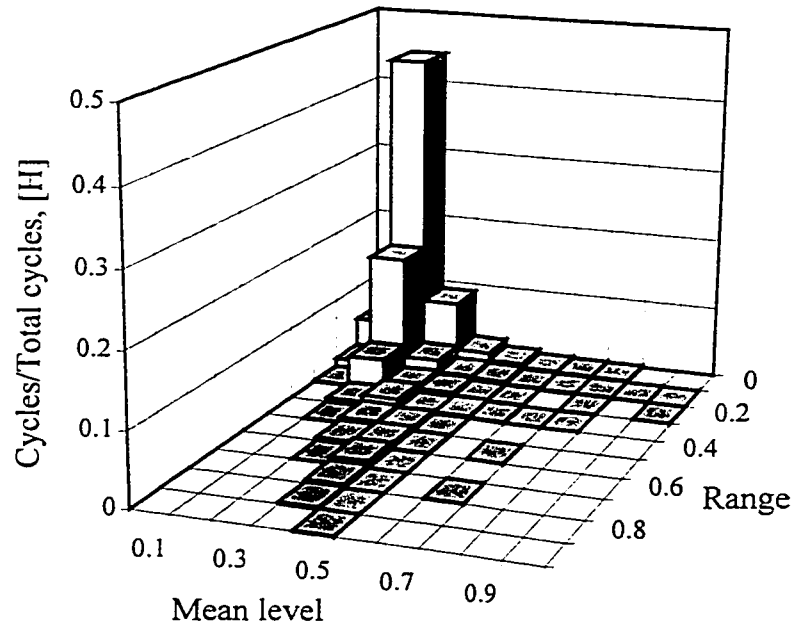
Fig. 9.3 Cycle histogram of S50 (Measured).
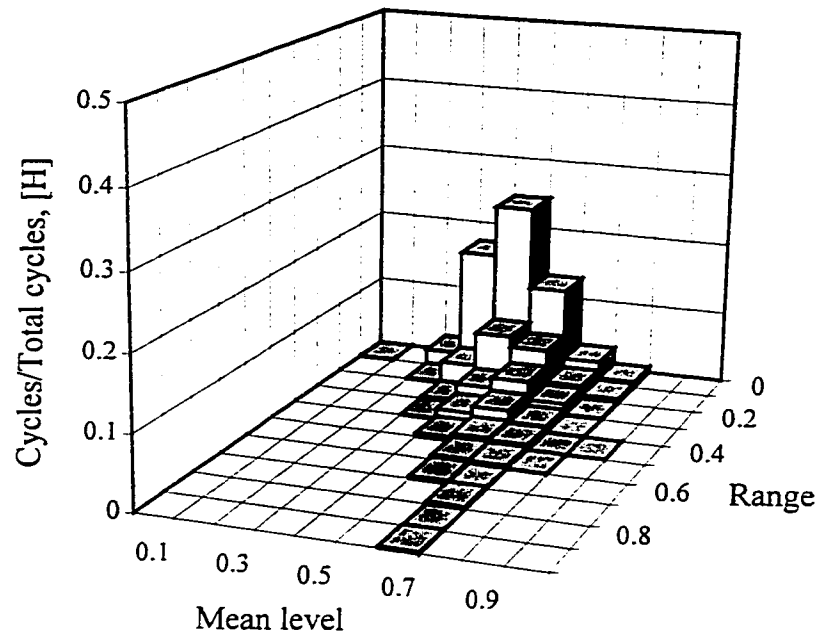
Fig. 9.4 Cycle histogram of S64 (Simulated).
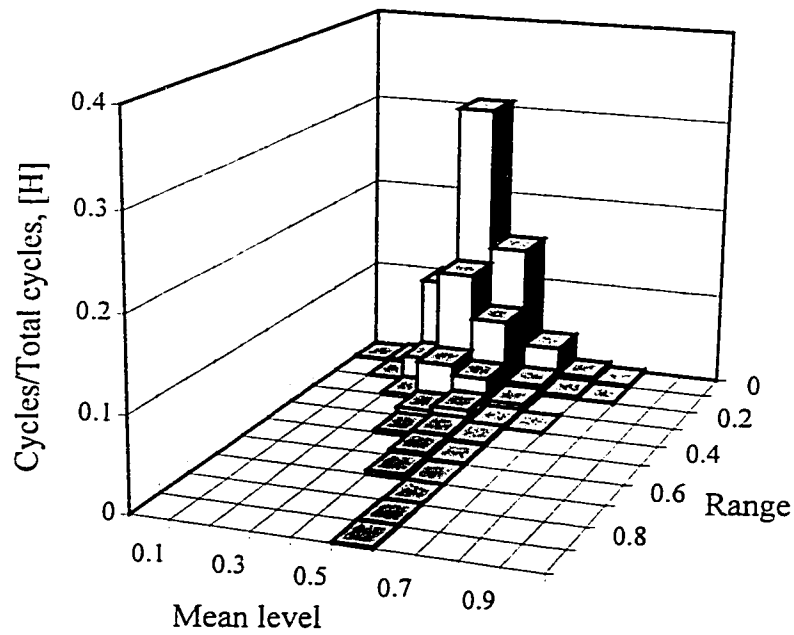
Fig. 9.5 Cycle histogram of S64 (Measured).

indicate that simulated pressure fluctuations can be used to determine fatigue characteristics of wind pressures on roofs. The cycle histogram and the number of cycles, together with the information on long-term wind climate, can be used to determine the total fatigue loading on roof cladding. Furthermore, the cycle histogram of the corresponding simulated Gaussian time histories is shown in Figs. 9.6 and 9.7. The cycle histogram for both cases obtained using Gaussian assumption is certainly different from those of the actual non-Gaussian cases shown in Figs. 9.2 and 9.4. Note that the cycles are more or less uniformly distributed under the Gaussian assumption.

Though the similarity between the simulated and measured cases has been shown in terms of distribution of cycles, it may be of interest to show the comparison between the damage caused by simulated and measured fluctuations to a roof system. On this basis, the simulated as well as measured pressure fluctuations have been applied to the trapezoidal roofing (see Table 9.2) and the corresponding fatigue mean life time of the roof was estimated using the MATLAB function **DAM_TH** (see Appendix - A). The results are provided in Fig. 9.8. Note the reasonable similarity between the measured and simulated cases which is encouraging. One of the advantages of the current simulation methodology in fatigue analysis is its flexibility in carrying out a parametric study. For instance, the effect of variance (σ^2) of pressure fluctuations on fatigue mean life time of the roof is shown in Fig. 9.9 with variance ranging from 0.1 to 0.3. For all simulations, the normalized spectrum S_{FNGI} was multiplied with different variance to obtain the actual power spectrum. The MATLAB functions **NGSPEC** and **DAM_TH** (see Appendix - A) were used for time series simulation and fatigue evaluation respectively. Clearly, when the intensity of fluctuations (variance) increases, the fatigue mean life time decreases. Further, note that as
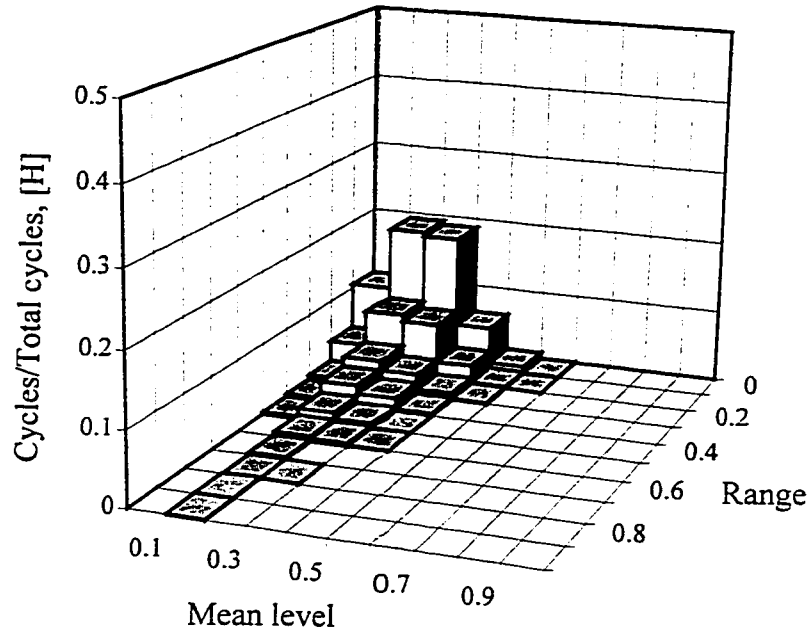
Fig. 9.6 Cycle histogram of S50 (Simulated, Gaussian).
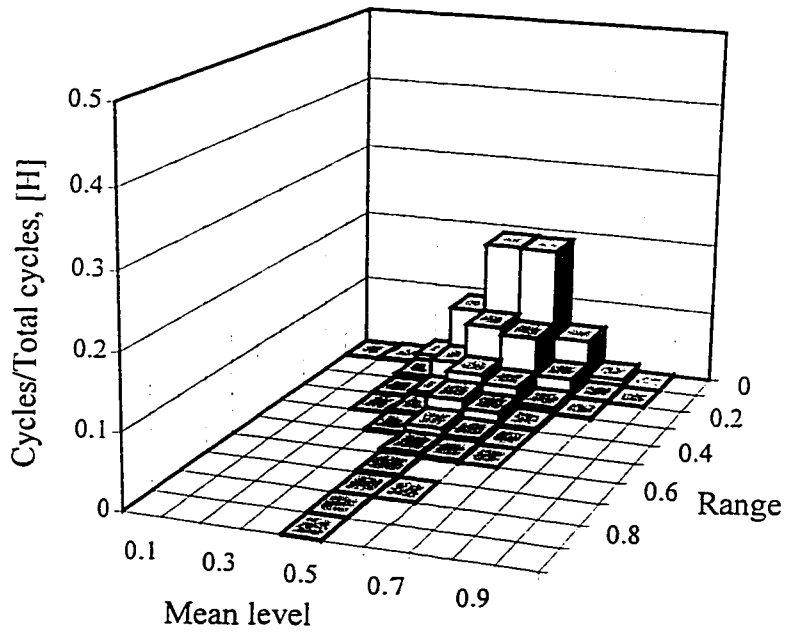
Fig. 9.7 Cycle histogram of S64 (Simulated, Gaussian).

196
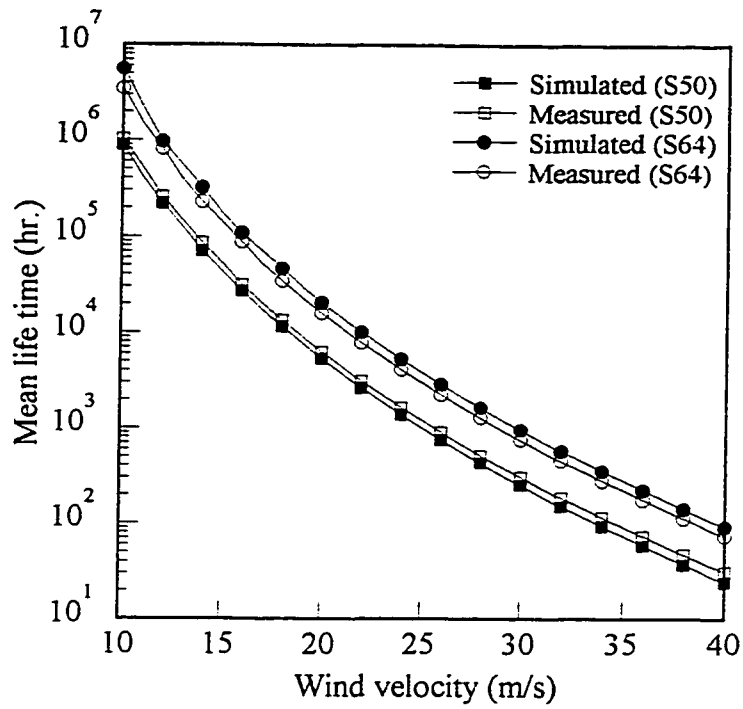
Fig. 9.8 Fatigue life time of trapezoidal roof under simulated and measured wind pressure fluctuations.
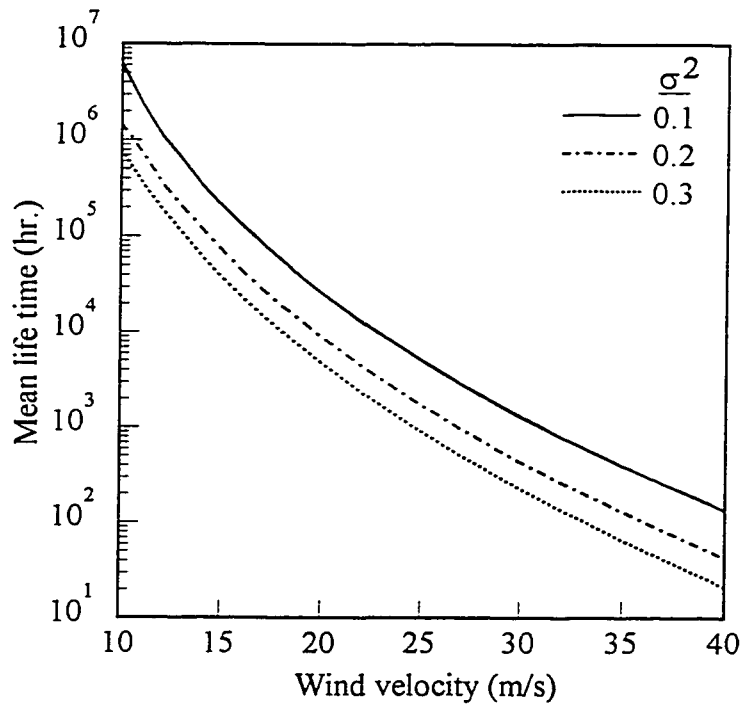
Fig. 9.9 Effect of variance of pressure fluctuations on fatigue life time of trapezoidal roof.

the wind velocity increases, the fatigue life time decreases. Overall, this section demonstrates the potential of the proposed simulation methodology to represent fatigue characteristics of roof pressures.

9.2.4 Total Fatigue Loading

Roof cladding is exposed to a spectrum of wind speeds during its life time. Corresponding to the variation of wind speed, the number of cycles present in pressure fluctuations vary as well. On the other hand, the fatigue damage of roof cladding usually accumulates throughout its life time depending on the material type. Therefore, for the design of roof cladding corresponding to a particular wind return period and specific life time, such fluctuations in wind speed have to be taken into account. In this study, the long-term wind climate of the corresponding location was integrated with the simulated fatigue characteristics of the pressure fluctuations to obtain the total fatigue loading using a probabilistic approach similar to that of Xu (1993). For demonstration purposes, it was assumed that the building is exposed to temperate climate of Montreal. The design mean hourly wind speed, corresponding to a 50-year return period ($\bar{V}$) was used for all computations; the design mean hourly wind speed at building height in an open country terrain exposure was estimated to be 26 m/s based on NBCC (1995).

9.2.4.1 Integrating long-term wind climate

The Weibull distribution has been adopted in this study for describing the probability

198

density of mean hourly wind velocity $(P(V_i))$. The probability that the mean hourly wind velocity V_i is in a small interval of specified velocity ΔV is

$$P\left[V_i - \frac{\Delta V}{2} \leq V_i \leq V_i + \frac{\Delta V}{2}\right] \approx P(V_i) \Delta V \tag{9.8}$$

Considering the mean hourly wind velocity at building site in Montreal from all 16 directions, the Weibull probability density function $P(V_i)$ (Wu 1994) has been estimated using

$$P(V_i) = \sum_{j=1}^{16} p_j \frac{k_j}{c_j^{k_j}} V_i^{k_j-1} e^{-\left(\frac{V_i}{c_j}\right)^{k_j}} \tag{9.9}$$

where, p_j = probability of wind coming from a particular direction and constants c_j and k_j determine the shape of the distribution; the corresponding values of the parameters shown in Table 9.4 are taken from Wu (1994). Consequently, for a given mean hourly wind

Table 9.4 Weibull constants based on meteorological records for Montreal, after Wu (1994).

i	Sector	p_j (%)	k_j	c_j (m/s)
1	N	4.10	1.51	3.34
2	NNE	8.10	1.05	3.11
3	NE	7.46	1.30	4.47
4	ENE	2.62	1.69	4.29
5	E	2.21	1.62	3.23
6	ESE	2.42	1.79	3.69
7	SE	4.45	1.81	4.35
8	SSE	5.07	1.76	4.33
9	S	3.39	1.57	3.14
10	SSW	5.39	1.62	3.80
11	SW	11.74	1.26	4.17
12	WSW	14.07	1.40	5.06
13	W	11.81	1.45	5.02
14	WNW	5.73	1.83	3.10
15	NW	3.59	1.67	3.97
16	NNW	2.83	1.43	3.07

velocity (V_i) at building height, the number of cycles at a point N_{vi} has been estimated using

$$N_{vi} = \bar{n}\, V_i\, P(V_i)\, \Delta V\, T \qquad (9.10)$$

where, $\bar{n}$ = number of cycles per hour per one m/s of mean hourly wind velocity at building height; and T = design life of roof cladding in hours. The distribution of the cycles N_{vi} over all cycle ranges and mean levels can be estimated by

$$[N_{vi}] = N_{vi}\, [H] \qquad (9.11)$$

where, [H] = cycle histogram. Thereafter, the following equation gives the total load cycle distribution of the designated tap:

$$[N_T] = \sum_i\, [N_{vi}] \qquad (9.12)$$

where, the mean level and range of [N_T] are expressed as the ratio of design wind pressure,

$\frac{1}{2}\rho \times \bar{V}^2 \times Cp_{rmax}$ (Cp_{rmax} is the maximum pressure cycle range and $\bar{V}$ is the design mean hourly wind velocity at building height corresponding to a specific return period). This shows that the above summation is not straightforward since each [N_{vi}] is a function of velocity, i.e., the cycle mean levels and ranges are a function of velocity. Therefore, it is necessary to carry out a proper summation according to the mean levels and ranges of each [N_{vi}]. This summation is coded in MATLAB function namely, **DAM_TOT** (see Appendix - A) which estimates the total number of cycles and the corresponding damage.

While estimating the total fatigue loading with respect to a given wind return period and design life, the threshold cycle range in all computations has been kept initially at 5% of the design wind pressure; this was also done by Xu (1993) to eliminate small cycles which

contribute little to fatigue damage. However, it was later decided to use a 4% of the global

maximum design wind pressure corresponding to the maximum pressure cycle range as the

hysteresis threshold in order to have a reasonable comparison of number of cycles at various

taps. The global maximum design wind pressure out of the cases considered is $\frac{1}{2}\rho$ x $\bar{V}^2$ x

Cp_{rmax} = 0.65 x 26^2 x 5.3/1000 = 2.37 kPa, which corresponds to the design mean hourly

wind speed of 26 m/s at building height and the largest pressure cycle range of 5.3 of

simulated time series of S50 - see Table 9.3; the threshold used in all computations was 0.1

kPa. Admittedly, finding an appropriate threshold limit for fatigue design considerations is

debatable, since such a limit is a function of the type of cladding material. Depending on the

threshold limit, the number of cycles as well as the estimated damage can increase or

decrease.

Figures 9.10 and 9.11 show the total load cycle distribution for S50 and S64. Both cycle

ranges and cycle mean levels are expressed as a ratio of the corresponding design wind

pressure. The design life of roof (T) is taken as 50 years. Figures 9.10 and 9.11 show that a

large number of cycles are concentrated at both low cycle ranges and low cycle mean levels.

As cycle ranges or cycle mean levels become larger, the number of cycles becomes smaller.

Another interesting feature of the total load cycle distribution is that the maximum number

of load cycles for a given range is approximately located at a mean level which is half of the

cycle range; this was also observed by Xu (1993). This property is discussed in detail in the

next section.
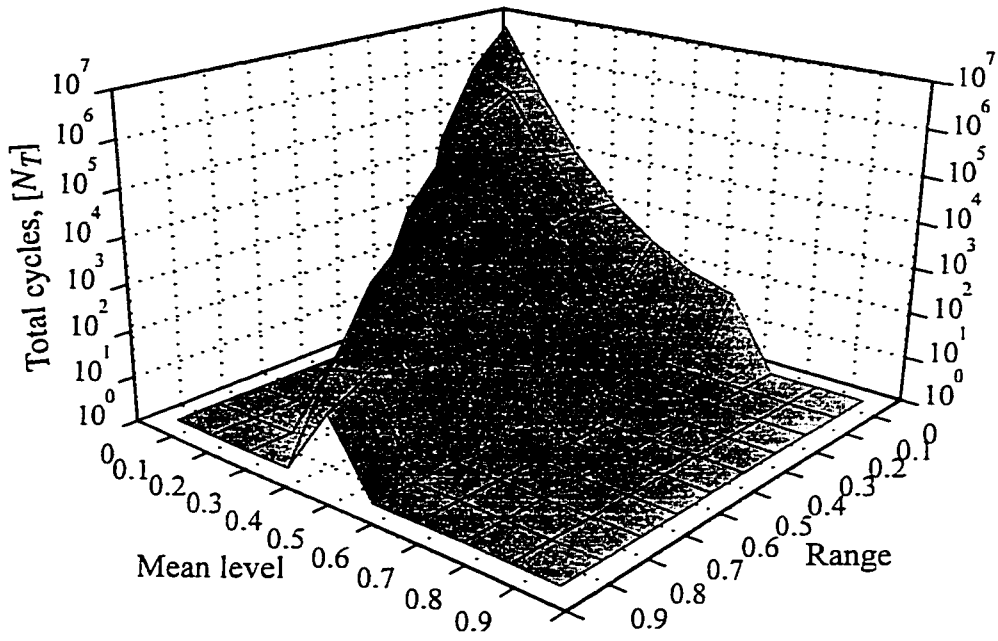
Fig. 9.10 Total load cycle distribution for S50 (Simulated).
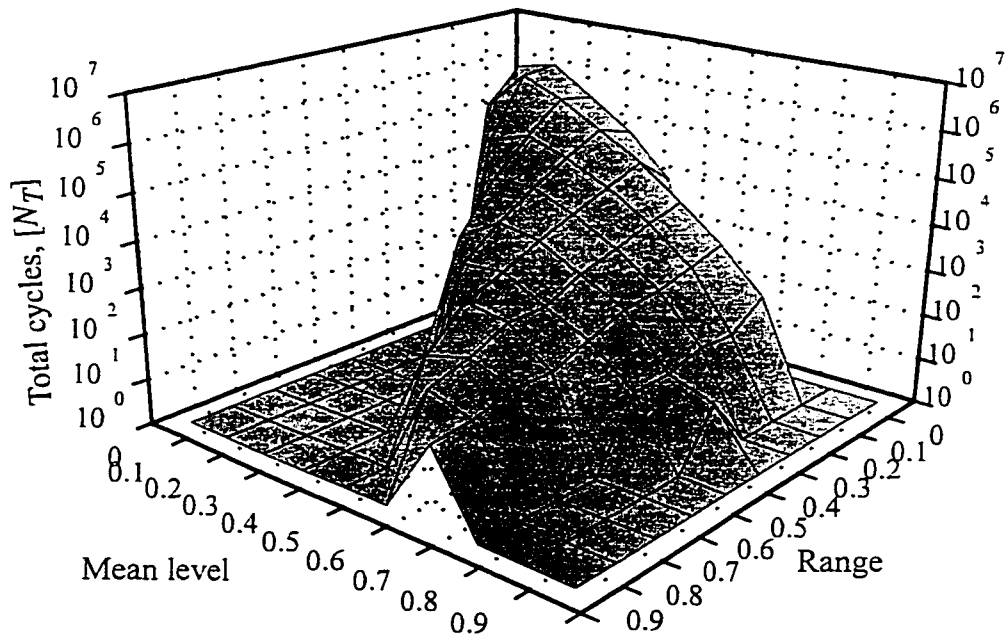
Fig. 9.11 Total load cycle distribution for S64 (Simulated).

202

9.2.4.2 Mean levels of load cycles

As previously mentioned, the total cycles are jointly distributed over both cycle ranges and mean levels. Though it is ideal to directly use the total load cycle distribution for fatigue tests, such an approach may be expensive and inconvenient. Therefore, it may be necessary to simplify the total load cycle distributions for practical applications. The typical nature of total load cycle distributions noted in Figs. 9.10 and 9.11 indicate that there is a possibility for further simplification of the loading.

An attempt has been made to clearly show the concentration of cycles in a given range. Figures 9.12 and 9.13 display the concentration of cycles in the case of sample S50 for the Montreal design hourly mean wind speed of 26 m/s and a design life of 50 years. The horizontal axis refers to the ratio of cycle range to the design wind pressure, while the vertical axis refers to the ratio of cycle mean level to the design wind pressure. The number in a cell is a proportion of the cycles in the cell to the total number of cycles in the same range in which the cell lies (i.e., the total number of cycles in the column in which this cell lies). The plus sign in a cell indicates that the proportion of this cell is less than 10% but larger than zero. The solid oblique line is a particular case in which the cycle mean level is always half of the given cycle range. Surprisingly, for a given cycle range, especially for cycle ranges of high values, most of the cycles in the corresponding range are concentrated in the cells around this solid oblique line. This result shows the possibility of simplifying the fatigue wind loading matrix; however, further work concerning this issue is required before drawing any conclusions. The similarity between simulated and measured cases shown in Figs. 9.12 and 9.13 respectively demonstrates once again the suitability of the proposed simulation method for wind-induced fatigue life prediction.
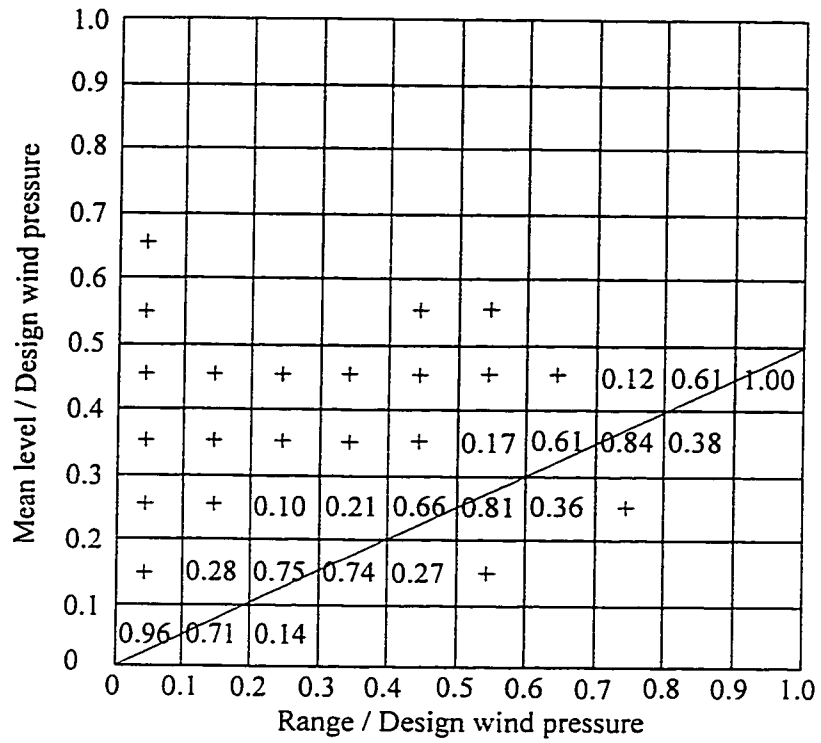
Fig. 9.12 Concentration of cycles of S50 (Simulated).
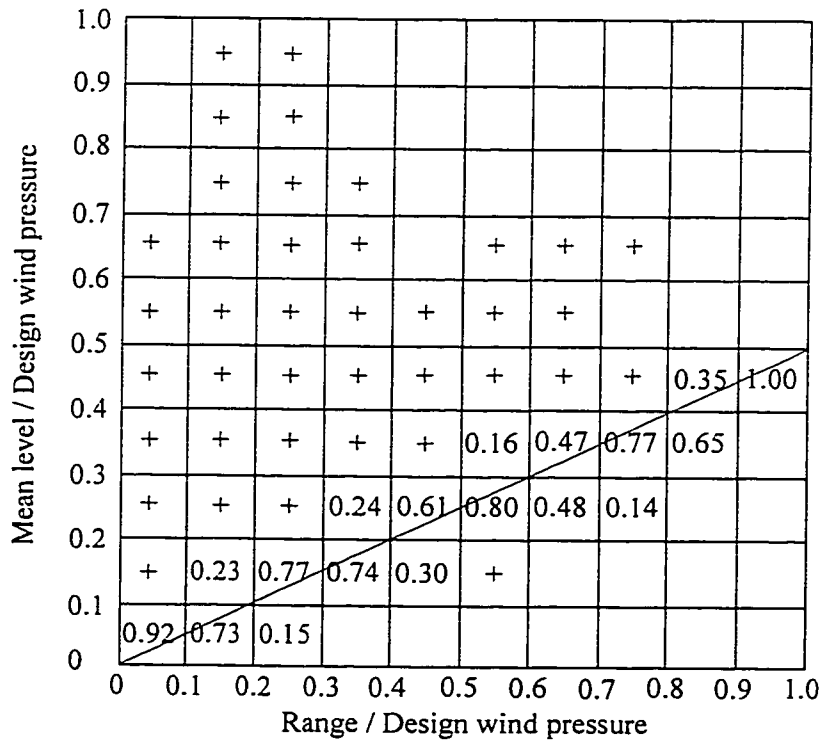
Fig. 9.13 Concentration of cycles of S50 (Measured).

204

9.2.5 Effect of non-Normality on Fatigue Damage Accumulation

The non-conservative effect of assuming Gaussian distribution of pressure fluctuations in simulations is shown in Fig. 9.14 in terms of pressure cycles. The horizontal axis represents the number of cycles exceeding the cycle range, while the vertical axis represents cycle range as a percentage of design wind pressure. The data provided are again based on design hourly mean wind velocity of 26 m/s at the height of the Montreal building and a design life of 50 years. In this analysis, the design wind pressure of the non-Gaussian pressure fluctuations has been used as the datum for their corresponding Gaussian counterparts. It is interesting to note the absence of cycles at higher cycle ranges (80% and 90% levels) in the case of simulated Gaussian fluctuations corresponding to S50; however, this is not valid in case of S64. A common feature found in both cases is that as the cycle range increases, the
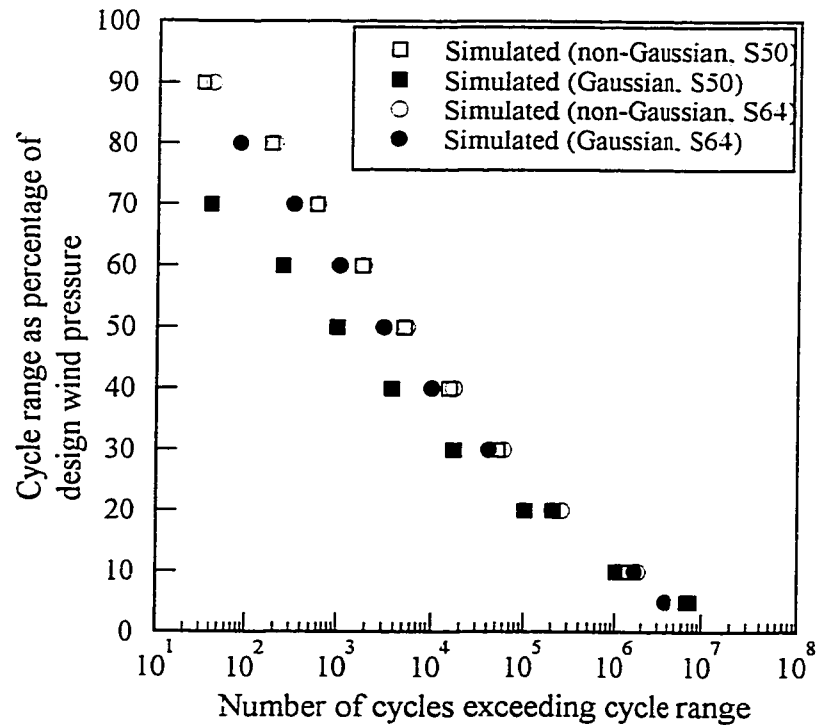
Fig. 9.14 Effect of Gaussian assumption in terms of cycles.

number of cycles corresponding to simulated Gaussian fluctuations greatly reduces compared to simulated non-Gaussian cases; however, such reduction depends on the intensity of non-normality. For instance, such a reduction is negligible in case of sample S64 which is less non-Gaussian compared to S50.

Further, this loading has been applied to the previously referred trapezoidal as well as ribbed roofing sheets. Using Miner's rule and the constant-amplitude S-N curves, damage D has been estimated using Eq. (9.5) as follows: the estimated total cycles corresponding to each mean and range values, n_i's, (Figs. 9.10 and 9.11) were divided by the corresponding number of cycles to failure, N_i's, obtained from the known behavior of roof cladding under constant-amplitude loading represented by Eq. (9.6). The ratio corresponding to each mean and range values represents an index of contribution of the corresponding pressure cycles towards damage. Thereafter, the ratios corresponding to each mean and range level were summed up to obtain the damage index, D. The estimated damage indices are provided in Table 9.5 where D_{ng} and D_g represent damage due to non-Gaussian process and Gaussian process respectively. Based on the calculations, the ribbed roof fails under the loading given in Fig. 9.10; however, the roof does not fail under the Gaussian assumption. In both cases

Table 9.5 Estimated damage indices.

	D_{ng}	D_g	D_{ng}/D_g present study	D_{ng}/D_g Winterstein (1988)
Trapezoidal roofing				
S50	0.25	0.14	1.78	1.91
S64	0.063	0.05	1.26	1.27
Ribbed roofing				
S50	1.05	0.67	1.57	1.51
S64	0.33	0.27	1.20	1.17

analyzed, the damage indices corresponding to Gaussian assumption are smaller than those of the actual non-Gaussian cases; this implies that the roof cladding designed based on Gaussian assumption is expected to fail prematurely. Since sample S50 is highly non-Gaussian compared to sample S64, the corresponding indices are also higher for sample S50. Furthermore, the ratio D_{ng}/D_g increases as the non-normality (expressed, say by skewness) increases; this ratio for sample S64 is consistently lower than that of sample S50 irrespective of the type of roof. Moreover, for the same loading, this ratio can be different depending on the strength of roofing. For instance, under the same loading conditions, D_{ng}/D_g for trapezoidal roofing is always higher than that of ribbed roofing. Finally, Table 9.5 presents the ratio D_{ng}/D_g estimated using the analytical expression (Eq. (9.4)) suggested by Winterstein (1988). Interestingly, these estimated ratios are closer to those predicted by the present study which reinforce the validity of the present results.

Figure 9.15 shows the effect of non-normality on total fatigue damage accumulation at tap 1 for a trapezoidal roofing sheet of 50-year design life. For all simulations corresponding to this figure, the spectrum (S_{FNG1}) of the same pressure time history has been used; however, the intensity of non-normality (for instance, in terms of skewness) was varied using the parameter b. The MATLAB functions **NGSPEC** and **DAM_TOT** (see Appendix - A) were used for time series simulation and damage estimation respectively. Note that the ratio D_{ng}/D_g is always greater than one even in case of pressure fluctuations with very low skewness; the minimum ratio is around 1.2. The ratio shoots up to very high values in case of highly non-Gaussian fluctuations; however, the ratio started increasing consistently when $b > 0.7$. The dependency of D_{ng}/D_g on strength of roofing already reported in Table 9.5 is pictorially shown in Fig. 9.16. For this
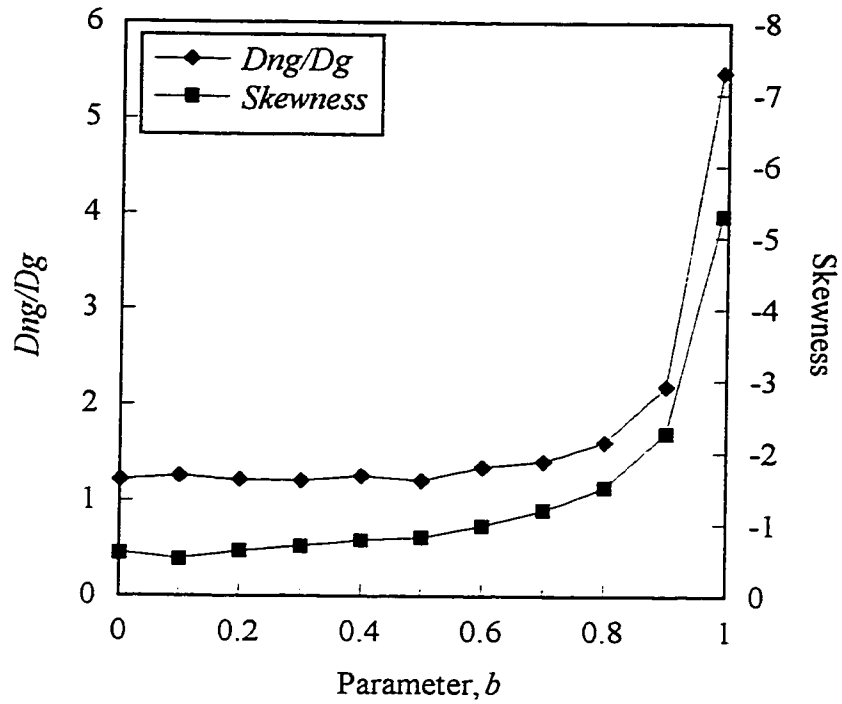
Fig. 9.15 Effect of non-normality on total fatigue damage accumulation.
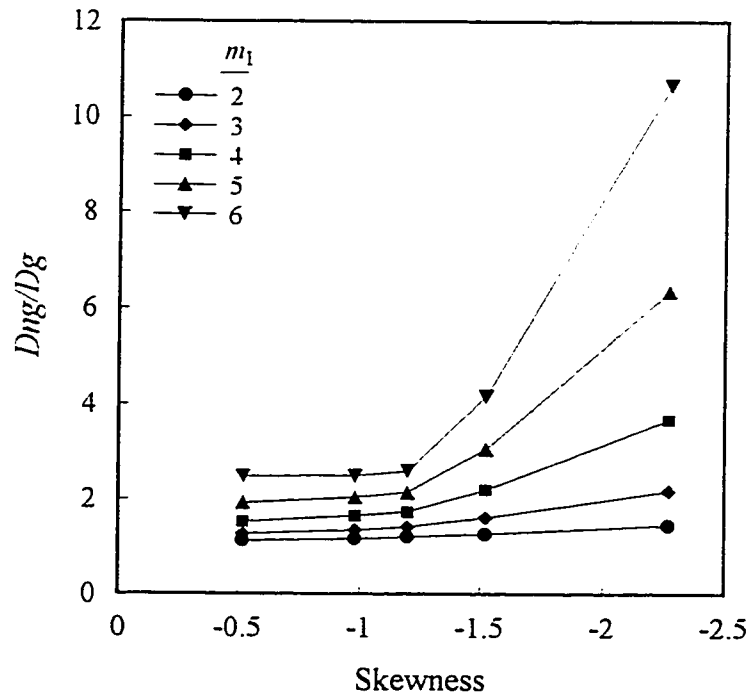
Fig. 9.16 Combined effect of strength of roofing and non-normality on fatigue damage.

demonstration, five non-Gaussian time histories with different intensity of non-normality (in terms of skewness) have been simulated using the synthetic spectra of tap 1 and five different b values. Thereafter, the total cycles counted from each of these time histories have been applied to five roofing materials having different strengths (in terms of m_1). Note that the ratio D_{ng}/D_g, based on Eqs. (9.5) and (9.6), is independent of the intercept K of the S-N curve, but depends on its slope m_1. The combined effect of non-normality (in terms of skewness) and strength of roofing (in terms of m_1) on ratio D_{ng}/D_g is shown for tap 1. As m_1 increases, D_{ng}/D_g increases drastically in case of very high non-Gaussian fluctuations. Similar observations have also been made in an analytical study by Lutes et al. (1984).

9.2.6 Comparison of Simulated Results with Other Sources

Figure 9.17 shows the comparison between the actual simulated non-Gaussian data with the simulated Gaussian data as well as with predictions made by Weibull (Eq. (9.2)), Rayleigh (Eq. (9.3)) and Gaussian (Eq. (3.28)) models in terms of mean life time in hours for tap 1. The parameters of the analytical models have been estimated by the expressions given in Lynn and Stathopoulos (1985). The required Weibull parameters c and k for peak factor (g) less than 2.5 have been estimated by fitting the tail part $(g < 2.5)$ of the PDF of the simulated fluctuations with the Weibull probability density function suggested by Stathopoulos (1980); the estimated parameters are $c = 0.5$ and $k = 0.7$. Additional parameters required for the evaluation of the fatigue life time by analytical models include shape factor, μ (see Eq. (3.28)) and cycling rate (N_0) which are found to be 0.41 and 52.46 respectively based on wind tunnel measurement results for this specific case. The
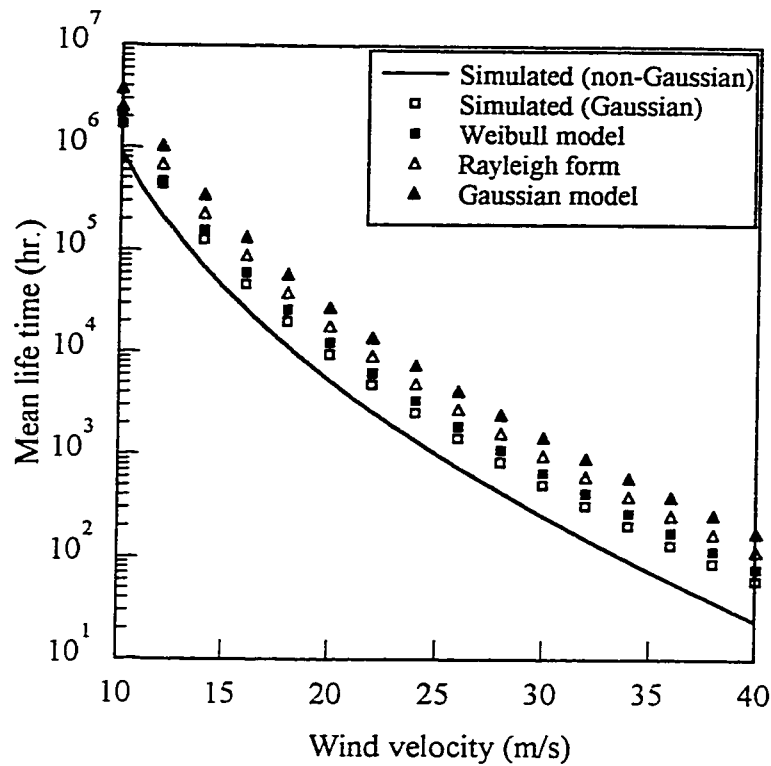
Fig. 9.17 Comparison of simulated results with the existing analytical models.

computations concerning simulated, Weibull and Gaussian cases have been carried out using MATLAB functions **DAM_TH**, **DAM_W**, and **DAM_G** (see Appendix - A) respectively. It is clear that the Gaussian assumption can lead to non-conservative estimates of cycles and mean life time. The difference between the results obtained from the Gaussian model and the simulated Gaussian data can be attributed to the different cycle counting methods used in these cases; the Gaussian model is based on peak cycle counting method while the simulated Gaussian data is based on rainflow cycle counting method. In the case of simulated Gaussian, since the cycles have been counted from the simulated time history using the more adequate rainflow counting technique, the mean life time predicted is more reliable than that predicted by the Gaussian model. The Weibull model is also based on peak cycle counting method; in addition, the selection of constants associated with this model causes

210

further uncertainty. The Rayleigh form is based on the assumption that the pressure fluctuations are narrow-banded and normally distributed for which case there is only one maximum and one minimum for every cycle. Therefore, this formulation overestimates the number of cycles present in broadband fluctuations and correspondingly, increases the damage and reduces the mean life time as shown in Fig. 9.17.

The simulated total fatigue loading (Figs. 9.10 and 9.11) has been compared with full-scale results (Tap 50501, Xu (1993)) as well as the British (BRE) and German (FRG) recommendations. Note that both BRE and FRG recommendations are based on 50 years of design life and 50-year return wind speed, as in the simulated case. Results of this comparison are shown in Fig. 9.18 in terms of cycle range, expressed as percentage of design wind pressure, and number of cycles exceeding the cycle range. The number of cycles computed by the present simulation in ranges above 50% of the design wind pressure
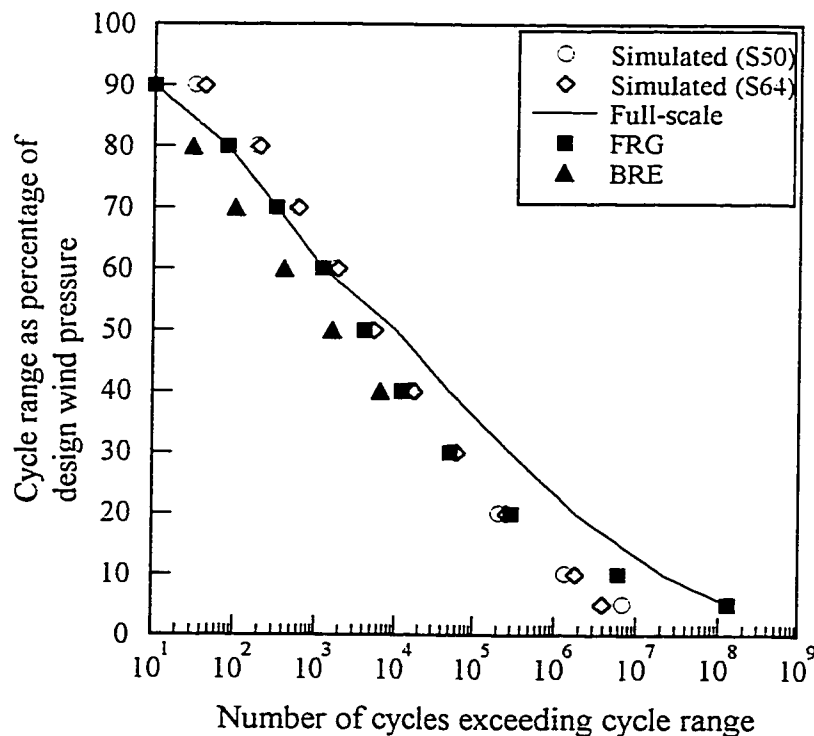
Fig. 9.18 Comparison of simulated results with full-scale and standard data.

211

are somewhat closer to those predicted from full-scale measurements. Differences in tap locations might be one of the reasons for discrepancies occurring towards lower ends of the data. It is interesting to note the increase in number of cycles at higher cycle ranges in the case of present simulations as compared with the other loadings. Note that these taps are located in zones of high pressure fluctuations and correspondingly, the fatigue loading sequences associated with these taps are also high. Note that the results of the present simulations are more or less close to the FRG recommendations. On the other hand, the BRE recommendations underestimate the number of cycles in the high cycle range levels. The number of cycles corresponding to both taps are more or less the same. Though sample S64 narrowly exceeds S50 in terms of number of cycles, the design wind pressure for sample S64 is only 1.4 kPa compared to 2.37 kPa for S50. This indicates that the cycles corresponding to sample S64 are at low mean levels and ranges compared to S50. Therefore, the estimated damage in case of S64 is expected to be less than that of S50 as previously shown in Table 9.5.

Overall, the previous demonstrations show that the roof pressure fluctuations generated using the simulation methodology proposed in this thesis can be used to investigate fatigue characteristics of roof cladding. Moreover, it is convenient to use the proposed simulation methodology to investigate the effects of various parameters such as intensity of non-normality and strength of roofing involved in the fatigue damage process. In addition to the above mentioned fatigue analysis of roof cladding, the simulated time history can also be used to investigate fatigue behaviour of roofs by applying it directly on a roof using facilities like BRERWULF, and by using it as a forcing function in Finite Element analysis of a modelled roof.

9.3 FURTHER THOUGHTS

The simulation of stationary Gaussian time series is straightforward and applicable in many fields. Note that the non-Gaussian time series simulation technique developed in this thesis is based on the stochastic characteristics of many measured roof pressure fluctuations on a variety of low buildings. As previously noted, the measured non-Gaussian time histories, in general, have only one sided negatively going sharp spikes. Based on this observation, a skeleton signal having negatively going spikes has been introduced to simulate the observed spike characteristics of the fluctuations. However, in order to simulate positively going sharp spikes in a time series, a skeleton signal having positively going spikes is possibly required. This would help the modelling of pressure fluctuations appearing on roofs with high slopes and walls of low buildings. For demonstration purposes, it was decided to reconstruct the modified target signal S1 shown in Fig. 9.19; this was obtained by reversing the spikes of sample S1 (Fig. 6.3). The modified target signal S1 has the same mean, variance, kurtosis and spectra as those of sample S1. The simulation procedure shown in Fig. 6.15 was also followed here by using $b = 0.87$; the only difference was in the simulation of skeleton signal. In order to simulate positively going spikes, the exponential parameter λ was taken as 1 (see Appendix - B). As a result, positively going sharp spikes were created in the skeleton as well as the simulated signal as shown in Fig. 9.19. Note that the spikes are just reversed in this simulated signal compared to the simulated signal shown in Fig. 6.16 corresponding to $\lambda = -1$; the absolute value of skewness is the same in both cases. This demonstration shows the capability of this methodology to model the time series having positively going spikes. Further, the same methodology can be used to simulate stationary random processes of similar nature encountered in other disciplines.
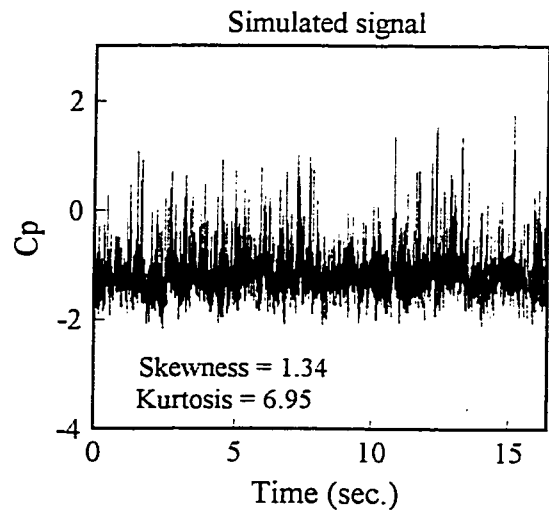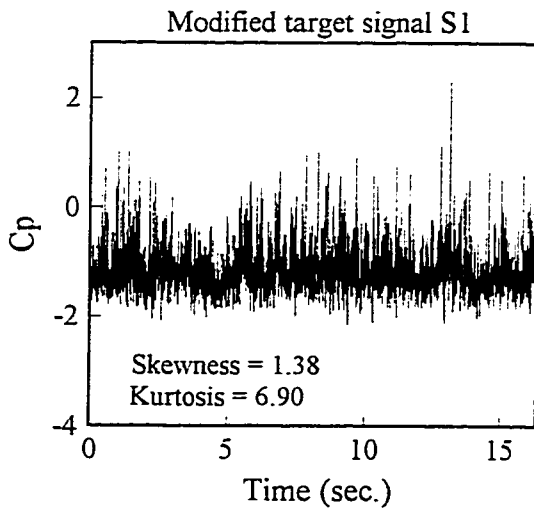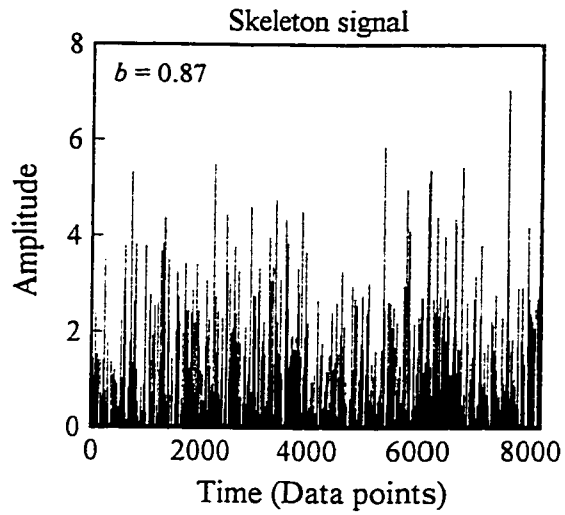
Fig. 9.19 Simulation of a signal having positively going spikes.

214

9.4 SUMMARY

The potential applications of the proposed simulation methodology have been described in this chapter. Simulated pressure fluctuations can be used to carry out extreme value as well as fatigue analysis; the later was fully elaborated.

Wind-induced fatigue characteristics of roof cladding have been investigated using digitally simulated pressure fluctuations on roofs. The reduction of time varying loading into pressure cycles has been carried out using the standardized rainflow technique. The long-term wind climate has been taken into account for the evaluation of total fatigue loading on roof cladding of low buildings located in temperate regions. Miner's law and Goodman method were employed to compute the corresponding damage caused by the total estimated loading cycles. The influence of non-normality as well as strength of roofing on fatigue damage accumulation were clearly demonstrated. Finally, simulated results have been compared with the existing analytical models as well as the British and the German recommendations. The results of the present study clearly indicate that the non-normality of the wind pressure fluctuations can significantly increase the rate of fatigue damage accumulation, and can result in non-conservative fatigue life estimates if its effects are not accounted for. Overall, the wind-induced fatigue life prediction of roof cladding using the proposed simulation methodology appears promising.

CHAPTER 10
CONCLUSIONS

"....Research is to see what everybody else has seen, and think what nobody has thought..."

Dr. Albert Szent-Cyoryi,
as quoted in Reader's Digest, Feb. 1958.

The emphasis of this dissertation is mainly on the development of a simple and efficient digital simulation methodology for the generation of wind pressure fluctuations on low building roofs under various conditions with application to extreme value analysis and fatigue design. The thesis consists of five major parts: (1) introduction, comprehensive review and theoretical background (Chapters 1, 2 and 3), (2) experimental investigation (Chapter 4), (3) modelling and simulation of pressure fluctuations (Chapters 5, 6 and 8), (4) modelling and classification of spectra on roofs (Chapter 7), and (5) application of the proposed simulation methodology in extreme value analysis and fatigue design (Chapter 9). Summaries of findings from each chapter are collapsed here to draw the final conclusions of this study.

10.1 CONCLUDING REMARKS

The results of this study can be summarized as follows:

(1)   A comprehensive review of digital simulation methods shows that the FFT model has the potential to represent non-Gaussian pressure fluctuations compared to ARMA models.

(2)   Extensive wind tunnel measurements show that wind pressure fluctuations on low building roofs are broad-banded and have either Gaussian or non-Gaussian distributional characteristics depending on the situation. Two distinct elements of sharp spikes responsible for non-normality are the frequency of occurrence and the magnitude of spikes.

(3)   Wind pressure fluctuations are modelled using the FFT approach. The simulation methodology requires Fourier amplitude and Fourier phase as inputs; the former is constructed either from sample time series or from sample spectra, while the latter is represented as uniform random numbers ranging between $-\pi$ and π for Gaussian fluctuations and by using a simple stochastic model with a single parameter b for non-Gaussian fluctuations. This parameter b has been estimated by minimizing the sum of the squared errors in target skewness and kurtosis. The ability of the proposed methodology to represent the characteristics of the pressure fluctuations is summarized as follows:

(a) This technique can control the probability distribution properties of a time series by controlling the magnitude and frequency of sharp spikes through the phase part of the DFT without disturbing its spectral properties.

(b) This technique can induce wide range of desired non-Gaussian properties such as skewness and kurtosis in time series by using a single parameter b.

(c) The proposed model is capable of representing pressure fluctuations from various zones of several roof geometries under various conditions. The efficiency of this approach is verified by matching statistics (mean, variance, skewness, kurtosis, PDF, extreme values and crossing rates) of the target signal

217

with those of the corresponding simulated signal.

(d) The proposed model is proved to be successful in providing stationarity in the simulated signals.

(e) Overall, the proposed methodology is simple, in terms of the reduced number of parameters involved; flexible, in terms of the efficient parametric estimation procedure used; and accurate, in terms of preserving the first four moments (mean, variance, skewness and kurtosis) and spectra of the time series.

(4)   Investigation concerning overall characteristics of pressure spectra on roofs shows that, although pressure spectra at various roof locations are different, certain distinct spectral shapes can be identified. Based on the similarity between normalized spectra at various locations, an empirical equation has been suggested for their representation. Spectra have been classified for each roof (monoslope, flat and gable) and fitted with the proposed empirical equation. The standard spectral shapes for various zones of different roof geometries have been used for the synthetic generation of Fourier amplitude part in the simulation.

(5)   Potential applications of the proposed simulation scheme in extreme value analysis and fatigue design have been described. The results indicate that simulated pressure fluctuations can be used to determine extremes as well as fatigue characteristics of pressures on roofs. The fatigue analysis of roof cladding using simulated loading strongly shows the non-conservative effect of assuming Gaussianity in conventional signal simulation.

218

10.2 CONTRIBUTIONS

The major contributions of the present research work can be summarized as follows:

(1)   Extensive wind tunnel measurements followed by analysis of local wind pressure fluctuations on several low building roofs provide comprehensive knowledge of their stochastic as well as fatigue characteristics under different conditions.

(2)   The development and application of a novel digital simulation technique based on the FFT approach contribute an effective means for the representation of non-Gaussian wind pressure fluctuations.

(3)   Investigation of various measured spectra from several low building roofs establishes their overall characteristics. Similarity between normalized spectra measured under different conditions assists not only in suggesting a simple empirical equation for their representation but also in classifying their complex shapes on roofs. The standard spectral shapes and their parameters for various roof geometries established as a result of this exercise are useful for the synthetic generation of spectra.

(4)   The development and application of a new approach for fatigue analysis of roof cladding based on simulated pressure fluctuations and long-term wind climate prove to be successful.

10.3 RECOMMENDATIONS FOR FURTHER STUDY

The potential improvements and possible extensions of the present study are:

219

(1) Extension of the proposed model to apply for area-averaged pressures by considering the cross-correlation function of time series from adjacent taps.

(2) Extensive investigation of the present model to find out a means to accommodate the non-stationarity present in some full-scale fluctuations.

(3) Improvement of the present skeleton model by considering better exponential random number generators. Further, a study to explore new skeleton models for controlling various different fluctuating features of similar time series observed in other fields with a view to extend the application of the proposed model.

(4) Improvement of the present categorization of spectra on roofs by carrying out extensive wind tunnel measurements of pressure spectra on several low building roofs. Further, extension of the present categorization of the spectra as well as associated parameters of the model for various zones on other building geometries including walls. This procedure will help in systemizing pressure fluctuations on building envelopes for practical applications. The present work covers pressure time series only on roofs by considering three different roof geometries.

(5) Extensive fatigue analysis study using simulated pressure fluctuations to investigate the influence of several parameters on fatigue damage accumulation process. Further, it would be of interest to carry out fatigue analysis of roof cladding by directly applying the simulated pressure fluctuations on roofs using test rigs such as BRERWULF, and by using the simulated pressure fluctuations as forcing function in Finite Element Analysis of modelled roof.

(6) Codification of pressure time series as well as pressure spectra by utilizing the proposed simulation methodology and empirical equation for spectra.

REFERENCES

AFNOR A03 - 406 (1993). "Produits metalliques - Fatigue sous sollicitations d'amplitude variable - Methode rainflow de comptage des cycles." *AFNOR*, France.

Ammon, D. (1990). "Approximation and generation of Gaussian and non-Gaussian stationary processes." *Structural Safety*, 8, 153-160.

Amzallag, C., Gerey, J. P., and Bahuaud, J. (1994). "Standardization of the rainflow counting method for fatigue analysis." *Fatigue*, 16, 287-293.

AS 1170.2. (1989). *Minimum Design Loads on Structures, Part 2: Wind Loads*. Standards Association of Australia, North Sydney.

ASCE Committee on Fatigue and Fracture Reliability. (1982). "Fatigue reliability: Variable amplitude loading." *Journal of Structural Engineering*, ASCE, 108(1), 47-69.

ASCE Committee on Wind Tunnel Studies of Buildings and Structures. (1996). "Wind tunnel studies of building and structures." *Journal of Aerospace Engineering*, ASCE, 9(1), 19-36.

Assessment of damage to single-family homes caused by Hurricanes Andrew and Iniki. (1993). Report HUD-PD and R-1432, U.S. Department of Housing and Urban Development, Washington.

Bendat, J. S., and Piersol, A. G. (1986). *Random Data: Analysis and Measurement Procedures*. John Wiley & Sons, Second Edition.

Bienkiewicz, B., and Sun, Y. (1992). "Local wind loading on the roof of a low-rise building." *Journal of Wind Engineering and Industrial Aerodynamics*, 45, 11-24.

Borgman, L. E. (1969). "Ocean wave simulation for engineering design." *Journal of Waterways Harbours*, ASCE, 95(4), 557-583.

Box, G. E. P., and Jenkins, G. M. (1976). *Time Series Analysis: Forecasting and Control*. Holden Day, San Francisco, California.

Brockwell, P. J., and Davis, R. A. (1991). *Time Series: Theory and Methods*. Springer Verlag.

Brook, D., and Wynne, R. J. (1988). *Signal Processing; Principles and Applications*. Edward Arnold, London.

Brown, B. G., Katz, R. W., and Murphy, A. H. (1984). "Time series models to simulate and forecast wind speed and wind power." *Journal of Climate and Applied Meteorology*, 23, 1184-1195.

Cermak, J. E. (1995). "Progress in physical modeling for wind engineering." *Journal of Wind Engineering and Industrial Aerodynamics*, 54/55, 439-455.

Chatfield, C. (1989). *The Analysis of Time Series, An Introduction*. Fourth Edition, Chapman and Hall.

Clark, C. E., and Holz, B. W. (1960). "Exponentially distributed random numbers." Published for Operations Research Office, The John Hopkins University, Baltimore.

Cook, N. J. (1985). *The Designer's Guide to Wind Loading of Building Structures, Part-1*. Butterworths, London.

Cook, N. J. (1990). *The Designer's Guide to Wind Loading of Building Structures, Part-2. Static Structures*. Butterworth's, London.

Cook, N. J. (1992). "Dynamic response of single-ply membrane roofing systems." *Journal of Wind Engineering and Industrial Aerodynamics*, 41-44, 1525-1536.

Cook, N. J., Keevil, A. P., and Stobart, R. K. (1988). "BRERWULF - The Big Bad Wolf." *Journal of Wind Engineering and Industrial Aerodynamics*, 29, 99-107.

Council on Low-Rise Buildings (1993). *Guidelines for Design of Low-Rise Buildings subjected to Lateral Forces*. Edited by A.K. Gupta and P.J. Moss, CRC Press, Boca Raton, Florida.

Crandall, S. H., and Zhu, W. Q. (1983). "Random Vibrations: A survey of recent developments." *Journal of Applied Mechanics*, ASME, 50, 953-962.

DABM (1976). *Darwin area building manual*. Darwin Reconstruction Commission, Darwin, Australia.

Dalgliesh, W. A. (1979). "Assessment of wind loads for glazing design." *IAHR/IUTAM Symposium on Practical Experiences with Flow-Induced Vibrations*, Karlsruhe, Germany.

Dalgliesh, W. A., Templin, J. T., and Cooper, K. R. (1980). "Comparisons of wind tunnel and full-scale building surface pressures with emphasis on peaks." *Proceedings of the Fifth International Conference on Wind Engineering*, Pergamon Press.

Davenport, A. G. (1961). "The spectrum of horizontal gustiness near the ground in high winds." *Quarterly Journal of Royal Meteorological Society*, 87, 194-211.

Davenport, A. G. (1966). "The estimation of load repetitions on structures with application to wind induced fatigue and overload." *Proceedings of the International Symposium on the Effects of Repeated Loading of Materials and Structures*, RILEM Instituto de Ingeneria, Mexico City, Mexico.

Davenport, A. G. (1968). "The dependence of wind loads on meteorological parameters." *Proceedings of the International Research Seminar on Wind Effects on Buildings and Structures*, University of Toronto Press, Toronto, Canada.

Dowling, N. E. (1972). "Fatigue failure predictions for complicated stress-strain histories." *Journal of Materials*, JMLSA, 7(1), 71-87.

Fortier, L. J., and Scanlan, R. H. (1979). "A cooling tower wind loading model based on full scale data." *Proceedings of the Fifth International Conference on Wind Engineering*, Fort Collins, Colorado.

Fuchs, H. O., and Stephens, R. I. (1980). *Metal Fatigue in Engineering*. John Wiley & Sons, New York.

Gaver, D. P., and Lewis, P. A. W. (1980). "First-order autoregressive gamma sequences and point processes." *Advances in Applied Probability*, 12, 727-745.

Gerhardt, H. J., and Kramer, C. (1986). "Wind induced loading cycle and fatigue testing of light weight roofing fixations." *Journal of Wind Engineering and Industrial Aerodynamics*, 23, 237-247.

Goto, H., and Toki, K. (1969). "Structural response to nonstationary random excitation." *Proceedings of 4th World Conference on Earthquake Engineering*, Santiago, Chile, 1, 130-144.

Grigoriu, M. (1984). "Crossings of non-Gaussian translation processes." *Journal of Engineering Mechanics*, ASCE, 110(4), 610-620.

Grigoriu, M. (1993). "On the spectral representation method in simulation." *Probabilistic Engineering Mechanics*, 8, 75-90.

Grigoriu, M. (1995). *Applied Non-Gaussian Processes*. PTR Prentice Hall, NJ.

Gumbel, E. J. (1958). *Statistics of Extremes*. Columbia University Press, N.Y.

Gurley, K. R., Kareem, A., and Tognarelli, M. A. (1996). "Simulation of a class of non-normal random processes." *International Journal of Non-Linear Mechanics*, 31(5), 601-617.

Holmes, J. D. (1981). "Non-Gaussian characteristics of wind pressure fluctuations." *Journal of Wind Engineering and Industrial Aerodynamics*, 7, 103-108.

Islam, M. S., Ellingwood, B. R., and Corotis, R. B. (1988). "Generation of Statistically Consistent Time Histories using Transfer Function Models." *CE Research Report*, #1988-3-7, Dept.of Civil Engineering, The Johns Hopkins University, Baltimore, MD.

Iyengar, R. N., and Jaiswal, O. R. (1993). "A new model for non-Gaussian random excitations." *Probabilistic Engineering Mechanics*, 8, 281-287.

Janacek, G. J., and Swift, A. L. (1990). "A class of models for non-Normal time series." *Journal of Time Series Analysis*, 11(1), 19-31.

Jancauskas, E. D., Mahendran, M., and Walker, G. R. (1994). "Computer simulation of the fatigue behaviour of roof cladding during the passage of a tropical cyclone." *Journal of Wind Engineering and Industrial Aerodynamics*, 51, 215-227.

Jones, N. P., Reed, D. A., and Cermak, J. E. (1995). "National wind hazards reduction program." *Journal of Professional Issues in Engineering Education and Practice*, ASCE, 121(1), 41-46.

Kareem, A. (1993). "Simulation of stochastic wind effects." *Proceedings of the Seventh U.S. National Conference on Wind Engineering*, Los Angeles, California.

Kareem, A., Gurley, K., and Tognarelli, M. A. (1995). "Advanced analysis and simulation tools for wind engineering." *Proceedings of the 9th International Conference on Wind Engineering*, New Delhi, India.

Kasperski, M., and Koss, H. (1996). "Beatrice joint project wind action on low-rise buildings. Part 2: Analysis in the frequency domain." *Third International Colloquium on Bluff Body Aerodynamics and Applications*, Blacksburg, Virginia.

Kawai, H., and Nishimura, G. (1996). "Characteristics of fluctuating suction and conical vortices on a flat roof in oblique flow." *Journal of Wind Engineering and Industrial Aerodynamics*, 60, 211-225.

Knuth, D. E. (1981). *The art of Computer Programming, Vol. 2 : Seminumerical Algorithms*. 2nd Edition, Addison-Wesley.

Kramer, C. (1985). "Wind Effects on Roofs and Roof Coverings." *Proceedings of the Fifth U.S.National Conference on Wind Engineering*, Texas Tech University, Lubbock.

Lawrence, A. J., and Lewis, P. A. W. (1985). "Modelling and residual analysis of nonlinear autoregressive time series in exponential variables." *Journal of the Royal Statistical Society*, Series B , 47(2), 165-202.

Leicester, R. H., and Reardon, G. F. (1976). "Wind Damage in Australia- A Pictorial Review with particular Reference to Domestic and other Low-Rise Structures." *Division of Building Research*, CSIRO, Melbourne.

Letchford, C. W., Iverson, R. E., and McDonald, J. R. (1993). "The application of the Quasi-steady Theory to full scale measurements on the Texas Tech Building." *Journal of Wind Engineering and Industrial Aerodynamics*, 48, 111-132.

Letchford, C. W., and Norville, H. S. (1994). "Wind pressure loading cycles for wall cladding during hurricanes." *Journal of Wind Engineering and Industrial Aerodynamics*, 53, 189-206.

Li, Y., and Kareem, A. (1990). "ARMA systems in wind engineering." *Probabilistic Engineering Mechanics*, 5(2), 50-59.

Li, Y., and Kareem, A. (1993). "Simulation of multivariate random processes: hybrid DFT and digital filtering approach." *Journal of Engineering Mechanics*, ASCE, 119(5), 1078-1098.

Logan, L., Graham, V., and Unny, T. E. (1988). "Probability and stochastic modelling of water quality parameters in the Thames river." *Canadian Journal of Civil Engineering*, 15, 430-436.

Lutes, L. D., Corazao, M., Hu, S. J., and Zimmerman, J. (1984). "Stochastic fatigue damage accumulation." *Journal of Structural Engineering*, ASCE, 110(11), 2585-2601.

Lynn, B. A., and Stathopoulos, T. (1985). "Wind-Induced Fatigue on Low Metal Buildings." *Journal of Structural Engineering*, ASCE, 111(4), 826-839.

Mahendran, M. (1994). "Steel roof claddings under simulated cyclonic wind forces." *Civil Engineering Transactions*, IEA, CE36(1), 1-10.

Mahendran, M. (1995). "Wind-resistant low-rise buildings in the tropics." *Journal of Performance of Constructed Facilities*, ASCE, 9(4), 330-346.

Mardia, K. V. (1970). "A translation family of bivariate distributions and Frechet's bounds." *Sankya, The Indian Journal of Statistics*, 32, Series A (part 1), 119-122.

MATLAB (1992). *High Performance Numeric Computation and Visualization Software*. The MathWorks Inc., Massachusettes.

MATLAB (1994a). *Optimization ToolBox User's Guide*. The MathWorks Inc., Massachusetts.

MATLAB (1994b). *Statistics ToolBox User's Guide*. The MathWorks Inc., Massachusetts.

McDonald, J. R. (1985). "Extreme winds and tornados: An overview." *A Minicourse presented at DOE Natural Phenomena Hazards Mitigation Conference*, Las Vegas.

225

Melbourne, W. H. (1977). "Loading cycles for simulation of wind loading." *Proceedings of the Workshop on Guidelines for Cyclone Product Testing and Evaluation*, Experimental Building Station, Department of Housing and Construction, Australia.

Mengali, G., and Micheli, M. (1994). "Simulation of turbulent fluctuations." *AIAA Journal*, 32(11), 2210-2216.

Mignolet, M. P., and Spanos, P. D. (1990). "MA to ARMA modelling of wind." *Journal of Wind Engineering and Industrial Aerodynamics*, 36, 429-438.

Milford, R. V., Waldeck, J. L., and Goliger, A. M. (1992). "JAN SMUTS EXPERIMENT: Details of full-scale experiment." *Journal of Wind Engineering and Industrial Aerodynamics*, 41-44, 1693-1704.

Mohammadian, A. R. (1989). "Wind Loads on Buildings with Monosloped Roofs: Stochastic Modelling of Wind Pressure Fluctuations." *Ph.D Thesis*, Concordia University, Montreal.

Morgan, J. W., and Beck, V. R. (1977). "Failure of sheet-metal roofing under repeated wind loading." *Civil Engineering Transactions*, IEA, CE19(1), 1-5.

Murakami, S., Hibi, K., and Mochida, A. (1991). "Numerical study of unsteady pressure fields around buildings by means of large eddy simulation." *The Fourth International Conference on Computing in Civil and Building Engineering*, Tokyo, Japan.

NBCC. (1995). *User's Guide - NBC 1995, Structural Commentaries (Part 4)*. National Research Council of Canada, Ottawa, Canada.

Nigam, N. C. (1983). *Introduction to Random Vibrations*. The MIT Press, Massachusetts.

Osgood, C. C. (1982). *Fatigue Design*. Second Edition, Pargamon Press.

Pankrats, A. (1983). *Forecasting with Univariate Box-Jenkins Models, Concepts and cases*. John Wiley & Sons Inc.

Panofsky, H. A., and McCormick, R. A. (1954). "Properties of spectra of atmospheric turbulence at 100 metres." *Quarterly Journal of Royal Meteorological Society*, 80, 546-564.

Papoulis, A. (1984). *Probability, Random Variables and Stochastic Processes*. McGraw-Hill Inc., Second Edition.

Park, S. K., and Miller, K. W. (1988). "Random number generators: Good ones are hard to find." *Communications of the ACM*, 31(10), 1192-1201.

226

Patel, K., and Freathy, P. (1984). "A simplified method for assessing wind-induced fatigue damage." *Engineering Structures*, 6, 268-273.

Peterka, J. A. (1981). "Probability distributions of local peak pressures." *Proceedings of the fourth U.S. National Conference on Wind Engineering*, Seattle.

Peterka, J. A., and Cermak, J. E. (1975). "Wind pressures on buildings - probability densities." *Journal of Structural Engineering*, ASCE, 101(6), 1255-1267.

Reed, D. A. (1993). "Influence of non-Gaussian local pressures on cladding glass." *Journal of Wind Engineering and Industrial Aerodynamics*, 48, 51-61.

Reed, D. A., and Scanlan, R. H. (1983). "Time series analysis of cooling tower wind loading." *Journal of Structural Engineering*, ASCE, 109(2), 538-554.

Reed, D. A., and Scanlan, R. H. (1984). "Autoregressive representation of longitudinal, lateral and vertical turbulence spectra." *Journal of Wind Engineering and Industrial Aerodynamics*, 17, 199-214.

Rice, S. O. (1954). "Mathematical analysis of random noise." Selected papers on noise and stochastic processes, N.Wax, ed., Dover, New York, 133-294.

Robson, J. D. (1963). *An Introduction to Random Vibration.* Edinburgh University Press.

Schiess, J. K. (1986). "Composite statistical method for modelling wind gusts." *Journal of Aircraft*, 23(2), 131-135.

Seong, S. H. (1993). "Digital Synthesis of Wind Pressure Fluctuations on Building Surfaces." Ph.D Thesis, Colorado State University, Fort Collins.

Seong, S. H., and Peterka, J. A. (1993). "Computer simulation of non-Gaussian wind pressure fluctuations." *Proceedings of the Seventh U.S. National Conference on Wind Engineering*, Los Angeles, California.

Shinozuka, M. (1971). "Simulation of multivariate and multidimensional random processes." *Journal of Acoustical Society of America*, 49(1), (part 2), 357-367.

Shinozuka, M., and Jan, C.M. (1972). "Digital simulation of random processes and its applications." *Journal of Sound and Vibration*, 25(1), 111-128.

Shinozuka, M., and Tan, R. (1981). "Probabilistic load combinations and crossing rates." *EMD/STD Symposium on Probabilistic Methods in Structural Engineering*, St.Louis.

Siddall, J. N. (1983). *Probabilistic Engineering Design: Principles and Applications.* Marcel Dekker, Inc.

227

Simiu, E., and Scanlan, R. H. (1986). *Wind Effects on Structures: An Introduction to Wind Engineering.* John Wiley & Sons, Second Edition.

Simpson, R. L. (1989). "Turbulent boundary-layer separation." *Annual Review of Fluid Mechanics*, 21, 205-234.

Spanos, P. D., and Mignolet, M. P. (1988). "ARMA Monte-Carlo simulation in probabilistic structural analysis." *Shock and Vibration Digest*, 20, 3-14.

Stathopoulos, T. (1980). "PDF of wind pressures on low-rise buildings." *Journal of Structural Engineering*, ASCE, 106(5), 973-990.

Stathopoulos, T. (1983). "Fluctuating wind pressures on low building roofs." Technical Note, *Journal of Structural Engineering*, ASCE, 109(1), 266-271.

Stathopoulos, T. (1984a). "Design and fabrication of a wind tunnel for building aerodynamics." *Journal of Wind Engineering and Industrial Aerodynamics*, 16, 361-376.

Stathopoulos, T. (1984b). "Wind Loads on Low-Rise Buildings: A Review of the State of the Art." *Engineering Structures*, 6, 119-135.

Stathopoulos, T., and Mohammadian, A. R. (1991). "Modelling of wind pressures on monoslope roofs." *Engineering Structures*, 13, 281-292.

Stathopoulos, T., Suresh Kumar, K., and Mohammadian, A. R. (1997). "Design wind pressure coefficients for monoslope roofs: A time series approach." *Journal of Wind Engineering and Industrial Aerodynamics*, in press.

Stathopoulos, T., Surry, D., and Davenport, A. G. (1981). "Effective wind loads on flat roofs." *Journal of Structural Engineering*, ASCE, 107(2), 281-298.

Suresh Kumar, K., and Stathopoulos, T. (1995). "Stochastic modelling of wind pressure fluctuations on low building roofs." 15th Canadian Congress in Applied Mechanics *(CANCAM '95)*, University of Victoria, Victoria.

Suresh Kumar, K., and Stathopoulos, T. (1996a). "Computer simulation of fluctuating wind pressures on low building roofs." *Third International Colloquium on Bluff Body Aerodynamics and Applications*, Blacksburg, Virginia.

Suresh Kumar, K., and Stathopoulos, T. (1996b). "Computer simulation of wind-induced fatigue on roof cladding." *Proceedings of the third Canadian Conference on Computing in Civil and Building Engineering*, CSCE, Montreal, Canada.

Suresh Kumar, K., and Stathopoulos, T. (1997a). Discussion on "Random field modelling of railway track irregularities" by R.N. Iyengar and O.R. Jaiswal, *Journal of Transportation Engineering*, ASCE, 123(3), 245.

Suresh Kumar, K., and Stathopoulos, T. (1997b). "Synthesis of non-Gaussian wind pressure time series on low building roofs." *Engineering Structures*, (submitted for publication).

Suresh Kumar, K., and Stathopoulos, T. (1997c). "SDF of wind pressures on low building roofs." *Journal of Structural Engineering*, ASCE, (submitted for publication).

Suresh Kumar, K., and Stathopoulos, T. (1997d). "Fatigue analysis of roof cladding under simulated wind loading." *Proceedings of the 8th U.S. National Conference on Wind Engineering*, Baltimore, Maryland.

Suresh Kumar, K., and Stathopoulos, T. (1997e). "Power spectra of wind pressures on low building roofs." *Proceedings of the 2nd European and African Conference on Wind Engineering*, Genova, Italy.

Texas Tech Field Experiment Data Package. (1992). Texas Tech University, Lubbock, Texas.

Tieleman, H. W. (1992). "Problems associated with flow modelling procedures for low-rise structures." *Journal of Wind Engineering and Industrial Aerodynamics*, 41-44, 923-934.

Tieleman, H. W. (1995). "Universality of velocity spectra." *Journal of Wind Engineering and Industrial Aerodynamics*, 56, 55-69.

Tieleman, H. W., and Hajj, M. R. (1995). "Pressures on flat roof - Application of Quasi-Steady theory." *Proceedings of the 10th Conference in Engineering Mechanics*, Boulder, Colorado.

Tong, H. (1990). *Non-Linear Time Series: A Dynamical System Approach*. Clarendon, Oxford.

TR440 (1978). "Guidelines for the testing and evaluation of products for cyclone prone areas." Tech. Record 440, Experimental Building Station, Department of Housing and Construction, Australia.

Vanmarcke, E. H. (1972). "Properties of spectral moments with applications to random vibration." *Journal of Engineering Mechanics*, ASCE, 98(2), 425-446.

Vanmarcke, E. H. (1983). *Random Fields: Analysis and Synthesis*. The MIT Press, Cambridge.

229

Walker, G. R. (1975). "Report on Cyclone Tracy - Effect on Buildings - December 1974, Vol. 1." *Australian Department of Housing and Construction*, Melbourne, Australia.

Winterstein, S. R. (1988). "Nonlinear vibration models for extremes and fatigue." *Journal of Engineering Mechanics*, ASCE, 114(10), 1772-1790.

Winterstein, S. R., and Lange, C. H. (1995). "Moment-based probability models for wind engineering applications." *Proceedings of 10th Conference in Engineering Mechanics*, Boulder, Colorado.

Wirsching, P. H., and Light, M. C. (1980). "Fatigue under wide band random stresses." *Journal of Structural Engineering*, ASCE, 106(7), 1593-1607.

Wittig, L. E., and Sinha, A. K. (1975). "Simulation of multi-correlated random processes using the FFT algorithm." *Journal of the Acoustical Society of America*, 58(3), 630-634.

Wu, H. (1994). "Pedestrian-level wind environment around buildings." *Ph.D Thesis*, Centre for Building Studies, Concordia University, Montreal.

Wyatt, T. A., and May, H. I. (1973). "The generation of stochastic load functions to simulate wind loading on structures." *Earthquake Engineering and Structural Dynamics*, 1, 217-224.

Xu, Y. L. (1993). "Wind-induced fatigue loading on roof cladding of low-rise buildings." *Technical Report No. 41*, Cyclone Testing Station, Department of Civil and Systems Engineering, James Cook University, Townsville, Australia.

Xu, Y. L. (1995a). "Model and full-scale comparison of fatigue-related characteristics of wind pressures on the Texas Tech building." *Journal of Wind Engineering and Industrial Aerodynamics*, 58, 147-173.

Xu, Y. L. (1995b). "Fatigue performance of screw-fastened light-gauge-steel roofing sheets." *Journal of Structural Engineering*, ASCE, 121(3), 389-398.

Yamazaki, F., and Shinozuka, M. (1988). "Digital generation of non-Gaussian stochastic fields." *Journal of Engineering Mechanics*, ASCE, 114(7), 1183-1197.

Appendix - A
Matlab Functions

The MATLAB functions developed for all numerical applications in this thesis are provided in this appendix. The functions are grouped under four directories: **statistics, simulation of random processes, empirical fitting,** and **estimation of fatigue damage**. The MATLAB High-Performance Computation and Visualization Software (1992) and a personal computer are needed to use these functions. All the numerical results in this thesis were obtained using Pentium-60 computer system. Further, these functions can be converted to stand-alone C programs using MATLAB C compiler.

A.1 Statistics

In this section, there are four functions. The function **MOM_ST** can be used to calculate the first four moments (mean, variance, skewness and kurtosis) of a given time series, x. The function **SPECM_ST** can be used to estimate the basic spectral properties such as number of zero up-crossings and peaks, bandwidth and irregularity factor based on given spectrum. The function **CROSS_ST** can be used to compute the number of mean up-crossings or down-crossings at specified levels of a given time series. The number of positive or negative peaks of a given time series can be estimated using the function **PEAK_ST**.

A.2 SIMULATION OF RANDOM PROCESSES

There are five functions provided in this section. The functions **GSPEC** and **GTIME** can be used to generate Gaussian time series samples based on given spectra and time history respectively. While, the functions **NGSPEC** and **NGTIME** can be used to generate non-Gaussian time series samples based on given spectra and time history respectively. The parameter b, which induces the specified non-normality in terms of skewness and kurtosis in a time series can be estimated using the function **PAR_EST**.

A.3 EMPIRICAL FITTING

There are two functions included in this section. The functions **FIT** and **FUNFIT** can be used to fit any spectral data. The user can even change the equation to be fitted, but the program should accordingly be modified based on the new equation.

A.4 ESTIMATION OF FATIGUE DAMAGE

There are five functions in this section. The function **RFLOW** can be used to calculate total number of cycles involved in a time series as well as the histogram showing the number of cycles at various range and mean level of cycles. The standardized rainflow algorithm (Amzallag et al. 1994) is applied to count the number of cycles. The function **DAM_TH** can be used to estimate the damage rate caused by a given time series on to a specific

building component, and the mean life time of the building component. The function **DAM_W** can be used to calculate the wind-induced damage based on Gaussian-Weibull extremum model suggested by Lynn and Stathopoulos (1985). The function **DAM_G** can be used to estimate the wind-induced fatigue damage based on Gaussian model (Robson 1963). Finally, the function **DAM_TOT** can be used to compute the total fatigue wind loading matrix after including the long-term wind climate and the corresponding damage caused by the total loading.

MOM_ST

```
function [m1,m2,m3,m4]=mom_st(x)
%mom_st
%       Estimates mean(m1), variance(m2),
%       skewness(m3), and kurtosis(m4) of a
%       time series, x.
%
%       x = data in column vector format.
%
m1=mean(x);
m2=var(x);
m3=mean(((x-m1)./std(x)).^3);
m4=mean(((x-m1)./std(x)).^4);
```

SPECM_ST

```
function [No,Np,irf,bp]=specm_st(sdf,T)
%specm_st
%       Estimates the basic spectral properties
%       assuming that the given spectrum corresponds
%       to stationary narrowband Gaussian time series
%
%       No      = number of zero up-crossing or down-crossing
%       Np      = number of upward or downward peaks
%       irf     = irregularity factor
%       bp      = bandwidth parameter
%       sdf     = one sided physical spectrum (column vector (n,2))
%                 Ist column corresponds to frequency and the other represents
%                 spectral ordinates.
%       T       = time in seconds (length of time history)
%
f=sdf(:,1);
df=f(3)-f(2);
s=sdf(:,2);
m0=sum(s.*df);
m2=sum(s.*((f.^2).*df));
m4=sum(s.*((f.^4).*df));
No=sqrt(m2/m0)*T;
Np=sqrt(m4/m2)*T;
irf=No/Np;
bp=sqrt(1-(irf^2));
```

CROSS_ST

```
function Nu=cross_st(x,lc)
%cross_st
%       Estimates the number of mean up-crossing or down-crossing
%       of a time series (x) at specified levels (lc)
%
%       lc      = vector showing the levels to be considered.
%       x       = data in column vector format.
%
%       Note: First the data is normalized with respect to
%       its standard deviation after the mean is subtracted.
%       Therefore, the levels (lc) can be either negative or
%       positive.
%
z=(x-mean(x))./std(x);
[m,n]=size(z);
ll=length(lc);
z1=z;
z2=[z(2:m);z(1)];
for i=1:ll,
  Nu(i)=sum(z1<=lc(i) & z2>lc(i));
end
```

PEAK_ST

```
function Np=peak_st(x)
%peak_st
%       Estimates the number of positive and negative peaks
%       of a time series, x.
%
%       x = data in column vector format.
%
[m,n]=size(x);
j=1;
j1=1;
for i=1:m-2;
  s1=x(i+1)-x(i);
  s2=x(i+2)-x(i+1);
    if(s1>0 & s2<0),
      z1(j)=i+1;
      j=j+1;
```

```
elseif (s1<0 & s2>0),
   z2(j1)=i+1;
   j1=j1+1;
 end
 if (s1>0 & s2==0),
   s3=x(i+3)-x(i+2);
    if (s3<0),
      z1(j)=i+1;
      j=j+1;
    end
 end
 if(s1<0 & s2==0),
   s3=x(i+3)-x(i+2);
    if (s3>0),
      z2(j1)=i+1;
      j1=j1+1;
    end
  end
end
Np(1)=sum(ones(size(z1)));
Np(2)=sum(ones(size(z2)));
```

GSPEC

```
function [t,y]=gspec(spp,me,vari,fs,n,n1)
%gspec
%        Generates Gaussian time histories
%        based on given spectra
%
%      spp    = one sided normalized spectra (variance=1)
%               (length = n/2-1)
%      me     = mean of the time series
%      vari   = variance of the time series
%      fs     = sampling frequency
%      n      = length of time series (data points)
%      n1     = number of samples to be generated
%      t      = time vector
%      y      = simulated time history
%
%        Estimation of time vector and
```

```
%          frequency resolution (df)
%
df = fs/n;
t  = [1/fs:1/fs:n/fs]';
%
%          Construction of amplitude
%
sp1 = spp.*(vari/2);
sp2 = [0;sp1;sp1((n/2)-1);flipud(sp1)];
amp = ((sp2.*df).*(length(sp2)^2)).^(1/2);
%
%          Construction of phase
%
rand('seed',0)
for i1  = 1:1:n1;
  unif  = unifrnd(-pi,pi,n/2,1);
  phase = [0;unif;-flipud(unif(1:(n/2)-1))];
%
%          Construction of signal
%
  z      = amp.* exp(sqrt(-1).* phase);
  y(1:n,i1) = real(ifft(z))+me;
end
```

GTIME

```
function [t,y]=gtime(th,n1)
%gtime
%          Generates Gaussian time histories
%          based on given Gaussian time history (th)
%
%          th      = given time history in column vector format,
%                    Ist column represents time vector, t and IInd
%                    column corresponds to the ordinates.
%          n1      = number of samples to be generated
%          t       = time vector
%          y       = simulated time history
%
%
t = th(:,1);
```

```
th1 = th(:,2);
[n,c] = size(th1);
me   = mean(th1);
%
%        Construction of amplitude
%
amp = abs(fft(th1-me));
%
%        Construction of phase
%
rand('seed',0)
for i1  = 1:1:n1;
  unif = unifrnd(-pi,pi,n/2,1);
  phase = [0;unif;-flipud(unif(1:(n/2)-1))];
%
%        Construction of signal
%
  z      = amp.* exp(sqrt(-1).* phase);
  y(1:n,i1) = real(ifft(z))+me;
end
```

PAR_EST

```
function b=par_est(spp,vari,fs,n,sk,ku)  % use this if spectra is given
%function b=par_est(th)  % use this if time history is given
%par_est
%        Estimates the parameter (b) which induces
%        non-normality in time series.
%
%        spp     = one sided normalized spectra (variance=1)
%                  (length = n/2-1)
%        th      = given time history in column vector format
%        vari    = variance of the time series
%        fs      = sampling frequency
%        sk      = skewness of the time series
%        ku      = kurtosis of the time series
%
%        Construction of amplitude
%        (Use this section if spectra is given)
df = fs/n;
```

```
sp1=spp.*(vari/2);
sp2=[0;sp1;sp1((n/2)-1);flipud(sp1)];
amp=((sp2.*df).*(length(sp2)^2)).^(1/2);
%
%        Construction of amplitude
%        (Use this section if time history is given)
%vari=var(th);
%[n,c]=size(th);
%sk=mean(((th-mean(th))./std(th)).^3);
%ku=mean(((th-mean(th))./std(th)).^4);
%amp=abs(fft(th-mean(th)));
%
%
sqd1=10^51;
b1=0.0:0.01:0.99;
rand('seed',0);
unif=unifrnd(0,1,2*n,1);
for k=1:100;
%
%        Construction of phase
%
  e = 99999* ones(n,1);
  l = 0;
  for i = 1:2:(2*n)-1;
    if (unif(i) < b1(k) & unif(i) > 0),
      e(i-l) = 0;
    else
      e(i-l) = (1).* log(unif(i+1));
    end
  l=l+1;
  end
  index = find(e == 99999);
  e(index) = [];
  z    = fft(e);
  phase = angle(z);
%
%        Construction of signal
%
Z    = amp.* exp(sqrt(-1).* phase);
y    = real(ifft(Z));
%
%        Finding the optimum value of b which
%        achieves the given sk and ku
```

```
%
skew(k)   = mean(((y-mean(y))./std(y)).^3);
ersk      = (sk-skew(k));
kurt(k)   = mean(((y-mean(y))./std(y)).^4);
erku      = (ku-kurt(k));
sqd(k)    = ersk^2 + erku^2;
  if (sqd(k) <=sqd1),
    sqd1  = sqd(k);
    res   = [b1(k) sqd];
    b     = b1(k);
  end
end
```

NGSPEC

```
function [t,y]=ngspec(spp,me,vari,b,fs,n,n1)
%ngspec
%       Generates Non-Gaussian time histories
%       based on given spectra (spp).
%
%       spp    = one sided normalized spectra (variance=1)
%                 (length = n/2-1)
%       me     = mean of the time series
%       vari   = variance of the time series
%       b      = parameter which induces non-normality
%       fs     = sampling frequency
%       n      = length of time series
%       n1     = number of samples to be generated
%       t      = time vector
%       y      = simulated time history
%
%
%       Construction of time vector and
%       frequency resolution (df)
%
df = fs/n;
t = [1/fs:1/fs:n/fs]';
%
%
%       Construction of Amplitude
```

```
%
sp1=spp.*(vari/2);
sp2=[0;sp1;sp1((n/2)-1);flipud(sp1)];
amp=((sp2.*df).*(length(sp2)^2)).^(1/2);
%
%
%        Construction of Phase using EPG model
%
rand('seed',0);
for i1 = 1:1:n1;
  unif=unifrnd(0,1,2*n,1);
    e = 99999* ones(n,1);
    l = 0;
  for i = 1:2:(2*n)-1;
    if (unif(i) < b & unif(i) > 0),
      e(i-l) = 0;
      else
      e(i-l) = (l).* log(unif(i+1));
    end
  l=l+1;
  end
    index = find(e == 99999);
    e(index) = [];
  phase=angle(fft(e));
%
%
%        Construction of signal
%
  z        = amp.* exp(sqrt(-1).* phase);
  y(1:n,i1)  = real(ifft(z))+me;
end
```

NGTIME

```
function [t,y]=ngtime(th,b,n1)
%ngtime
%        Generates non-Gaussian time histories
%        based on given non-Gaussian time history (th)
%
%        th      = given time history in column vector format,
```

```
%                 Ist column - time vector, IInd column - ordinates
%       b       = parameter which induces non-normality
%       n1      = number of samples to be generated
%       t       = time vector
%       y       = simulated time history
%
%
t = th(:,1);
th1 = th(:,2);
[n,c] = size(th1);
me   = mean(th1);
%
%
%       Construction of Amplitude
%
amp = abs(fft(th1-me));
%
%       Construction of Phase using EPG model
%
rand('seed',0);
for i1 = 1:1:n1;
  unif=unifrnd(0,1,2*n,1);
    e = 99999* ones(n,1);
    l = 0;
  for i = 1:2:(2*n)-1;
    if (unif(i) < b & unif(i) > 0),
      e(i-l) = 0;
      else
      e(i-l) = (1).* log(unif(i+1));
    end
  l=l+1;
  end
    index = find(e == 99999);
    e(index) = [];
  phase=angle(fft(e));
%
%       Construction of signal
%
  z        = amp.* exp(sqrt(-1).* phase);
  y(1:n,i1) = real(ifft(z))+me;
end
```

FIT

```
function [c]=fit(sdf,c);
echo on; clc
%fit (This is a modified form of the demo file available in MATLAB)
%       This program can be used to fit a nonlinear function to a
%       set of data. It determines the optimum parameters of the
%       proposed function described in the M-file 'fitfun'.
%       Many of the different methods, available in
%       the OPTIMIZATION TOOLBOX, are introduced here in order to
%       provide the user to have full freedom about his choice of
%       method.
%
%       sdf = [fr s], data to be fitted
%       The data has two columns. The first column is independent variable (frequency) %
%       and the second column is dependent variable (spectral ordinates).
%
%       We would like to fit the function
%       exp(fr.*(-c(1))).*a(1)+exp(fr.*(-c(2))).*a(2)
%       to the data.  This function has 2 position parameters (a(1)
%       and a(2)) and 2 shape parameters (c(1) and c(2)).
%
%       Here c (2,1) vector is assumed based on experience; The optimum parametric %
%       values and the fitting will be shown in a figure window.
%
%       Note: This program can be easily modified to fit other
%       functions of the user's choice.
%
Data=sdf;
fr = Data(:,1);
s = Data(:,2);
clf
plot(fr,s,'o'), title('Input data'),
clc
%
echo off
disp('Please Wait - Compiling Optimization Routines')
%
% test_long is a variable used for auto testing of this routine
if ~exist('test_long') test_long = 0; end
if exist('method')~=1 method = 8; end
if ~length(method) method = 8; end
l = 2;
%
while 1
```

```
%
  if ~test_long
    clc
    disp('')
    disp('  Choose any method for datafit')
    disp('')
    disp('UNCONSTRAINED: 1) Broyden-Fletcher-Golfarb-Shanno')
    disp('            2) Davidon-Fletcher-Powell')
    disp('            3) Steepest Descent')
    disp('            4) Simplex Search')
    disp('LEAST SQUARES: 5) Gauss-Newton ')
    disp('            6) Levenberg-Marquardt ')
    disp('MINIMAX      7) Seq. Quadratic Progr.')
    disp('')
    disp('            0) Quit')
    disp('')
    disp('Note: Options 1:6 perform a least squares fit')
    disp('    Option 7 minimizes the worst case error')
    disp('    Gauss-Newton is the fastest method')
  end
%
  if test_long
    if l>=2
        method=method-1;
        l = 0;
    end
  else
      method= -1;
  end
  while (method<0 | method>7)
      method = [];
    while ~length(method)
      method = input('Select a method number: ');
    end
  end
%
  if (method == 0)
        return
  end
%
        OPTIONS=0;
        if method==2, OPTIONS(6)=1;
        elseif method==3, OPTIONS(6)=2;
```

```
          elseif method==4, OPTIONS(5)=1;
          elseif method==5, OPTIONS(5)=1;
          end
          if test_long
                1 = 1 + 1;
          else
                1 = [];
          end
%
  if method~=4&method~=7
    disp('')
    disp(' Choose any of the following line search methods')
    disp('')
    disp('        1) Mixed Polynomial Interpolation')
    disp('        2) Cubic Interpolation')
    disp('')
%
    while ~length(l)
        l = input('Select a line search number: ');
    end
    if l==2, OPTIONS(7)=1; end
  end
%
%
disp('')
OPTIONS(2)=1e-3;
t0=clock;
%
  if method==5|method==6
%
    disp('[c,OPTIONS]=leastsq("funfit", c,OPTIONS,[],Data);')
    [c,OPTIONS]=leastsq('funfit', c,OPTIONS,[],Data);
%
  elseif method==4
%
    disp('[c,OPTIONS]=fmins("norm(funfit(x,P1))",c, OPTIONS,[],Data); ')
    [c,OPTIONS]=fmins('norm(funfit(x,P1))',c, OPTIONS,[],Data);
%
  elseif method~=7;
%
    disp('[c,OPTIONS]=fminu("norm(funfit(x,P1))",c,OPTIONS,[],Data);')
    [c,OPTIONS]=fminu('norm(funfit(x,P1))',c,OPTIONS,[],Data);
%
```

```
    else
%
    OPTIONS(15)=length(t);
    disp('[c,OPTIONS]=minimax("f=funfit(x,P1); g=[];",c, OPTIONSR,[],[],[],Data);')
    [c,OPTIONS]=minimax('f=funfit(x,P1); g=[];', c, OPTIONS,[],[],[],Data);
%
  end
%
  if test_long
        if (method<=4) OPTIONS(8) = OPTIONS(8).^2; end
        if OPTIONS(8)-0.03*(method==7)-(method==3) > 0.15,
      error('Optimization Toolbox in datdemo'), end
  end
%
execution_time=etime(clock, t0)
disp('Strike any key for menu')
pause
%
end
```

FUNFIT

```
function f = funfit(c,Data)
%funfit
%      Returns the error between the data and the predicted
%      values computed using
%
fr = Data(:,1); s = Data(:,2);
A(:,1)=exp(fr.*(-c(1)));
A(:,2)=exp(fr.*(-c(2)));
a=A\s;
z=A*a;
f = (z-s);
sq=sum(f.*f);
% Statements to plot progress of fitting:
loglog(fr,z,'-b',fr,s,'-r')
xt = 0.01*max(abs(fr));
yt = max(s);
text(xt, yt,['(c = ' num2str(c(1)) '  ' num2str(c(2)),')'])
text(xt,0.5*yt,['(a = ' num2str(a(1)) '  ' num2str(a(2)),')'])
```

```
function [tot_cyc,fwlm]=rflow(x)
%rflow
%        Cycle counting using RAINFLOW algorithm from pressure
%        fluctuations. Based on Amzallag,C. , Gerey, J.P. ,
%        Robertt, J.L. and Bahuaud,J. (1994), "Standardization
%        of the rainflow counting method for fatigue analysis."
%        Fatigue, 16, 287-293.
%
%        x      = data in column vector format
%        tot_cyc = total number of cycles in data set, x
%        fwlm   = cycle histogram with m rows and n columns;
%                 which shows the ratios of the number of cycles
%                 in each cell to the tot_cyc; the two axes refer
%                 to the range (rows) and mean level (columns)
%                 of cycles expressed as a ratio of the
%                 largest pressure coefficient range of the
%                 time history.
%
%
% EXTRACTING EXTREMA
%
% ext=sequences of extrema;
z = x;
[r,c] = size(z);
j = 1;
j1 = 1;
  for i = 1:r-2;
    s1 = z(i+1)-z(i);
    s2 = z(i+2)-z(i+1);
      if (s1 > 0 & s2 < 0),
        z1(j) = i+1;
        j = j+1;
      elseif (s1 < 0 & s2 > 0),
        z2(j1) = i+1;
        j1 = j1+1;
      end
      if (s1 > 0 & s2 == 0),
        s3 = z(i+3)-z(i+2);
        if (s3 < 0),
          z1(j) = i+1;
          j = j+1;
        end
      end
```

```
      if (s1 < 0 & s2 == 0),
        s3 = z(i+3)-z(i+2);
          if (s3 > 0),
            z2(j1) = i+1;
            j1 = j1+1;
          end
        end
    end
z1 = z1';
z2 = z2';
z3 = [1;z1;z2;r];
z4 = sort(z3);
ext = z(z4);
clear r c j j1 z1 z2 z3 i
%
%
%  EXTRACTING CYCLES
%
[r,c] = size(ext);
cyc1 = [ 0 0 0 0];
i = 1;
  while ((i+3) <= r),
    s1 = abs(ext(i+1)-ext(i));
    s2 = abs(ext(i+2)-ext(i+1));
    s3 = abs(ext(i+3)-ext(i+2));
      if (s2 <= s1 & s2 <= s3),
        cyc1 = [cyc1; ext(i+1) ext(i+2) abs(ext(i+1)-...
            ext(i+2)) abs(ext(i+1)+ext(i+2))/2];
        ext = [ext(1:i);ext(i+3:r,1)];
        r = r-2;
        i = 1;
      else
        i = i+1;
      end
  end
res = ext;
clear i r c s1 s2 s3
%
%
%  TREATMENT OF THE RESIDUE (res)
%  [residue] + [residue] ------> [residue] + {cycles}
%
[h1,h2] = size(res);
```

```
r1 = res(1);
r2 = res(2);
m1 = res(h1-1);
m = res(h1);
  if ((m-m1)*(r2-r1) > 0 & (m-m1)*(r1-m) < 0)
    res1 = [res;res];
  end
  if ((m-m1)*(r2-r1) > 0 & (m-m1)*(r1-m) >= 0)
    res1 = [res(1:h1-1);res(2:h1)];
  end
  if ((m-m1)*(r2-r1) < 0 & (m-m1)*(r1-m) <= 0)
    res1 = [res;res(2:h1)];
  end
  if((m-m1)*(r2-r1) < 0 & (m-m1)*(r1-m) >= 0)
  res1 = [res(1:h1-1); res];
  end
[r,c] = size(res1);
cyc2 = cyc1;
i = 1;
  while ((i+3) <= r),
    s1 = abs(res1(i+1)-res1(i));
    s2 = abs(res1(i+2)-res1(i+1));
    s3 = abs(res1(i+3)-res1(i+2));
      if (s2 <= s1 & s2 <= s3),
        cyc2 = [cyc2; res1(i+1) res1(i+2) abs(res1(i+1)-...
            res1(i+2)) abs(res1(i+1)+res1(i+2))/2];
        res1 = [res1(1:i);res1(i+3:r,1)];
        r = r-2;
        i = 1;
      else
        i = i+1;
      end
  end
mi = max(cyc2(:,3));
mi1 = max(cyc2(:,4));
cyc3 = [cyc2(:,3)./mi cyc2(:,4)./mi];
clear i  r c s1 s2 s3 r1 r2 m m1
%
%
%  APPLYING THRESHOLD LEVEL
%  0.05*mi is considered as the threshold level.
%
```

```
%c1 = find(cyc3(:,3) >= 0.05);
%cyc = cyc3(c1,:);
%clear c1
cyc = cyc3;
%
%
% QUANTIFYING THE MEAN AND RANGE VALUES INTO CLASSES
% mea = mean value of a cycle; ran = range of a cycle.
%
[r,c]  = size(cyc);
mea    = cyc(1:r,2);
ran    = cyc(1:r,1);
me     = mea;
ra     = ran;
cl     = 0:0.1:1;
cl     = cl';
cl1    = 0.05:0.1:0.95;
cl1    = cl1';
  for k2 = 1:10;
    r2  = find(ra > cl(k2) & ra <= cl(k2+1));
    ra(r2) = ones(size(r2)).*cl1(k2);
    clear r2
  end
  for k3  = 1:10
    r1   = find(me > cl(k3) & me <= cl(k3+1));
    me(r1) = ones(size(r1)).*cl1(k3);
    clear r1
  end
clear r1 r2 k2 k3
%
%
% STORING CYCLES IN MATRIX FORMAT
%
FWLM1  = zeros([10,10]);
ra1    = (ra-0.05).*10+1;
me1    = (me-0.05).*10+1;
r1 = find(ra1 <= 10  &  me1 <= 10);
[r,c] = size(r1);
me2 = me1(r1);
ra2 = ra1(r1);
  for i = 1:r;
    k1 = ra2(i);
    k2 = me2(i);
```

```
FWLM1(k1,k2) = FWLM1(k1,k2)+1;
  end
ss     = sum(FWLM1);
tot_cyc = sum(ss);
fwlm   = FWLM1./tot_cyc; % Cycle histogram
clear k1 k2 k3 h ss cl
%
%
% 3-D Bar plot
%
xr = 0.05:.1:0.95;
xr = xr';
ym = 0.05:.1:0.95;
ym = ym';
bar33(ym,xr,fwlm)
```

DAM_TH

```
function [D, life]=dam_th(fwlm,V,n1,mi,Su,c1,b1)
%dam_th
%        Estimation of mean life time (life) and damage rate (D)
%
%
%        fwlm   = cycle histogram
%        V      = mean hourly wind velocity range of interest
%                 (column vector format)
%        n1     = number of cycles per hour per 1m/s of mean
%                 hourly wind velocity at building height
%        mi     = largest pressure coefficient range
%
%        Note: fwlm, V, n1, mi can be obtained from RFLOW function.
%
%        Constant-amplitude test results of the specimen
%        ----------------------------------------------
%        Su     = ultimate static strength of specimen
%        c1     = multiplying constant for S-N curve
%        b1     = slope of S-N curve
%
[m,n]=size(V);
xr = 0.05:0.1:0.95;
```

```
ym = 0.05:0.1:0.95;
i3 = 1;
  for i = 1:m;
    D1 = 0;
      for i1 = 1:10;
        Sf = xr(i1)*mi*(V(i)^2)*0.65/1000;
          for i2 = 1:10;
            Sm = ym(i2)*mi*(V(i)^2)*0.65/1000;
            Sre = Sf/(1-Sm/Su); % Goodman method
            Ns = c1*(Sre^b1); % Number of cycles to failure
            n = n1*V(i)*fwlm(i1,i2); % Cycles in each cell
            D1 = D1+(n/Ns); % Miner's law
          end
      end
    D(i) = D1; % Damage rate for corresponding wind velocity
      if (D(i) > 0)
        life(i3,:) = [V(i) 1/D(i)]; % Mean life time in hr.
        i3 = i3+1;
      end
  end
semilogy(life(:,1),life(:,2))
```

DAM_W

```
function [life,D]=dam_w(mu,Cpmean,Cprms,c,k,V,gg,nu1,T,Vh,Su,c1,b1)
%dam_w
%       This program calculates the wind-induced damage
%       based on Gaussian-Weibull extremum model.
%       (Ref: Lynn and Stathopoulos, 1985)
%
%       mu          = shape factor
%       Cpmean      = mean pressure coefficient
%       Cprms       = rms pressure coefficient
%       c, k        = weibull constants
%       V           = wind velocity range of interest (m/s)
%                       in column vector format
%       gg          = peak factor range of interest
%                       in column vector format
%       nu1         = cycling rate of measured time series
%       T           = time scale
```

```
%       Vh              = wind velocity at building height
%                         in full-scale
%       Su, c1, b1      = constant-amplitude test results
%
dg=gg(2)-gg(1);
i1=1;
[m,n]=size(V);
[m1,n1]=size(gg);
for i = 1:m;
  Sm = Cpmean*0.65*(V(i)^2)/1000; % Estimating mean pressure
  D1 = 0;
  nu = (V(i)/Vh)*(nu1/T); % Estimating cycling rate
    for j = 1:m1;
      if (abs(gg(j)) > 0),
        Sf = Cprms*gg(j)*0.65*(V(i)^2)/1000;
        Sre = abs(Sf/(1-Sm/Su)); % Applying Goodman method
        Ns = c1*(Sre^b1); % Estimating number of cycles to failure
          if (abs(gg(j)) > 2.5)
% weibull extremum model
          gg(j) = abs(gg(j));
          nw1 = (k/c)*((k-1)/c)*((gg(j)/c)^(k-2))*exp(-(gg(j)/c)^k);
          nw2 = ((gg(j)/c)^(2*k-2))*exp(-(gg(j)/c)^k)*(-(k^2)/(c^2));
% Estimating number of cycles (n) corresponding to a peak factor
          n = -(sqrt(2*pi)*nu*(nw1+nw2));
          D1 = D1+(n/Ns)*dg;
          else
% gaussian extremum model
          ng1 = 1+erf(mu*gg(j)/sqrt(2))+sqrt(2/pi)*(1/(mu*gg(j)))*
              exp(-(mu^2)*(gg(j)^2)/2);
          n = (1/2)*nu*gg(j)*exp(-(gg(j)^2)/2)*ng1;
          D1 = D1+(n/Ns)*dg;
        end
      end
    end
  D(i) = D1; % Damage rate for corresponding wind velocity
    if (D(i) > 0),
      life(i1,:) = [V(i) 1/(D(i)*3600)]; %  Mean life time in hr
      i1 = i1+1;
    end
end
semilogy(life(:,1),life(:,2))
axis([40 70 0.1 1000])
```

DAM_G

```
function [life,D]=dam_g(mu,Cpmean,Cprms,V,gg,nu1,T,Vh,Su,c1,b1)
%dam_g
%        This program calculates the wind-induced damage
%        based on Gaussian extremum model.
%        (Ref: Robson, 1963)
%
%        mu              = shape factor
%        Cpmean          = mean pressure coefficient
%        Cprms           = rms pressure coefficient
%        V               = wind velocity range of interest (m/s)
%                          in column vector format
%        gg              = peak factor range of interest
%                          in column vector format
%        nu1             = cycling rate of measured time series
%        T               = time scale
%        Vh              = wind velocity at building height
%                          in full-scale
%        Su, c1, b1      = constant-amplitude test results of roofing
%
%
dg=gg(2)-gg(1);
i1=1;
[m,n]=size(V);
[m1,n1]=size(gg);
for i = 1:m;
  Sm = Cpmean*0.65*(V(i)^2)/1000; % Estimating mean pressure
  D1 = 0;
  nu = (V(i)/Vh)*(nu1/T); % Estimating cycling rate
    for j = 1:m1;
      if (abs(gg(j)) > 0),
        Sf = Cprms*gg(j)*0.65*(V(i)^2)/1000;
        Sre = abs(Sf/(1-Sm/Su)); % Applying Goodman method
        Ns = c1*(Sre^b1); % Estimating number of cycles to failure
% gaussian extremum model
        ng1 = 1+erf(mu*gg(j)/sqrt(2))+sqrt(2/pi)...
            *(1/(mu*gg(j)))*exp(-(mu^2)*(gg(j)^2)/2);
        n = (1/2)*nu*gg(j)*exp(-(gg(j)^2)/2)*ng1;
        D1 = D1+(n/Ns)*dg;
      end
    end
  D(i) = D1; % Damage rate for corresponding wind velocity
  if (D(i) > 0),
    life(i1,:) = [V(i) 1/(D(i)*3600)]; %  Mean life time in hr.
```

```
    i1 = i1+1;
  end
end
semilogy(life(:,1),life(:,2))
axis([40 70 0.1 1000])
```

DAM_TOT

```
function [N,D]=dam_tot(fwlm,mi,Pd,V1,n,T,Su,c1,b1,Pth)
%dam_tot
%       First, the program estimates the total fatigue wind
%       loading matrix (N) considering the long-term climate.
%       Then, it computes the total damage (D) caused by this loading
%       on to a specified roofing material.
%
%       N       = total fatigue wind loading matrix
%       D       = total damage caused by this loading on to a specified
%                 roofing material whose constant amplitude properties
%                 are Su, b1 and c1.
%       fwlm    = cycle histogram
%       mi      = largest pressure coefficient range from the time series
%       n       = number of cycles per hour per 1m/s of wind velocity
%                 in full-scale
%       V1      = wind velocity range of interest (m/s), column vector
%       Pd      = design wind pressure (kPa)
%       T       = design life
%       Pth     = threshold level
%
% Integrating Fatigue Wind Loading Matrix (fwlm) or Cycle
% Histogram with Long-Term Wind Climate
%
p = ([4.1 8.1 7.46 2.62 2.21 2.42 4.45 5.07 3.39 5.39 11.74...
    14.07 11.81 5.73 3.59 2.83].*0.01)';
k = [1.51 1.05 1.30 1.69 1.62 1.79 1.81 1.76 1.57 1.62 1.26...
    1.40 1.45 1.83 1.67 1.43]';
c = [3.34 3.11 4.47 4.29 3.23 3.69 4.35 4.33 3.14 3.80 4.17...
    5.06 5.02 3.10 3.97 3.07]';
% p, c and k are constants for Weibull pdf of wind velocity. The above
% provided data corresponds to Montreal climate. In case of other locations,
% the above data (p, k and c)should be changed.
```

```
dv = V1(5)-V1(4);
Tr = T*365*24; % design life of structure
H = fwlm; % Cycle histogram
[m1,n1]=size(V1);
ii=1;
for i3 = 1:m1
  Pi=0.65*(V1(i3)^2)*mi/1000;
    if(Pi>=Pth)
      V(ii)=V1(i3);
      ii=ii+1;
    end
end
V=V';
[m2,n3]=size(V);
C = 0;
cl = 0:0.1:1;
N = zeros(10,10);
rang = 0.05:0.1:0.95;
meaa = 0.05:0.1:0.95;
  for i = 1:m2
    P2 = 0;
      for j = 1:16
        P1 = sum(p(j)*(k(j)/(c(j)^k(j)))*(V(i)^(k(j)-1))*exp(-(V(i)/c(j))^k(j)));
        P2 = P2+P1;
      end
    P(i) = P2;
    C1 = n*V(i)*P(i)*dv*Tr;
    Pi = 0.65*(V(i)^2)*mi/1000;
      for j1 = 1:10
        if (rang(j1)*Pi >= Pth);
          for j2 = 1:10
            if (rang(j1)*Pi > cl(j2)*Pd & rang(j1)*Pi <= cl(j2+1)*Pd)
              for j3 = 1:10
                for j4 = 1:10
                  if(meaa(j3)*Pi > cl(j4)*Pd & meaa(j3)*Pi <= cl(j4+1)*Pd)
                    N(j2,j4) = N(j2,j4)+H(j1,j3).*C1;
                  end
                end
              end
            end
          end
        end
      end
  end
```

```
  end
%
% Estimating damage using Miner's rule, Goodman's model
% and S-N curve.
%
Sm = ([0.05:0.1:0.95].*Pd)'; % mean pressure
Sr = ([0.05:0.1:0.95].*Pd)';  % pressure range
D = 0;
  for i1 = 1:10;
    for i2 = 1:10;
      Sre = Sr(i1)/(1-Sm(i2)/Su); % Goodman method
      Ns = c1*(Sre^b1);
      D1 = N(i1,i2)/Ns;
      D = D+D1;
    end
  end
```

APPENDIX - B
INTERMITTENT EXPONENTIAL RANDOM VARIABLES

The intermittent exponential random variable (ε_t) required for EARPG as well as EPG model has the form,

$$\varepsilon_t = I_t E_t \tag{B.1}$$

where, I_t is the $i.i.d$ sequence of random variables having the discrete probability density function,

I	0	1
$P_I (I = i)$	b	$(1-b)$

for $0 \leq b < 1$ $\tag{B.2}$

and E_t is the $i.i.d.$ sequence of exponential random variables having the continuous probability density function,

$$f_E(e) = \lambda \exp(-\lambda e) \tag{B.3}$$

where, the parameter λ governs the properties of this distribution. Seong (1993) used $\lambda = 1$ and as a result, the simulated preliminary signal has positively going spikes; however, through phase shift operation, negatively going spikes have been generated to represent negatively skewed roof pressure fluctuations. In the present study, $\lambda = -1$ is used which directly generates negatively going spikes. From the previously discussed properties of I_t and E_t, the first four moments (mean, variance, skewness and kurtosis) of ε_t are derived using the principles of mathematical expectation (Papoulis 1984). The derived moments are

$$mean\ (\varepsilon_t) \quad = \mu = E(\varepsilon_t) = \quad (b-1) \tag{B.4}$$

$$variance\ (\varepsilon_t) \quad = \sigma^2 = E[(\varepsilon_t - \bar{\varepsilon}_t)^2] = \quad (1 - b^2) \tag{B.5}$$

$$skewness\ (\varepsilon_t) \quad = \quad \frac{E[(\varepsilon_t - \bar{\varepsilon}_t)^3]}{\sigma^3} \quad = \quad \frac{2(b^3 - 1)}{(1 - b^2)^{3/2}} \tag{B.6}$$

$$kurtosis\ (\varepsilon_t) \quad = \quad \frac{E[(\varepsilon_t - \bar{\varepsilon}_t)^4]}{\sigma^4} \quad = \quad \frac{3(3 - 2b^2 - b^4)}{(1 - b^2)^2} \tag{B.7}$$

Since, I_t and E_t are *i.i.d.* sequences, theoretically, ε_t must also be an *i.i.d.* sequence. Therefore, ε_t at two different times are uncorrelated.

APPENDIX - C
MEASURED AND FITTED WIND PRESSURE SPECTRA

Measured pressure spectra from several low building roofs have been classified and fitted

with the proposed empirical expression as discussed in section 7.4. The results are provided

in this appendix in the form of fitted spectra along with the envelopes of measured spectra

(shaded region) for various roof zones of different roof geometries.
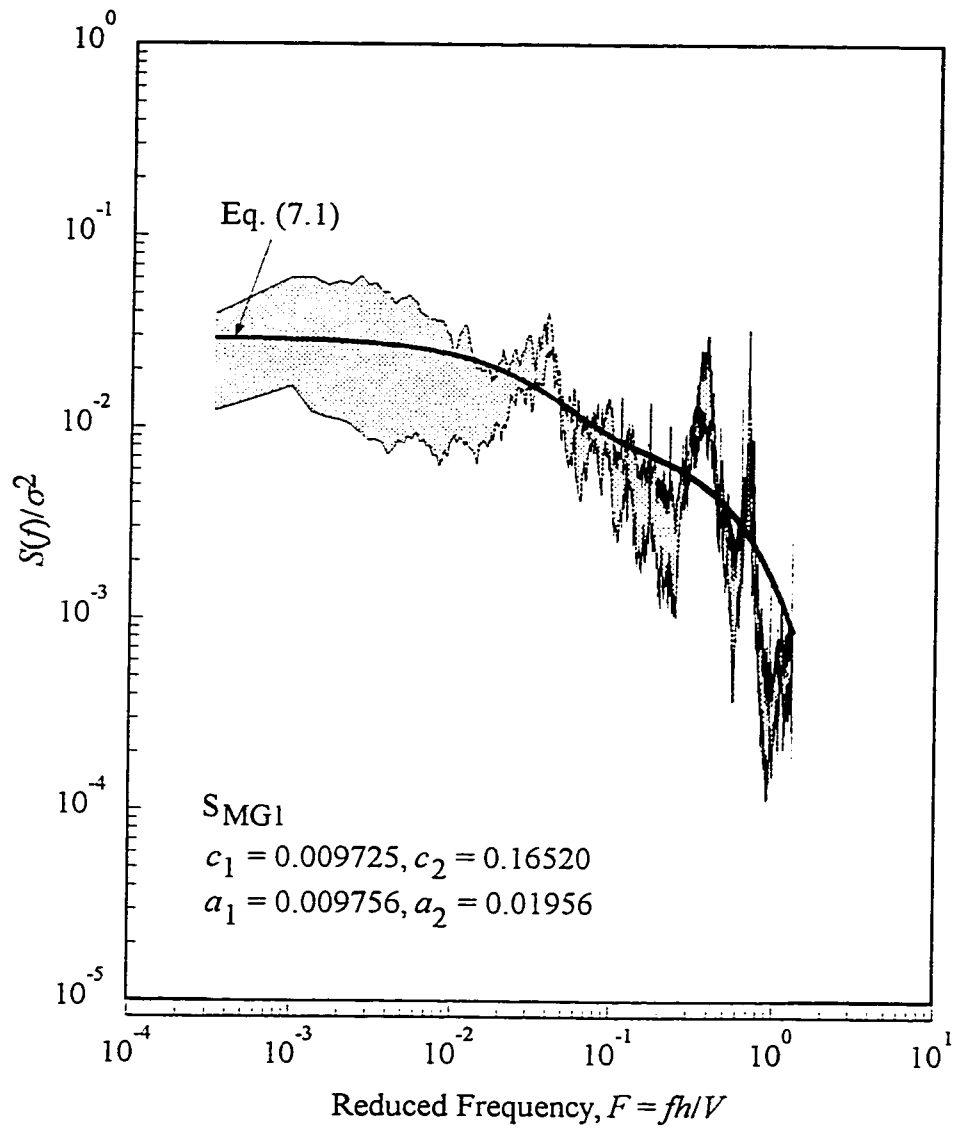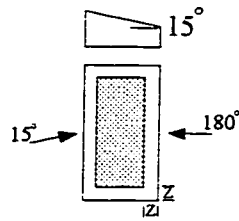
Fig. C.1 Measured and fitted wind pressure spectra
(Monoslope roof, Gaussian zone, 1st type).
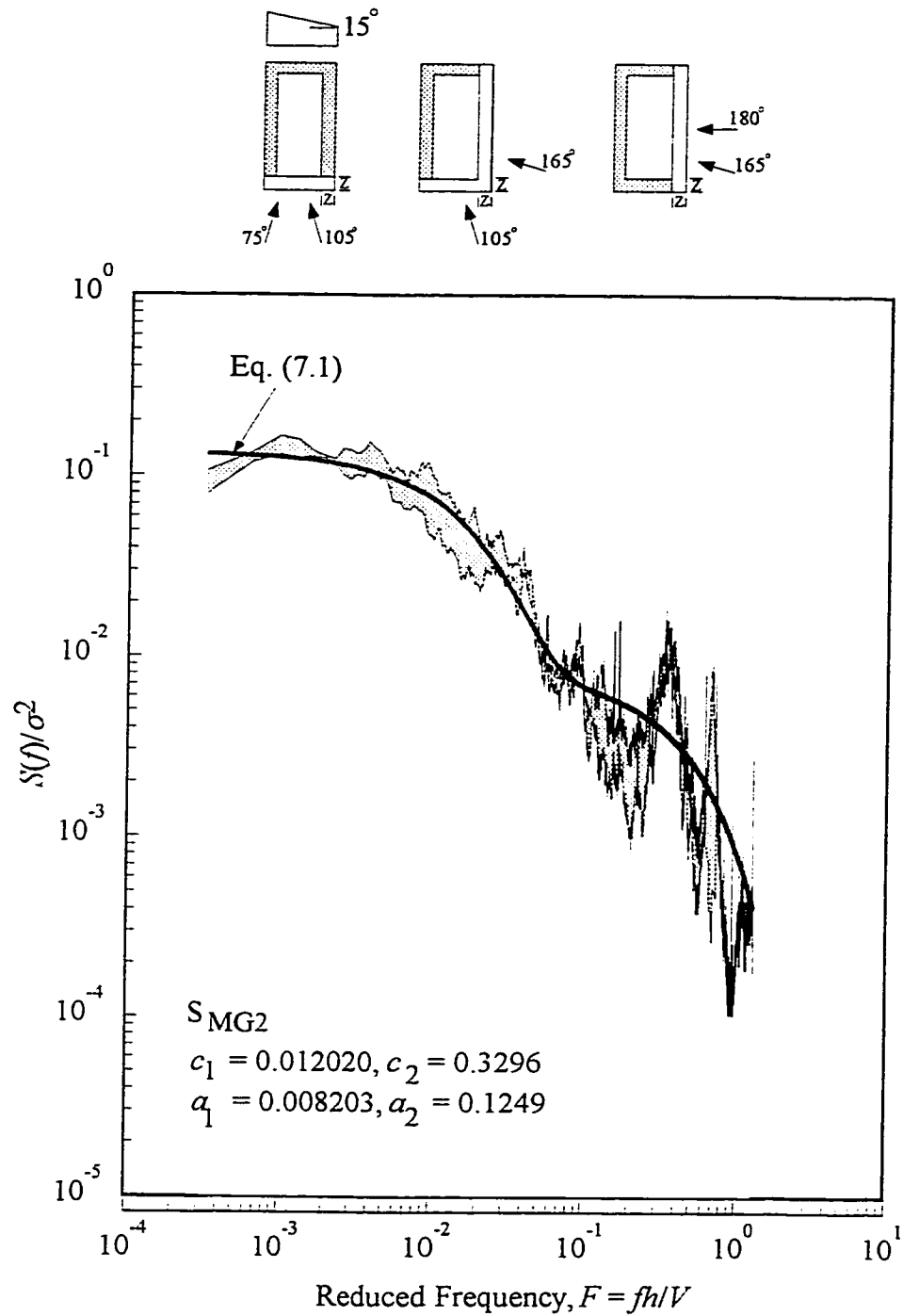
Fig. C.2 Measured and fitted wind pressure spectra
(Monoslope roof, Gaussian zone, 2nd type).
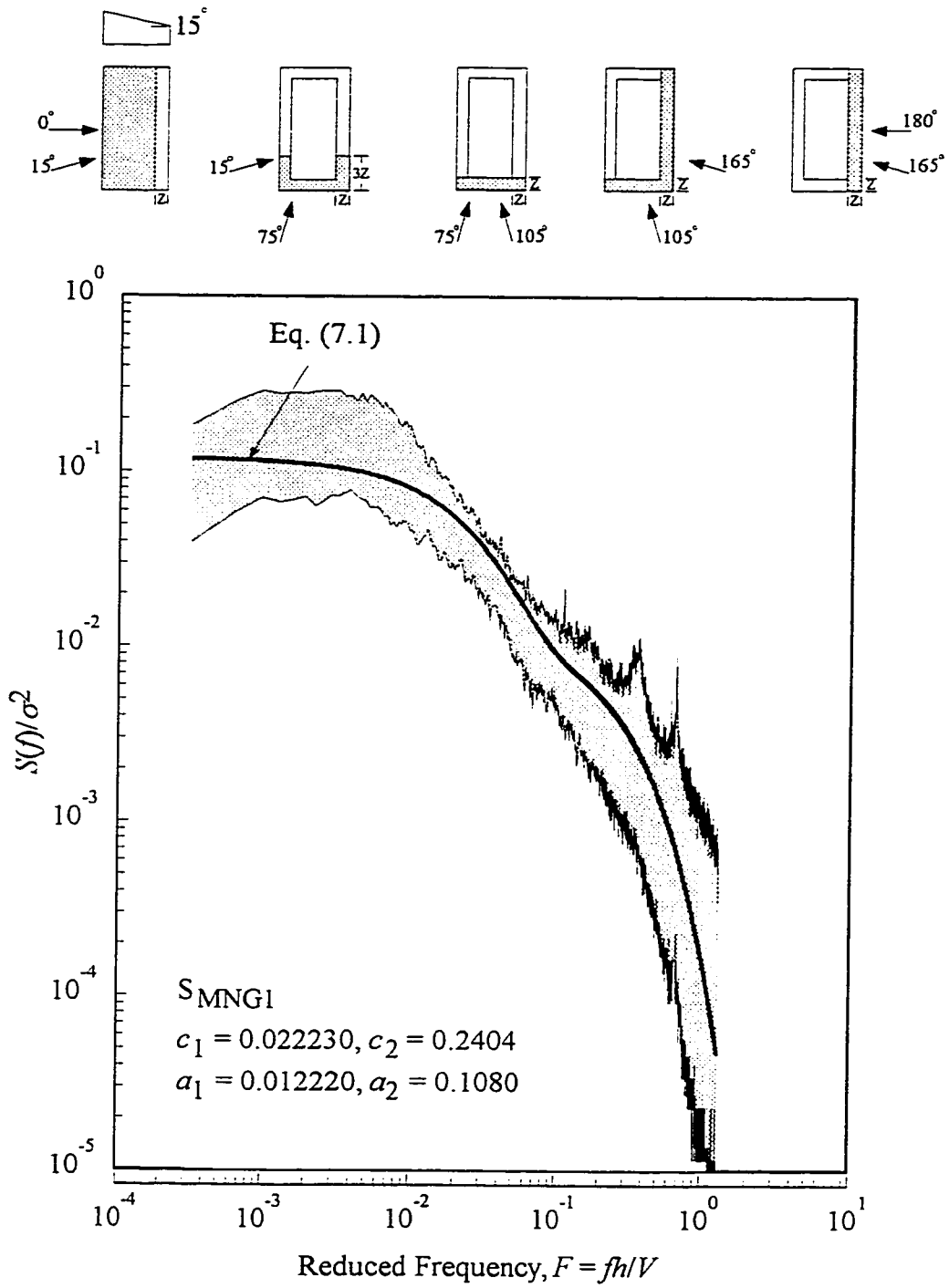
Fig. C.3 Measured and fitted wind pressure spectra (Monoslope roof, non-Gaussian zone, 1st type).
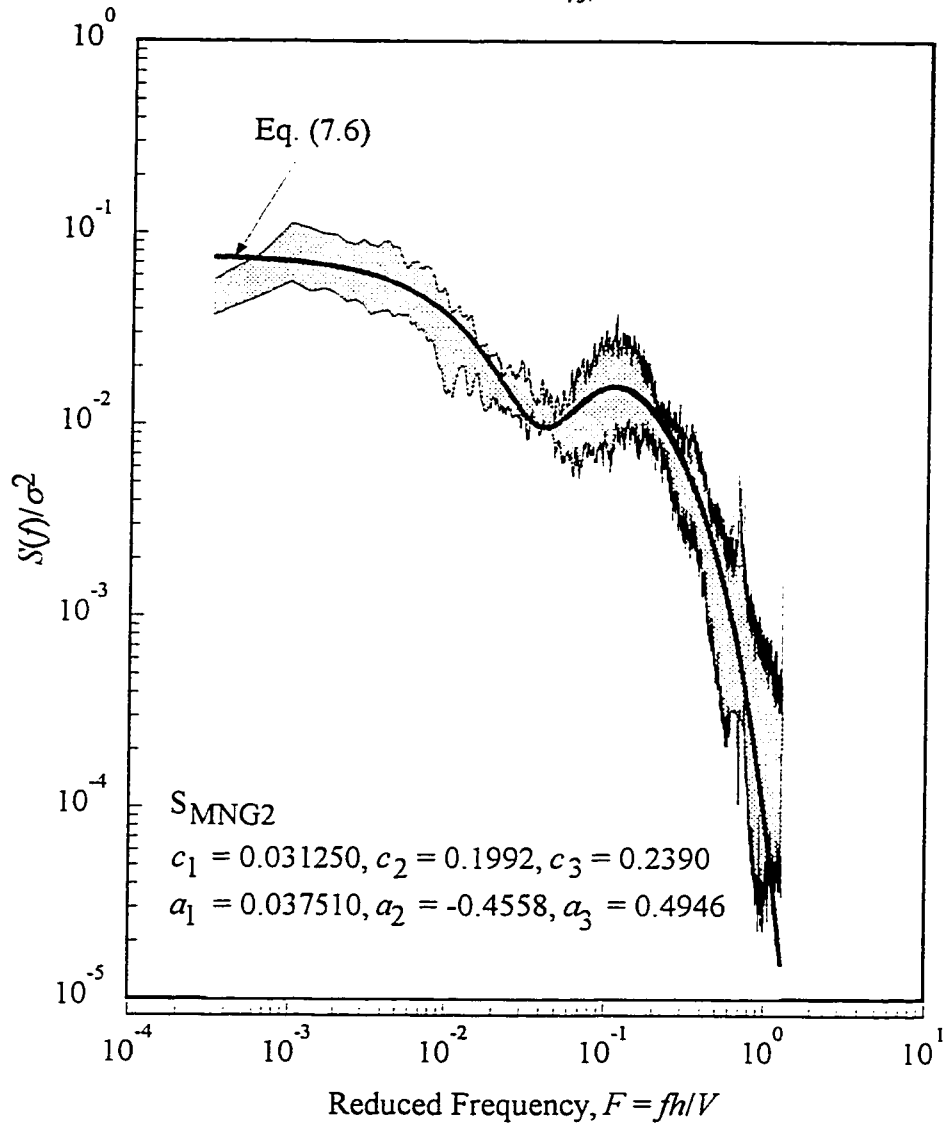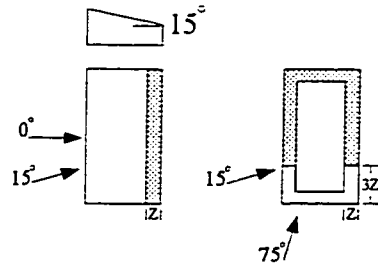
Fig. C.4 Measured and fitted wind pressure spectra
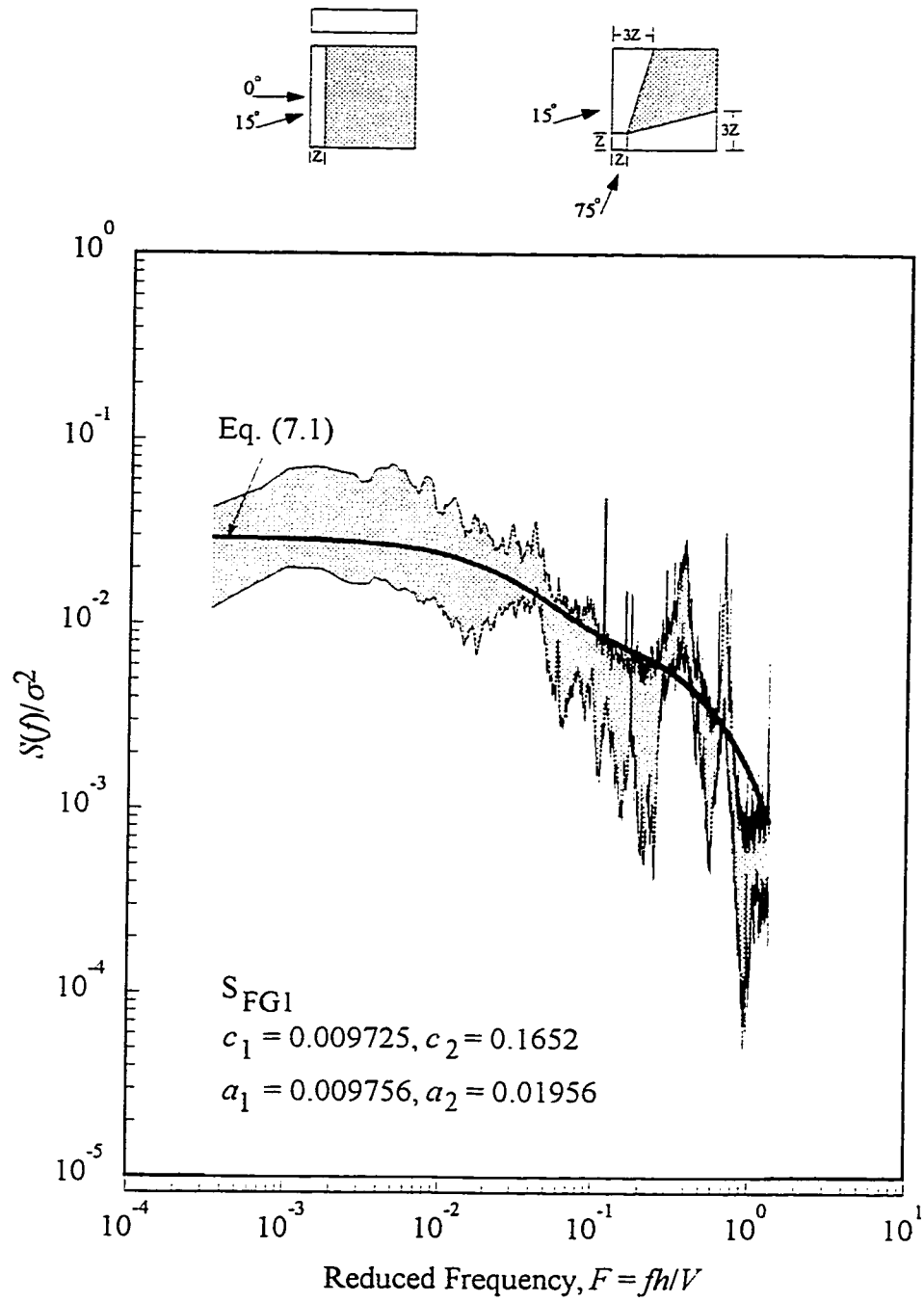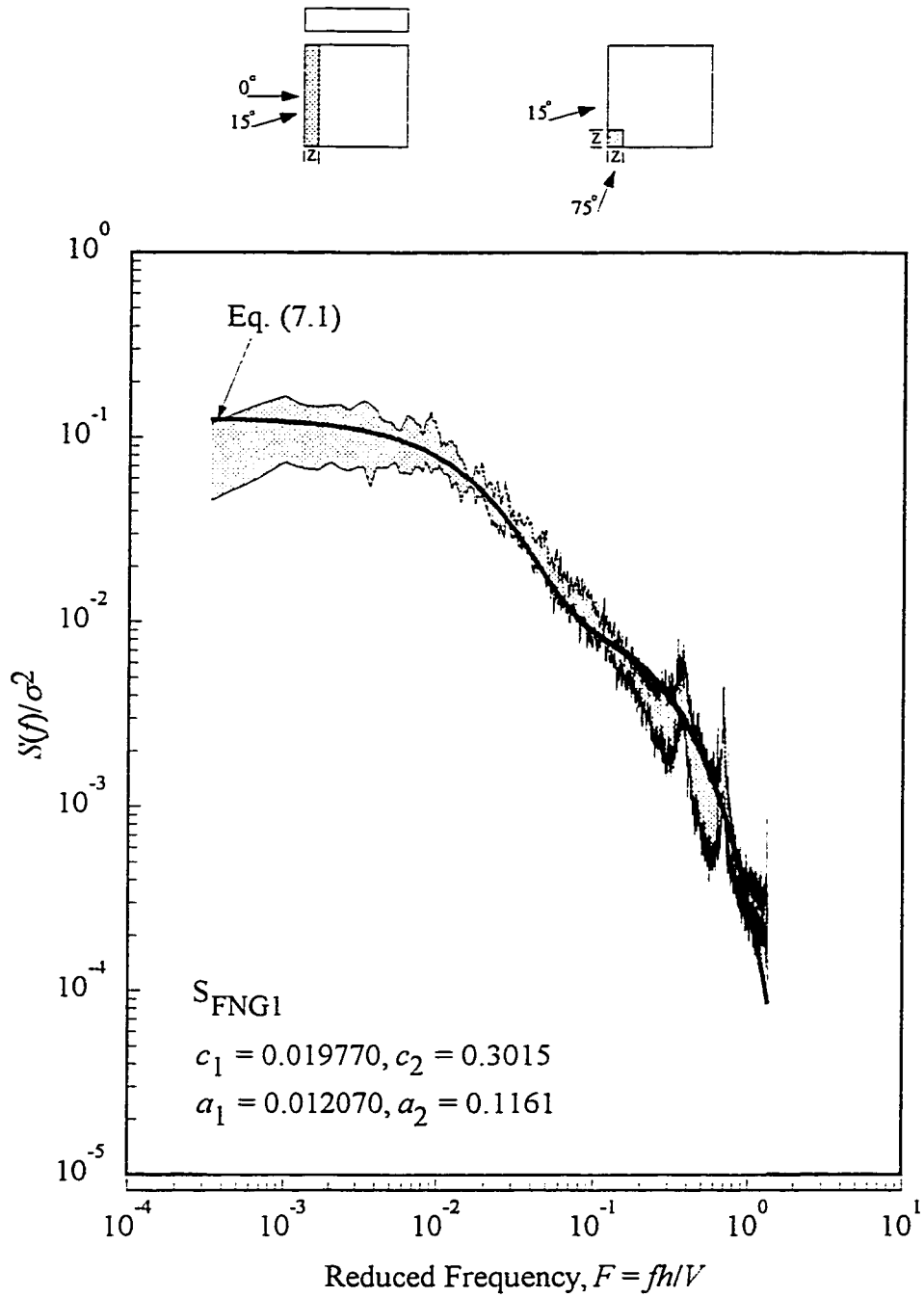(Monoslope roof, non-Gaussian zone, 2nd type).

Fig. C.5 Measured and fitted wind pressure spectra
(Flat roof, Gaussian zone, 1st type).

Fig. C.6 Measured and fitted wind pressure spectra
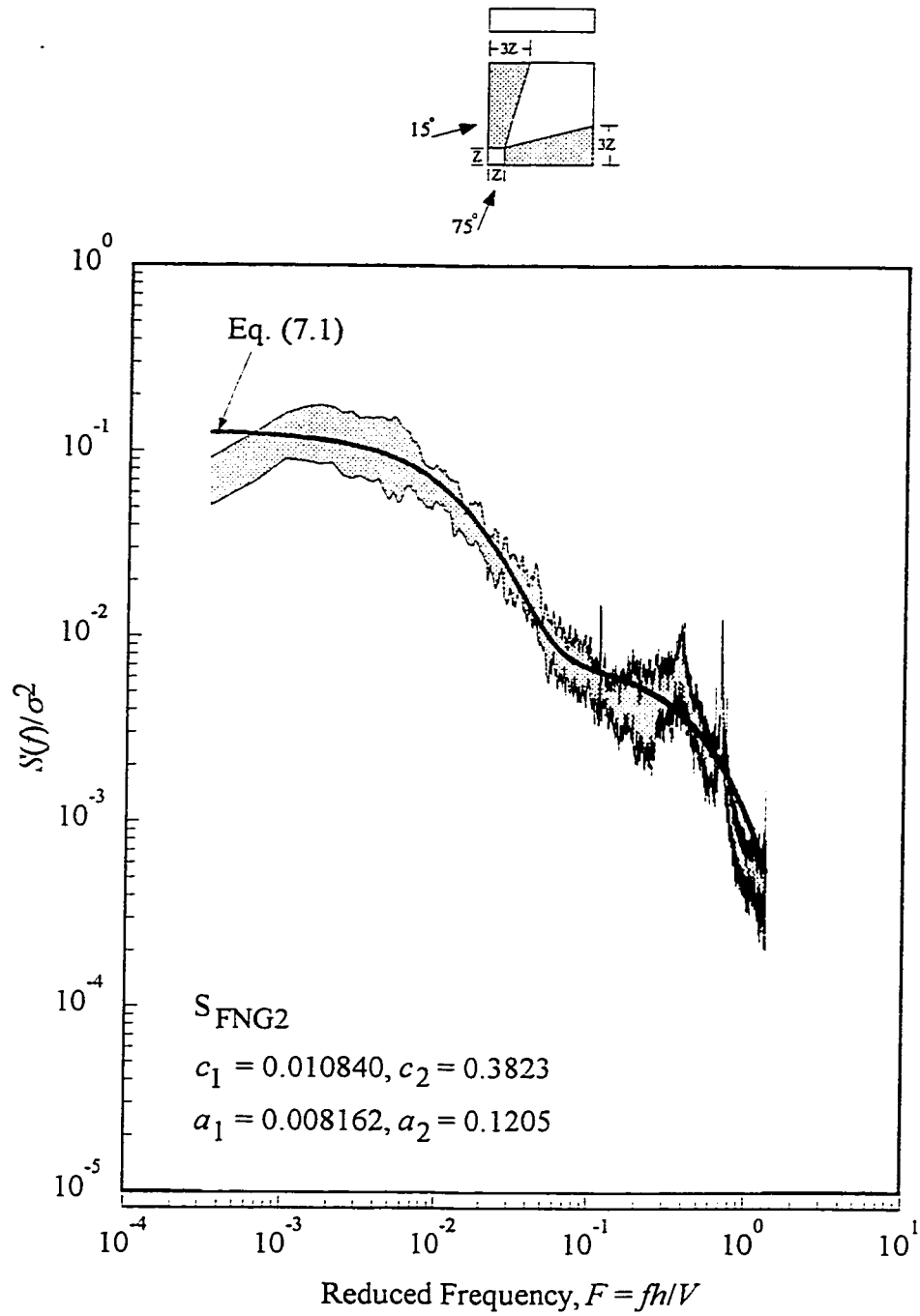(Flat roof, non-Gaussian zone, 1st type).

Fig. C.7 Measured and fitted wind pressure spectra
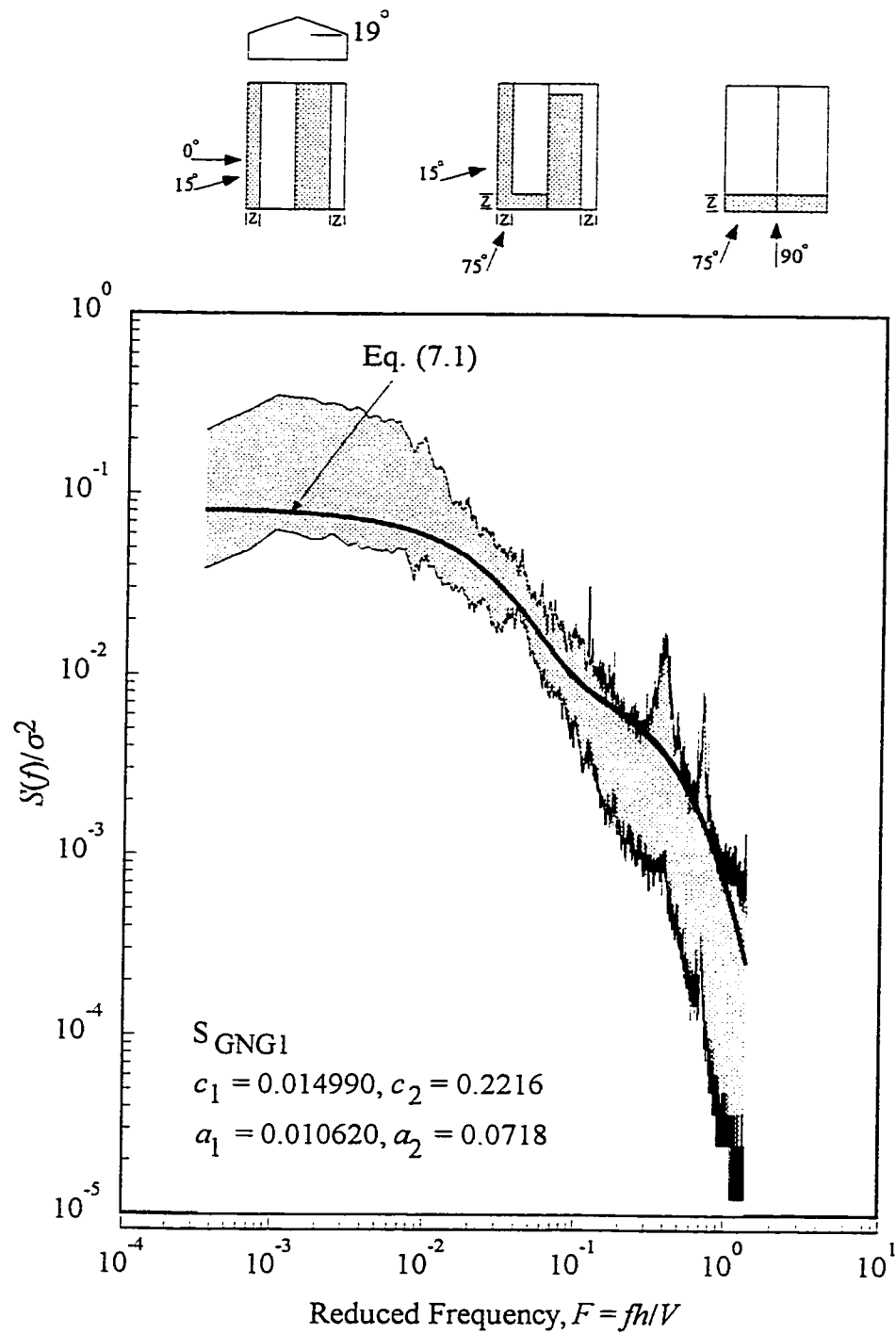(Flat roof, non-Gaussian zone, 2nd type).

Fig. C.8 Measured and fitted wind pressure spectra
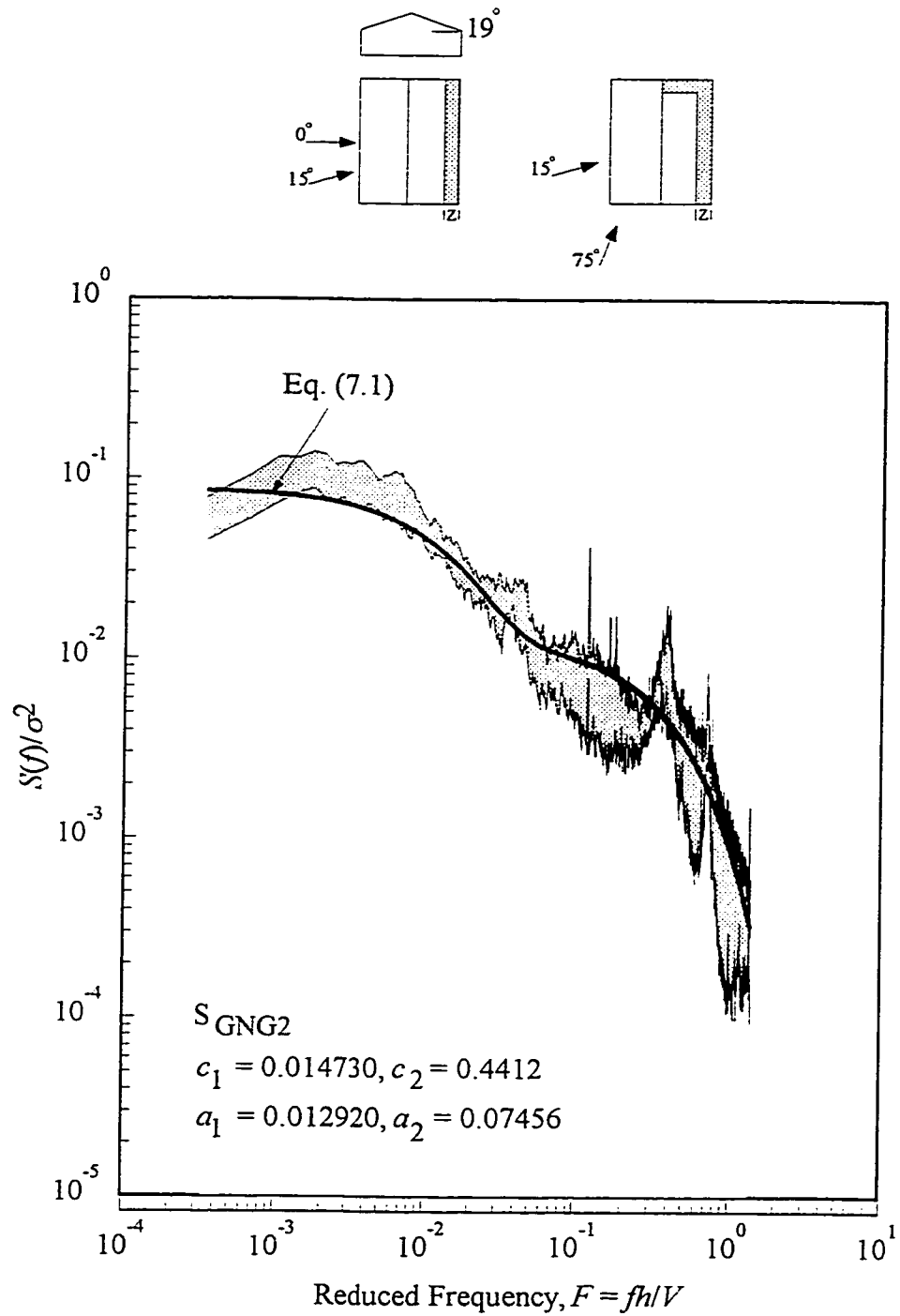(Gable roof, non-Gaussian zone, 1st type).

Fig. C.9 Measured and fitted wind pressure spectra
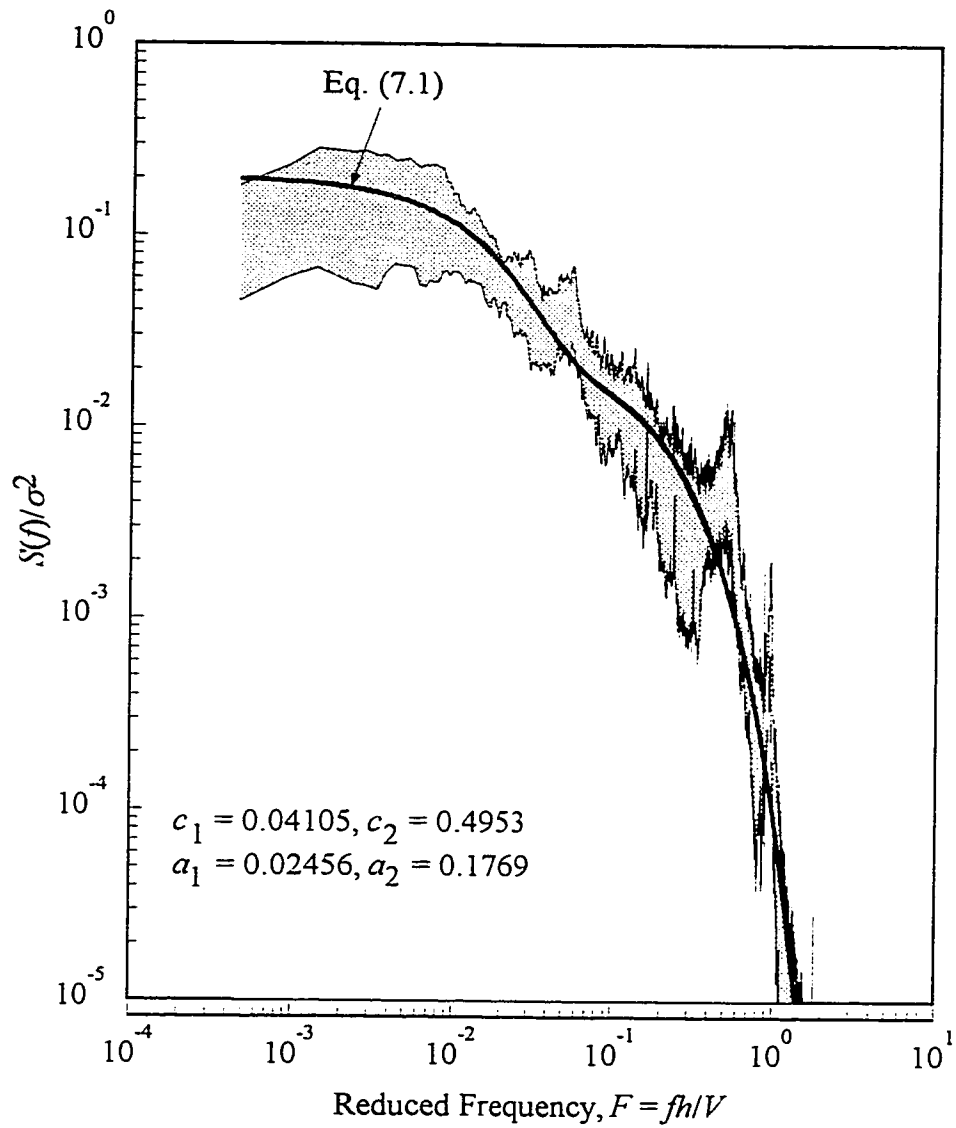(Gable roof, non-Gaussian zone, 2nd type).

Fig. C.10 Measured and fitted wind pressure spectra (Gable roof (roof angle = 45°), Gaussian zone).

The figure shows axes with vertical axis labeled $S(f)/\sigma^2$ ranging from 10^{-5} to 10^0 and horizontal axis labeled Reduced Frequency, $F = fh/V$ ranging from 10^{-4} to 10^1. The fitted curve is labeled Eq. (7.1).

$c_1 = 0.04105, c_2 = 0.4953$
$a_1 = 0.02456, a_2 = 0.1769$

APPENDIX - D
RAINFLOW COUNTING METHOD

One of the major tasks of fatigue analysis is to establish a proper expression for the load and its relationship with time or frequency. Generally, the loads can be classified as true random process or a single-amplitude sine wave or a set of discrete amplitude sine waves. For the latter two cases the definition of cycle is clear and the number of cycles can be determined by simple counting based on the type of events to be counted such as peaks, level crossings etc. However, the wind pressure fluctuations are random in nature for which the term cycle is rather confusing and counting of cycles is complex. Common cycle counting techniques in use today are peak, range, range-pair and rainflow. Of these various methods, rainflow has been shown to be superior and yields the best fatigue life estimates, especially in the case of broadband non-Gaussian process (Dowling 1972). The rainflow method can identify cycles as closed hysteresis loops and can provide range and mean values for each cycle. This method was recently used by Xu (1993) and Jancauskas et al. (1994) to count cycles of wind-induced roof pressures. Moreover, the recent standardization of this methodology by Amzallag et al. (1994) eliminates the presence of half cycles appearing in the conventional rainflow method. Therefore, this method has been adopted in this study to count the number of cycles present in pressure fluctuations. The complete procedure is coded as a MATLAB function, namely, **RFLOW** and is presented in Appendix - A.

D.1 EXTRACTION OF EXTREMA

A basic treatment of the loading, namely extraction of extrema, is required before the rainflow procedure has been applied. Peaks as well as valleys (S) of a pressure time series can be identified and stored using simple MATLAB program. The first part of MATLAB function named **RFLOW** (see Appendix - A) is used to identify peaks and valleys of a given time series in all the calculations.

D.2 EXTRACTION OF CYCLES

The cycle extraction procedure starts with the first four successive points (1,2,3, and 4 in Fig. D.1) in a sequence of extrema (S). Thereafter, three consecutive ranges are determined: $\Delta S_1 = |S_2 - S_1|$, $\Delta S_2 = |S_3 - S_2|$ and $\Delta S_3 = |S_4 - S_3|$. If $\Delta S_2 \leq \Delta S_1$ and $\Delta S_2 \leq \Delta S_3$, then: (1) the cycle represented by its extreme values S_2 and S_3 is extracted; (2) the two points S_2 and S_3 are discarded; (3) the two remaining parts are connected to each other. If not, the following point is considered and the same procedure is applied using points 2,3,4 and the new point, 5. The procedure is repeated until the last point of the sequence is reached. The leftover points (points which are not included in cycle extraction) constitute the residue.

D.3 TREATMENT OF RESIDUE

The residue is a sequence representing number of half cycles left out after the extraction of
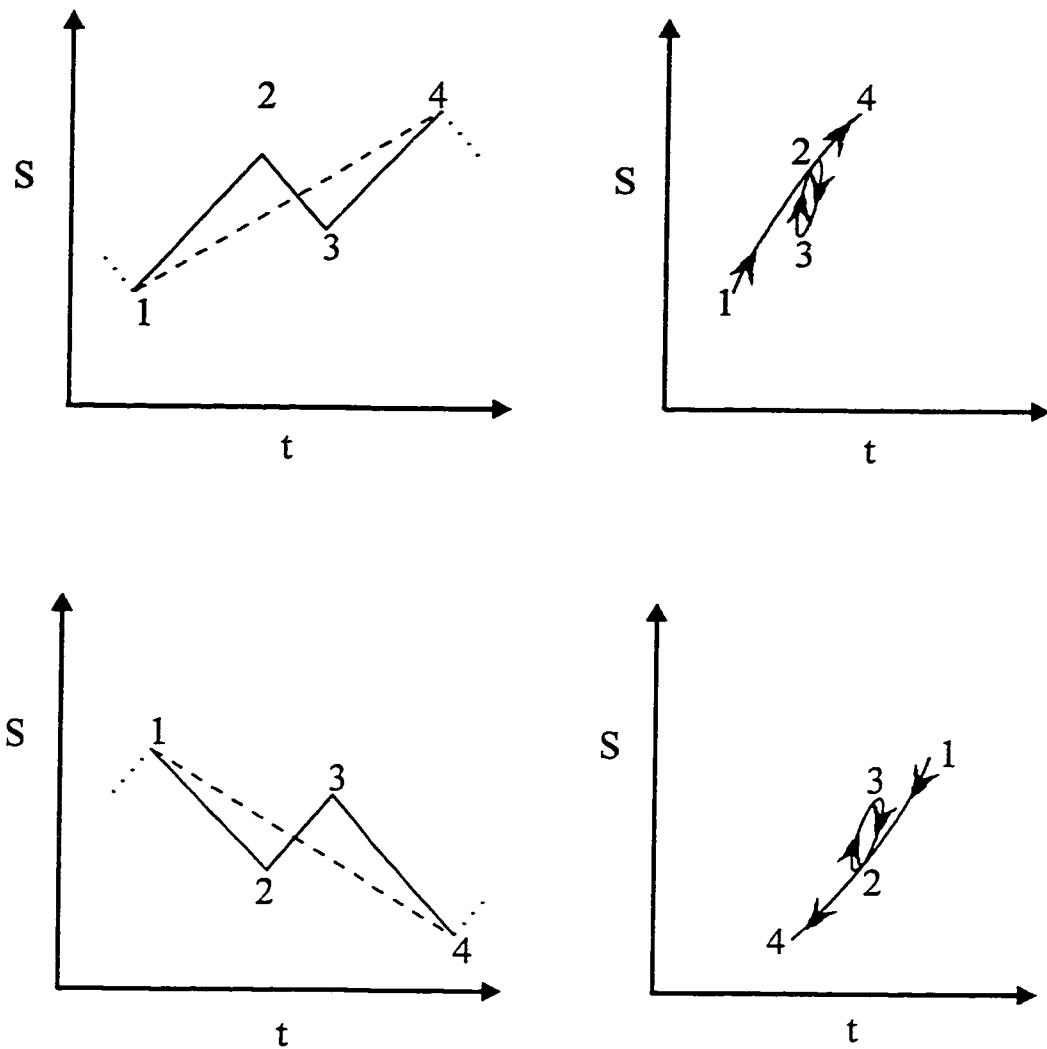
Fig. D.1 Principles of cycle extraction, after Amzallag et al. (1994).

cycles. Further, the cycles can be extracted from a residue by adding the residue to itself and applying the previous rainflow technique to the sequence composed of two residues. The residue left out of this procedure is identical to the first one. In this way, the sequence can be decomposed into cycles completely. Note that care should be taken while joining the two residues. Depending on their initial and final relative values and slopes, AFNOR A03 - 406 (1993) provides some special way of joining two residues as shown in Fig. D.2
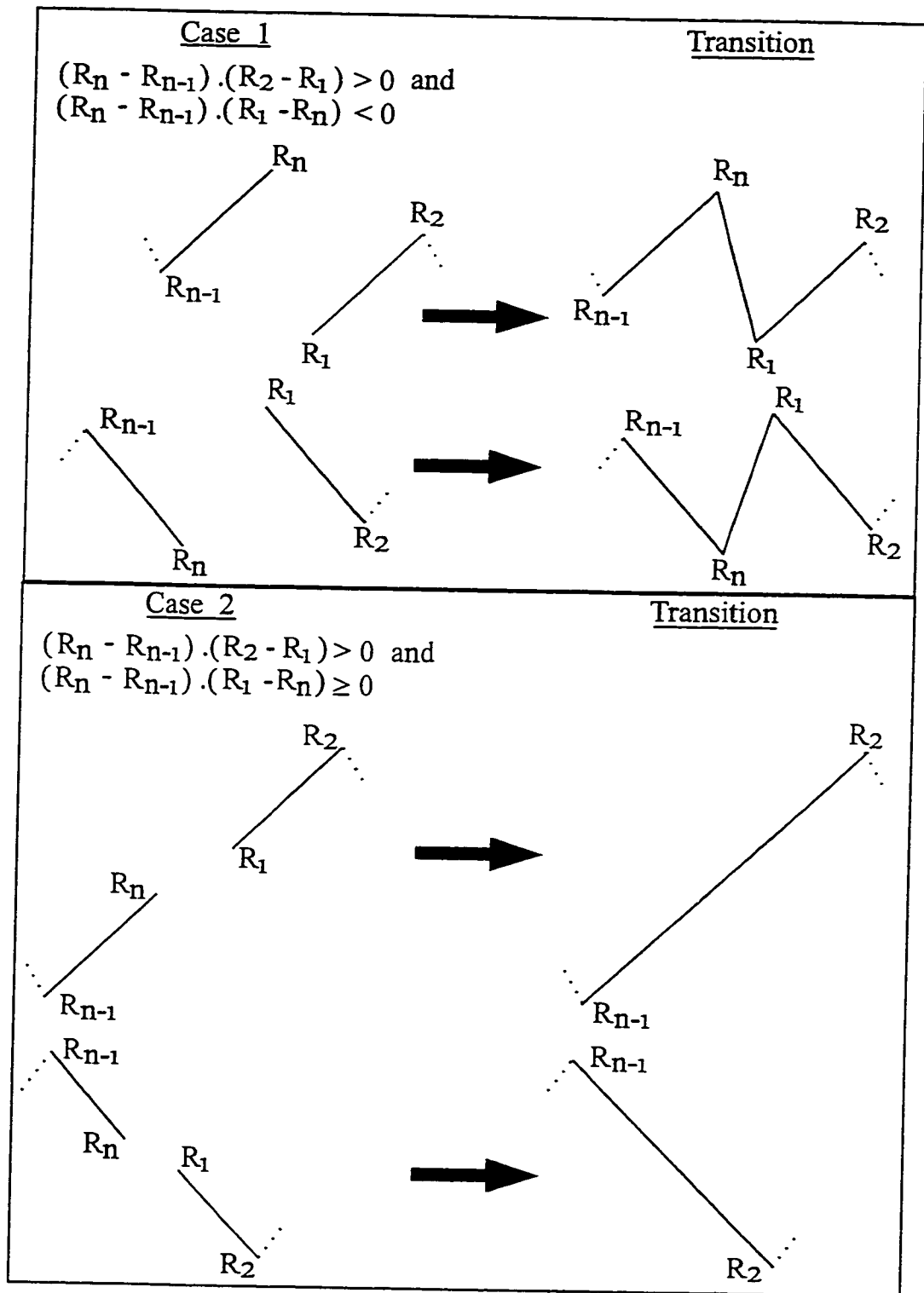
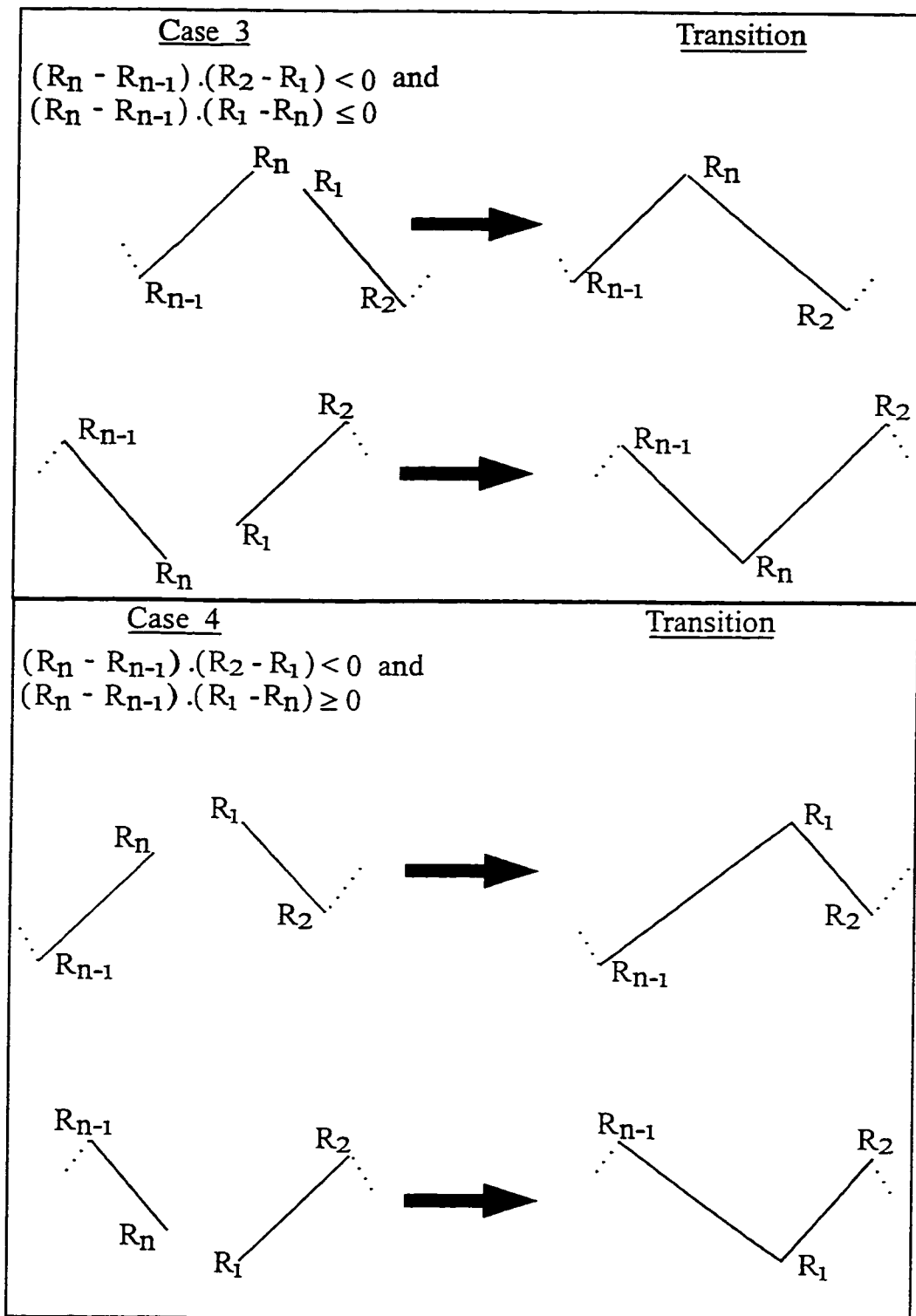**Fig. D.2** Joining two residues, after AFNOR A03 - 406 (1993).

Fig. D.2 Continued.

D.4 STORING CYCLES

The application of rainflow method will result in number of cycles corresponding to various mean and range values of pressures. It may be further necessary to quantify these established cycles in a more comprehensive and simplistic way so that it can be applied in practice. Within this context, the mean and range values of cycles are divided into certain number of classes of constant width interval, and all values (mean and range) located in a given class are replaced by a representative value of this class (the mean value is usually chosen). Finally, the number of cycles corresponding to representative mean and range of each class are stored in a matrix format for further analysis. A flowchart showing the complete rainflow procedure is presented in Fig. D.3.
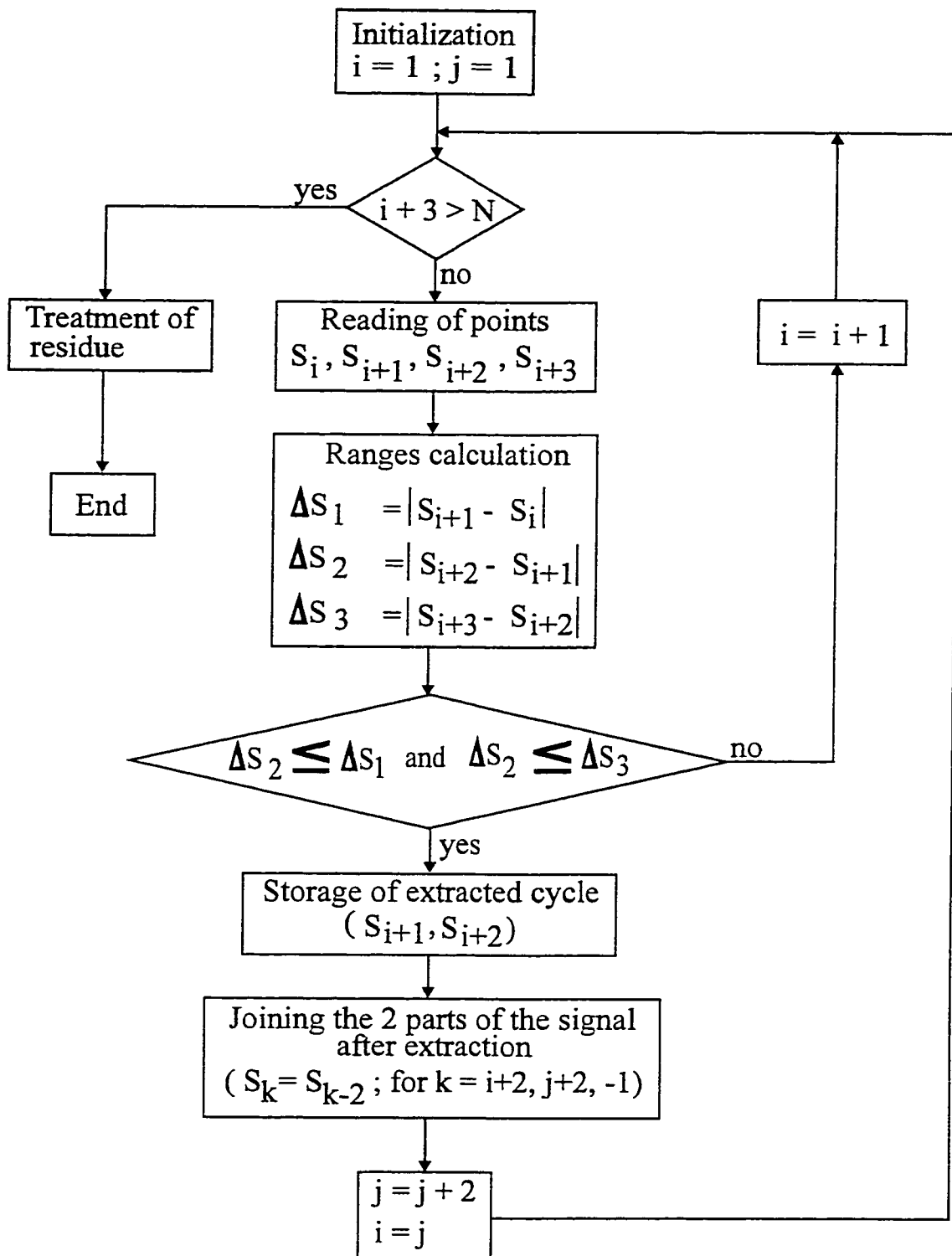
Fig. D.3 Rainflow algorithm, after Amzallag et al. (1994).